Superpixel Spectral Photoacoustic Imaging of Tissue Chromophores: "En Route to the Clinics"

A dissertation by

Valeria Grasso

Submitted in Fulfillment of the Requirements for the

Degree of Doctor of Engineering Science (Dr.-Ing.)

Faculty of Engineering

Christian-Albrechts-Universität zu Kiel

Kiel, 2023

Supervisors:

Dr. Jithin Jose

Prof. Dr. Regine Willumeit-Römer

Examination Committee:

First reviewer: Prof. Dr. Regine Willumeit-Römer

Second reviewer: Prof. Dr. Jan-Bernd Hövener

Prof. Dr. Zeynep Altintas

Prof. Dr. Rainer Adelung

Date of the oral examination: 28 April 2023

Declaration

I hereby declare that the work embodied in this dissertation is the result of original research, is free of plagiarized materials, and to the best of my knowledge I believe that I have identified and referred other authors' work and used none but the indicated sources.

I declare that this dissertation has not been submitted either partially or wholly as part of a doctoral degree to another examining body of any other University or Institution and it has not been published or submitted for publication.

I declare that this dissertation has been prepared subject to the Rules of Good Scientific Practice of the German Research Foundation.

I declare that this dissertation has not been withdrawn from an academic institution.

Valeria Grasso

Christian-Albrechts-Universität zu Kiel

Date:
23 Dec 2022

Signature:


Authorship/Co-authorship Attribution Statement

I, Valeria Grasso, state here the nature of my involvement to the work in the following publications which form this dissertation. In particular, this thesis contains material from 5 papers published in the following peer-reviewed journals in which I am listed as an author. Specifically:

- **Chapter 2** is published as:

Valeria Grasso, Hafiz Wajahat Hassan, Peyman Mirtaheri, Regine Willumeit-Römer, and Jithin Jose. "Recent advances in photoacoustic blind source spectral unmixing approaches and the enhanced detection of endogenous tissue chromophores." *Frontiers in Signal Processing*: 67 Volume 2 – (2022).

VG: prepared the tissue-mimicking phantoms, conducted the *in vivo* and *ex vivo* experiments, designed and performed data analysis, implemented the algorithm script, and wrote the original draft of the manuscript.

- **Chapter 3** is published as:

Valeria Grasso, Joost Holthof, and Jithin Jose. "An automatic unmixing approach to detect tissue chromophores from multispectral photoacoustic imaging." *Sensors* 20, no. 11 (2020): 3235.

VG: implemented *in silico* data, conducted the tissue-mimicking phantoms experiments, assisted the *in vivo* experiments, implemented data analysis and image processing, designed the algorithm script, and wrote the original draft of the manuscript.

- Part of **Chapter 4** is published as:

Valeria Grasso, Jason Raymond, Regine Willumeit-Römer, James Joseph, and Jithin Jose. “Development and characterization of a durable tissue-mimicking phantom for calibration and standardization of photoacoustic imaging." *Photons Plus Ultrasound: Imaging and Sensing* 2023. SPIE, 2023.

VG: was involved in initial discussions in developing the idea of this project, designed/developed/fabricated the 3D printed morphologically realistic mouse phantom, conducted the phantoms experiments, prepared tissue-mimicking material samples for optical and acoustic characterization, implemented data analysis and image processing, and wrote the original draft of the manuscript.

- Part of **Chapter 4** is under review for publication as:

Valeria Grasso, Jason Raymond, Regine Willumeit-Römer, James Joseph, and Jithin Jose. "Development of a morphologically realistic mouse phantom for pre-clinical photoacoustic imaging." *Medical Physics* (2023).

VG: was involved in initial discussions in developing the idea of this project, designed/developed/fabricated the 3D printed morphologically realistic mouse phantom, conducted the phantoms experiments, prepared tissue-mimicking material samples for optical and acoustic characterization, implemented data analysis and image processing, and wrote the original draft of the manuscript.

- **Chapter 5** is published as:

Valeria Grasso, Regine Willumeit-Römer, and Jithin Jose. "Superpixel spectral unmixing framework for the volumetric assessment of tissue chromophores: A photoacoustic data-driven approach." *Photoacoustics* 26 (2022): 100367.

VG: was involved in initial discussions in developing the idea of this project, implemented *in silico* data, prepared the tissue-mimicking phantoms, conducted the *in vivo* experiments, designed and performed data analysis, design/development/test of the algorithm framework, and wrote the original draft of the manuscript.

- **Chapter 6** is published as:

Valeria Grasso, Regine Willumeit-Römer, and Jithin Jose. "Unsupervised multi-spectral photoacoustic framework for the detection and quantification of tissue chromophores." In *2021 IEEE International Ultrasonics Symposium (IUS)*, pp. 1-4. IEEE, 2021.

VG: prepared the tissue-mimicking phantoms, conducted the *in vivo* experiments, designed and performed data analysis, design/development/test of the algorithm framework, and wrote the original draft of the article.

- Part of **Chapter 7** is published as:

Hafiz Wajahat Hassan, **Valeria Grasso**, Olga Korostynska, Haroon Khan, Jithin Jose, and Peyman Mirtaheri. "An overview of assessment tools for determination of biological Magnesium implant degradation." *Medical Engineering & Physics* 93 (2021): 49-58.

VG: conducted the tissue-mimicking phantom experiment, performed validation experiments, wrote sections of the manuscript, and edited the article draft.

- Part of **Chapter 7** is published as:

Hafiz Wajahat Hassan, Eduarda Mota-Silva, **Valeria Grasso**, Leon Riehakainen, Jithin Jose, Luca Menichetti, and Peyman Mirtaheri. “Near-infrared spectroscopy for the in vivo monitoring of biodegradable implants in rats.” *Sensors* 23.4 (2023): 2297.

VG: conducted the photoacoustic image processing and analysis, wrote sections of the manuscript, and edited the article draft.

- Part of **Chapter 8** is published as:

Valeria Grasso, Regine Willumeit-Römer, and Jithin Jose. "Development of an AI-assisted multi-spectral photoacoustic imaging for volumetric molecular tissue composition: a multi-frequency translational approach." *Photons Plus Ultrasound: Imaging and Sensing* 2023. Vol. 12379. SPIE, 2023.

VG: implemented *in silico* photoacoustic data, prepared the tissue-mimicking phantoms, conducted the experiments, designed and performed data analysis, design/development/test of the algorithm framework, and wrote the original draft of the manuscript.

- Part of **Chapter 8** is submitted for publication as:

Valeria Grasso, Regine Willumeit-Römer, and Jithin Jose. "Multi-frequency photoacoustic imaging for tissue monitoring in presence of biodegradable bone implants: “En route to the clinics”.” *Sensors* (2023).

VG: implemented *in silico* photoacoustic data, prepared the tissue-mimicking phantoms, conducted the experiments, designed and performed data analysis, design/development/test of the algorithm framework, and wrote the original draft of the manuscript.

Date:
June 2023

Signature:


To my lovely family

Abbreviations

2D	Two-Dimensional	**FIR**	Far Infrared
3D	Three-Dimensional	**FOV**	Field Of View
3R	Replacement-Refinement-Reduction	**FWHM**	Full Width At Half Maximum
AI	Artificial Intelligence	**GPU**	Graphics Processing Units
BAT	Brown Adipose Tissue	**iBAT**	Interscapular Brown Adipose Tissue
BSS	Blind Source Separation	**ICA**	Independent Component Analysis
CAD	Computer-Aided Design	**ICG**	Indocyanine Green
CEUA	Animal Use And Ethics Committee	**IL**	Intralipid
CM	Confocal Microscopy	**IPASC**	International Photoacoustic Standardization Consortium
CMUT	Capacitive Micromachined Ultrasonic Transducer	**LED**	Light-Emitting Diode
CPU	Central Processing Unit	**LMM**	Linear Mixture Model/Matrix
CT	Computed Tomography	**LU**	Linear Unmixing
DAQ	Data Acquisition	**MBD**	Methylene Blue Dye
DAS	Delay And Sum	**MC**	Monte Carlo
DL	Deep Learning	**MCR**	Multivariate Curve Resolution Analysis
DMAS	Delay Multiply And Sum	**Mg**	Magnesium
DOT	Diffuse Optical Tomography	**MIP**	Maximum Intensity Projection
ECG	Electrocardiogram	**ML**	Machine Learning
FDA	Food And Drug Administration	**MRI**	Magnetic Resonance Imaging
FFT	Fast Fourier Transform	**NIR**	Near-Infrared

NIRS	Near-Infrared Spectroscopy	**RTE**	Radiative Transfer Equation
NNMF	Non-Negative Matrix Factorization	**SEBS**	Styrene-Ethylene-Butylene-Styrene
OCT	Optical Coherence Tomography	**SLA**	Stereolithographic
OPO	Optical Parametric Oscillator	**SNR**	Signal-To-Noise Ratio
PA	Photoacoustic	**SO_2**	Oxygen Saturation
PAI	Photoacoustic Imaging	**SOS**	Speed Of Sound
PBS	Phosphate Buffered Saline	**sPAI**	Spectral Photoacoustic Imaging
PC	Principle Component	**SPAX**	Superpixel Photoacoustic Unmixing
PCA	Principle Component Analysis	**SPECT**	Single-Photon Emission Computed Tomography
PDMS	Polydimethylsiloxane	**STL**	Standard Tessellation Language
PET	Positron Emission Tomography	**SVD**	Singular Value Decomposition
PML	Perfectly Matched Boundary Layer	**TGC**	Time Gain Compensation
PMUT	Piezoelectric Micromachined Ultrasound Transducer	**Ti**	Titanium
PVA	Polyvinyl Alcohol	**TMM**	Tissue-Mimicking Material
PVCP	Polyvinyl Chloride Plastisol	**US**	Ultrasound
PZT	Piezoelectric	**US-PA**	Ultrasound-Photoacoustic
RAM	Random Access Memory	**UV**	Ultraviolet
RF	Radio Frequency	**WAT**	White Adipose Tissue
RICA	Reconstruction Independent Component Analysis	**µCT**	Micro Computed Tomography
ROI	Region Of Interest		

Abstract

Photoacoustic imaging (PAI) is an emerging biomedical imaging technology that has the potential to monitor tissue molecular composition in addition to structural and functional information. PAI is a hybrid modality that combines optical and acoustic imaging. Specifically, the technology is based on the conversion of absorbed nanosecond pulsed laser light into acoustic waves that can be detected just as conventional ultrasound (US) signals. This guarantees the advantages of strong optical contrast as well as high US resolution and imaging depth (up to several cm). Further advantages, such as the non-invasive, label-free, and radiation-free nature of PAI have also facilitated its exponential growth over the last two decades, among a wide range of applications including cardiovascular, oncology, dermatology, neurology, and developmental biology. Since tissue chromophores have distinct wavelength-dependent spectral absorption signatures, spectral PAI (sPAI) is intrinsically sensitive to visualize and quantify molecular component distribution in tissues. Thus, by illuminating the tissues at different wavelengths, molecular information based on either endogenous chromophores (like oxygenated and deoxygenated hemoglobin, lipid, melanin, collagen, and water) or a variety of exogenous contrast agents or both can potentially be differentiated.

Linear unmixing methods based on differential or fitting algorithms are commonly used to separate the underlying tissue components contributing to the sPAI. Although this fitting-based approach yields acceptable results, it requires user supervision in the form of providing the spectral curves as *a priori* information. This can be challenging, as the theoretical spectral signatures of the tissue components could differ concerning to the disease conditions and the results can be biased. Furthermore, this approach assumes that the most prominent absorbers such as hemoglobin, are the sole tissue absorbers, not accounting for the presence of other less prominent or weaker absorbing molecules (e.g., extrinsic molecules, melanin, lipids, etc.). Therefore the less prominent absorbers are discarded with the conventional unmixing, thus leading to incomplete tissue composition. In addition, this conventional approach can also be hampered due to spectral coloring. This is a prominent distortion effect that induces spectral changes at depth, due to light fluence attenuation, and consequently leads to misinterpretations of the components' absorption spectra. Therefore, there still exist some limitations in the current PAI unmixing in terms of molecular sensitivity and specificity.

Another limitation of PAI is the lack of standardized methods to test imaging system configurations or newly developed algorithms with high fidelity and accuracy. In comparison to well-established medical imaging modalities such as MRI, CT/PET, and Ultrasound, these rely on realistic and commercially available tissue-mimicking phantoms. On the other end, since PAI is a

pretty recent technology, an unmet need still exists to establish anthropomorphic heterogeneous phantoms that can accelerate advanced applications of the technology.

Finally, photoacoustic (PA) signals have a broadband frequency content by nature, which can span from Kilohertz to several tens of Megahertz. However, the US transducers used for measuring the photoacoustic signals are not ideal point detectors with infinite bandwidth. Thus, the limited frequency bandwidth of the US transducers might exclude the acquisition of significant PA imaging details. This is crucial, especially for translational research with patients. Recently advanced applications such as the use of biodegradable bone implants are becoming increasingly popular for treating bone fractures in humans. In this case, it would be more effective the combination of photoacoustic imaging at high-frequency to monitor superficial revascularization and low frequency for implant osseointegration at depth. Thus, the combination of multi-frequency band transducers in PAI would lead to a complete and more exhaustive tissue characterization that can facilitate translational research.

In this thesis work, I aim to optimize the potential of the innovative photoacoustic imaging technology, by developing advanced machine learning algorithms that can automatically monitor and quantify the tissue molecular features of vital importance. I primarily focused to identify tissue biomarkers from PAI without any *a priori* knowledge and user interactions as it can enhance the diagnosis, treatment, and monitoring of the tissue changes in a large number of diseases. In addition, the development of durable anthropomorphic phantoms would minimize animal experiments in compliance with the 3R (Replacement, Reduction, and Refinement) principle. This opens many possibilities to accurately test advanced methods in PAI, which leads to higher chances of success in the in-vivo experiments. Finally, the use of multiple US transducers with different frequency bandwidths for photoacoustic imaging and its impact on translational applications are investigated. Thus, having PA images at multiple scales, resolutions, and depths will lay the foundation for future advances in clinical translation of the technology. This is fundamental, especially in applications where photoacoustic can contribute by providing novel insights such as to follow-up tissue regeneration in presence of biodegradable implants used to fix bone fractures in human patients.

Zusammenfassung

Die fotoakustische Bildgebung (Photoacoustic Imaging, PAI) ist eine aufstrebende biomedizinische Bildgebungstechnologie, die das Potenzial hat, neben strukturellen und funktionellen Informationen gleichzeitig die molekulare Zusammensetzung von Gewebe darzustellen. Dabei kombiniert die PAI optische und akustische Bildgebung. Die Technologie basiert auf der Umwandlung von absorbiertem, im Nanosekundenbereich gepulstem Laserlicht in Schallwellen, die wiederum wie herkömmliche Ultraschallsignale (US) detektiert werden. So werden die Vorteile eines starken optischen Kontrastes mit der hohen Auflösung und Abbildungstiefe (bis zu mehreren cm) von Ultraschallsignalen kombiniert. Weitere Vorteile der PAI sind ihre nicht-invasive, kontrastmittel- und strahlungsfreie Natur, so dass PAI in den letzten zwei Jahrzehnten zunehmend in einem breiten Spektrum kardiovaskulärer Anwendungen eingesetzt wurde, von der Onkologie, Dermatologie und Neurologie bis hin zur Entwicklungsbiologie.

Da im Gewebe bereits vorhandene Chromophore unterschiedliche wellenlängenabhängige spektrale Absorptionssignaturen aufweisen, eignet sich die spektrale PAI (sPAI) dazu, die Verteilung molekularer Komponenten im Gewebe gleichzeitig zu visualisieren und zu quantifizieren. Durch Bestrahlen von Gewebe mit Licht verschiedener Wellenlängen können ggf. molekulare Informationen gewonnen werden, die auf der Nutzung endogener Chromophoren wie z.B. oxigeniertem oder desoxigeniertem Hämoglobin, Fett, Melanin, Kollagen und Wasser beruhen. Gleichzeitig bietet sich eine Vielzahl von möglichen exogenen Kontrastmitteln an, so dass auch die Nutzung einer Kombination und von endo- und exogenen Chromophoren für die Bildgebung mittels PAI möglich ist.

Üblicherweise werden lineare spektrale Differenzierung-Methoden, die auf Differential- oder Anpassungsalgorithmen (fitting) basieren, verwendet, um die einzelnen Gewebekomponenten, die zum sPAI beitragen, voneinander zu unterscheiden. Dieser auf fitting basierende Ansatz liefert zwar akzeptable Ergebnisse, erfordert aber gleichzeitig eine Überwachung durch den Benutzer, der Spektralkurven als a priori Informationen bereitstellen muss. Dies kann eine Herausforderung darstellen, da die theoretischen spektralen Signaturen der Gewebekomponenten je nach Gesundheitszustand unterschiedlich sein und so das Ergebnis verzerren können. Darüber hinaus geht dieser Ansatz davon aus, dass die stärkeren Absorber wie z.B. Hämoglobin die einzigen Absorber im Gewebe sind, und andere, weniger prominente oder schwächer absorbierende Moleküle wie z. B. bestimmte Kontrastmittel, Melanin, oder Lipide werden nicht berücksichtigt. Dies führt zu einer unvollständigen Wiedergabe der Gewebezusammensetzung. Zusätzlich kann dieser herkömmliche Ansatz durch einen Verzerrungseffekt (spectral colouring) beeinträchtigt werden: aufgrund des verminderten Lichtdurchflusses werden spektrale Verschiebungen in der Tiefe induziert und führen so zu Fehlinterpretationen der Absorptionsspektren der einzelnen Komponenten. Zusammenfassend

gibt es aktuell also noch einige Einschränkungen bei der spektralen Differenzierung in Bezug auf die molekulare Empfindlichkeit und Spezifität der PAI.
Eine weitere Einschränkung von PAI ist das Fehlen standardisierter Methoden zum Testen von Systemkonfigurationen oder neu entwickelten Algorithmen mit hoher Wiedergabetreue und Genauigkeit. So können etablierte medizinische Bildgebungsverfahren wie Magnetresonanztomographie (MRT), Computertomographie (CT), Positronen-Emissions-Tomographie (PET), und Ultraschall auf realistische und kommerziell verfügbare Gewebephantome zurückgreifen. Da die PAI eine ziemlich neue Technologie ist, besteht hier noch ein dringender Bedarf an anthropomorphen und heterogenen Phantomen, um weitere zukunftsweisende Anwendungen für diese Technologie erschließen und deren Einführung beschleunigen zu können.
Fotoakustische (PA) Signale können von Natur von Kilohertz bis zu mehreren -zig Megahertz reichen. Die zur Messung der fotoakustischen Signale verwendeten US-Wandler sind jedoch keine idealen Punktdetektoren mit unendlicher Bandbreite. So könnten signifikante PA-Bildgebungsdetails unterschlagen werden. Dies ist insbesondere für die translationale Forschung im Hinblick auf Patienten von entscheidender Bedeutung.
Für innovative Anwendungen wie die Verwendung von biologisch abbaubaren orthopädischen Implantaten in der Humanmedizin, wäre z.B. eine Kombination von fotoakustischer Bildgebung mit hoher Frequenz zur Überwachung der oberflächlichen Revaskularisierung und PAI mit niedriger Frequenz zur Überwachung der Osseointegration des Implantats in der Tiefe denkbar. Die Kombination von Mehrfrequenzbandwandlern in der PAI würde eine vollständigere und umfassendere Gewebecharakterisierung ermöglichen, die wiederum die translationale Forschung außerordentlich befördern könnte.
In dieser Dissertation ziele ich darauf ab, das Potenzial der innovativen fotoakustischen Bildgebungstechnologie zu optimieren, indem ich fortschrittliche maschinelle Lernalgorithmen entwickele, die die lebenswichtigen molekularen Eigenschaften des Gewebes automatisch überwachen und quantifizieren können. Ich habe mich dabei in erster Linie darauf konzentriert, Gewebebiomarker aus der PAI ohne Vorkenntnisse und Benutzerinteraktionen zu identifizieren, um so die Diagnose, sowie Behandlung und Überwachung der Gewebeveränderungen bei einer großen Anzahl von Krankheiten zu verbessern. Darüber hinaus würde die Entwicklung geeigneter anthropomorpher Phantome die Zahl erforderlicher Tierversuche deutlich reduzieren. Außerdem können fortschrittliche PAI Methoden vorab getestet werden, was wiederum zu höheren Erfolgschancen der *in vivo* Experimente führt.
Schließlich wird die Verwendung mehrerer US-Wandler mit unterschiedlichen Frequenzbandbreiten für die fotoakustische Bildgebung und ihre Auswirkungen auf translationale Anwendungen untersucht. PA-Bilder mit verschiedenen Maßstäben, Auflösungen und Eindringtiefen zur Verfügung zu haben, wird daher den Grundstein für zukünftige Fortschritte bei der klinischen Umsetzung dieser Technologie legen . Dies ist von grundlegender Bedeutung, insbesondere bei Anwendungen, bei denen die Fotoakustik durch die Bereitstellung neuer Erkenntnisse beitragen kann, z. B. bei der Nachverfolgung der Geweberegeneration auf biologisch abbaubare Implantate in der Humanmedizin.

Contents

Chapter 1

Introduction

Abstract:

In this chapter, a brief introduction of the fundamentals and an overview of the current state of the innovative photoacoustic imaging technology are provided. Besides, we introduce the idea behind the developments presented within this dissertation highlighting the importance of data-driven spectral unmixing algorithms for the accurate monitoring of tissue molecular composition in a variety of applications. The main objective of this work is to develop, optimize, and investigate photoacoustic imaging technology, to detect and visualize all possible tissue molecular components without any user interaction. Specifically, our research focused on the potential use of multi-spectral photoacoustic technology to monitor tissue remodeling in presence of advanced biodegradable bone implants as well as further developments to translate the technology into clinical settings. Finally, the key objectives of the research project and the outline of the thesis content are described.

1.1. Introduction

In 1880, Alexander Graham Bell [1] first introduced the "photoacoustic" (PA) effect phenomenon. However, this effect of "hearing the sound of light", has been further exploited for biomedical imaging applications only over the last few decades. Specifically, in the medical field, photoacoustic imaging (PAI), which is also referred to as optoacoustic imaging, is an emerging modality based on the absorption of nano-second pulsed laser light by tissue chromophores. Tissue chromophores are molecules that absorb light such as oxygenated/deoxygenated hemoglobin (HbO_2 / Hb_R), melanin, lipid, water, and also exogenous contrast agents [2]. In particular, a laser beam is shone into the tissue, while through its optical path, photons undergo multiple scattering within the tissue before being absorbed by the chromophores. Due to short-pulsed laser light, the optical energy absorbed by chromophores is converted into heat, which induces a localized temperature increase (< mK). Consequently, this causes a thermoelastic expansion that leads to the emission of ultrasonic pressure waves within the Megahertz range, which can be detected by standard ultrasound transducers [3]. Assuming that the speed of sound in biological tissue is homogenous (≈ 1540m/s for soft tissues) and by identifying the time of arrival of light-induced acoustic waves, the respective optical absorption in the tissue can be reconstructed. Conventional delay and sum (DAS) beamforming or more advanced algorithms can then be used for photoacoustic image formation [4]. Thus, the reconstructed photoacoustic image represents a map of the initial pressure distribution, which is directly related to the absorbed light, with the spatial resolution of ultrasound images [5].

Fig. 1 depicts a simplified schematic of the "Light IN - Sound OUT" principle that is behind the PA image formation. This shows the optical forward (Light-IN, see Fig. 1 (A)) and acoustic backward (Sound-OUT, see Fig. 1 (B-C)) processes that lead to recording the light-induced acoustic signals and thus the PA image reconstruction. The recorded acoustic signals correspond to the initial pressure distribution $p_0(\vec{r},\lambda)$ that is proportional to the optical absorption coefficient $\mu_a(\vec{r},\lambda)$, as well as the light fluence distribution Φ, and the temperature-dependent Grüneisen coefficient $\Gamma\big(\vec{r},T(\vec{r})\big)$, thus defined as follows:

$$p_0(\vec{r},\lambda) = \mu_a(\vec{r},\lambda)\cdot\Phi(\vec{r},\lambda,\mu_a,\mu_s,g)\cdot\Gamma\big(\vec{r},T(\vec{r})\big) + \varepsilon(\vec{r},\lambda) \quad (1)$$

where $\vec{r}$ represents the spatial coordinates of the voxel, λ is the light wavelength, $\mu_s(\vec{r},\lambda)$ is the scattering coefficient, g is the optical anisotropy factor that is the mean cosine of the scattering angle, $T(\vec{r})$ is the spatially varying temperature, and $\varepsilon(\vec{r},\lambda)$ is a term to represent noise. Thus, Eq. 1 describes the relationship between the detected photoacoustic waves with the absorption coefficient of the irradiated tissue components (μ_a). Since this relation depends also on the light fluence Φ that is a function of $(\vec{r},\lambda,\mu_a,\mu_s,g)$, the absolute quantification and identification of the underlying tissue chromophores from PA images is still an open challenge.

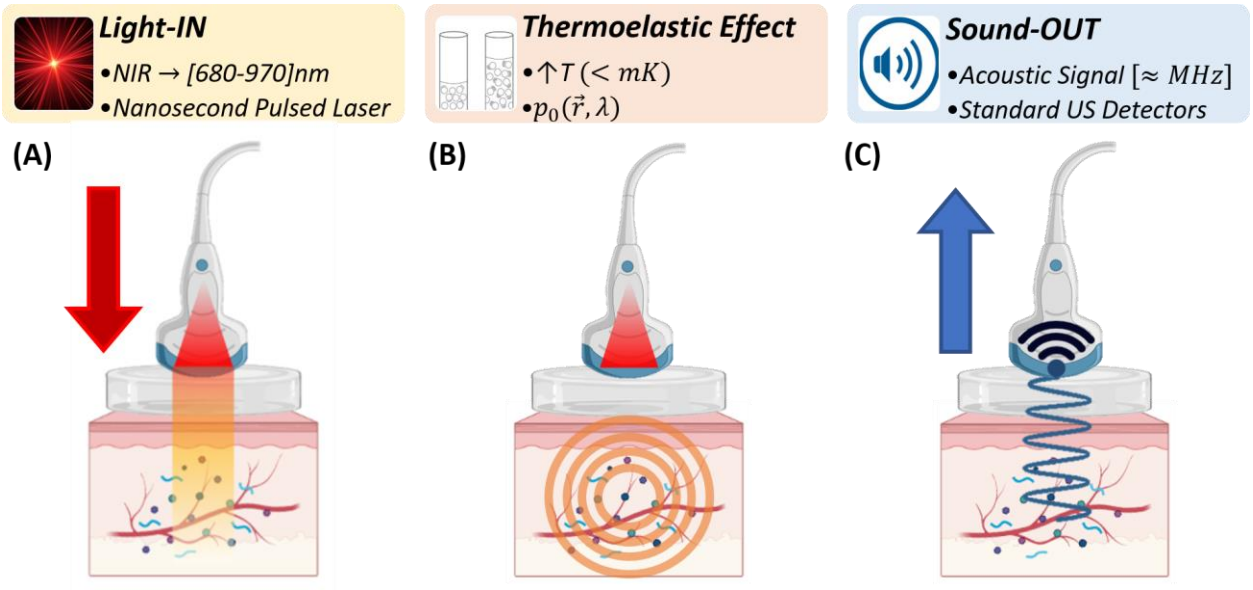

Fig. 1. Schematic representation of the PA effect. The individual images include (from top to bottom) a US transducer with optical fibers on the sides, a coupling material (gel pad), and tissue including absorbing chromophores. In particular, the image shows, the light fluence distribution in the tissue (A), the thermoelastic expansion of the areas where the light is absorbed (B), and the propagation of the light-induced sound waves recorded by the US transducer (C).

1.2. Light-tissue interaction

The ability of light to interact with tissues and deposit energy is vital for photoacoustic applications. In particular, when light interacts with biological tissue, it can undergo several fundamental interactions. The two most dominant mechanisms contributing to PAI techniques within the near-infrared I (NIR-I) wavelength range (680-970 nm) are optical absorption and scattering. The effective penetration and imaging depth are limited by both scattering and absorption events that restrict the mean free path of photon propagation. However, within the NIR-I window, there is a minimum attenuation and the potential imaging depth is maximized (see Fig. 2).

When photon absorption occurs the energy of the photon is transferred to a molecule, changing the electric state of the molecule, from the ground state to an excited state. As the tissue chromophores have a characteristic wavelength-dependent absorption spectrum, the detection of the optical properties from the energy deposition in tissues enables the interpretation of the molecular composition. Hence, PAI enables non-invasive and radiation-free imaging of underlying absorbing molecular components present in tissues such as oxygenated hemoglobin, deoxygenated hemoglobin, melanin, lipid, and water as well as exogenous contrast agents up to several centimeters deep in living tissues.

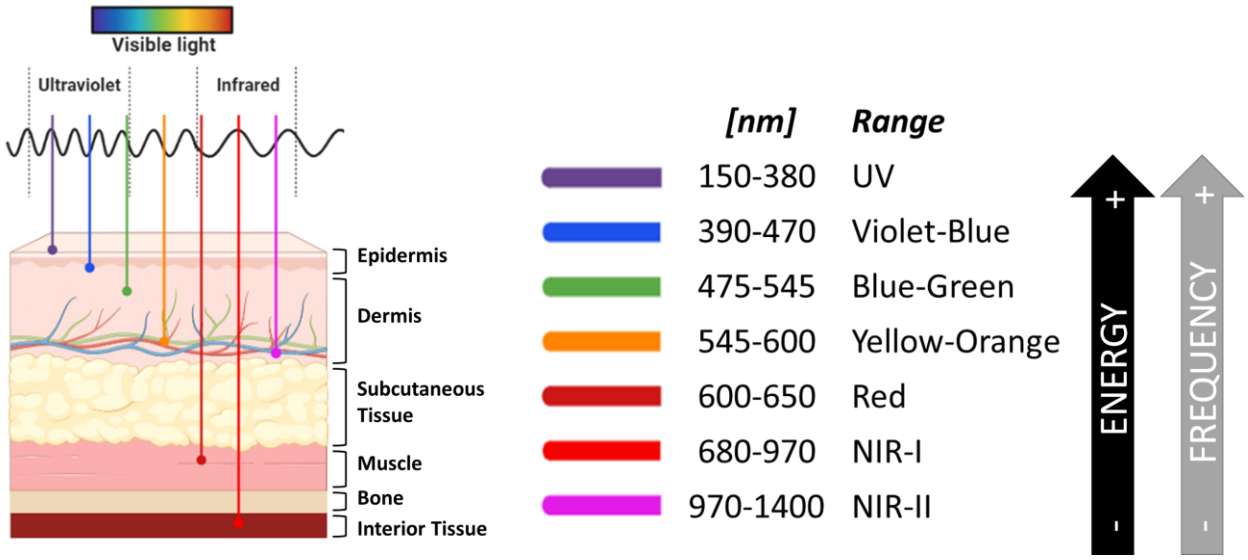

Fig. 2. Schematic representation of the light attenuation through tissue. The illustration includes the light within the range between ultraviolet (UV) to near-infrared II (NIR-II) and its tissue penetration. Increasing the light wavelength leads to an energy and frequency decrease [6].

1.3. Photoacoustic signal detection

In PAI, to record light-induced acoustic waves, ultrasound (US) transducers based on piezoelectric (PZT) elements are commonly used [7]. Other alternatives are also becoming popular such as the capacitive micromachined ultrasonic transducer (CMUT) [8] and piezoelectric micromachined ultrasound transducer (PMUT) [9], [10]. Micromachined ultrasonic transducers may offer higher sensitivity and wider frequency bandwidth as well as a higher acceptance angle than conventional PZT transducers. These features are all crucial, cause photoacoustic signals have broadband frequency content by nature, which can span from Kilohertz to several tens of Megahertz.

Besides, another class of acoustic sensors is based on optical ultrasound detection technologies. These are promising detectors as they have much broader frequency bandwidth than the PZT-based detectors. These methods are based on optical resonators to detect incident elastic waves. The optical resonator geometries that are most frequently used in photoacoustic imaging are Fabry–Pérot interferometers [11]–[13]. Although the optical ultrasound detection has some advantages over the PZT-based detection, the translation from the lab bench to routine practice is limited, as these are highly motion and vibration sensitive [14]–[16].

1.4. Photoacoustic image reconstruction

For PAI the inverse problem of image formation aims to accurately retrieve the initial pressure distribution $p_0(\vec{r},\lambda)$ from the recorded photoacoustic signals. Since PA images are obtained based on laser-induced ultrasound (US) signals, there are many similarities between PA and US image formation. Consequently, several US beamforming algorithms can be used in PA beamforming with some modifications. The reconstruction can be performed by back projecting

the recorded temporal photoacoustic signals into the image space, knowing the time of flight, speed of sound (SOS) wherein the signals have propagated, as well as amplitude and duration of the irradiation source. In most situations, the SOS is considered homogeneous and assumed to be equal to 1540 m/s for soft tissue. However, SOS heterogeneity may be crucial in some ultrasound applications [17], [18]. Thus, several algorithms for PA image reconstruction in acoustically homogeneous and heterogeneous media have been reported [19]–[22].

Commonly, the PAI reconstruction is performed with the Delay-And-Sum (DAS) beamforming method [23], [24] as well as Delay-Multiply-And-Sum (DMAS) and its adapted versions [4], [25], [26]. These beamforming algorithms are used when PA signals are detected by a linear array of US transducers. Thus to reconstruct the PA images, the DAS algorithms calculate and apply delays to the recorded signals corresponding to each specific element of the transducer array and then sum the resulting signals. In this way, the array sensitivity is maximized to incoming waves from a particular direction toward the source. For DMAS beamformers, before summation, the calculated samples are combinatorially coupled and multiplied. A number of approaches reported in the literature cover the various advanced image reconstruction algorithms proposed for improving high-fidelity reconstruction of photoacoustic imaging [27]–[29]. However, the details of the different reconstruction approaches are out of the scope of this dissertation, where the DAS beamforming has been used and the developed algorithms have been applied in post-processing on the reconstructed PAI.

1.5. Multi-spectral photoacoustic imaging

Multi-spectral PAI mode, also named as multi-wavelength PAI, consists in sequentially illuminating the same structures at multiple wavelengths, thus obtaining a spectral PAI data set. The main goal of multi-spectral PAI is to gain information on the different molecular tissue constituents, in order to infer functional and molecular properties [30]–[35]. In particular, each tissue chromophore responds to excitation light at multiple wavelengths in a unique way. Besides, the absorption coefficient spectrum of different chromophores can also vary with regard to the theoretical spectrum in case of disease conditions. Thus, multi-spectral PAI has the potential to distinguish different chromophores in different physiological or pathological conditions.

1.6. Spectral unmixing

Tissue chromophores can be distinguished, by measuring PA signals of the same structure at different wavelengths of excitation light. Spectral unmixing techniques are capable of separating the constituent tissue chromophores that contribute to the measured multi-spectral PA signals. Linear unmixing algorithms are commonly applied to separate the individual chromophores.

Fig. 3 schematizes the linear unmixing algorithm used to solve this ill-posed problem. This approach assumes that the source tissue chromophores are linearly combined. Thus, each pixel of the spectral PAI includes a linear combination (mixture) of a number of source absorbers. The linear unmixing algorithm is a linear regression-based approach that identifies the best fit of *a*

priori source spectra to the acquired mixed spectral PAI. As such, the fundamental pre-requisite is the *a priori* knowledge of the photoacoustic absorption spectra of the constituent chromophores and the user interaction in the form of providing these expected spectral signatures.

However, in real cases, the linear unmixing can miss the mark due to its lack of sensitivity and specificity. In particular, for translational research with patients, these types of supervised spectral unmixing can be challenging, as the spectral signature of the tissues can differ with respect to the disease condition. Imaging exogenous contrast agents and accessing their biodistribution can also be problematic, as some of the contrast agents are susceptible to changes in spectral properties after interaction with living tissues.

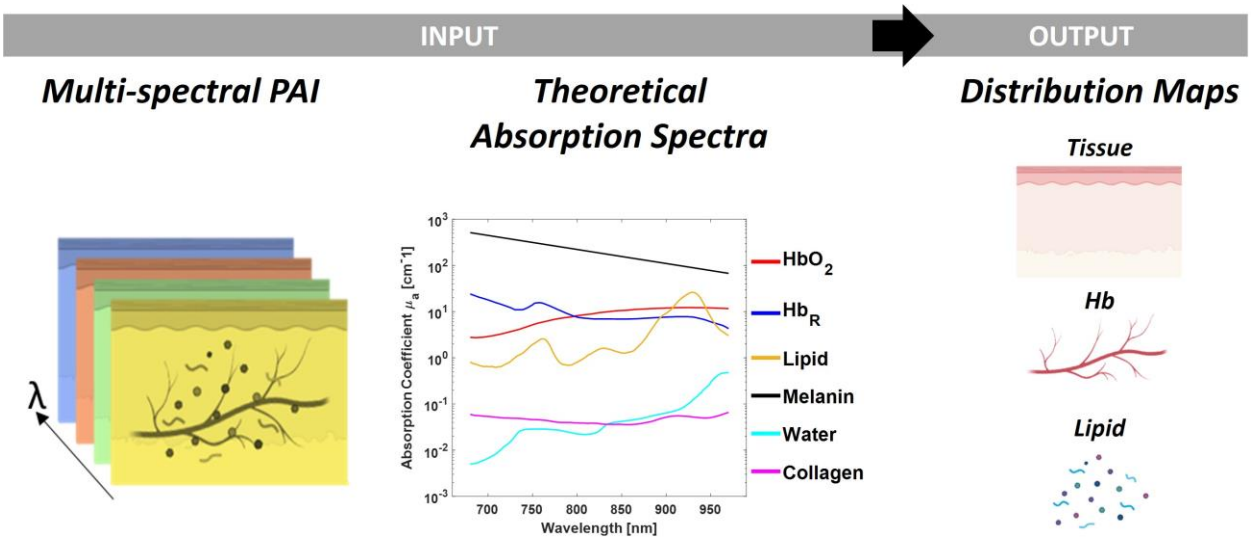

Fig. 3. Schematic representation of the linear unmixing approach. This is a fitting-based procedure where the acquired multi-spectral PAI represent one of the input. In addition, the wavelength-dependent theoretical absorption spectra of different tissue chromophores present in biological tissue are also provided as *a priori* information. The spectra were collected from the literature [36]. Finally, the distribution maps that show the selected tissue chromophores per pixel are obtained as output.

Additional factors can also compromise the accuracy of the linear unmixing. For instance, the spectral coloring effect is a known artifact that plays a crucial role in the sensitivity and specificity of tissue biomarkers detection. Spectral coloring is a corruption effect that alters the spectrum of the incident light along the tissue heterogeneity at depth and consequently leads to misinterpretations of the absorption spectrum shape of the tissue components [37]. This also limits the absolute quantification of the unmixed absorbers. Besides, unmixing weaker absorbers (such as lipids, collagen, etc.) in the presence of strong absorbers (such as hemoglobin) using the standard linear unmixing method, can also be challenging.

1.7. Spectral coloring effect

Linear unmixing algorithms rely on the assumption that the reconstructed photoacoustic image intensities $PAI(\vec{r},\lambda)$ is an estimation of the underlying initial pressure distribution $p_0(\vec{r},\lambda)$ which is approximated as only proportional to the optical absorption coefficients $\mu_a(\vec{r},\lambda)$ as:

$$PAI(\vec{r},\lambda) \approx p_0(\vec{r},\lambda) \propto \mu_a(\vec{r},\lambda) \tag{2}$$

However, as expressed in Eq. 1, this assumption in Eq. 2 is not applicable in a real scenario, because the reconstructed image is also proportional to both the Grüneisen parameter $\Gamma\big(\vec{r},T(\vec{r})\big)$, and the light fluence $\Phi(\vec{r},\lambda,\mu_a,\mu_s,g)$. While Γ is assumed to be wavelength-independent, the fluence Φ depends on the tissue's optical properties and consequently to the wavelength λ, as well as to the spatial position according to the excitation light configuration. These light fluence spectral and spatial inhomogeneities have an impact on the recorded light-induced photoacoustic signals and consequently on the reconstructed photoacoustic image. This effect, generally known as spectral corruption or spectral coloring, causes unmixing misinterpretation and absolute quantification challenges at depth. Thus, assuming Γ as a constant, by having an accurate estimation of the fluence Φ, the correspondence from the photoacoustic intensity and absorption coefficient of the tissues would be more accurate as such:

$$\frac{\boldsymbol{PAI}(\vec{\boldsymbol{r}},\boldsymbol{\lambda})}{\boldsymbol{\Phi}(\vec{\boldsymbol{r}},\boldsymbol{\lambda},\boldsymbol{\mu_a},\boldsymbol{\mu_s},\boldsymbol{g})} \approx \frac{p_0(\vec{r},\lambda)}{\Phi(\vec{r},\lambda,\mu_a,\mu_s,g)} \approx \mu_a(\vec{r},\lambda)\cdot\Gamma\big(\vec{r},T(\vec{r})\big) \propto \boldsymbol{\mu_a}(\vec{\boldsymbol{r}},\boldsymbol{\lambda}) \tag{3}$$

Various methods have been proposed to estimate the light fluence distribution Φ to have a refined correspondence between $PAI(\vec{r},\lambda) \propto \mu_a(\vec{r},\lambda)$ and thus, compensating the photoacoustic imaging for the spectral coloring effect at depth [35], [38]–[43]. Specifically, different approaches have attempted to model the photons' propagation in biological tissues based on solving the Radiative Transfer Equation (RTE) [44]. Generally, the RTE diffusion differential equation can be approximated with an analytical solution derived by using diffusion theory. In particular, considering a pulsed laser beam incident on a homogeneous medium, the irradiance decreases exponentially along the axis of the incident laser beam in accordance with Beer-Lambert's law [45]. Thus, the light fluence exponentially attenuates along the axial direction of the laser source and can be modeled using diffusion theory [46]–[49]. Such that the intensity along depth $I(z)$ is espressed as follows:

$$I(z) = k \cdot I(0)\cdot e^{-\mu eff\cdot z} \tag{4}$$

where k is a constant and μeff is the effective attenuation coefficient that is given by:

$$\mu eff = \sqrt{3\mu_a[\mu_a + (1-g)\mu_s]} \tag{5}$$

Thus, following the diffusion theory for light propagation and assuming a point source and time independence [50], the light fluence can be simply formulated as:

$$\phi(\vec{r}) = \frac{S_0 \cdot e^{-\mu eff \cdot \vec{r}}}{4\pi D\vec{r}} \tag{6}$$

where $\vec{r}$ is the distance from the source, S_0 is the incident light source energy, and the diffusion coefficient is $D = \frac{1}{3[\mu_a + (1-g)\mu_s]}$.

However, for complex tissue geometries and heterogenous tissue properties, the diffusion model might lead to a suboptimal solution of light distribution. Therefore, Monte Carlo light fluence simulation can be used as a method to accurately estimate the propagation of photons through heterogeneous tissue [51], [52]. This simulation relies on light absorption and scattering, which are two of the fundamental photons-tissue interactions during light propagation. Besides, the optical properties of the geometrical domain in terms of absorption coefficient (μ_a), scattering coeffiecient (μ_s), anisotropy factor (g), and refractive index (n) needs to be defined.

Although Monte Carlo simulation is the gold standard to estimate the light distribution, in complex geometrical domains this can be computationally expensive as it requires a high number of simulated photons and a large number of voxels. In addition, the accuracy of the tissue optical properties still limits the precision of the simulation as well as the modeling of the light source and its energy details can also be challenging.

1.8. Photoacoustic and multimodal imaging

Photoacoustic imaging (PAI) uses the same data acquisition process as ultrasound (US) imaging, thus representing a dual-modal imaging system (US-PA). This has the advantage that can simultaneously provide anatomical, functional, and molecular assessment of tissue properties during *in vivo* tissue monitoring. Besides, since acoustic scattering in tissues is a few orders of magnitude less than optical scattering, the PAI technology guarantees the unique combination of strong optical imaging contrast to the higher depth of penetration and spatial resolution [53]. Fig. 4 provides a comparative overview of US-PA with existing biomedical imaging techniques, along with their respective resolution and imaging depth.

Microscopy imaging techniques such as confocal microscopy (CM), optical coherence tomography (OCT), Micro Computed Tomography (μCT), can provide high resolution with limited penetration depth. Hence, these techniques are suitable for imaging microstructural information spanning across superficial structures up to small animals. On the other hand, macroscopic imaging techniques such as MRI, X-ray, and CT mainly provide anatomical information of bigger structures with limited resolution. Besides, positron emission tomography (PET) and single-photon emission computed tomography (SPECT) provide good detection sensitivity and functional information but at the expense of low spatial resolution.

Ultrasound-Photoacoustic (US-PA) imaging fills the gap between microscopy techniques and conventional macroscopic systems maintaining an optimal compromise of spatial resolution and imaging depth. In particular, as compared with other imaging modalities, photoacoustic has the advantage of combining deep penetration of biological tissue (~3-5 cm) with a high spatial resolution (~ 50-500 μm). The ability of PA to image deep tissue derives from the frequency of the ultrasound detector and the light excitation within the NIR wavelength range. Finally, PA is one of the most promising techniques for non-invasive and non-ionizing molecular imaging based on strong optical contrast at high ultrasound resolution in deep tissue. In addition, PA technology in comparison to the PET, MRI, and CT can have a portable configuration similar to ultrasound, and it does not require extensive user training.

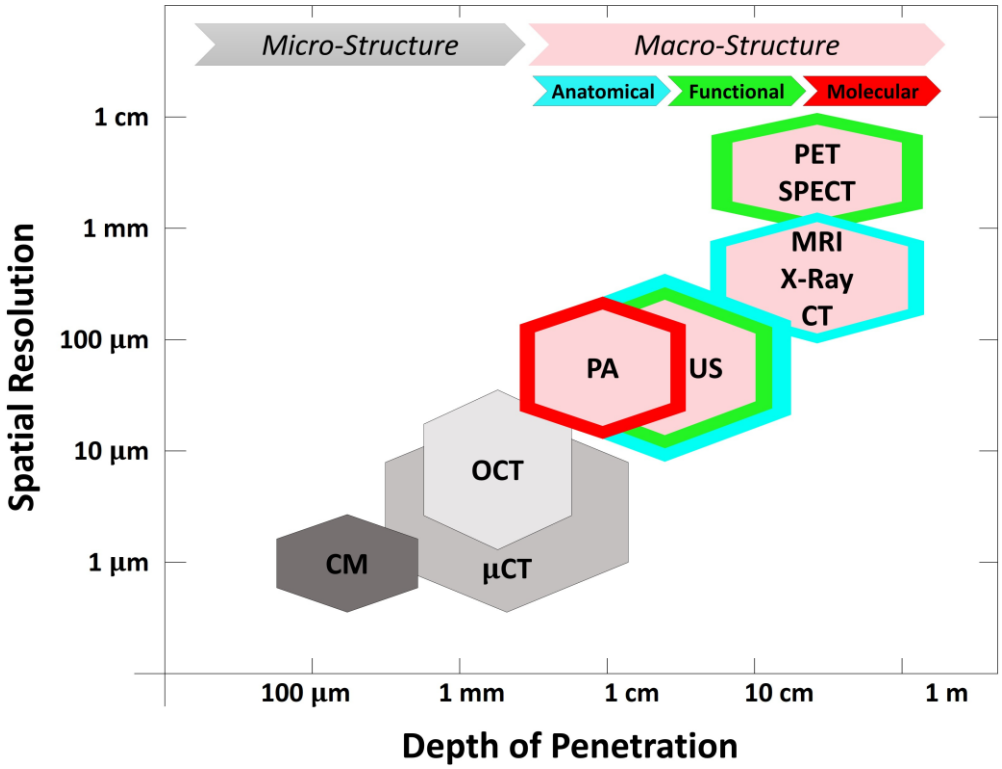

Fig. 4. Illustration of the relative comparison in terms of depth of penetration and feature resolution, occupied by several microscopic and macroscopic imaging modalities such as: Confocal Microscopy (CM), Optical Coherence Tomography (OCT), Micro Computed Tomography (μCT), Ultrasound (US), Photoacoustic (PA), Magnetic Resonance Imaging (MRI), Radiography (X-ray), Computed Tomography (CT), Positron Emission Tomography (PET), and Single Photon Emission Computed Tomography (SPECT).

1.9. Applications and translation impact

The characteristics shown in the previous sections made photoacoustic imaging (PAI) attractive for a wide range of preclinical studies involving cancer research [54]–[58], angiogenesis, vascular remodeling [59]–[62], cutaneous melanoma monitoring [63]–[65], mapping of sentinel lymph nodes [66]–[69], visualization of inflammatory processes [70]–[72], and biodistribution of exogenous contrast agents [73]–[75].

Over the last decade, the experience gained from PAI in preclinical settings has been transferred into clinics. In particular, various PAI system configurations have been adapted for clinical applications [76]. For instance, depending on the applications and imaging target size, the transducer array can be mounted on a stationary platform [30], [77] or be used in hand-held imaging mode [78], [79]. The 2D array transducer can be either linear or curved. Linear array-based PA systems are constrained in detecting acoustic signals at limited angles from the region of interest as compared to curved transducer array systems [77]. If multiple transducers can be arranged spatially in 3D, or if the transducer can be moved coherently in space, then acoustic waves can be detected from all in-plane directions and hence perform the tomographic imaging. Advanced 3D array transducers with wide field-of-view (FOV) [80], [81] can also be used to capture volumetric images at a single frame. However, the latter is still a laboratory prototype solution. Besides, the optical excitation source can be focused or wide field according to the application as well as the position and size of the target of interest. Specifically, focused light configuration conventionally enables optical resolution PA microscopy, thus the lateral resolution is determined by the optical setup, and the axial resolution by the US transducer frequency [82]. On the other hand, in acoustic resolution PA macroscopy the illumination is more uniform and unfocused around the transducer thus enabling greater penetration and both the lateral and axial resolutions are determined by the acoustic sensor.

Various PAI system configurations have been optimized for clinical applications such as dermatology, vascular, musculoskeletal, gastrointestinal, breast, and adipose tissue imaging [83]. In recent years, many clinical studies have been reported. Kim et al. [84], [85] have proposed a setup that includes a linear array US transducer combined with a custom-designed fiber bundle to differentiate malignant and benign thyroid nodules in humans. Manohar et al. [86]–[88] have developed a tomographic configuration arranging US detectors in a hemispherical geometry for photoacoustic breast imaging. Further, the studies reported by the university of Lund [89]–[92] have shown an optimized use of high-resolution linear array US transducer combined with optical fibers for cutaneous microvasculature, melanoma, tissue remodeling in wounds, and temporal artery applications. All these works show that photoacoustic is rapidly growing and has great potential to expand into clinics. Recently, a PA technology has also been approved by FDA for breast imaging applications. This encourages several companies of PA imaging technology that have not yet been approved for clinical use due to a lack of clinical data, to explore the clinical potential of the technology.

Here we are intended to explore advanced applications for PAI where other imaging technologies have limitations and photoacoustic can have great potential to fill the gap. In particular, photoacoustic imaging has never been used for monitoring tissue remodeling in presence of biodegradable bone implants. Biodegradable metallic implants based on Magnesium (Mg) and its alloys, have been recently introduced for stabilizing bone fractures [93]–[96]. The material degrades under physiological conditions without releasing toxic products, thus making them promising candidates as biodegradable materials for medical applications [97]. These implants degrade while the fracture heals, thus avoiding a second surgery to remove the implant. The

monitoring of biodegradable implant integration within living tissues is crucial to predict the course of tissue regeneration during the healing process. Thus, it is vital to determine the influence of the degradable implant on the surrounding tissues during the initial inflammation, angiogenesis, and tissue oxygenation stages after implantation as well as the following processes of tissue remodeling.

Although biodegradable implants seem a really promising alternative to inert implants, the *in vivo* follow-up of molecular tissue remodeling is still challenging with conventional imaging techniques as these provide mainly structural information. In particular, techniques such as X-ray and CT imaging are conventionally used to monitor bone healing and implant osseointegration. Besides, PET can be used to image the metabolic activity of the tissues affected by the implantation. However, due to ionizing radiation and radiotracers, the frequent use of these imaging approaches is not recommended during follow-up, especially in pediatric patients, where it is crucial to limit the dose exposure. Furthermore, MRI which is widely used in clinics has a hardware limitation due to the massive magneton that in presence of metallic implants causes artifacts and patient safety concerns due to the electrical currents induced by the use of conducting metals in presence of magnetic fields. Moreover, ultrasound (US) imaging has recently attracted significant interest in the evaluation of bone fracture healing, since the speed of sound waves propagating across fractured bones can be used as an indicator of healing. Therefore, standard imaging techniques used in clinics currently provide limited information. Advanced developments in multi-spectral PAI and unmixing techniques have the potential to enable PAI to reveal intrinsic tissue chromophores within tissue in presence of implants. Thus PAI represents a promising alternative to non-invasively reveal tissue biomarkers to monitor tissue remodeling/healing during implant degradation.

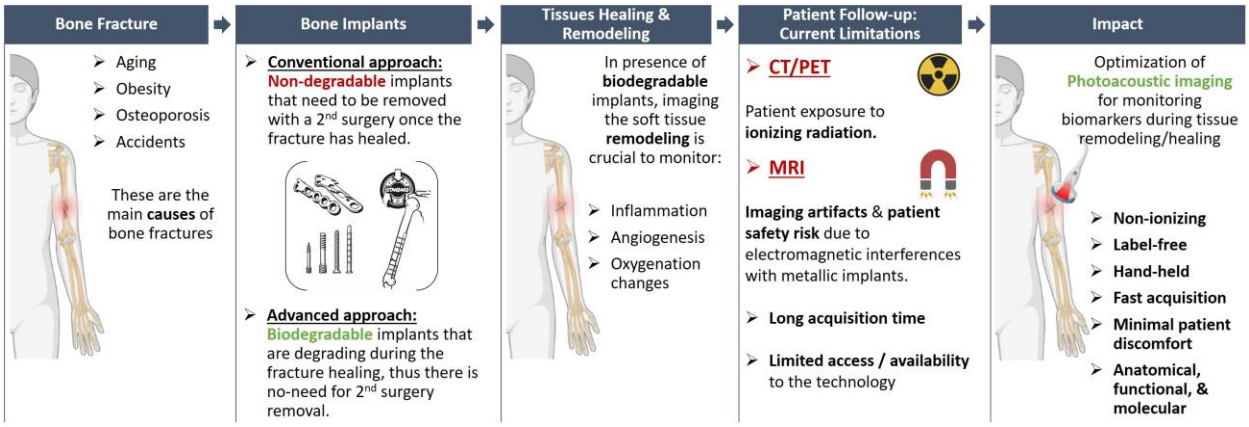

Fig. 5. Schematic representation of the potential impact of PAI on advanced applications as tissue remodeling monitoring in presence of biodegradable bone implants and possibilities for translational research.

Fig. 5 summarizes the current problem and the proposed approach of using photoacoustic imaging to non-invasively monitor the surrounding tissues during the inflammatory/angiogenesis stage occurring after implantation and the following processes of tissue remodeling. Being a

recently evolved technology, PAI has never been used before for this purpose. Hence, the aim of the thesis is to optimize and promote the use of PAI to monitor tissue composition and molecular changes during tissue remodeling processes, such as in presence of biodegradable bone implants, and its translational aspects.

1.10. Open challenges and possible solutions

Photoacoustic imaging (PAI) technology is label-free, real-time, and uses non-ionizing radiations, thus it would be ideal to non-invasively monitor molecular changes in different biological applications. However, several fundamental problems need to be tackled to achieve a successful tissue composition monitoring by using PAI. Specifically, the automated detection of endogenous and exogenous chromophores with high sensitivity and specificity will be ideal. To this end, the key focus of this thesis is the development of advanced methods to overcome the current existing limitations in the photoacoustic field, and to open up new applications both in preclinical and translational research. The identified challenges and formulated possible solutions include:

- **Challenge 1. (C1) Spectral Unmixing sensitivity and specificity of the tissue biomarker detection.**

Conventionally, to detect and separate the chromophores from multi-spectral PAI, linear spectral unmixing is used where an input of the expected tissue absorption spectra is required. However, in pathological conditions, the prediction of the absorption spectra is difficult as it can change with respect to the physiological state. Besides, imaging exogenous contrast agents and accessing their biodistribution can also be problematic, as some of the contrast agents are susceptible to changes in spectral properties after the injection and interaction within living tissues. Due to unpredictable spectral changes in disease conditions or in clinical scenarios, linear unmixing is challenging and can lead to suboptimal results.

To effectively demonstrate this challenge here we report an example obtained from our initial observations and evaluations (see Fig. 6). In particular, the kidney–spleen area of a healthy mouse model, was imaged after the intravenous injection of Indocyanine Green (ICG). The theoretical absorption spectra of ICG and oxy/deoxy hemoglobin known from the literature [36] have been provided as *a priori* information for the linear unmixing. The conventional linear unmixing by using the spectral PAI and the selected absorption spectra as input provides the distribution maps of each selected tissue component as output. From the kinetic of the contrast agent in a healthy animal, the ICG should be mainly accumulated in the spleen before being completely washed out from the body. However, the distribution maps obtained as output by the conventional linear unmixing approach (see Fig. 6), where the user provides the absorption spectra of the expected components as *a priori* information, show low specificity and sensitivity, thus the result is not optimal. In particular, focusing on the ICG distribution map, although the ICG resulted mainly distributed in the spleen, a lot of noise signal is detected in the surrounding tissues, thus reducing the accuracy of the unmixing. The same issue can be noticed for endogenous tissue components such as oxygenated and deoxygenated hemoglobin maps.

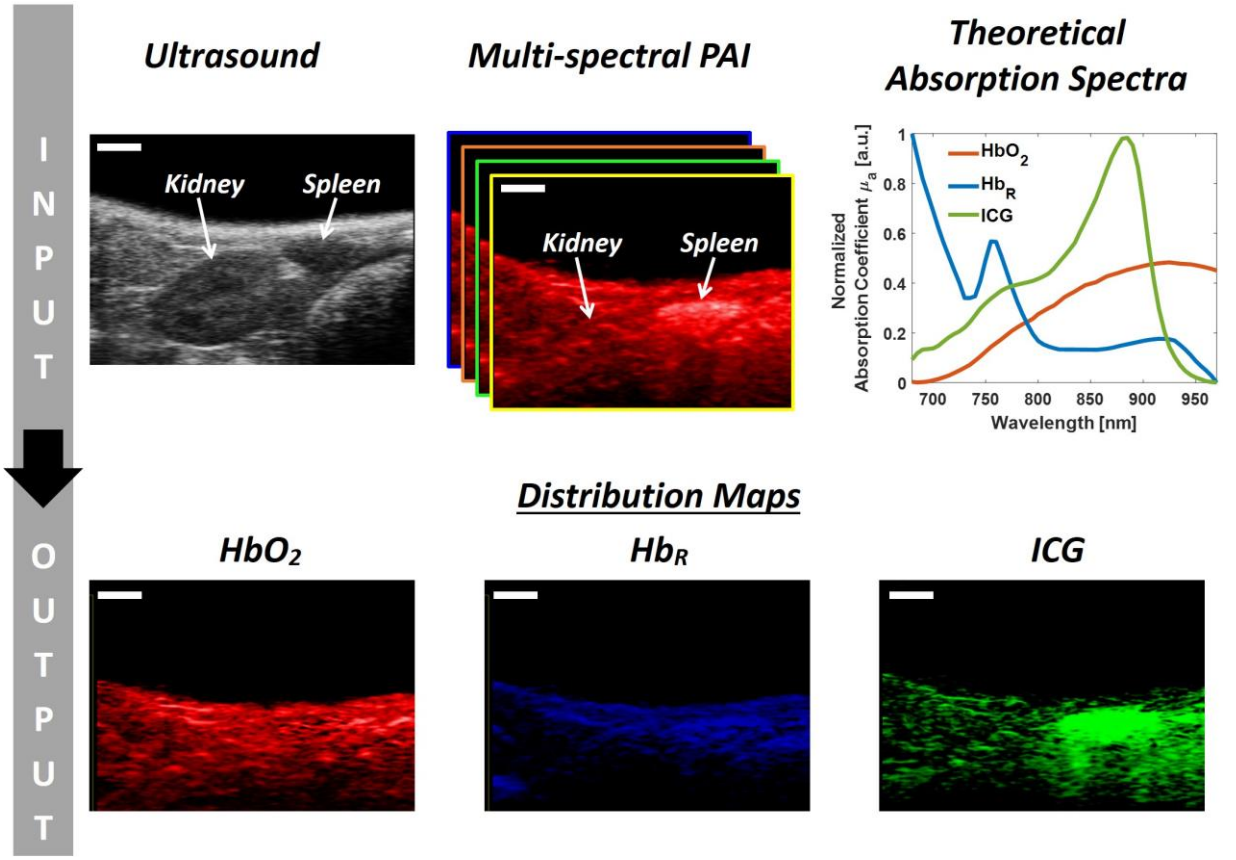

Fig. 6. Input-Output *in vivo* example of linear unmixing. Specifically, the acquired ultrasound and multi-spectral PAI of the kidney-spleen area of a mouse post-ICG injection represent the input. In addition, the theoretical absorption spectra of oxy/deoxy hemoglobin $(\mathrm{HbO_2}\ /\ \mathrm{Hb_R})$ and ICG are also provided as *a priori* information. Finally, the unmixed distribution maps of oxy/deoxy hemoglobin $(\mathrm{HbO_2}\ /\ \mathrm{Hb_R})$ and ICG that show the selected chromophores per pixel are obtained as the output of the linear unmixing approach. The scale bar size is 2mm.

In particular, the lack of sensitivity and specificity of the unmixing output can be due to linear unmixing, which is a supervised approach. Thus, the obtained unmixed maps are biased by the use of theoretical spectral characteristics of the tissue chromophores provided as a priori information. Besides, this conventional linear unmixing may assume that the most prominent absorbers such as hemoglobin, are the sole tissue chromophores, not accounting for the presence of other absorbing molecules (e.g. extrinsic molecules, melanin, lipids, etc.) that are less prominent or weaker absorbers. Therefore the less prominent/weaker absorbers are discarded and considered as noise, thus leading to incomplete and inaccurate tissue composition. Besides, the unmixing result is hampered by the user's selection of the number of components to be extracted (hyperparameter) and is jeopardized by the spectral coloring effect. This effect is caused due the optical light fluence attenuation and its complex spatial distribution. Thus, the same absorber at different depths can be perceived as altered as the light distribution is non-uniform. All of these causes can lead to misinterpretations since the conventional unmixing approach has low sensitivity and specificity.

❖ **Hypothesis 1. (H1) Investigation and development of unsupervised machine learning methods to overcome the conventional spectral unmixing.**

Work towards H1 aims to firstly examine the feasibility of using unsupervised machine learning approaches to solve the ill-posed photoacoustic unmixing problem without the use of *a priori* knowledge of the tissue components spectra. In particular, the blind source separation (BSS) class of unsupervised algorithms is investigated in detail. These methods may have great potential to solve the unmixing problem iteratively by learning from the spectral PAI data the relevant features without training data sets. These methods are based on modeling the spectral data, making assumptions about their distribution, and solving an optimization problem. Thus, providing as output both the tissue component spectra and their spatial distribution per pixel from spectral PAI. To this end, the development of innovative data-driven unmixing approaches can overcome further limitations shown by conventional linear unmixing and provide an improved assessment of the tissue chromophores directly by exploring within the spectral data. Therefore, the development and testing of novel advanced data-driven methods for accurate PA spectral unmixing aim to overcome the limitations described in C1 in realistic scenarios. We aim to formulate, develop, and implement a fully blind and automatic unmixing approach that does not require any user interaction or *a priori* input of the expected chromophore absorption spectra. The proposed method should be robust to unmixing misinterpretation by including automated choice of the hyperparameter. Furthermore, we would explore the beneficial effects of the spectral decoloring approach to compensate for the light fluence inhomogeneities at depth caused by ununiformed light absorption and distribution. Besides, investigate the possibility of automatically distinguishing both strong and less prominent absorbers from *in vivo* spectral photoacoustic data. Finally, inspect the possibility of extending the newly developed unsupervised unmixing for 3-Dimensional (3D) multi-wavelength photoacoustic data.

➢ **Challenge 2. (C2) Lack of standardized anthropomorphic, heterogeneous, and durable tissue-mimicking phantoms to test the newly developed methods in PAI.**

A major limitation when validating newly developed PAI methods is the fact that there is no gold standard method to obtain information on the light fluence or optical tissue properties *in vivo*. As such, newly developed methods typically rely on mathematical models of the PA effect or on simulated PA data, thus limiting their generalization. To this end, extensive animal experiments are necessary to significantly test and validate novel PAI methods in more detail. Besides, established imaging methods, like MRI and CT, rely on commercially recognized phantoms as standard tools to test methods and assess image quality. Since PAI is a pretty recent imaging technology, further efforts are still required to establish such standards with a community consensus, to accelerate the device design optimization. Typical phantoms used in PAI, include capillary tubes filled with contrast agents, which are embedded in gelatin-based material. These tube phantoms are useful to test the spectral response of contrast agents in PAI. However, generally, the PAI phantoms have a simple geometry, thus it still remains a challenge to realistically mimic an *in vivo* complex scenario. Therefore, having realistic and heterogenous

phantoms for extensively testing imaging system configurations or newly developed algorithms before performing in vivo studies would be ideal in PAI.

Besides, over the years, a wide range of tissue-mimicking materials (TMM) has been proposed as photoacoustic imaging phantom candidates, including materials based on hydrogels (i.e. agarose, gelatin) and gel wax. Hydrogels-based TMM for PAI, for example, can be prepared following a straightforward fabrication protocol. However, these are susceptible to mechanical damage, dehydration, and bacterial growth in storage and therefore do not offer a suitable combination of durability, long-term stability, and realistic acoustic/optical properties. On the other hand, gel wax-based TMM is an optically transparent mineral-oil-based material that is more durable but it is more complex to be mixed with absorbing components such as water-based inks and dyes. Table 1 summarizes the main properties of the widely used material as TMM in PAI.

Table 1. The fabrication characteristics of PA-compatible phantom based on different tissue-mimicking materials.

Characteristic	Hydrogel-based TMM	Gel wax-based TMM
Stability	Low	Medium
Durability	Low	Medium
Preparation	Simple	Medium
Integration with Inclusions	Simple	Medium
Melting Temperature	60 ^{0}C	200 ^{0}C

Thus the current challenge is related to having simple geometry as well as non-durable and low-performing TMM for PAI phantoms. This causes a lack of standardized testing methods useful for PAI characterization.

❖ **Hypothesis 2. (H2) Design and fabrication of anthropomorphic heterogeneous tissue-mimicking PA-compatible phantoms for imaging standardization.**

An ideal phantom for photoacoustic imaging (PAI) should:

- Have tissue-realistic acoustic and optical properties;

- Be durable and stable over time under storage and repeated use;
- Have a reproducible fabrication protocol;
- Have anthropomorphic and versatile resemblance;
- Produce realistic imaging.

Although a variety of phantoms are reported for PAI applications, an unmet need still exists to establish anthropomorphic heterogeneous phantoms that can accelerate preclinical applications of the technology. The purpose of work towards H2 is to design and fabricate anthropomorphic heterogenous tissue-mimicking phantoms to overcome this lack of ground truth data, standardize the PA imaging protocols, and accurately test the newly developed methods towards H1. Besides, we also aim to develop durable tissue-mimicking phantoms, which maintain stable characteristics over time under storage and repeated use. These phantoms would be ideal to consistently characterize the system. Thus, the development of customized and realistic tissue-mimicking PAI phantoms could help to accurately test and optimize newly developed methods, thus reducing the number of animal studies, in accordance with the 3Rs principle. Recently, a copolymer-in-oil-based tissue-mimicking material has been formulated by the International Photoacoustic Standardization Consortium (IPASC) and proposed as a candidate photoacoustic-compatible material [98], [99]. This base material showed to offer independently tunable acoustic and optical properties similar to soft tissue and has good longitudinal stability characteristics. Furthermore, the material has shown sufficient photo-, thermomechanical- and longitudinal- stability for short- and long-term precision studies [100]. Here, we investigated the possibility to optimize and tune the properties of durable TMM for PAI. Besides, we explored the potential to design, develop and fabricate a phantom that mimics the detailed morphology of a mouse, including the skeleton and the main abdominal organs, using a combination of image modeling, copolymer in oil-based materials, and 3D printing techniques.

- **Challenge 3. (C3) PAI for advanced applications "en route to the clinics".**

The automated extraction of biomarkers related to tissue composition and regeneration in presence of biodegradable bone implants is still an unexplored area where photoacoustic can contribute by providing novel insights. Thus, it would be crucial to explore the potential of photoacoustic imaging in presence of biodegradable bone implants made of magnesium (Mg). In particular, exploring *in vivo* preclinical studies in presence of Mg-based implants, where also many tissue chromophores are prominent absorbers that can be detected, would be investigated. This could open new possibilities for comprehensive tissue investigations *in vivo* in presence of biodegradable implants.

Photoacoustic signals contain broadband frequency content by nature, which can span from Kilohertz to several tens of Megahertz. On the other hand, the transducers used for measuring the PA signals are not ideal point detectors with infinite bandwidth. Thus, the limited frequency bandwidth of the US-PA transducers might exclude the acquisition of significant imaging details.

This will affect the quality of the image and it limits the translation of the technology into clinics. Conventionally, photoacoustic imaging (PAI) systems typically work either at a lower frequency or at a higher frequency due to the limited frequency bandwidth of the transducers and data acquisition (DAQ) systems. In PAI, the limited frequency bandwidth has a significant impact on the resolution and depth of the reconstructed image. Specifically, the use of lower frequency transducers (below 10 MHz), enables imaging at depth and provides spatial resolutions in the range of 150 − 200 microns. On the other hand, high-frequency transducers within the range of 15 − 50 MHz can enable spatial resolutions of around 40 microns. However, this results in increased acoustic attenuation, which limits the imaging depth. Therefore, PAI may require the use of a low or high-frequency transducer depending on the application. For instance, for skin cancer imaging, a high-frequency transducer may be beneficial to retrieve high details of the angiogenesis processes at a superficial level. While for breast cancer imaging, a low-frequency transducer might be preferred to access bigger structures with lower resolution at a deeper level. Furthermore, advanced applications such as the use of biodegradable bone implants are becoming increasingly popular for treating bone fractures in humans. In this case, it would be more effective the combination of photoacoustic imaging at high-frequency to monitor superficial revascularization and low frequency for implant osseointegration at depth.

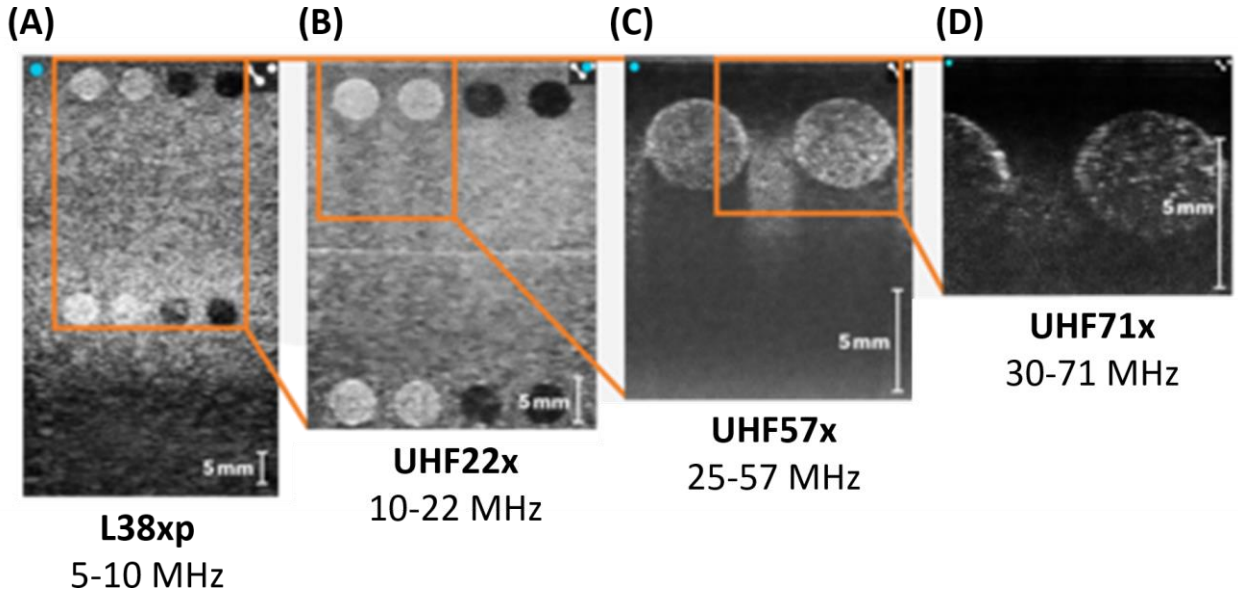

Fig. 7. Example of ultrasound imaging of a phantom by using multiple transducers with different frequency bandwidths such as: L38xp (A), UHF22x (B), UHF57x (C), and UHF71x (D) transducers ranging from low to high frequency respectively.

Fig. 7 for example reports the change in resolution and imaging depth depending on the frequency bandwidth of the US transducer used for US-PA imaging. These represent the ultrasound images obtained by using multiple US transducers with different frequency bands of 5-10 MHz (Fig. 7 (A)), 10-22 MHz (Fig. 7 (B)), 25-57 MHz (Fig. 7 (C)), and 30-71 MHz (Fig. 7 (D)) respectively. When using a low-frequency transducer like L38xp (Fig. 7 (A)) higher imaging depth

can be obtained at the expense of the spatial resolution. On the other end, when using a high-frequency transducer like UHF71x (Fig. 7 (D)) high imaging resolution can be obtained at the expense of the imaging depth. For translational research where it is crucial to image bigger areas, the use of different transducers with their respective frequency bandwidth might have a beneficial impact. Thus, exploring the combination of multiple frequency bandwidths could be crucial for translational research and to fuse multiple features with unprecedented detail. This can enable the use of PAI for advanced applications, such as non-invasively monitoring the soft tissue changes in human patients treated with biodegradable bone implants made of Mg in case of bone fractures.

- **Hypothesis 3. (H3) Multiple frequency bandwidth photoacoustic imaging to achieve multi-scale imaging and expand the translational applications of PAI.**

The purpose of work towards H3 aims to combine the multiple frequency bandwidth PAI and fully-automated spectral unmixing approach. To this end, we aim to characterize and evaluate the advantages of using different transducers with multiple frequency bandwidths for photoacoustic imaging and its impact on translational applications. In particular, we investigated the feasibility of using multiple-frequency bandwidth US transducers to obtain PA images at multiple scales, resolutions, and depths thus analyzing its advantages and limits. This characterization study will lay the foundation for future hardware and software development of the current photoacoustic imaging setup and protocol. Therefore, this will facilitate the clinical translation of the technology, especially to follow-up the tissue regeneration around biodegradable implants used to fix bone fractures in human patients.

1.11. Thesis outline

The primary objective of the work presented in this Ph.D. thesis is to investigate the feasibility of developing data-driven methods to tackle the listed challenges and to explore the capabilities for accurate and reliable unmixing of PA signals. Data-driven unmixing methods could enable to have tissue molecular composition details with unprecedented sensitivity, thus opening many applications of PAI. This is true, especially for tissue regeneration monitoring, where non-invasive methods that do not involve the use of ionizing radiation are crucial to predicting the outcome of treatment. The work presented in this thesis contributes to several hypotheses that relate to the open challenges as described in Section 1.10.

The thesis starts with an overview of the commonly used unsupervised machine learning techniques applied to unmixing spectral PAI (**Chapter 2**). The section concludes with an overview of the open questions in PAI that have not been sufficiently solved yet. **Chapter 3** includes the proof of principle for using unsupervised machine learning algorithms to unmix PAI endogenous and exogenous chromophores. **Chapter 4** presents the work conducted to design and fabricate anthropomorphic heterogenous photoacoustic phantoms that aim to emulate realistic scenarios to accurately test advanced PAI approaches. **Chapter 5** gives a detailed presentation of the newly developed superpixel photoacoustic unmixing, which has been conducted towards hypothesis

H1 outlined in the previous section. **Chapters 6** and **7** show the validation *in vivo* models of the superpixel unmixing framework, which is described in detail in Chapter 5. Finally, **Chapter 8** describes the initial attempts of multi-frequency photoacoustic system characterization and optimization, to translate PAI for clinical applications.

Finally, **Chapter 9** discusses the methods and results presented in this thesis as well as contains a general discussion of the advantages and limitations of using data-driven methods for the PAI unmixing problem. It also contains a summary of the scientific contributions achieved through this thesis and an outlook of the next steps that could be made toward PAI to facilitate its translation into clinical practice.

References

[1] N. B. Roozen, C. Glorieux, L. Liu, M. Rychtáriková, T. Van der Donck, and A. Jacobs, "Converting sunlight into audible sound by means of the photoacoustic effect: The Heliophone," *J. Acoust. Soc. Am.*, 2016.

[2] D. Wu, L. Huang, M. S. Jiang, and H. Jiang, "Contrast agents for photoacoustic and thermoacoustic imaging: A review," *International Journal of Molecular Sciences*. 2014.

[3] M. Xu and L. V. Wang, "Photoacoustic imaging in biomedicine," *Rev. Sci. Instrum.*, vol. 77, no. 4, 2006.

[4] G. Matrone, A. S. Savoia, G. Caliano, and G. Magenes, "The delay multiply and sum beamforming algorithm in ultrasound B-mode medical imaging," *IEEE Trans. Med. Imaging*, 2015.

[5] J. Kim, D. Lee, U. Jung, and C. Kim, "Photoacoustic imaging platforms for multimodal imaging," *Ultrasonography*, vol. 34, no. 2, 2015.

[6] C. Ash, M. Dubec, K. Donne, and T. Bashford, "Effect of wavelength and beam width on penetration in light-tissue interaction using computational methods," *Lasers Med. Sci.*, vol. 32, no. 8, 2017.

[7] Q. Zhou, K. H. Lam, H. Zheng, W. Qiu, and K. K. Shung, "Piezoelectric single crystal ultrasonic transducers for biomedical applications," *Progress in Materials Science*, vol. 66. 2014.

[8] Ö. Oralkan *et al.*, "Capacitive micromachined ultrasonic transducers: Next-generation arrays for acoustic imaging?," *IEEE Trans. Ultrason. Ferroelectr. Freq. Control*, vol. 49, no. 11, 2002.

[9] J. Jung, W. Lee, W. Kang, E. Shin, J. Ryu, and H. Choi, "Review of piezoelectric micromachined ultrasonic transducers and their applications," *Journal of Micromechanics and Microengineering*, vol. 27, no. 11. 2017.

[10] Y. Qiu *et al.*, "Piezoelectric micromachined ultrasound transducer (PMUT) arrays for integrated sensing, actuation and imaging," *Sensors (Switzerland)*, vol. 15, no. 4. 2015.

[11] R. Nuster, M. Holotta, C. Kremser, H. Grossauer, P. Burgholzer, and G. Paltauf, "Photoacoustic microtomography using optical interferometric detection," *J. Biomed. Opt.*, vol. 15, no. 2, 2010.

[12] E. Zhang, J. Laufer, and P. Beard, "Backward-mode multiwavelength photoacoustic scanner using a planar Fabry-Perot polymer film ultrasound sensor for high-resolution three-dimensional imaging of biological tissues," *Appl. Opt.*, vol. 47, no. 4, 2008.

[13] S. W. Huang, Y. Hou, S. Ashkenazi, and M. O'Donnell, "High-frequency low-noise ultrasonic detection arrays based on parallelly probing an etalon," in *Proceedings - IEEE Ultrasonics Symposium*, 2007.

[14] R. Manwar, K. Kratkiewicz, and K. Avanaki, "Overview of ultrasound detection technologies for photoacoustic

imaging," *Micromachines*, vol. 11, no. 7. 2020.

[15] H. Grün, T. Berer, P. Burgholzer, R. Nuster, and G. Paltauf, "Three-dimensional photoacoustic imaging using fiber-based line detectors," *J. Biomed. Opt.*, vol. 15, no. 2, 2010.

[16] C. Zhang, T. Ling, S. L. Chen, and L. J. Guo, "Ultrabroad Bandwidth and Highly Sensitive Optical Ultrasonic Detector for Photoacoustic Imaging," *ACS Photonics*, vol. 1, no. 11, 2014.

[17] A. Kyriakou, E. Neufeld, B. Werner, M. M. Paulides, G. Szekely, and N. Kuster, "A review of numerical and experimental compensation techniques for skull-induced phase aberrations in transcranial focused ultrasound," *Int. J. Hyperth.*, vol. 30, no. 1, 2014.

[18] S. J. Sanabria, E. Ozkan, M. Rominger, and O. Goksel, "Spatial domain reconstruction for imaging speed-of-sound with pulse-echo ultrasound: Simulation and in vivo study," *Phys. Med. Biol.*, vol. 63, no. 21, 2018.

[19] Y. Hristova, P. Kuchment, and L. Nguyen, "Reconstruction and time reversal in thermoacoustic tomography in acoustically homogeneous and inhomogeneous media," *Inverse Probl.*, vol. 24, no. 5, 2008.

[20] A. Rosenthal, V. Ntziachristos, and D. Razansky, "Acoustic Inversion in Optoacoustic Tomography: A Review," *Curr. Med. Imaging Rev.*, vol. 9, no. 4, 2014.

[21] M. Haltmeier and L. V. Nguyen, "Reconstruction Algorithms for Photoacoustic Tomography in Heterogeneous Damping Media," *J. Math. Imaging Vis.*, 2019.

[22] J. Poudel, Y. Lou, and M. A. Anastasio, "A survey of computational frameworks for solving the acoustic inverse problem in three-dimensional photoacoustic computed tomography," *Phys. Med. Biol.*, vol. 64, no. 14, 2019.

[23] C. G. A. Hoelen and F. F. M. de Mul, "Image reconstruction for photoacoustic scanning of tissue structures," *Appl. Opt.*, vol. 39, no. 31, 2000.

[24] K. E. Thomenius, "Evolution of ultrasound beamformers," in *Proceedings of the IEEE Ultrasonics Symposium*, 1996, vol. 2.

[25] M. Mozaffarzadeh, A. Mahloojifar, M. Orooji, S. Adabi, and M. Nasiriavanaki, "Double-stage delay multiply and sum beamforming algorithm: Application to linear-array photoacoustic imaging," *IEEE Trans. Biomed. Eng.*, vol. 65, no. 1, 2018.

[26] T. Kirchner, F. Sattler, J. Gröhl, and L. Maier-Hein, "Signed real-time delay multiply and sum beamforming for multispectral photoacoustic imaging," *J. Imaging*, vol. 4, no. 10, 2018.

[27] "Efficient nonlinear beamformer based on P'th root of detected signals for linear-array photoacoustic tomography: application to sentinel lymph node imaging," *J. Biomed. Opt.*, vol. 23, no. 12, 2018.

[28] J. Schwab, S. Antholzer, and M. Haltmeier, "Learned backprojection for sparse and limited view photoacoustic tomography," 2019.

[29] H. Shan, C. Wiedeman, G. Wang, and Y. Yang, "Simultaneous reconstruction of the initial pressure and sound speed in photoacoustic tomography using a deep-learning approach," 2019.

[30] N. C. Burton *et al.*, "Multispectral Opto-acoustic Tomography (MSOT) of the Brain and Glioblastoma Characterization," *Neuroimage*, vol. 65, 2013.

[31] A. Needles *et al.*, "Development and initial application of a fully integrated photoacoustic micro-ultrasound system," *IEEE Trans. Ultrason. Ferroelectr. Freq. Control*, vol. 60, no. 5, pp. 888–897, 2013.

[32] G. P. Luke, S. Y. Nam, and S. Y. Emelianov, "Optical wavelength selection for improved spectroscopic photoacoustic imaging," *Photoacoustics*, vol. 1, no. 2, pp. 36–42, 2013.

[33] L. An and B. T. Cox, "Estimating relative chromophore concentrations from multiwavelength photoacoustic

images using independent component analysis," *J. Biomed. Opt.*, vol. 23, no. 07, 2018.

[34] S. Sethuraman, J. H. Amirian, S. H. Litovsky, R. W. Smalling, and S. Y. Emelianov, "Spectroscopic intravascular photoacoustic imaging to differentiate atherosclerotic plaques," *Opt. Express*, vol. 16, no. 5, 2008.

[35] F. M. Brochu, J. Brunker, J. Joseph, M. R. Tomaszewski, S. Morscher, and S. E. Bohndiek, "Towards quantitative evaluation of tissue absorption coefficients using light fluence correction in optoacoustic tomography," *IEEE Trans. Med. Imaging*, 2017.

[36] S. L. Jacques, "Optical properties of biological tissues: A review," *Physics in Medicine and Biology*, vol. 58, no. 11. 2013.

[37] R. Hochuli, L. An, P. C. Beard, and B. T. Cox, "Estimating blood oxygenation from photoacoustic images: can a simple linear spectroscopic inversion ever work?," *J. Biomed. Opt.*, vol. 24, no. 12, 2019.

[38] T. Kirchner, J. Gröhl, and L. Maier-Hein, "Context encoding enables machine learning-based quantitative photoacoustics," *J. Biomed. Opt.*, vol. 23, no. 05, 2018.

[39] S. Tzoumas *et al.*, "Eigenspectra optoacoustic tomography achieves quantitative blood oxygenation imaging deep in tissues," *Nat. Commun.*, 2016.

[40] B. Cox, J. G. Laufer, S. R. Arridge, and P. C. Beard, "Quantitative spectroscopic photoacoustic imaging: a review," *J. Biomed. Opt.*, vol. 17, no. 6, p. 061202, 2012.

[41] T. Tarvainen, B. T. Cox, J. P. Kaipio, and S. R. Arridge, "Reconstructing absorption and scattering distributions in quantitative photoacoustic tomography," *Inverse Probl.*, vol. 28, no. 8, 2012.

[42] J. Buchmann, B. Kaplan, S. Powell, S. Prohaska, and J. Laufer, "Quantitative PA tomography of high resolution 3-D images: Experimental validation in a tissue phantom," *Photoacoustics*, vol. 17, no. December 2019, 2020.

[43] M. N. Fadhel, E. Hysi, H. Assi, and M. C. Kolios, "Fluence-matching technique using photoacoustic radiofrequency spectra for improving estimates of oxygen saturation," *Photoacoustics*, 2020.

[44] L. V. Wang and Hsin-I Wu, *Biomedical Optics: Principles and Imaging*. 2012.

[45] A. Sassaroli and S. Fantini, "Comment on the modified Beer-Lambert law for scattering media," *Physics in Medicine and Biology*, vol. 49, no. 14. 2004.

[46] R. Fainchtein, B. J. Stoyanov, J. C. Murphy, D. A. Wilson, and D. F. Hanley, "<title>Local determination of hemoglobin concentration and degree of oxygenation in tissue by pulsed photoacoustic spectroscopy</title>," in *Biomedical Optoacoustics*, 2000, vol. 3916.

[47] R. O. Esenaliev, Y. Y. Petrov, O. Hartrumpf, D. J. Deyo, and D. S. Prough, "Continuous, noninvasive monitoring of total hemoglobin concentration by an optoacoustic technique," *Appl. Opt.*, vol. 43, no. 17, 2004.

[48] J. Laufer, D. Delpy, C. Elwell, and P. Beard, "Quantitative spatially resolved measurement of tissue chromophore concentrations using photoacoustic spectroscopy: Application to the measurement of blood oxygenation and haemoglobin concentration," *Phys. Med. Biol.*, vol. 52, no. 1, 2007.

[49] W. M. Star, J. P. A. Marijnissen, and M. J. C. Van Gemert, "Light dosimetry in optical phantoms and in tissues: I. Multiple flux and transport theory," *Phys. Med. Biol.*, vol. 33, no. 4, 1988.

[50] R. Graaff and B. J. Hoenders, "Diffusion theory for light propagation in biological tissue: limitations and adaptations (Invited Paper)," in *Saratov Fall Meeting 2004: Optical Technologies in Biophysics and Medicine VI*, 2005, vol. 5771.

[51] L. Wang and S. Jacques, "Monte Carlo modeling of light transport in multi-layered tissues in standard C," *Univ. Texas*, 1992.

[52] M. Keijzer, S. L. Jacques, S. A. Prahl, and A. J. Welch, “Light distributions in artery tissue: Monte Carlo simulations for finite-diameter laser beams,” *Lasers Surg. Med.*, vol. 9, no. 2, 1989.

[53] J. Yao and L. V. Wang, “Recent progress in photoacoustic molecular imaging,” *Current Opinion in Chemical Biology*, vol. 45. 2018.

[54] C. L. Bayer, B. J. Wlodarczyk, R. H. Finnell, and S. Y. Emelianov, “Ultrasound-guided spectral photoacoustic imaging of hemoglobin oxygenation during development,” *Biomed. Opt. Express*, vol. 8, no. 2, 2017.

[55] D. J. Lawrence, M. E. Escott, L. Myers, S. Intapad, S. H. Lindsey, and C. L. Bayer, “Spectral photoacoustic imaging to estimate in vivo placental oxygenation during preeclampsia,” *Sci. Rep.*, vol. 9, no. 1, 2019.

[56] M. Li, Y. Tang, and J. Yao, “Photoacoustic tomography of blood oxygenation: A mini review,” *Photoacoustics*, vol. 10. 2018.

[57] I. Stoffels *et al.*, “Metastatic status of sentinel lymph nodes in melanoma determined noninvasively with multispectral optoacoustic imaging,” *Sci. Transl. Med.*, vol. 7, no. 317, 2015.

[58] M. L. Li *et al.*, “Simultaneous molecular and hypoxia imaging of brain tumors in vivo using spectroscopic photoacoustic tomography,” *Proc. IEEE*, vol. 96, no. 3, 2008.

[59] S. Hu and L. V. Wang, “Photoacoustic imaging and characterization of the microvasculature,” *J. Biomed. Opt.*, vol. 15, no. 1, 2010.

[60] S. Iskander-Rizk *et al.*, “Micro Spectroscopic Photoacoustic (μsPA) imaging of advanced carotid atherosclerosis,” *Photoacoustics*, vol. 22, 2021.

[61] M. U. Arabul, M. C. M. Rutten, P. Bruneval, M. R. H. M. van Sambeek, F. N. van de Vosse, and R. G. P. Lopata, “Unmixing multi-spectral photoacoustic sources in human carotid plaques using non-negative independent component analysis,” *Photoacoustics*, vol. 15, no. June, p. 100140, 2019.

[62] G. S. Sangha and C. J. Goergen, “Label-free photoacoustic and ultrasound imaging for murine atherosclerosis characterization,” *APL Bioeng.*, vol. 4, no. 2, 2020.

[63] J.-T. Oh, M.-L. Li, H. F. Zhang, K. Maslov, G. Stoica, and L. V. Wang, “Three-dimensional imaging of skin melanoma in vivo by dual-wavelength photoacoustic microscopy,” *J. Biomed. Opt.*, vol. 11, no. 3, 2006.

[64] K. Kratkiewicz *et al.*, “Photoacoustic/ultrasound/optical coherence tomography evaluation of melanoma lesion and healthy skin in a swine model,” *Sensors (Switzerland)*, vol. 19, no. 12, 2019.

[65] J. Kim *et al.*, “Multispectral ex vivo photoacoustic imaging of cutaneous melanoma for better selection of the excision margin,” *British Journal of Dermatology*, vol. 179, no. 3. 2018.

[66] G. P. Luke, J. N. Myers, S. Y. Emelianov, and K. V. Sokolov, “Sentinel lymph node biopsy revisited: Ultrasound-guided photoacoustic detection of micrometastases using molecularly targeted plasmonic nanosensors,” *Cancer Res.*, vol. 74, no. 19, 2014.

[67] A. Forbrich, A. Heinmiller, and R. J. Zemp, “Photoacoustic imaging of lymphatic pumping,” *J. Biomed. Opt.*, vol. 22, no. 10, p. 1, 2017.

[68] G. P. Luke, D. Yeager, and S. Y. Emelianov, “Biomedical applications of photoacoustic imaging with exogenous contrast agents,” *Ann. Biomed. Eng.*, vol. 40, no. 2, 2012.

[69] Y. Dai *et al.*, “Metastatic status of sentinel lymph nodes in breast cancer determined with photoacoustic microscopy via dual-targeting nanoparticles,” *Light Sci. Appl.*, vol. 9, no. 1, 2020.

[70] Z. Xie *et al.*, “In vivo assessment of inflammation in carotid atherosclerosis by noninvasive photoacoustic imaging,” *Theranostics*, vol. 10, no. 10, 2020.

[71] J. Jo *et al.*, "Photoacoustic tomography for human musculoskeletal imaging and inflammatory arthritis detection," *Photoacoustics*, vol. 12. 2018.

[72] J. Jo *et al.*, "A Functional Study of Human Inflammatory Arthritis Using Photoacoustic Imaging," *Sci. Rep.*, vol. 7, no. 1, 2017.

[73] J. Lavaud *et al.*, "Noninvasive monitoring of liver metastasis development via combined multispectral photoacoustic imaging and fluorescence diffuse optical tomography," *Int. J. Biol. Sci.*, vol. 16, no. 9, 2020.

[74] Y. Liu *et al.*, "Low-toxicity FePt nanoparticles for the targeted and enhanced diagnosis of breast tumors using few centimeters deep whole-body photoacoustic imaging," *Photoacoustics*, vol. 19, 2020.

[75] Q. Yang, H. Jin, Y. Gao, J. Lin, H. Yang, and S. Yang, "Photostable Iridium(III)-Cyanine Complex Nanoparticles for Photoacoustic Imaging Guided Near-Infrared Photodynamic Therapy in Vivo," *ACS Appl. Mater. Interfaces*, vol. 11, no. 17, 2019.

[76] G. Paltauf, R. Nuster, and M. Frenz, "Progress in biomedical photoacoustic imaging instrumentation toward clinical application," *Journal of Applied Physics*, vol. 128, no. 18. 2020.

[77] Y. Goh *et al.*, "Multispectral Optoacoustic Tomography in Assessment of Breast Tumor Margins During Breast-Conserving Surgery: A First-in-human Case Study," *Clin. Breast Cancer*, vol. 18, no. 6, 2018.

[78] V. Neuschmelting *et al.*, "Performance of a Multispectral Optoacoustic Tomography (MSOT) System equipped with 2D vs. 3D Handheld Probes for Potential Clinical Translation," *Photoacoustics*, vol. 4, no. 1, 2016.

[79] M. W. Schellenberg and H. K. Hunt, "Hand-held optoacoustic imaging: A review," *Photoacoustics*, vol. 11. 2018.

[80] L. Lin *et al.*, "Single-breath-hold photoacoustic computed tomography of the breast," *Nat. Commun.*, vol. 9, no. 1, 2018.

[81] M. Heijblom *et al.*, "The state of the art in breast imaging using the Twente Photoacoustic Mammoscope: results from 31 measurements on malignancies," *Eur. Radiol.*, vol. 26, no. 11, pp. 3874–3887, 2016.

[82] M. Schwarz, M. Omar, A. Buehler, J. Aguirre, and V. Ntziachristos, "Implications of ultrasound frequency in optoacoustic mesoscopy of the skin," *IEEE Trans. Med. Imaging*, vol. 34, no. 2, 2015.

[83] A. B. E. Attia *et al.*, "A review of clinical photoacoustic imaging: Current and future trends," *Photoacoustics*, vol. 16. 2019.

[84] J. Kim *et al.*, "Multispectral photoacoustic assessment of thyroid cancer nodules in vivo," 2020.

[85] A. Dima and V. Ntziachristos, "In-vivo handheld optoacoustic tomography of the human thyroid," *Photoacoustics*, vol. 4, no. 2, 2016.

[86] S. Manohar and M. Dantuma, "Current and future trends in photoacoustic breast imaging," *Photoacoustics*, vol. 16, no. February, p. 100134, 2019.

[87] S. Manohar, A. Kharine, J. C. G. Van Hespen, W. Steenbergen, and T. G. Van Leeuwen, "The Twente Photoacoustic Mammoscope: System overview and performance," *Physics in Medicine and Biology*, vol. 50, no. 11. 2005.

[88] M. Heijblom, W. Steenbergen, and S. Manohar, "Clinical photoacoustic breast imaging: The twente experience.," *IEEE Pulse*, vol. 6, no. 3, 2015.

[89] J. Hult *et al.*, "Comparison of photoacoustic imaging and histopathological examination in determining the dimensions of 52 human melanomas and nevi ex vivo," *Biomed. Opt. Express*, vol. 12, no. 7, 2021.

[90] R. Sheikh *et al.*, "Clinical Translation of a Novel Photoacoustic Imaging System for Examining the Temporal Artery," *IEEE Trans. Ultrason. Ferroelectr. Freq. Control*, vol. 66, no. 3, pp. 472–480, 2019.

[91] M. Naumovska *et al.*, "Mapping the architecture of the temporal artery with photoacoustic imaging for diagnosing giant cell arteritis," *Photoacoustics*, vol. 27, p. 100384, Sep. 2022.

[92] M. Petri *et al.*, "Photoacoustic imaging of real-time oxygen changes in chronic leg ulcers after topical application of a haemoglobin spray: A pilot study," *J. Wound Care*, vol. 25, no. 2, 2016.

[93] F. Witte *et al.*, "Degradable biomaterials based on magnesium corrosion," *Curr. Opin. Solid State Mater. Sci.*, vol. 12, no. 5–6, 2008.

[94] J. L. Wang, J. K. Xu, C. Hopkins, D. H. K. Chow, and L. Qin, "Biodegradable Magnesium-Based Implants in Orthopedics—A General Review and Perspectives," *Advanced Science*, vol. 7, no. 8. 2020.

[95] B. Wiese *et al.*, "Biodegradable magnesium-based implants in bone studied by synchrotron radiation microtomography," 2017.

[96] Y. Sun, H. Helmholz, and R. Willumeit-Römer, "Preclinical in vivo research of magnesium-based implants for fracture treatment: A systematic review of animal model selection and study design," *Journal of Magnesium and Alloys*, vol. 9, no. 2. 2021.

[97] H. Windhagen *et al.*, "Biodegradable magnesium-based screw clinically equivalent to titanium screw in hallux valgus surgery: Short term results of the first prospective, randomized, controlled clinical pilot study," *Biomed. Eng. Online*, vol. 12, no. 1, 2013.

[98] L. C. Cabrelli, F. W. Grillo, D. R. T. Sampaio, A. A. O. Carneiro, and T. Z. Pavan, "Acoustic and Elastic Properties of Glycerol in Oil-Based Gel Phantoms," *Ultrasound Med. Biol.*, vol. 43, no. 9, 2017.

[99] L. C. Cabrelli, J. H. Uliana, L. B. Da Cruz Junior, L. Bachmann, A. A. O. Carneiro, and T. Z. Pavan, "Glycerol-in-SEBS gel as a material to manufacture stable wall-less vascular phantom for ultrasound and photoacoustic imaging," *Biomed. Phys. Eng. Express*, vol. 7, no. 6, 2021.

[100] L. Hacker *et al.*, "A copolymer-in-oil tissue-mimicking material with tuneable acoustic and optical characteristics for photoacoustic imaging phantoms," *IEEE Trans. Med. Imaging*, 2021.

Chapter 2

Recent advances in photoacoustic blind source spectral unmixing approaches and the enhanced detection of endogenous tissue chromophores*

Abstract:

In this chapter, we have investigated the performance of different blind source separation (BSS) algorithms, typically used for automated unmixing of spectral photoacoustic imaging (sPAI). Specifically, a comparative analysis of Principal Component Analysis (PCA), Independent Component Analysis (ICA), and Non-negative Matrix Factorization (NNMF) has been conducted through an experimental phantom study at different signal-to-noise ratio (SNR) conditions. Besides, a cross-correlation analysis has been performed to benchmark the unmixing performance of the different unmixing algorithms with near-infrared spectroscopy (NIRS). Finally, the comparative analysis has shown that the NNMF has superior photoacoustic unmixing performance than ICA and PCA in terms of correlation and processing time.

*This chapter is part of the manuscript published as: **Grasso, V.**, Hassan, H. W., Mirtaheri, P., Willumeit-Römer, R., & Jose, J. (2022). *"Recent advances in photoacoustic blind source spectral unmixing approaches and the enhanced detection of endogenous tissue chromophores."* Frontiers in Signal Processing, p.67.

**To improve the readability of the chapter, some sections of the publication have been rearranged.

frontiers | Frontiers in Signal Processing

TYPE Original Research
PUBLISHED 10 November 2022
DOI 10.3389/frsip.2022.984901

OPEN ACCESS

EDITED BY
James Joseph,
University of Dundee, United Kingdom

REVIEWED BY
Mithun Kuniyil Ajith Singh,
Cyberdyne,Inc., Netherlands
Mohesh Moothanchery,
University of Liverpool, United Kingdom

*CORRESPONDENCE
Jithin Jose,
jithin.jose@fujifilm.com

SPECIALTY SECTION
This article was submitted to Biomedical Signal Processing,
a section of the journal
Frontiers in Signal Processing

RECEIVED 02 July 2022
ACCEPTED 31 October 2022
PUBLISHED 10 November 2022

CITATION
Grasso V, Hassan HW, Mirtaheri P, Willumeit-Römer R and Jose J (2022), Recent advances in photoacoustic blind source spectral unmixing approaches and the enhanced detection of endogenous tissue chromophores. *Front. Sig. Proc.* 2:984901.
doi: 10.3389/frsip.2022.984901

Recent advances in photoacoustic blind source spectral unmixing approaches and the enhanced detection of endogenous tissue chromophores

Valeria Grasso [1,2], Hafiz Wajahat Hassan [3], Peyman Mirtaheri [3], Regine Willumeit-Römer [2,4] and Jithin Jose [1]*

[1]FUJIFILM VisualSonics, Amsterdam, Netherlands,
[2]Faculty of Engineering, Institute for Materials Science, Christian-Albrecht University of Kiel, Kiel, Germany,
[3]Department of Mechanical, Electronic and Chemical Engineering, Faculty of Technology, Art and Design, Oslo Metropolitan University, Oslo, Norway,
[4]Division Metallic Biomaterials, Institute of Materials Research, Helmholtz-Zentrum Hereon GmbH, Geesthacht, Germany

Recently, the development of learning-based algorithms has shown a crucial role to extract features of vital importance from multi-spectral photoacoustic imaging. In particular, advances in spectral photoacoustic unmixing algorithms can identify tissue biomarkers without *a priori* information. This has the potential to enhance the diagnosis and treatment of a large number of diseases. Here, we investigated the latest progress within spectral photoacoustic unmixing approaches. We evaluated the sensitivity of different unsupervised Blind Source Separation (BSS) techniques such as Principal Component Analysis (PCA), Independent Component Analysis (ICA), and Non-negative Matrix Factorization (NNMF) to distinguish absorbers from spectral photoacoustic imaging. Near-infrared spectroscopy (NIRS) has been used to validate the performance of the different unmixing algorithms. Although the NNMF has shown superior unmixing performance than PCA and ICA in terms of correlation and processing time, this is still prone to unmixing misinterpretation due to spectral coloring artifact. Phantom experimental studies have been conducted to benchmark the performance of the BSS algorithms.

KEYWORDS

blind source separation, photoacoustic, spectral coloring, spectral imaging, ultrasound, unsupervised machine learning

1 Introduction

In recent years, there has been special attention on developing new learning-based signal processing approaches as it plays a crucial role in medical image analysis and its interpretation. In addition to the enhanced visualization of the images, one of the main aims of these advanced signal-processing approaches is to identify specific signal markers that can distinguish physiological and pathological conditions. Commonly, expert radiologists are required for analyzing and interpreting biomedical images. Although this is a standard operating procedure, in most cases the approach is tedious, user-dependent, and can be biased. To this end, the development and implementation of an automated feature extraction algorithm will have an added value as this can be used also as a surrogate marker to improve the diagnosis and interpretation (Ali et al., 2008; Chowdhary and Acharjya, 2020).

Photoacoustic is an emerging biomedical imaging modality that has the potential to non-invasively extract molecular tissue composition at a volumetric scale (Cassidy and Radda, 2005). The approach is real-time and over the last decade, it has been used in many preclinical applications such as tissue inflammatory monitoring (Jo et al., 2017; Jo et al., 2018; Xie et al., 2020), vascular remodeling (Hu and Wang, 2010; Arabul et al., 2019; Sangha and Goergen, 2020; Iskander-Rizk et al., 2021), cancer oxygen saturation changes (Li et al., 2008; Stoffels et al., 2015; Bayer et al., 2017; Li et al., 2018; Lawrence et al., 2019), and biodistribution of exogenous contrast agents (Yang et al., 2019; Lavaud et al., 2020; Liu et al., 2020). Although the photoacoustic imaging technology is well established in preclinical research, the clinical aspect of the technology is comparatively limited as it has regulatory concerns and requires local ethical approvals to conduct clinical research studies. This scenario could change soon as most of these technology providers are looking into the translational aspect of this technology and applying for Food and Drug Administration (FDA) approval. Recently, FDA has granted premarket approval to one of the industrial providers of breast cancer photoacoustic imaging technology, which helps physicians to differentiate between benign and malignant lesions (Kuniyil Ajith Singh et al., 2020). This clearly demonstrates the expanding potential of photoacoustic technology for clinical applications. However, to facilitate this translation, a significant improvement to the hardware and image analysis algorithms is necessary. Specifically, multi-spectral photoacoustic imaging (sPAI) mode enables the detection of molecular components of vital importance. In sPAI the tissues are illuminated with pulsed laser light at different wavelengths within the visible or near-infrared (NIR) spectral range (Kim et al., 2015; Allen and Beard, 2016; Das et al., 2021; Park et al., 2022). The light absorbed by the tissue chromophores induces a thermoelastic expansion which consequently generates pressure waves that are recorded just as conventional ultrasound signals. Thus, the contrast of PA imaging is due to light-absorbing molecules that can be either endogenous to tissue, (e.g., hemoglobin, melanin, water, and lipid) or administered exogenous agents. Therefore, the photoacoustic image represents the spatial distribution of the initial pressure generated by the optical contrast of a variety of tissue chromophores (Wang, 2017). The light absorption is dependent on the wavelength, consequently, different wavelengths of optical excitation are absorbed differently by the distinct tissue components. Thus, the generated sPAI data include per pixel the spectral fingerprints of multiple absorbers present within the tissue (Deán-Ben and Razansky, 2014).

Despite the high spatial resolution of sPAI, a pixel usually corresponds to more than one chromophore present in the tissue. Thus, the spectrum per pixel is a linear combination of the spectral responses of all the absorbers. However, to characterize the tissue composition from sPAI, the spectral profile of each individual chromophore must be efficiently distinguished. Thus, advanced spectral unmixing methods are required to solve this problem (Manwar et al., 2020).

To date, the most commonly used spectral unmixing methods are based on differential or linear fitting algorithms (Keshava, 2003). But generally, these algorithms require user interaction to provide the expected source spectral curves as an input to unmix the signals. For translational research with patients, these types of supervised spectral unmixing can be challenging, as the spectral signature of the tissues differs with respect to the disease conditions. Thus, the reliability of these spectral fitting methods depends on the *a priori* knowledge of the spectral information including all potential components and the quality of the data.

The automatic spectral unmixing algorithms that do not require *a priori* spectral information and can effectively unmix the data without user interaction are an ideal choice to overcome all these limitations. Recently there have been a lot of efforts in the implementation of deep learning (DL) architectures to solve the unmixing problem in sPAI (Lee et al., 2017; Cai et al., 2018; Gröhl et al., 2021; Yang et al., 2021). Although DL approaches can lead to ultra-high accurate results, the data set constructed to train the network determines the generalization ability and robustness of the learning model. As a result, since sPAI is an innovative technology, there are currently insufficient data sets for deep neural network training. Consequently, common remedies to this problem include using simulated data for proof-of-concept verification (Allman et al., 2018; Gröhl et al., 2019), conducting transfer learning with “real” experimental data (Jnawali et al., 2019), or techniques of data augmentation (Rodrigues et al., 2021). To generate these PA *in silico* data, numerical simulations of the forward light diffusion (“light-IN”) and backward US propagation (“sound-OUT”) processes are required. Hence, the current limitation of these approaches is that they are application-specific and challenging to generalize for “unseen” cases.

On the other hand, unsupervised feature learning methods have resulted effective in learning representations without training data sets. However, many existing feature-learning algorithms are hard to use and require extensive hyperparameter tuning (Durairaj et al., 2020). Blind source separation (BSS) algorithms are a class of more sophisticated approaches, requiring only one hyperparameter, as the number of features to learn (Jutten and Karhunen, 2004; Benyamin et al.,2020). These are based on modeling the data, making assumptions about their distribution, and solving an optimization problem. Although the BSS methods perform well on image object recognition, and

video/audio classification (Smita et al., 2014), these are not optimized for spectral photoacoustic unmixing. Specifically, the sPAI unmixing is an ill-posed inverse problem where the *a priori* information related to the spectral fingerprints of tissue components and their spatial distribution are both unknown. Glatz et al. 2011 have shown that BSS techniques such as Principal Component Analysis (PCA) and Independent Component Analysis (ICA) have great potential to solve the sPAI unmixing problem efficiently, without prior knowledge of the constituent spectra (Buehler et al., 2010).

Although these BSS approaches are promising to detect the spectral components, the light fluence variation along the depth could be a major challenge, because the absorption spectra of the tissue components along the depth can be perceived as altered and thus creating misinterpretations in the unmixing process. Specifically, in sPAI the detected spectra are not unique per each molecular component. This is because the acquired absorption spectrum is influenced by the position of the moiety within the tissue. Thus, the actual spectrum is altered due to the light fluence $\Phi(\vec{r}, \lambda)$ attenuation, which is depth- and wavelength-dependent. This phenomenon is also referred to as the "spectral coloring effect". Although the light fluence estimation *via* explicit model has been widely investigated (Cox et al., 2006; Yuan et al., 2007; Cox et al., 2009), for experimental data, this is complex due to uncertainties in precisely evaluating the tissues' optical properties. Recently, Tzoumas et al. (2016) have proposed an eigenspectra-based fluence correction approach to improve the estimation of blood oxygen saturation (sO_2) in deep tissue. They modeled the fluence through the eigenspectra analysis which is mainly used to compensate for sO_2. In another study, Bulsink et al., 2021) have proposed a dual-wavelength LED array-based photoacoustic imaging including an ultrasound image-guided fluence compensation approach to monitor oxygen saturation in translational research settings.

In one of our previous works (Grasso et al., 2020), we optimized a specialized class of BSS algorithm, the Non-negative Matrix Factorization (NNMF) for the spectral unmixing of sPAI. This method has great potential to accurately extract the prominent tissue chromophores from sPAI. However, the problem of automatically distinguishing weak absorbers, such as lipids, from prominent tissue chromophores like hemoglobin makes the unmixing procedure more complex by leading to incomplete identification of tissue constituents.

In this study, we have investigated the performance of different blind source separation (BSS) algorithms, typically used for automated unmixing in sPAI. Specifically, a comparative analysis of Principal Component Analysis (PCA), Independent Component Analysis (ICA), and Non-negative Matrix Factorization (NNMF) has been conducted through an experimental phantom study at different signal-to-noise ratio (SNR) conditions. These are promising methods to automatically distinguish prominent absorbers. On the other end, their sensitivity for distinguishing less prominent absorbers and components with similar spectra is still limited. The near-infrared spectroscopy (NIRS) has been used to measure the pure absorption spectra of the chromophores involved in the study. Finally, a cross-correlation analysis has been performed to benchmark the unmixing performance of the different unmixing algorithms with NIRS.

2 Materials and methods

2.1 Blind source separation theory

Spectral photoacoustic imaging (sPAI) can be modeled as a set of mixed observations $M \in \mathrm{R}^{n \times m}$, where n is the number of pixels and m is the number of wavelengths. In a Linear Mixture Model (LMM), the mixture matrix M can be formalized as $M = WS$, where the underlying individual source spectra S and the respective distribution maps W are mixed and unknown. Thus, spectral unmixing is then a process of estimating the distinctive spectral signatures from the sPAI mixture. Although in simple cases it is possible to approximate the absorption spectra S of the tissue components from their theoretical optical properties and assumptions made, this became complex during *in vivo* studies (Li et al., 2018). Therefore, blind source separation (BSS) is a category of algorithms that aims to separate the mixed pixel spectra M into a collection of constituent spectra S (called endmembers) and a set of fractional abundance maps W without providing *a priori* information about S (Comon and Jutten, 2010).

The matrices $W \in \mathrm{R}^{n \times k}$ and $S \in \mathrm{R}^{k \times m}$ contain the abundance maps and the absorption spectra of k source components, respectively. Generally, a maximum of k endmembers that can be obtained with the BSS algorithms, has to be specified by the user as the only hyperparameter. Since the unmixing problem is ill-posed, the BSS algorithms are based on iterative optimization procedures to retrieve both W and S. The different BSS algorithms such as Principal Component Analysis (PCA), Independent Component Analysis (ICA), and Non-negative Matrix Factorization (NNMF) make different assumptions regarding the linear combined source components, the cost function, and the iterative rules, thus leading to different unmixing results.

The following subsections initially provide the theoretical background of the main BSS methods. Moreover, a summary of the features of the different BSS approaches is reported in Table 1.

2.1.1 Singular value decomposition and principal component analysis

The singular value decomposition (SVD) and principal component analysis (PCA) are related methods that rely on the hypothesis that the source components S are uncorrelated and orthogonal (Roweis, 1998; Tipping and Bishop, 1999; Ahnet al., 2007). These approaches compute the orthogonal transformation that decorrelates the variables and keeps the ones with the largest variance. Thus, SVD splits the mixed data matrix $M \in \mathrm{R}^{n \times m}$ into a product of three matrices:

$$M = U\Sigma V^T \quad (1)$$

where $\Sigma \in \mathrm{R}^{n \times m}$ is a diagonal matrix containing the eigenvalues, and $U \in \mathrm{R}^{n \times n}$, $V \in \mathrm{R}^{m \times m}$ are orthogonal matrices containing the respective eigenvectors. Principal component analysis (PCA) identifies orthogonal vectors for dimension reduction by performing an eigen-decomposition of the covariance matrix of the observed data M. Therefore, the PCA could be performed by using the SVD and *vice versa* (Oblefias et al., 2004). Finally, the principal components (PCs) are the columns of the V matrix and the projection of the original data M onto the PCs directions are:

TABLE 1 BSS algorithms' technical specifications.

	Hypothesis	Data pre-processing	Model	Optimization algorithm	Cost function	Hyperparameter	Ref
PCA	Source components are statistically uncorrelated	-	$M = U\Sigma V^T$ $Z_{pca} = \Sigma V^T$	Eigenvalue decomposition Lanczos bidiagonalization Alternating least squares	$\min_{W,S} \frac{1}{2} \| M - WS \|_F^2$	k: number of features to learn	Tipping and Bishop, (1999)
ICA	Source components are statistically independent	Centering $\tilde{M} = M - E[M]$ Whitening $\hat{M} = Z\tilde{M}, E[ZZ^T] = 1$	$\hat{M} \approx WS$	FastICA Infomax JADE RICA	$\min_W g(W^T\hat{M}) + r$ $g(\cdot) = \log(\cosh(\cdot))$ r: *reconstruction cost*	k: number of features to learn	(Bell and Sejnowski, 1995; Hyvärinen, 1999; Zhang et al., 2012; Rutledge and Jouan-Rimbaud Bouveresse, 2013)
NNMF	Source components are a low-rank approximation of the mixture matrix	-	$M \approx WS$	Alternating non-negative least squares Multiplicative update	$\min_{W,S} \frac{1}{2} \| M - WS \|_F^2$ $W, S \geq 0$	k: number of features to learn	(Lee and Seung, 2001; Santosh Kumar et al., 2016)

$$Y = V^T M \quad (2)$$

The first PC (which corresponds to the eigenvectors) represents the subspace in which the variance of the data is the largest. Therefore, the variance (which corresponds to the eigenvalues) is related to the respective prominence of the principal component. Often the SVD/PCA method is used as *a priori* step of other blind approaches, which consequently use the achieved components as a starting point of the optimization process.

2.1.2 Independent component analysis

Independent component analysis (ICA) is another BSS method that assumes that the observed data are a superimposition of a number of stochastically independent components (Hyvärinen, 2013). This is based on the hypothesis that the source components are maximally independent and non-Gaussian. The non-Gaussianity of the source data is the crucial assumption that makes this method more effective than PCA (uncorrelated and Gaussian). Following the Central Limit Theorem, the sum of independent variables tends toward a normal distribution (Kwak and Kim, 2017). Therefore, with the non-Gaussianity assumption, the independence hypothesis of the unmixed components is stricter and consequently more robust than uncorrelatedness. Usually, the ICA algorithm requires a pre-processing step of mixed data centering and whitening to reduce the correlation of the observed data. During the centering step the mean is subtracted from all the mixed signals. Then the whitening includes two main steps: a decorrelation (covariance is zero) and scaling (unit variance) of the centered mixed signals. After the centering and whitening, the mixed data $\hat{M} = ZM$ have zero mean and variance one, where Z can be found by PCA, normalizing the PCs to unit variance. The observed whitened mixed data matrix $\hat{M}$ is then modeled following the linear mixture model (LMM):

$$\hat{M} \approx WS \quad (3)$$

Here, the reconstruction independent component analysis (RICA) method has been used to minimize the cost function and estimate the source components $S \in R^{k \times m}$ and the unmixed abundance maps $W \in R^{n \times k}$. This adds a "reconstruction regularization cost" to the cost function with respect to the standard Aapo Hyvarinen ICA method that uses the fast fixed-point optimization approach (Hyvärinen, 1999). Thus, RICA (Le et al., 2011) ensures more accurate convergence and more robust results even in the case of incomplete and unwhitened data.

2.1.3 Non-negative matrix factorization

Like ICA, non-negative matrix factorization (NNMF) is a BSS method that performs a factorization of mixed observations $M \approx WS$, but here a positively constrained cost function has been added (Berry et al., 2007). These positivity constraints $W \geq 0$ and $S \geq 0$ provide an advantage in applications where data are non-negative, as in sPAI, thus leading to better interpretability of the results. Hence, the optimization problem can be formulated as follows:

$$[W, S] = \min_{W \geq 0, S \geq 0} \frac{1}{2} \| M - WS \|_F^2 \quad (4)$$

Lee and Seung (2001) have proposed the Multiplicative Update Rules to solve this optimization problem. Since no elements are negative, the LMM can be intuitively interpreted as a process of generating the original data by linear combinations (parts-based) of the prominent components (subtraction operations are not involved). This is known as a parts-based linear representation for non-negative data. Besides, literature studies have shown that imposing the positivity condition enhances the convergence of the optimization algorithm used for the unmixing problem (Lipovetsky, 2009; Hervé, 2010).

In addition, the NNMF approach is considered a special version of PCA including the non-negativity constraint and without orthogonality of factors (Sotiras et al., 2015). Although both approaches are similar, there is a fundamental difference between them. While the goal of PCA is to reduce the correlated observed variables, factor analysis aims to explain the correlation between the variables underlining the latent factors causing the observations. Furthermore, considering another comparison, NNMF and ICA are two closely related unmixing approaches. The main difference is that NNMF over ICA can recover the sources without requiring knowledge about the mean and variance

of the sources.

Table 1 shows a comparison of the different BSS algorithms including the details of the mixture model and assumptions as well as the cost function model and optimization iterative algorithms adopted by the BSS approaches to unmix the source spectra *S* and the respective abundance maps *W* from sPAI.

2.2 Ultrasound and photoacoustic image acquisition

High-resolution Ultrasound (US) and spectral Photoacoustic imaging (sPAI) have been acquired by using the platform Vevo LAZR-X (FUJIFILM VisualSonics, Inc., Toronto, ON, Canada). The imaging setup includes a high-frequency US system, an optical parametric oscillator (OPO) integrated Nd:YAG nanosecond pulsed laser, and the animal imaging platform. The system is equipped with a linear US transducer array (MX250) that consists of 256 elements at a nominal center frequency of 21 *MHz* and bandwidth of 15 − 30 *MHz*. Light from the laser is delivered to the tissue through optical fibers, mounted on either side of the transducer. To obtain the homogenous light illumination, the sample to be imaged is placed on the converging area of the two light beams. The spectral photoacoustic images have been acquired by tuning the laser wavelengths within the range of 680 − 970 *nm* with 20 nm step size. During the volumetric US-PA acquisitions, a stepper motor is used for the linear translation of the US transducer and optical fibers along the sample. The linear stepper motor moves in steps of a minimum of 0.1 mm while capturing 2-D parallel images, for a maximum 3D range distance of 64 mm.

2.3 Near-infrared spectroscopy

A portable near-infrared spectroscopic (NIRS) probe that has been used to validate the spectral absorption curves of the chromophores involved in the study. To this end, a customized NIRS probe was designed at the Optical lab in OsloMet (Oslo Metropolitan University, Norway) (Hassan et al., 2021a; Hassan et al., 2021b). Unlike commercially available solutions, this NIRS probe is designed to target two regions of interest at two different depths. Specifically, the OsloMet's probe uses a broadband LED light source (650–1050 nm) and works with two depth ranges (2–2.25 mm and 3–3.5 mm respectively). In addition, the optical probe's light sources ensure the safety of the operations, in compliance with the NIR safety guidelines (IEC, 2015). This NIRS probe uses a source-detector pair that generates a banana-shaped optical path that narrows at the source and detector's locations and broadens as it penetrates deeper into the tissue (Feng et al., 1995). The depth of a photon before detection is proportional to the square root of the source-detector separation (Weisset al., 1989). Hence, optical depth is generally 1/2 to 1/3 of the source-detector distance (Papazoglou et al., 2006). The spectra from the optical probe are then collected by a spectrometer (Avaspec 2048x14, Avantes BV, Netherlands). An integration time of 4 s, was selected to make sure that enough photons are collected by the detector. In this experiment, a distance of 6 mm between the source and detector was used to get a focal depth of 2–2.5 mm and the wavelength range has been fixed to 680–970 nm as the one used for sPAI. Finally, the obtained spectra from NIRS have been used as a reference to be compared with the automatically unmixed signatures from sPAI.

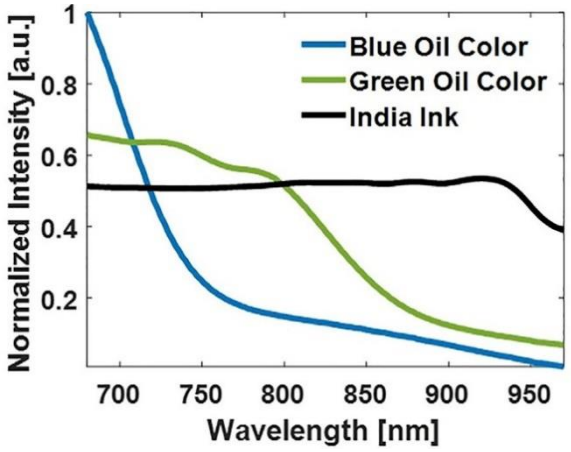

FIGURE 1
Absorption spectra of the dyes used within the vessel-mimicking phantoms measured by the NIRS probe.

To obtain the spectral curves for the correlation analysis, the NIRS measurements have been performed on the dyes used for the vessel-mimicking phantoms. Blue, green oil colors (Winsor and Newton, London, United Kingdom), and India Ink (Higgins Ink, Leeds, MA, United States) were used, and the colors have been overspread on white paper. These have been placed at the optimal distance from the NIRS probe during the measurements using a transparent gel pad as a spacer. This guarantees the optimal position of the sample at the focal zone of the NIRS probe design. Figure 1 depicts the absorption spectra of the dyes measured *via* the OsloMet NIRS probe. While the Blue Oil Color absorption spectrum shows the highest absorption at 680 nm and has a quasi-exponential decrease afterward, the Green Oil Color shows wider absorption until around 800–830 nm before decreasing at higher wavelengths. Finally, India Ink shows a broad absorption spectrum within the 680–900 nm region and a gradual absorption decrease toward 900 nm.

2.4 Experimental vessel-mimicking phantoms

Phantom measurements were first performed to investigate the sensitivity of the BSS unmixing algorithms at different signal-to-noise ratio (SNR) conditions. Three vessel-mimicking phantoms have been fabricated with different optical properties. A vessel-mimicking shape has been painted with green and blue oil colors (Winsor and Newton, London, United Kingdom) on white paper (see Figure 2A). After the paint has dried, this has been embedded in each turbid agarose solution. The paper is carefully retrieved from the agarose to sequentially reuse it in all of the phantoms. All the phantoms have been designed to have a reduced scattering coefficient of ~5 cm^{-1}. Thus, the phantoms were made with 1.5% (w/v) agar (Alfa Aesar, Heysham, Lancaster) and 2% (w/v) Intralipid (20%, Sigma-Aldrich, Canada). To challenge the unmixing algorithms, in two of the phantoms, black India Ink (Higgins Ink, Leeds, MA, United States) was added to the agar-Intralipid mixture before solidification, to simulate background absorption. Specifically, these resulted in a background absorption of 0.05% v/v and 0.1%

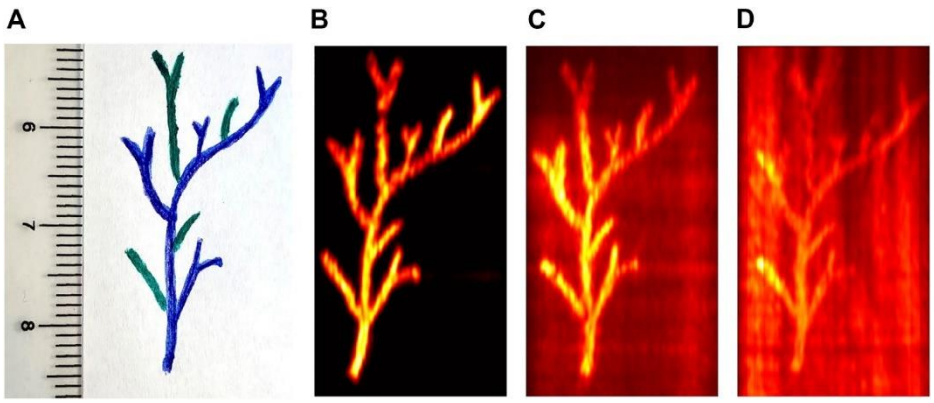

FIGURE 2
Vessel-mimicking phantom shape (A) and the single wavelength photoacoustic images acquired at 700 nm for the three phantoms with different levels of absorbing background. Specifically, without India Ink (B), with 0.05% v/v India Ink (C), and with 0.1% v/v India Ink (D) as background absorption.

v/v respectively. Hence, this leads to three vessel-mimicking phantoms that have no background absorption, medium background absorption, and high background absorption respectively.

Figures 2B–D show the PA image at a single wavelength (700 *nm*) of the phantoms prepared with different backgrounds. The images show the maximum intensity projection (MIP) of the 3D single wavelength PA image, from the top view of the phantom. After preparation, the phantom is positioned orthogonally to the transducer coupled with optical fibers, which are linearly translated along the phantom during the sPAI acquisition. Therefore, the phantoms' sPAI have been acquired in 3D. In particular, the absorbers on the paper are reached by homogenous light fluence at almost the same depth ($\approx$ 15 *mm*). Although the light reaching the absorbers would be slightly attenuated, this remains a common factor in all the slices ofthe 3D sPAI. Thus, this enables to investigate the unmixing performance of the different unmixing algorithms without being hampered by the fluence variation along the depth.

3 Results

3.1 Blind unmixing sensitivity and specificity

The vessel-mimicking phantoms have been used to evaluate the unmixing performances of PCA, ICA, and NNMF, which have been applied to unmix the absorbers included within the phantoms. Overall, the analysis has been performed on the three phantoms, that have no background absorption, 0.05% v/v, and 0.1% v/v India Ink as background absorption. Thus, the phantoms without background absorption and medium/high background absorption result in sPAI with SNR values of 30dB, 15dB, and 8dB, respectively. The only hyperparameter of these BSS methods was the number of endmembers. This has been manually selected to 2 in the absence of background absorption and 3 in the other cases to unmix blue/green oil colors and India ink. Figure 3 presents the source spectra obtained as a result of the different BSS unmixing methods. The detection sensitivity of the BSS methods depends not only on the ability to unmix the molecular targets of interest from the absorbing background but is also hampered by the SNR, which indicates the quality of the images. Specifically, the presence of bulk absorption at different concentrations resembles possible real scenarios where it is more complex to reveal the absorber targets of interest. The unmixing results show that all three BSS methods managed to isolate the target components (Blue and Green Oil Colors) and the background (India Ink), when present. However, PCA and ICA algorithms exhibited unwanted negative values in the spectra, which are attributed to the non-constrained optimization process. Besides, the BSS methods show unique solutions only up to sign ambiguities. In particular, PCA and ICA are more prone to error when the sources of interest have low variance. Thus, often the iterative optimization procedure converges into inverted unmixed components as compared to the expected spectra.

On the other hand, the phantom studies showed that NNMF could detect the vessel-tree branches colored in green and blue with higher accuracy than PCA and ICA. High performance of the NNMF method was obtained even in the case where the background was highly absorbing (0.1% v/v India Ink) and the SNR value was almost three times lower (8 dB). The NNMF accurately unmixed the components and the detected spectra are very close to the expected spectra measured by the NIR spectrophotometer (see Figure 1). From the unmixing results, all the phantoms qualitatively demonstrate the superiority of the NNMF as a detection method in resolving the different absorbers from sPAI. Furthermore, the non-negativity constraint was found to maintain the most robust and accurate unmixing performance in all experiments.

Finally, the unmixed source components from sPAI, by applying the different BSS methods, have been compared using the correlation with the curves measured *via* NIRS. Table 2 reports the spectral correlation values obtained from the different phantoms. Although in some instances PCA and ICA show higher absolute correlation values than NNMF, often this results in negative correlation values.

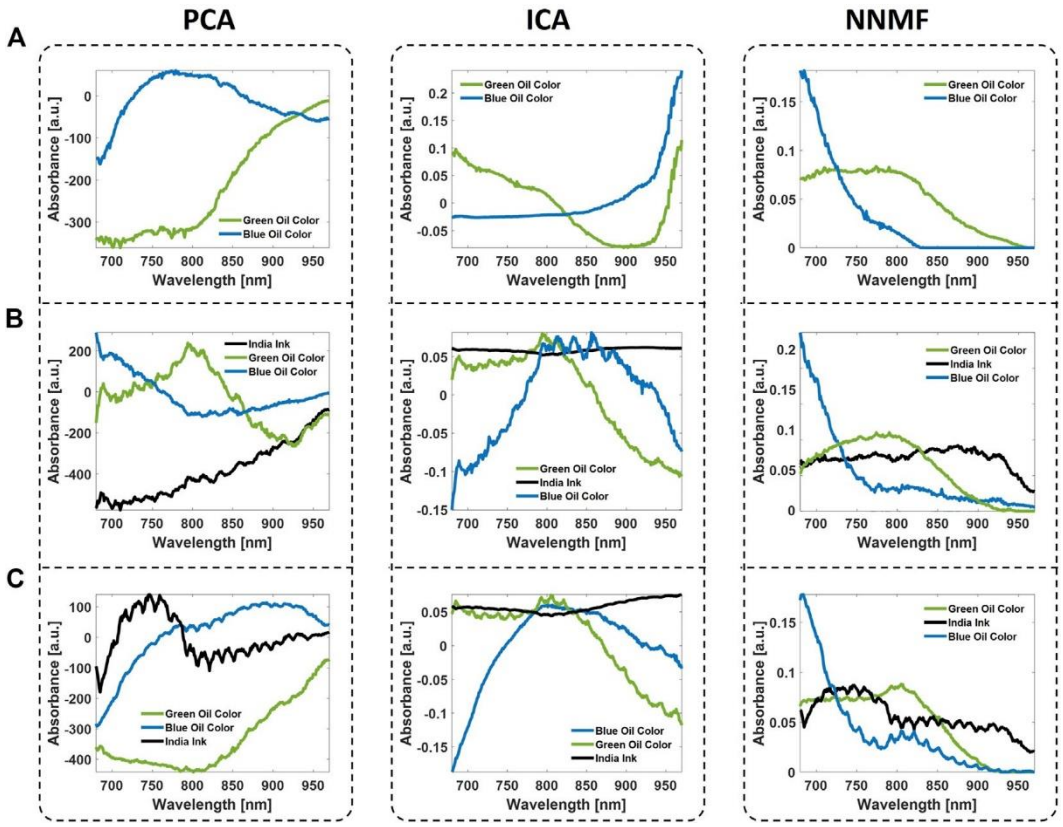

FIGURE 3
Unmixed spectra obtained from the vessel-mimicking phantoms with no background absorption (row (A)), medium background absorption (row (B)), and high background absorption (row (C)). The unmixing has been performed by means of the BSS algorithms PCA, ICA, and NNMF.

The latter leads to the identification of the components but with opposite signs. On the contrary, the NNMF performance is superior and more robust in all the vessel-mimicking phantoms conditions.

Besides, Table 3 reports the processing time of the BSS algorithms used in the experimental phantoms. Here we have performed the processing on a portable laptop with Intel(R) Core(TM) i7-9750H CPU 2.60GHz and 16.0 GB of RAM. Although the processing time depends on the dimensionality reduction chosen by the user (number of endmembers), PCA has shown the advantage of being faster than ICA when background absorption is present. On the other hand NNMF, despite the non-negativity constraint, seems computationally faster to implement and leads to converging to more interpretable data. Since the main focus of the experimental vessel-mimicking phantoms was to test the BSS unmixing algorithms' performance, especially their accuracy in detecting the spectral signatures of the components, in this study, the local fluence was assumed to be constant. This is a reasonable assumption for the design of the vessel- mimicking phantoms since the absorbers are all placed at the same distance from the excitation light source.

4 Discussion

Spectral photoacoustic imaging (sPAI) has shown high potential to determine detailed information on molecular tissue composition. Conventionally, linear unmixing (LU) and blind source separation (BSS) approaches are implemented to differentiate the tissue components from sPAI.

Although the linear spectral unmixing method (Erhayiem et al., 2011; Reber et al., 2018) is widely used, this has some drawbacks as it requires user interaction to provide the expected spectral signatures of the tissue components. Due to unpredictable spectral changes in disease conditions or in clinical scenarios, linear unmixing is challenging and can lead to suboptimal results.

Thus, unsupervised approaches that can automatically reveal any spectral change or fingerprints that might be related to pathological conditions are beneficial. Over the years, blind source separation (BSS) algorithms have shown promising automated unmixing performances in sPAI. Thus the BSS methods present a possible solution to this ill-posed unmixing problem and open up more photoacoustic applications both in preclinical and translational research.

Here, we evaluated the unmixing performance of various BSS algorithms to solve the sPAI unmixing problem in an unsupervised way. The performance of previously reported blind unmixing algorithms as principal component analysis (PCA), independent component analysis (ICA), and non-negative matrix factorization (NNMF) have been investigated in detail on experimental vessel-mimicking phantoms. Although these different methods are all part of the BSS category of algorithms, they implement different hypotheses, constraints, and optimization procedures, thus producing different results. Besides, near-infrared spectroscopy (NIRS) technology has been used as a reference to validate the unmixed spectra obtained by the different unmixing algorithms.

TABLE 2 Correlation values between reference spectra obtained *via* NIRS probe and the unmixed spectra *via* BSS algorithms for the vessel-mimicking phantoms with different background absorption.

Vessel-mimicking phantom	Components	PCA (%)	ICA (%)	NNMF (%)
No Background Absorption	Blue Oil Color	−49.7	−41.7	97.7
	Green Oil Color	−97.9	74.5	88.9
Medium Background Absorption	India Ink	−94.1	64.1	87.3
	Blue Oil Color	88.3	−72.5	97.6
	Green Oil Color	73.3	81.6	88.1
High Background Absorption	India Ink	37.8	−80.1	77.9
	Blue Oil Color	−97.5	−85.1	97.1
	Green Oil Color	−84.3	83.4	85.9

TABLE 3 Unmixing processing time of the BSS algorithms (PCA, ICA, and NNMF) to distinguish the source components from the vessel-mimicking phantoms with different background absorption.

Vessel-mimicking phantom	PCA (s)	ICA (s)	NNMF (s)
No Background Absorption	3.28	2.77	1.01
Medium Background Absorption	3.02	6.69	1.77
High Background Absorption	1.81	7.03	0.91

The phantom experiment has shown that all the studied BSS algorithms achieved the separation of the absorbers and PCA has shown the advantage of being faster than ICA when background absorption is present. On the other hand NNMF, despite the non-negativity constraint, computationally appears to be the fastest method to implement and converges to more interpretable data. Furthermore, the cross-correlation values measured between the reference NIR spectra and the unmixed spectra by the NNMF range between 77.9–97.7%. Thus, this has confirmed that the NNMF enabled more accurate unmixing performance for sPAI, as compared to PCA and ICA. Specifically, the NNMF has shown promising unmixing performance even in more complex scenarios, where the phantom has a highly absorbing background that confounds the included absorbers of interest and thus drastically reduces the quality/SNR of the sPAI. This confirms that the imposed positivity constraints are crucial to unmix tissue chromophores from sPAI. While NNMF has shown superior unmixing performance compared to the other BSS approaches, this is sensitive to uncertainties and misinterpretation, especially of less prominent chromophores at depth. In particular, NNMF assumes that the most prominent absorbers such as hemoglobin,are the sole tissue absorbers, not accounting for the presence of other absorbing molecules (e.g., extrinsic molecules, melanin, lipids, etc.) that are weaker absorbers. Therefore the less prominent absorbers are discarded within the NNMF unmixing, thus leading to incomplete tissue composition. Besides, the unmixing result is hampered by the choice of the hyperparameter and is jeopardized by the spectral coloring effect. Specifically, the excitation light fluence used in sPAI generally decreases with depth, and thus degrades the image uniformity, causing spatial fluence variations within the tissue. Therefore the NNMF could lead to significant errors in unmixing the tissue spectra, especially in deeper areas where spectral coloring is dominant.

References

Ahn, J. H., Oh, J. H. and Choi, S. (2007) 'Learning principal directions: Integrated-squared-error minimization', *Neurocomputing*, 70(7–9). doi: 10.1016/j.neucom.2006.06.004.

Ali, M., Magee, D. and Dasgupta, U. (2008) 'Signal processing overview of ultrasound systems for medical imaging', *SPRAB12, Texas …*, (November).

Allen, T. J. and Beard, P. C. (2016) 'High power visible light emitting diodes as pulsed excitation sources for biomedical photoacoustics', *Biomedical Optics Express*, 7(4). doi: 10.1364/boe.7.001260.

Allman, D., Reiter, A. and Bell, M. A. L. (2018) 'Photoacoustic Source Detection and Reflection Artifact Removal Enabled by Deep Learning', *IEEE Transactions on Medical Imaging*, 37(6). doi: 10.1109/TMI.2018.2829662.

Arabul, M. U. *et al.* (2019) 'Unmixing multi-spectral photoacoustic sources in human carotid plaques using non-negative independent component analysis', *Photoacoustics*. Elsevier, 15(June), p. 100140. doi: 10.1016/j.pacs.2019.100140.

Bayer, C. L. *et al.* (2017) 'Ultrasound-guided spectral photoacoustic imaging of hemoglobin oxygenation during development', *Biomedical Optics Express*, 8(2). doi: 10.1364/boe.8.000757.

Bell, A. J. and Sejnowski, T. J. (1995) 'An information-maximization approach to blind separation and blind deconvolution.', *Neural computation*, 7(6). doi: 10.1162/neco.1995.7.6.1129.

Benyamin, M. *et al.* (2020) 'Autoencoder based blind source separation for photoacoustic resolution enhancement', *Scientific Reports*, 10(1). doi: 10.1038/s41598-020-78310-5.

Berry, M. W. *et al.* (2007) 'Algorithms and applications for approximate nonnegative matrix factorization', *Computational Statistics and Data Analysis*, 52(1). doi: 10.1016/j.csda.2006.11.006.

Buehler, A. *et al.* (2010) 'Video rate optoacoustic tomography of mouse kidney perfusion', *Optics Letters*. doi: 10.1364/ol.35.002475.

Bulsink, R. *et al.* (2021) 'Oxygen saturation imaging using LED-based photoacoustic system', *Sensors (Switzerland)*, 21(1). doi: 10.3390/s21010283.

Cai, C. *et al.* (2018) 'End-to-end deep neural network for optical inversion in quantitative photoacoustic imaging', *Optics Letters*, 43(12). doi: 10.1364/ol.43.002752.

Cassidy, P. J. and Radda, G. K. (2005) 'Molecular imaging perspectives', *Journal of the Royal Society Interface*. doi: 10.1098/rsif.2005.0040.

Chowdhary, C. L. and Acharjya, D. P. (2020) 'Segmentation and Feature Extraction in Medical Imaging: A Systematic Review', in *Procedia Computer Science*. doi: 10.1016/j.procs.2020.03.179.

Comon, P. and Jutten, C. (2010) *Handbook of Blind Source Separation*, *Handbook of Blind Source Separation*. doi: 10.1016/C2009-0-19334-0.

Cox, B. T. *et al.* (2006) 'Two-dimensional quantitative photoacoustic image reconstruction of absorption distributions in scattering media by use of a simple iterative method', *Applied Optics*, 45(8). doi: 10.1364/AO.45.001866.

Cox, B. T., Arridge, S. R. and Beard, P. C. (2009) 'Estimating chromophore distributions from multiwavelength photoacoustic images', 26(2), pp. 443–455.

Das, D. *et al.* (2021) 'Another decade of photoacoustic imaging', *Physics in Medicine and Biology*. doi: 10.1088/1361-6560/abd669.

Deán-Ben, X. L. and Razansky, D. (2014) 'Adding fifth dimension to optoacoustic imaging: Volumetric time-resolved spectrally enriched tomography', *Light: Science and Applications*, 3. doi: 10.1038/lsa.2014.18.

Durairaj, D. A. *et al.* (2020) 'Unsupervised deep learning approach for photoacoustic spectral unmixing', in. doi: 10.1117/12.2546964.

Erhayiem, B. *et al.* (2011) 'Ratio of Visceral to Subcutaneous Fat Area Is a Biomarker of Complicated Crohn's Disease', *Clinical Gastroenterology and Hepatology*, 9(8). doi: 10.1016/j.cgh.2011.05.005.

Feng, S., Zeng, F.-A. and Chance, B. (1995) 'Photon migration in the presence of a single defect: a perturbation analysis', *Applied Optics*, 34(19). doi: 10.1364/ao.34.003826.

Glatz, J. *et al.* (2011) 'Blind source unmixing in multi-spectral optoacoustic tomography', *Optics Express*, 19(4), p. 3175. doi: 10.1364/oe.19.003175.

Grasso, V., Holthof, J. and Jose, J. (2020) 'An automatic unmixing approach to detect tissue chromophores from multispectral photoacoustic imaging', *Sensors (Switzerland)*. doi: 10.3390/s20113235.

Gröhl, J. *et al.* (2019) 'Estimation of blood oxygenation with learned spectral decoloring for quantitative photoacoustic imaging (LSD-qPAI)'. Available at: http://arxiv.org/abs/1902.05839.

Gröhl, J. *et al.* (2020) 'Deep learning for biomedical photoacoustic imaging: A review', *arXiv*. doi: 10.1016/j.pacs.2021.100241.

Hassan, H. W., Grasso, V., *et al.* (2021) 'An overview of assessment tools for determination of biological Magnesium implant degradation', *Medical Engineering and Physics*. doi: 10.1016/j.medengphy.2021.05.016.

Hassan, H. W., Mathew, A., *et al.* (2021) 'Feasibility Study of Multi-Wavelength Optical Probe to Analyze Magnesium Implant Degradation Effects', in *Proceedings of IEEE Sensors*. doi: 10.1109/SENSORS47087.2021.9639741.

Hervé, L. (2010) 'Nonnegative matrix factorization: a blind spectra separation method for <italic>in vivo</italic> fluorescent optical imaging', *Journal of Biomedical Optics*, 15(5), p. 056009. doi: 10.1117/1.3491796.

Hu, S. and Wang, L. V. (2010) 'Photoacoustic imaging and characterization of the microvasculature', *Journal of Biomedical Optics*, 15(1). doi: 10.1117/1.3281673.

Hyvärinen, A. (1999) 'Fast and robust fixed-point algorithms for independent component analysis', *IEEE Transactions on Neural Networks*, 10(3). doi: 10.1109/72.761722.

Hyvärinen, A. (2013) 'Independent component analysis : recent advances Subject Areas ':, *Phil. Trans. R. Soc. A*.

IEC (2015) 'IEC 80601-2-71 : 2015 Medical electrical equipment – Part 2-71: Particular requirements for the basic safety and essential performance of functional near-infrared spectroscopy (NIRS) equipment', *International Standard*, EN80601(Part 2-71).

Iskander-Rizk, S. *et al.* (2021) 'Micro Spectroscopic Photoacoustic (μsPA) imaging of advanced carotid atherosclerosis', *Photoacoustics*, 22. doi: 10.1016/j.pacs.2021.100261.

Jnawali, K. *et al.* (2019) 'Transfer learning for automatic cancer tissue detection using multispectral photoacoustic imaging', in. doi: 10.1117/12.2506950.

Jo, J. *et al.* (2017) 'A Functional Study of Human Inflammatory Arthritis Using Photoacoustic Imaging', *Scientific Reports*, 7(1). doi: 10.1038/s41598-017-15147-5.

Jo, J. *et al.* (2018) 'Photoacoustic tomography for human musculoskeletal imaging and inflammatory arthritis detection', *Photoacoustics*. doi: 10.1016/j.pacs.2018.07.004.

Jutten, C. and Karhunen, J. (2004) 'Advances in blind source separation (BSS) and independent component analysis (ICA) for nonlinear mixtures.', *International journal of neural systems*, 14(5). doi: 10.1142/S012906570400208X.

Keshava, N. (2003) 'A Survey of Spectral Unmixing Algorithms', *Lincoln Laboratory Journal*, 14(1).

Kim, J. *et al.* (2015) 'Photoacoustic imaging platforms for multimodal imaging', *Ultrasonography*, 34(2). doi: 10.14366/usg.14062.

Kuniyil Ajith Singh, M. *et al.* (2020) 'Clinical Translation of Photoacoustic Imaging—Opportunities and Challenges from an Industry Perspective', in. doi: 10.1007/978-981-15-3984-8_16.

Kwak, S. G. and Kim, J. H. (2017) 'Central limit theorem: The cornerstone of modern statistics', *Korean Journal of Anesthesiology*, 70(2). doi: 10.4097/kjae.2017.70.2.144.

Lavaud, J. *et al.* (2020) 'Noninvasive monitoring of liver metastasis development via combined multispectral photoacoustic imaging and fluorescence diffuse optical tomography', *International Journal of Biological Sciences*, 16(9). doi: 10.7150/ijbs.40896.

Lawrence, D. J. *et al.* (2019) 'Spectral photoacoustic imaging to estimate in vivo placental oxygenation during preeclampsia', *Scientific Reports*, 9(1). doi: 10.1038/s41598-018-37310-2.

Le, Q. V. *et al.* (2011) 'ICA with reconstruction cost for efficient overcomplete feature learning', *Advances in Neural Information Processing Systems 24: 25th Annual Conference on Neural Information Processing Systems 2011, NIPS 2011*, pp. 1–9.

Lee, D. D. and Seung, H. S. (2001) 'Algorithms for non-negative matrix factorization', in *Advances in Neural Information Processing Systems*.

Lee, J. G. *et al.* (2017) 'Deep learning in medical imaging: General overview', *Korean Journal of Radiology*. doi: 10.3348/kjr.2017.18.4.570.

Li, M. L. *et al.* (2008) 'Simultaneous molecular and hypoxia imaging of brain tumors in vivo using spectroscopic photoacoustic tomography', *Proceedings of the IEEE*, 96(3). doi: 10.1109/JPROC.2007.913515.

Li, M., Tang, Y. and Yao, J. (2018) 'Photoacoustic tomography of blood oxygenation: A mini review', *Photoacoustics*. doi: 10.1016/j.pacs.2018.05.001.

Lipovetsky, S. (2009) 'PCA and SVD with nonnegative loadings', *Pattern Recognition*, 42(1), pp. 68–76. doi: 10.1016/j.patcog.2008.06.025.

Liu, Y. *et al.* (2020) 'Low-toxicity FePt nanoparticles for the targeted and enhanced diagnosis of breast tumors using few centimeters deep whole-body photoacoustic imaging', *Photoacoustics*, 19. doi: 10.1016/j.pacs.2020.100179.

Manwar, R., Zafar, M. and Xu, Q. (2020) 'Signal and Image Processing in Biomedical Photoacoustic Imaging: A Review', *Optics*, 2(1). doi: 10.3390/opt2010001.

Oblefias, W. R., Soriano, M. N. and Saloma, C. A. (2004) 'SVD vs PCA : Comparison of Performance in an Imaging Spectrometer', *Science*, (December).

Papazoglou, E. S. *et al.* (2006) 'Optical properties of wounds: Diabetic versus healthy tissue', *IEEE Transactions on Biomedical Engineering*, 53(6). doi: 10.1109/TBME.2006.873541.

Park, E. Y. *et al.* (2022) 'Photoacoustic imaging systems based on clinical ultrasound platform', *Experimental Biology and Medicine*. doi: 10.1177/15353702211073684.

Rodrigues, J. *et al.* (2021) 'Exploring photoacoustic spectroscopy-based machine learning together with metabolomics to assess breast tumor progression in a xenograft model ex vivo', *Laboratory Investigation*, 101(7). doi: 10.1038/s41374-021-00597-3.

Roweis, S. (1998) 'EM algorithms for PCA and SPCA', in *Advances in Neural Information Processing Systems*.

Rutledge, D. N. and Jouan-Rimbaud Bouveresse, D. (2013) 'Independent Components Analysis with the JADE algorithm', *TrAC - Trends in Analytical Chemistry*. doi: 10.1016/j.trac.2013.03.013.

Sangha, G. S. and Goergen, C. J. (2020) 'Label-free photoacoustic and ultrasound imaging for murine atherosclerosis characterization', *APL Bioengineering*, 4(2). doi: 10.1063/1.5142728.

Santosh Kumar, S., Bharathi, S. H. and Archana, M. (2016) 'Non-negative matrix based optimization scheme for blind source separation in automatic speech recognition system', in *Proceedings of the International Conference on Communication and Electronics Systems, ICCES 2016*. doi: 10.1109/CESYS.2016.7889860.

Smita, S., Biswas, S. and Solanki, S. S. (2014) 'Audio Signal Separation and Classification: A Review Paper', *International Journal of Innovative Research in Computer and Communication Engineering ({IJIRCCE})*, 2(11).

Sotiras, A., Resnick, S. M. and Davatzikos, C. (2015) 'Finding imaging patterns of structural covariance via Non-Negative Matrix Factorization', *NeuroImage*. Elsevier Inc., 108, pp. 1–16. doi: 10.1016/j.neuroimage.2014.11.045.

Stoffels, I. *et al.* (2015) 'Metastatic status of sentinel lymph nodes in melanoma determined noninvasively with multispectral optoacoustic imaging', *Science translational medicine*, 7(317). doi: 10.1126/scitranslmed.aad1278.

Tipping, M. E. and Bishop, C. M. (1999) 'Probabilistic principal component analysis', *Journal of the Royal Statistical Society. Series B: Statistical Methodology*, 61(3). doi: 10.1111/1467-9868.00196.

Tzoumas, S. *et al.* (2016) 'Eigenspectra optoacoustic tomography achieves quantitative blood oxygenation imaging deep in tissues', *Nature Communications*. doi: 10.1038/ncomms12121.

Wang, L. V. (2017) *Photoacoustic imaging and spectroscopy*, *Photoacoustic Imaging and Spectroscopy*. doi: 10.1201/9781420059922.

Weiss, G. H., Nossal, R. and Bonner, R. F. (1989) 'Statistics of penetration depth of photons re-emitted from irradiated tissue', *Journal of Modern Optics*, 36(3). doi: 10.1080/09500348914550381.

Xie, Z. *et al.* (2020) 'In vivo assessment of inflammation in carotid atherosclerosis by noninvasive photoacoustic imaging', *Theranostics*, 10(10). doi: 10.7150/thno.41211.

Yang, C. *et al.* (2021) 'Review of deep learning for photoacoustic imaging', *Photoacoustics*. doi: 10.1016/j.pacs.2020.100215.

Yang, Q. *et al.* (2019) 'Photostable Iridium(III)-Cyanine Complex Nanoparticles for Photoacoustic Imaging Guided Near-Infrared Photodynamic Therapy in Vivo', *ACS Applied Materials and Interfaces*, 11(17). doi: 10.1021/acsami.9b04098.

Yuan, Z., Wang, Q. and Jiang, H. (2007) 'Reconstruction of optical absorption coefficient maps of heterogeneous media by photoacoustic tomography coupled with diffusion equation based regularized Newton method', *Optics Express*, 15(26). doi: 10.1364/oe.15.018076.

Zhang, M., Zhu, M. and Ma, W. (2012) 'Implementation of FastICA on DSP for blind source separation', in *Procedia Engineering*. doi: 10.1016/j.proeng.2012.01.648.

Chapter 3

An automatic unmixing approach to detect tissue chromophores from multispectral photoacoustic imaging*

Abstract:

In this chapter, we have investigated the feasibility of an unsupervised spectral unmixing algorithm to detect and extract the tissue chromophores without any *a-priori* knowledge and user interaction from spectral photoacoustic imaging. Specifically, the non-negative matrix factorization (NNMF) approach has been optimized for multispectral photoacoustic imaging in the spectral range of 680–900 nm. The performance of the algorithm has been tested on simulated data, tissue-mimicking phantom, and also on the detection of exogenous contrast agents after the intravenous injection in mice.

*This chapter has been published as: **Grasso, V.**, Holthof, J., & Jose, J. (2020). *"An automatic unmixing approach to detect tissue chromophores from multispectral photoacoustic imaging."* Sensors, 20(11), 3235.

sensors

MDPI

Letter

An Automatic Unmixing Approach to Detect Tissue Chromophores from Multispectral Photoacoustic Imaging

Valeria Grasso [1,2], Joost Holthof [1] and Jithin Jose [1,*]

[1] FUJIFILM VisualSonics, 1114 AB Amsterdam, The Netherlands; valeria.grasso@fujifilm.com (V.G.); joost.holthof@fujifilm.com (J.H.)

[2] Institute for Animal Science, Hannover Medical School, 30625 Hannover, Germany

* Correspondence: jithin.jose@fujifilm.com

Received: 29 April 2020; Accepted: 4 June 2020; Published: 6 June 2020

Abstract: Multispectral photoacoustic imaging has been widely explored as an emerging tool to visualize and quantify tissue chromophores noninvasively. This modality can capture the spectral absorption signature of prominent tissue chromophores, such as oxygenated, deoxygenated hemoglobin, and other biomarkers in the tissue by using spectral unmixing methods. Currently, most of the reported image processing algorithms use standard unmixing procedures, which include user interaction in the form of providing the expected spectral signatures. For translational research with patients, these types of supervised spectral unmixing can be challenging, as the spectral signature of the tissues can differ with respect to the disease condition. Imaging exogenous contrast agents and accessing their biodistribution can also be problematic, as some of the contrast agents are susceptible to change in spectral properties after the tissue interaction. In this work, we investigated the feasibility of an unsupervised spectral unmixing algorithm to detect and extract the tissue chromophores without any a-priori knowledge and user interaction. The algorithm has been optimized for multispectral photoacoustic imaging in the spectral range of 680–900 nm. The performance of the algorithm has been tested on simulated data, tissue-mimicking phantom, and also on the detection of exogenous contrast agents after the intravenous injection in mice. Our finding shows that the proposed automatic, unsupervised spectral unmixing method has great potential to extract and quantify the tissue chromophores, and this can be used in any wavelength range of the multispectral photoacoustic images.

Keywords: photoacoustic; optoacoustic; spectral imaging; blind source separation; unsupervised unmixing

1. Introduction

The accurate detection and quantification of tissue chromophores is vital in molecular imaging, as it can facilitate the early detection, prediction, and monitor the disease conditions. In recent years, multispectral photoacoustic imaging has emerged as a noninvasive tool to visualize the tissue chromophores [1–4]. The underlying principle of photoacoustic (PA) imaging is based on the conversion of absorbed nanosecond laser pulses into acoustic waves that can be detected just as conventional ultrasound [5,6]. Based on this approach, PA images combine the peculiar optical absorption contrast of the tissue chromophores and the spatial resolution of ultrasound imaging (US). Being a hybrid imaging modality of ultrasound and optical, this multimodal imaging technology can provide anatomical, functional, and molecular information several centimeters deep in the tissues with a resolution up to tens of micrometers. The potential of PA imaging has been demonstrated in various preclinical applications, such as tumor progression and the prediction of tumor recurrence, therapy monitoring, imaging of vasculature, and the biodistribution of the contrast agents [7–13].

Apart from the preclinical applications, PA imaging is also used in clinical research. In addition to breast cancer monitoring [14,15] and sentinel lymph node imaging [16,17], the PA approach is also used to examine inflammatory bowel disease (IBD) [18] and the temporal arteries in patients with suspected giant cell arteritis (GCA) [19]. To expedite the clinical applications of PA imaging, recently, there has been a lot of focus on developing affordable light sources and the use of this technology in low-resource settings. Xia et al. demonstrated the feasibility of a Light-Emitting Diode (LED) based PA imaging system for the visualization of superficial vasculatures and needle guidance for minimally invasive procedures [20]. Zhu et al. used the LED-based approach to explore more clinical applications, such as diagnosing inflammatory arthritis and assessing peripheral microvascular function in patients [21–23].

Although there has been a lot of emphasis on PA hardware development, in the field of affordable settings, data analysis and reconstruction algorithms also play a crucial role in increasing the utility of the technology. Multiwavelength acquisition and spectral image processing is one of the commonly used techniques in PA. Since the optical absorption coefficient of the tissue chromophores varies over the spectrum, multispectral image processing approach can be applied to distinguish and characterize the molecules present in the tissues [24].

In general, the pixel intensity of the multispectral photoacoustic image is proportional to the absorption value of the respective tissue at a specific wavelength. In reality, due to the finite dimension of the pixel (partial volume effect) and the presence of instrumental noise, each spectrum can be a combination of different tissue chromophores. Therefore, it is a challenging task to unmix these signals spectrally and estimate their concentrations. The most common solution to detect the tissue chromophores from multispectral PA imaging is the supervised unmixing [25]. Although this technique yields acceptable results, it requires user interaction to provide the expected source spectral curves as an input to unmix the signals. For translational research with patients, these types of supervised spectral unmixing can be challenging, as the spectral signature of the tissues differs with respect to the disease condition. Imaging exogenous contrast agents and accessing their biodistribution can also be problematic, as some of the contrast agents are susceptible to change in spectral properties after the tissue interaction; thus, the algorithm can forfeit the sensitivity and specificity of imaging.

Hence, an unsupervised unmixing algorithm that can automatically detect the tissue chromophores, without any a-priori knowledge and user interaction, will be optimal, as this can facilitate and improve sensitivity and specificity. Generally, this class of algorithms is referred to as blind source separation (BSS) algorithms, as no a-priori information is required. The study reported by Glatz et al. [26] demonstrated the potential of these approaches to "blindly" extract the oxygenated and deoxygenated hemoglobin absorption spectra from the multispectral photoacoustic images. In the study, they evaluated different unsupervised algorithms, such as multivariate curve resolution analysis (MCR), principal component analysis (PCA), and independent component analysis (ICA) [27–31]. PCA yields an orthogonal transformation that decorrelates the variables. This approach relies upon the hypothesis that the source components are uncorrelated. On the other hand, ICA is based on a different assumption that the source components are maximally independent and non-Gaussian. Recently, Arabul et al. [32] used a similar approach to explore human carotid plaques, in which the ICA blind unmixing approach was constrained non-negatively. Although these approaches demonstrated the potential to detect the tissue chromophores, they suffer from limitations related to the interpretability of the mixed-sign values of their outcomes. Indeed, these aim to fit the training data well but often do not generalize the real and positive data sets.

In this paper, we investigated the possibility of using another blind source separation approach, which is based on non-negative matrix factorization (NNMF) [33]. The concept of NNMF has been widely used in a variety of applications, such as image recognition [34], text classification [35,36], and recommender systems [37]. This approach uses only the non-negative matrices to estimate the prominent components and their spatial distribution, from a linear mixture model. Montcuquet et al. [38] used this approach for in-vivo fluorescent imaging and demonstrated that the positivity condition enhances the convergence and, thus, improves the sensitivity of spectral unmixing [39].

Here, we examine the performance of non-negative matrix factorization (NNMF) to unmix tissue chromophores from multispectral PA images. The algorithm has been optimized to extract the tissue chromophores in the wavelength range of 680–900 nm. We tested the NNMF on synthetic data and on experimental data that mimic the blood vessels. Further, we validated the potential of the approach on an in-vivo study to detect and quantify the endogenous absorbers and exogenous contrast agent accumulation. To our knowledge, this is the first time the NNMF algorithm has been used for PA imaging.

2. Non-Negative Matrix Factorization (NNMF)

NNMF is a data decomposition approach, and it is based on the linear mixing model [40]. In this algorithm, the acquired mixed pixel spectra are differentiated into a collection of constituent spectra (called endmembers) and a set of fractional abundance maps. The endmembers represent the pure molecule absorption spectra present in the imaged sample, and these are extracted from the mixed pixel spectra. The maps of abundance at each pixel represent the percentage of each endmember present in that pixel.

Since the acquired spectral images are known, and the rest has to be estimated, the mixed data (multispectral PA images) can be arranged as a matrix $\boldsymbol{X} \in \mathbb{R}^{\boldsymbol{n}\times\boldsymbol{m}}$, where $\boldsymbol{n}$ represents the number of observations (pixels), and $\boldsymbol{m}$ corresponds to the number of variables per object (different wavelengths). In particular, the unmixing problem can be formulated as a matrix factorization:

$$X \approx WS \tag{1}$$

where X represents the mixed multispectral PA images, W the abundance maps, and S the source spectra. The dimensions of the matrices W and S are $\boldsymbol{n}\times\boldsymbol{k}$ and $\boldsymbol{k}\times\boldsymbol{m}$, respectively, where $\boldsymbol{k}$ is the hyperparameter which represents the number of prominent components.

The NNMF constrained cost function of the optimization problem can be formulated as follows:

$$[W, S] = \min_{W,S} \frac{1}{2} \parallel X - WS \parallel_F^2 \tag{2}$$

$$W_{ij} \geq 0, \quad S_{ij} \geq 0 \tag{3}$$

where, in Equation (2), the defined cost function considers a Frobenius distance between the acquisition X and the model WS [33]. W and S are iteratively obtained until both matrices satisfy Equation (1), where the distance defined in the cost function (2) is constrained non-negatively (3). The NNMF learns a parts-based representation of the data, and the whole image is formed as a combination of additive components. The non-negativity constraint is computationally expensive to implement but it can lead to more interpretable data.

To solve the iterative optimization, the multiplicative update rules [41] can be used, and the steps can be defined as:

$$S\,(p+1) = S(p) \otimes \frac{\left(W^T \cdot X\right)}{\left(W^T W \cdot S\right)} \tag{4}$$

$$W(p+1) = W(p) \otimes \frac{\left(X \cdot S^T\right)}{\left(W \cdot S \cdot S^T\right)} \tag{5}$$

where $\boldsymbol{p}$ is the iteration step, and the operations of $\otimes$ and division in (4) and (5) are considered element by element. Each component is estimated only up to a multiplying scale factor. Hence, the factorization problem does not have a unique solution, where WS is a lower-rank approximation of X.

3. Experimental Methods

3.1. Simulated Multispectral PA Images

To evaluate the performance of the NNMF algorithm, simulation studies were performed by using a synthetic data set. The synthetic data set contains implemented photoacoustic spectral images within the wavelength range of 680–900 nm, with a step size of 5 nm. Each image at the respective wavelength contains 400 × 600 pixels. From the photoacoustic signal generation, it is evident that the PA signal is not only proportional to the absorption coefficient but also depends on the local fluence. The light fluence generally decreases with depth, and thus degrades the image uniformity, causing spatial fluence variations within the tissue. Consequently, the fluence compensation is significant for quantitative spectral imaging. Since the main focus of the simulation was to test the unmixing algorithm and its accuracy to detect the spectral signature of the prominent components, in this study, the local fluence was assumed to be constant.

Figure 1a depicts the schematic of the 2-dimensional (2-D) data set with six homogeneous inclusions. The inclusions mimic the cross section of blood vessels with different concentrations of oxyhemoglobin and deoxyhemoglobin. The inclusions 1, 2, and 3 contain oxyhemoglobin at 100%, 70%, and 30% of the intensity, respectively. Conversely, the inclusions 4, 5, and 6 include deoxyhemoglobin at 30%, 70%, and 100% of the intensity. Figure 1b shows the theoretical absorption spectra [42] expected from these inclusions, in addition to the background tissue absorption. To mimic the experimental conditions, a positive Gaussian distribution of noise ($mean = 0.04$; $std = 0.1\%$; $SNR = 30$ dB) was also added to the respective data set.

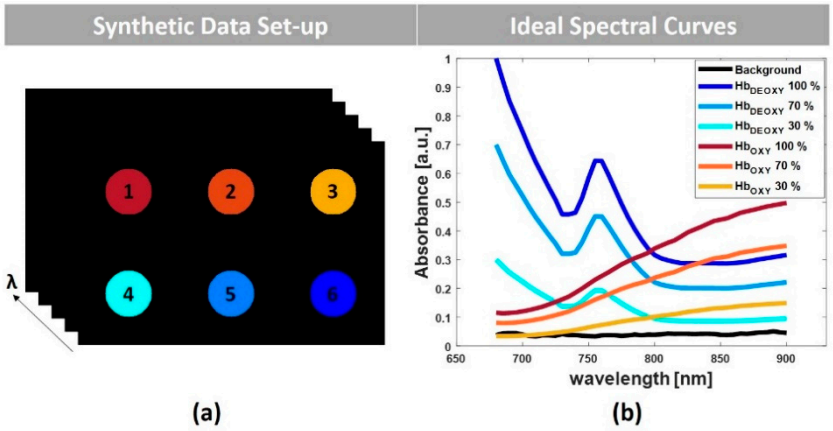

Figure 1. (**a**) Schematic representation of the simulated multispectral photoacoustic (PA) images with six inclusions, (**b**) ideal spectral curves of the inclusions.

3.2. Experimental Set-Up and Tissue-Mimicking Vessel Phantom

In addition to the simulation studies, experiments were performed by using Vevo LAZR-X photoacoustic image technology (FUJIFILM VisualSonics, Inc., Toronto, ON, Canada), as described elsewhere [43]. Vevo Phantom (FUJIFILM VisualSonics, Inc., Toronto, ON, Canada) containing two capillary tubes filled with Indocyanine Green (ICG, PULSION Verwaltungs, GmbH) and Methylene Blue (MB, Sigma-Aldrich), was used to mimic the blood vessels in the tissue. Transparent polyethylene (PE) tubes (SAI Infusion Technologies, Lake Villa, IL, USA), with an inner diameter of 15 µm and an outer diameter of 33 µm, were used. The tubes were positioned at a reciprocal distance of 6 mm and fixed at the same depth of 14 mm from the surface of the transducer. Demineralized water was used as a coupling medium, and the multispectral PA images were obtained in the wavelength range of 680–900 nm, with a step size of 5 nm. Figure 2a shows the schematic of the phantom and the experimental set-up. A 256-element linear array transducer with a central frequency of 21 MHz (MX250), including the integrated light delivery fibers from the sides of the transducer, was used

to acquire the PA images. The transducer was aligned perpendicular to the capillary tubes, and the cross-sectional image of the tubes was acquired throughout the wavelength range. 3-Dimensional (3-D) data sets were also collected by linearly translating the transducer with a stepper motor over the capillary tubes while capturing cross-sectional 2-D slices. Figure 2b shows the photoacoustic spectra measured from the capillary tubes by using the Spectro-Mode in the VevoLab software (FUJIFILM VisualSonics, Inc., Toronto, ON, Canada). In the measurement tool, the system allows the user to select the region of interest (ROI) and calculate the average intensity of the photoacoustic signal at different wavelengths. Although this is not quantitative and the values are in arbitrary units, it can provide the spectral absorption trend of the agents in the respective wavelength range.

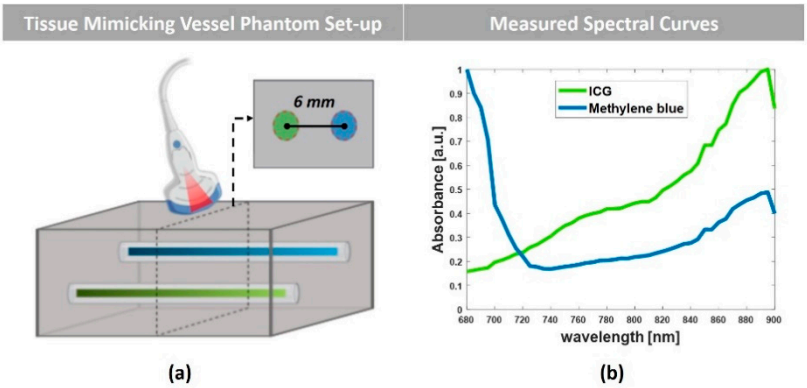

Figure 2. (**a**) Schematic of the tissue-mimicking vessel phantom. (**b**) The PA absorbance spectral graph of the agents measured by using VevoLab.

3.3. In-Vivo Study

Further, in-vivo animal experiments were performed to evaluate the feasibility of the NNMF data analysis on multispectral PA Imaging. The animal experiments were performed at the FUJIFILM Sonosite/VisualSonics facility in Amsterdam. The animal protocols used in this work were evaluated and approved by the Animal Use and Ethics Committee (CEUA) of The Netherlands (Protocol AVD2450020173644). They are in accordance with FELASA guidelines and the National Law for Laboratory Animal Experimentation (Law No. 18.611). The experiments were performed by using the same apparatus (Vevo LAZR-X) used for the phantom studies. A CD-1 female mouse model (Envigo, Horst, the Netherlands) was used for the experiments. The animal was anesthetized with isoflurane and placed on the animal imaging platform of the Vevo LAZR-X system, where temperature, heart rate, and respiration rate were monitored in real time. During the experiments, anesthesia was maintained using a vaporized isoflurane (1 L/min of oxygen and 0.75% isoflurane) gas system. The animal was positioned in right lateral recumbency, and the transducer was aligned perpendicularly. The kidney–spleen area of the animal was imaged before and after the intravenous injection of ICG. To obtain a concentration of 800 µM, 25-mg vial of ICG (PULSION Verwaltungs, GmbH) was resuspended in sterile water. With the help of an infusion pump (flowrate of 15 µL/sec), 80 µL of ICG was injected into the tail vein, and multispectral PA images were acquired in the wavelength range of 680–900 nm.

4. Results and Discussion

4.1. Simulated Multispectral PA Images

Figure 3 shows the main component spectra (a) and the respective abundance maps (b, c, and d) extracted from the synthetic PA data set by using the NNMF algorithm. The obtained spectral graphs (Figure 3a) show that the prominent absorbers present within the inclusions consist of two different endmembers: oxyhemoglobin and deoxyhemoglobin. As expected from the synthetic data,

the oxyhemoglobin is mainly distributed on the first row of inclusions, with decreasing intensity from left to right (Figure 3c). The deoxyhemoglobin is present in the second row of inclusions, with increasing intensity from left to right (Figure 3b). Figure 3d displays the spatial distribution of the detected third component (named as background in Figure 3a), which is principally present in the region around the inclusions.

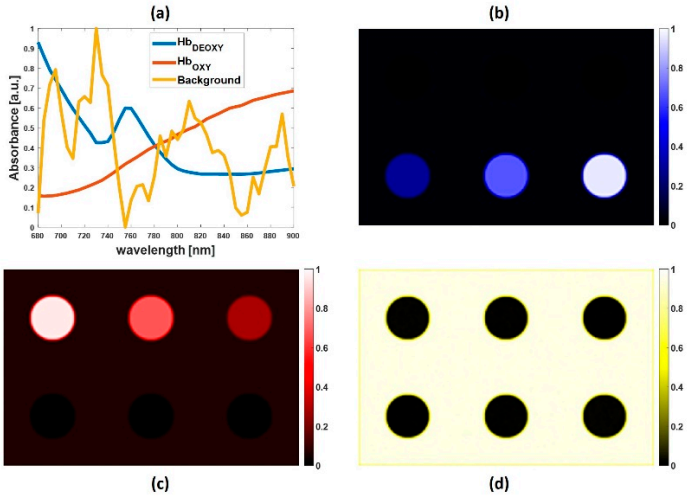

Figure 3. (**a**) Source spectra of oxyhemoglobin, deoxyhemoglobin, and background extracted by the non-negative matrix factorization (NNMF) algorithm. Abundance maps of (**b**) deoxyhemoglobin, (**c**) oxyhemoglobin, and (**d**) background.

NNMF appears to be an accurate method, yielding an explicit unmixing of specific tissue biomarkers, such as oxyhemoglobin and deoxyhemoglobin, and extracting the respective spectral signatures. The calculated Pearson correlation coefficient between the ideal spectra of the oxy and deoxyhemoglobin, and the extracted spectra was equal to 1 (Table 1). This confirms that NNMF can provide encouraging results on extracting tissue chromophores from multispectral PA images.

Table 1. Correlation values between the extracted source components by using the NNMF unmixing approach, and the respective absorption spectral curves used as a reference.

Data Set-Up	Chromophores	Correlation Value
Synthetic data	Oxyhemoglobin	1
	Deoxyhemoglobin	1
Vessel mimicking phantom	ICG	0.9943
	Methylene Blue	0.8344

Further, we investigated the performance of the NNMF approach to quantify the extracted prominent components. Figure 4a shows a graph with the quantitation of the source components (oxyhemoglobin, deoxyhemoglobin) per each circular inclusion of the synthetic data. Considering the synthetic data: inclusions 1, 2, and 3 present approximatively a decreasing content of oxyhemoglobin, and the regions 4, 5, and 6 present an increasing content of deoxyhemoglobin. In the graph, the variations are in the range of zero to one, and it is evident that these normalized intensities are matching the expected proportion of the components. Figure 4b shows the overlapped abundance maps of oxyhemoglobin and deoxyhemoglobin, and it also confirms the expected distribution of the prominent components.

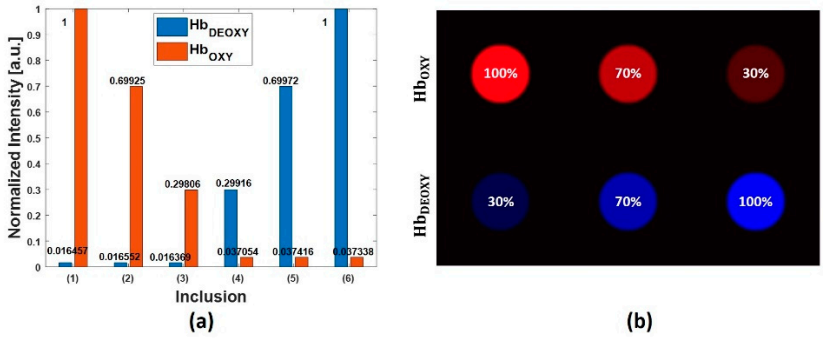

Figure 4. (**a**) Quantitative evaluation of the prominent source components (oxyhemoglobin and deoxyhemoglobin), per each circular region of the synthetic phantom. (**b**) Overlapped abundance maps of oxyhemoglobin and deoxyhemoglobin.

4.2. Tissue-Mimicking Vessel Phantom

Figure 5 shows the prominent spectral curves (a) and the abundance maps of the dyes in the capillary tubes, obtained by using the NNMF algorithm. The abundance maps overlapped in Figure 5b correspond to the 2-D spatial distribution of the contrast agents (ICG in green and MB in blue). Figure 5c shows the unmixing of the capillary tubes in 3-D, where the total imaged range was 6.5 mm with a step size of 200 µm. The Pearson correlation coefficient was evaluated between the extracted spectral curves, by using the NNMF, and the spectra measured by using the Spectro-Mode in the VevoLab.

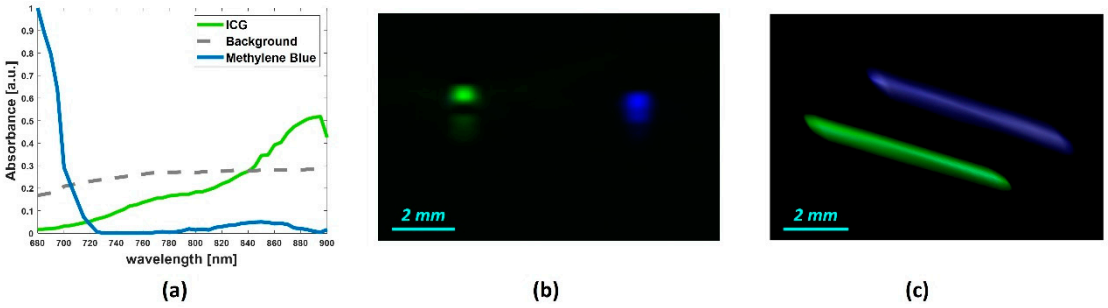

Figure 5. (**a**) Spectral absorption curves of the detected source components by NNMF, from 2-D spectral PA images of the tissue-mimicking vessel phantom. The overlapped abundance 2-D maps (**b**) and 3-D maps (**c**) of the detected source components: ICG and MB.

Table 1 reports the correlation coefficients measured for the ICG and methylene blue. The correlation value obtained for the methylene blue was 0.8344, and it was comparatively lower to the value obtained for the ICG, which was 0.9943. This could be due to the experimental conditions, as the tubes are located adjacently, into the phantom chamber. Hence, due to the short distance, the ICG that has an absorption peak at around 880 nm could influence the absorption spectrum of the MB. The graph reported in Figure 2b supports this assumption, as the MB spectrum shows an additional peak at around 880 nm. This may entail that measured spectral curves in Figure 2b are not the pure agent spectra. On the other hand, the spectra extracted by using NNMF are in accordance with the expected spectral signatures, and it shows promising unmixing performance.

4.3. In-Vivo Study

Figure 6a shows a high-resolution ultrasound (US) image of the kidney–spleen region and (b) is the PA image obtained at 880 nm. Figure 6c shows the oxygen saturation (SO_2) map, obtained before the contrast agent injection. To obtain the oxygen saturation map, we have followed the algorithm reported by Needles et al. [5], where the pixel values of the image are in the range of 0% (lower oxygenation) to 100% (higher oxygenation).

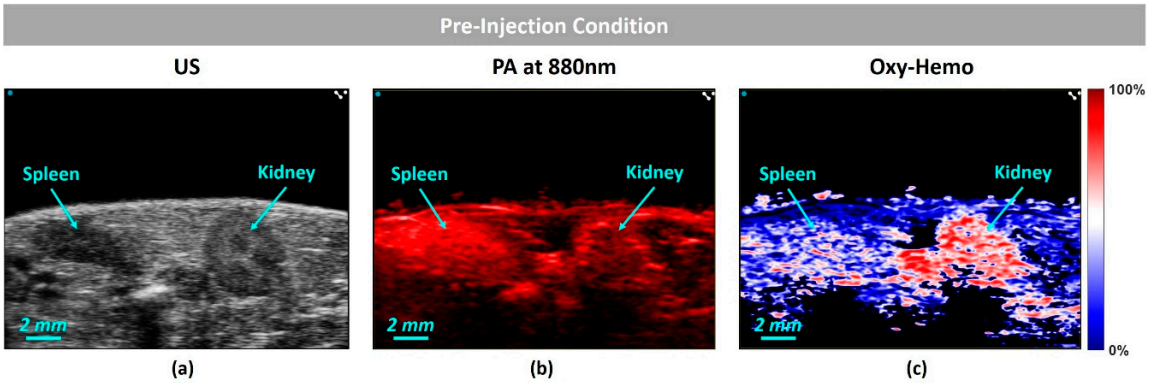

Figure 6. Pre-injection conditions: (**a**) ultrasound (US) image of the kidney–spleen view; respectively (**b**) photoacoustic (PA) image obtained at 880nm, and (**c**) SO_2 map.

Figure 7 shows the post-ICG injection condition. Figure 7a displays the source absorption spectra extracted by the NNMF approach. As expected, in the post-injection condition, the NNMF extracted the typical absorption spectral curve of the ICG, in addition to the endogenous chromophores such as oxy and deoxyhemoglobin spectra. The extracted spectrum of the ICG appears slightly different than the vessel mimicking phantom. Although the peak absorption was at 880 nm, the ICG spectrum at the lower wavelengths was altered. This could be due to the ICG interaction with other chromophores within the tissues. Figure 7 also shows the abundance maps of deoxyhemoglobin (b), oxyhemoglobin (c), and ICG (d). In the ICG map, it is evident that the dye is mostly accumulated in the spleen region. This is in accordance with the biodistribution of the ICG, as the kinetic of the kidney is much faster than the spleen [44].

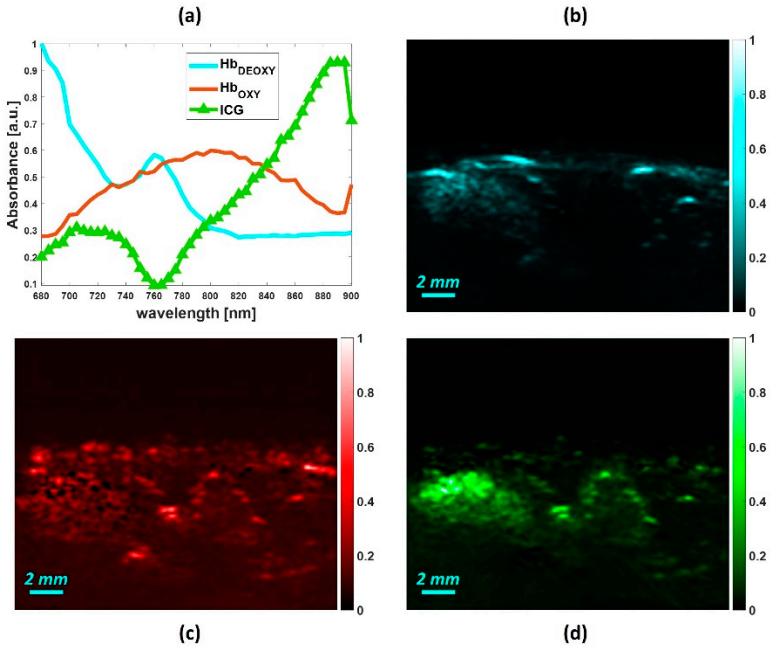

Figure 7. Post-injection conditions: (**a**) spectral signature of the endmembers obtained by using NNMF and abundance distribution maps of (**b**) deoxyhemoglobin, (**c**) oxyhemoglobin, and (**d**) ICG.

5. Conclusions

In summary, we investigated the spectral decomposition of various tissue biomarkers from multispectral PA images. In particular, we have explored the performance of an unsupervised spectral unmixing algorithm, NNMF, in the wavelength range of 680–900 nm. Considering the evidence

obtained from the initial results, the NNMF can extract both endogenous and exogenous agents from the multispectral PA data. The unmixing results obtained from the simulation studies performed on synthetic data revealed a high correlation with the expected spectra, and also yielded the quantification of the chromophores. The experiment performed on the tissue-mimicking phantom also supported the results obtained on the synthetic data. Indeed, the NNMF showed promising unmixing performance, allowing the accurate detection of ICG and MB, by eliminating the spectral influence of the other dyes. The in-vivo experiments in the animal model showed the detection of a contrast agent signature, accounting for the spectral variations that may ensue due to tissue–dye interactions. The NNMF can also provide the maps of abundance distribution of contrast agents in different anatomical targets, facilitating in-vivo biodistribution and kinetics studies. Since the algorithm facilitates the automatic unmixing of the tissue chromophores, without any a-priori knowledge about the source components and user interactions, it is easy to adapt, and promising for data-driven studies in multispectral photoacoustic imaging.

In the current algorithm, we have used the time gain compensation (TGC) approach to overcome the PA signal attenuation through depth. Although the approach is not quantitative, it gives improved results. Recent studies demonstrate that taking into account the fluence variance [45,46] can overcome the quantification limits of photoacoustic imaging. Therefore, in future studies, we will investigate the corruption effects of the fluence variation, the finite size, and band-limited frequency response of the detectors, to consider the respective changes on the absorption spectra. Besides, we will expand the current wavelength range of 680–900 nm to the far infrared (FIR), as this may entail the detection of less prominent tissue chromophores, such as melanin, lipids, and collagens.

In conclusion, to the best of our knowledge, this would be the first time that NNMF was used for unmixing multispectral PA imaging. The obtained results confirmed that the NNMF algorithm automatically and accurately detects the component spectra. This proves that the imposed positivity constraints, to the source spectra and abundance distribution maps, are appropriate requirements to unmix tissue chromophores from multispectral PA images.

Author Contributions: Conceptualization, V.G. and J.J.; Methodology, V.G., J.H. and J.J.; Software, V.G.; Validation, V.G. and J.J.; Investigation, J.J.; Resources, J.J.; Data curation, V.G., J.H. and J.J.; Writing—original draft preparation, V.G.; Writing—review and editing, V.G. and J.J.; Visualization, V.G. and J.J.; Supervision, J.J.; Project administration, J.J.; Funding acquisition, J.J. All authors have read and agreed to the published version of the manuscript.

Acknowledgments: This publication is part of a project that has received funding from the European Union's Horizon 2020 research and innovation program under the Marie Skłodowska-Curie grant, agreement No 811226.

Conflicts of Interest: The authors declare no conflict of interest.

References

1. Cox, B.; Laufer, J.G.; Arridge, S.R.; Beard, P.C. Quantitative spectroscopic photoacoustic imaging: A review. *J. Biomed. Opt.* **2012**, *17*, 061202. [CrossRef] [PubMed]
2. Razansky, D.; Vinegoni, C.; Ntziachristos, V. Multispectral photoacoustic imaging of fluorochromes in small animals. *Opt. Lett.* **2007**, *32*, 2891. [CrossRef] [PubMed]
3. Buchmann, J.; Kaplan, B.; Powell, S.; Prohaska, S.; Laufer, J. Quantitative PA tomography of high resolution 3-D images: Experimental validation in a tissue phantom. *Photoacoustics* **2020**, *17*, 100157. [CrossRef] [PubMed]
4. Jnawali, K.; Chinni, B.; Dogra, V.; Rao, N. Automatic cancer tissue detection using multispectral photoacoustic imaging. *Int. J. Comput. Assist. Radiol. Surg.* **2020**, *15*, 309–320. [CrossRef]
5. Needles, A.; Heinmiller, A.; Sun, J.; Theodoropoulos, C.; Bates, D.; Hirson, D.; Yin, M.; Foster, F. Development and initial application of a fully integrated photoacoustic micro-ultrasound system. *IEEE Trans. Ultrason. Ferroelectr. Freq. Control* **2013**, *60*, 888–897. [CrossRef]
6. Xu, M.; Wang, L.V. Photoacoustic imaging in biomedicine. *Rev. Sci. Instrum.* **2006**, *77*, 041101. [CrossRef]
7. Diot, G.; Metz, S.; Noske, A.; Liapis, E.; Schroeder, B.; Ovsepian, S.V.; Meier, R.; Rummeny, E.; Ntziachristos, V. Multispectral Optoacoustic Tomography (MSOT) of human breast cancer. *Clin. Cancer Res.* **2017**, *23*, 6912–6922. [CrossRef]

8. Wilson, K.E.; Wang, T.Y.; Willmann, J.K. Acoustic and photoacoustic molecular imaging of cancer. *J. Nucl. Med.* **2013**, *54*, 1851–1854. [CrossRef]
9. Heijblom, M.; Piras, D.; van den Engh, F.M.; van der Schaaf, M.; Klaase, J.M.; Steenbergen, W.; Manohar, S. The state of the art in breast imaging using the Twente Photoacoustic Mammoscope: Results from 31 measurements on malignancies. *Eur. Radiol.* **2016**, *26*, 3874–3887. [CrossRef]
10. Bauer, D.R.; Olafsson, R.; Montilla, L.G.; Witte, R.S. 3-D photoacoustic and pulse echo imaging of prostate tumor progression in the mouse window chamber. *J. Biomed. Opt.* **2011**, *16*, 026012. [CrossRef]
11. Margolis, R.; Wessner, C.; Stanczak, M.; Liu, J.B.; Li, J.; Nam, K.; Forsberg, F.; Eisenbrey, J.R. Monitoring Progression of Ductal Carcinoma In Situ Using Photoacoustics and Contrast-Enhanced Ultrasound. *Transl. Oncol.* **2019**, *12*, 973–980. [CrossRef] [PubMed]
12. Gargiulo, S.; Albanese, S.; Mancini, M. State-of-the-Art Preclinical Photoacoustic Imaging in Oncology: Recent Advances in Cancer Theranostics. *Contrast Media Mol. Imaging* **2019**, *2019*, 5080267. [CrossRef] [PubMed]
13. Jose, J.; Manohar, S.; Kolkman, R.G.M.; Steenbergen, W.; Leeuwen, T.G. Van Imaging of tumor vasculature using Twente photoacoustic systems. *J. Biophotonics* **2009**, *717*, 701–717. [CrossRef] [PubMed]
14. Manohar, S.; Dantuma, M. Current and future trends in photoacoustic breast imaging. *Photoacoustics* **2019**, *16*, 100134. [CrossRef] [PubMed]
15. Rao, A.P.; Bokde, N.; Sinha, S. Photoacoustic imaging for management of breast cancer: A literature review and future perspectives. *Appl. Sci.* **2020**, *10*, 767. [CrossRef]
16. Liu, S.; Wang, H.; Zhang, C.; Dong, J.; Liu, S.; Xu, R.; Tian, C. In Vivo Photoacoustic Sentinel Lymph Node Imaging Using Clinically-Approved Carbon Nanoparticles. *IEEE Trans. Biomed. Eng.* **2019**. [CrossRef]
17. Jose, J.; Grootendorst, D.J.; Vijn, T.W.; van Leeuwen, T.G.; Steenbergen, W.; Manohar, S.; Wouters, M.; Ruers, T.J.; van Boven, H. Initial results of imaging melanoma metastasis in resected human lymph nodes using photoacoustic computed tomography. *J. Biomed. Opt.* **2011**, *16*, 096021. [CrossRef]
18. Alaeian, M.; Orlande, H.R.B.; Machado, J.C. Temperature estimation of inflamed bowel by the photoacoustic inverse approach. *Int. J. Numer. Methods Biomed. Eng.* **2020**, *36*, e3300. [CrossRef]
19. Sheikh, R.; Cinthio, M.; Dahlstrand, U.; Erlov, T.; Naumovska, M.; Hammar, B.; Zackrisson, S.; Jansson, T.; Reistad, N.; Malmsjo, M. Clinical Translation of a Novel Photoacoustic Imaging System for Examining the Temporal Artery. *IEEE Trans. Ultrason. Ferroelectr. Freq. Control* **2019**, *66*, 472–480. [CrossRef]
20. Xia, W.; Singh, M.K.A.; Maneas, E.; Sato, N.; Shigeta, Y.; Agano, T.; Ourselin, S.; West, S.J.; Desjardins, A.E. Handheld real-time LED-based photoacoustic and ultrasound imaging system for accurate visualization of clinical metal needles and superficial vasculature to guide minimally invasive procedures. *Sensors* **2018**, *18*, 1394. [CrossRef]
21. Zhu, Y.; Lu, X.; Dong, X.; Yuan, J.; Fabiilli, M.L.; Wang, X. LEd-based photoacoustic imaging for monitoring angiogenesis in fibrin scaffolds. *Tissue Eng. Part C Methods* **2019**, *25*, 523–531. [CrossRef] [PubMed]
22. Jo, J.; Xu, G.; Zhu, Y.; Burton, M.; Sarazin, J.; Schiopu, E.; Gandikota, G.; Wang, X. Detecting joint inflammation by an LED-based photoacoustic imaging system: A feasibility study. *J. Biomed. Opt.* **2018**, *23*, 110501. [CrossRef] [PubMed]
23. Zhu, Y.; Xu, G.; Yuan, J.; Jo, J.; Gandikota, G.; Demirci, H.; Agano, T.; Sato, N.; Shigeta, Y.; Wang, X. Light emitting diodes based photoacoustic imaging and potential clinical applications. *Sci. Rep.* **2018**, *8*, 1–12. [CrossRef] [PubMed]
24. Razansky, D.; Distel, M.; Vinegoni, C.; Ma, R.; Perrimon, N.; Köster, R.W.; Ntziachristos, V. Multispectral opto-acoustic tomography of deep-seated fluorescent proteins in vivo. *Nat. Photonics* **2009**, *3*, 412–417. [CrossRef]
25. Cox, B.T.; Arridge, S.R.; Beard, P.C. Estimating chromophore distributions from multiwavelength photoacoustic images. *JOSA A* **2009**, *26*, 443–455. [CrossRef]
26. Glatz, J.; Deliolanis, N.C.; Buehler, A.; Razansky, D.; Ntziachristos, V. Blind source unmixing in multi-spectral optoacoustic tomography. *Opt. Express* **2011**, *19*, 3175. [CrossRef]
27. Bartholomew, D.J. Principal components analysis. *Int. Encycl. Educ.* **2010**, 374–377.
28. Hyvärinen, A. Independent component analysis: Recent advances. *Philos. Trans. R. Soc. A Math. Phys. Eng. Sci.* **2013**, *371*, 20110534. [CrossRef]

29. Le, Q.V.; Karpenko, A.; Ngiam, J.; Ng, A.Y. ICA with reconstruction cost for efficient overcomplete feature learning. In *Advances in Neural Information Processing Systems*; Neural Information Processing Systems Foundation, Inc.: San Diego, CA, USA, 2011; pp. 1017–1025.
30. Ngiam, J.; Koh, P.W.; Chen, Z.; Bhaskar, S.; Ng, A.Y. Sparse filtering. In *Advances in Neural Information Processing Systems*; Neural Information Processing Systems Foundation, Inc.: San Diego, CA, USA, 2011; pp. 1125–1133.
31. Wang, P.; Wang, P.; Wang, H.-W.; Cheng, J.-X. Mapping lipid and collagen by multispectral photoacoustic imaging of chemical bond vibration. *J. Biomed. Opt.* **2012**, *17*, 0960101. [CrossRef]
32. Arabul, M.U.; Rutten, M.C.M.; Bruneval, P.; van Sambeek, M.R.H.M.; van de Vosse, F.N.; Lopata, R.G.P. Unmixing multi-spectral photoacoustic sources in human carotid plaques using non-negative independent component analysis. *Photoacoustics* **2019**, *15*, 100140. [CrossRef]
33. Lee, D.D.; Seung, H.S. Learning the parts of objects by non-negative matrix factorization. *Nature* **1999**, *401*, 788–791. [CrossRef] [PubMed]
34. Lil, S.; Hou, X.; Zhangl, H.; Cheng, Q. Learning Spatially Localized, Parts-B ased Representation. In Proceedings of the 2001 IEEE Computer Society Conference on Computer Vision and Pattern Recognition. CVPR 2001, Kauai, HI, USA, 8–14 December 2001.
35. Buciu, I. Non-negative matrix factorization, a new tool for feature extraction: Theory and applications. *Int. J. Comput. Commun. Control* **2008**, *3*, 67–74.
36. Li, L.; Yang, J.; Xu, Y.; Qin, Z.; Zhang, H. Documents clustering based on max-correntropy nonnegative matrix factorization. *Proc. Int. Conf. Mach. Learn. Cybern.* **2014**, *2*, 850–855.
37. Luo, X.; Zhou, M.; Xia, Y.; Zhu, Q. An efficient non-negative matrix-factorization-based approach to collaborative filtering for recommender systems. *IEEE Trans. Ind. Inform.* **2014**, *10*, 1273–1284.
38. Montcuquet, A.-S.; Herve, L.; Garcia, F.P.N.Y.; Dinten, J.-M.; Mars, J.I. Nonnegative matrix factorization: A blind spectra separation method for in vivo fluorescent optical imaging. *J. Biomed. Opt.* **2010**, *15*, 56009.
39. Lipovetsky, S. PCA and SVD with nonnegative loadings. *Pattern Recognit.* **2009**, *42*, 68–76. [CrossRef]
40. Keshava, N.; Mustard, J.F. Spectral unmixing. *IEEE Signal Process. Mag.* **2002**, *19*, 44–57. [CrossRef]
41. Lee, D.D.; Seung, H.S. Algorithms for non-negative matrix factorization. In *Advances in Neural Information Processing Systems*; The MIT Press: Cambridge, MA, USA, 2001; pp. 556–562.
42. Prahl, S. Tabulated Molar Extinction Coefficient for Hemoglobin in Water. Available online: https://omlc.org/index.html (accessed on 5 June 2020).
43. Toumia, Y.; Cerroni, B.; Trochet, P.; Lacerenza, S.; Oddo, L.; Domenici, F.; Paradossi, G. Performances of a Pristine Graphene—Microbubble Hybrid Construct as Dual Imaging Contrast Agent and Assessment of Its Biodistribution by Photoacoustic Imaging. *Part. Part. Syst. Charact.* **2018**, *35*, 1800066. [CrossRef]
44. Song, W.; Tang, Z.; Zhang, D.; Burton, N.; Driessen, W.; Chen, X. RSC Advances Comprehensive studies of pharmacokinetics and biodistribution of indocyanine green and liposomal indocyanine green by multispectral optoacoustic. *RSC Adv.* **2014**, *5*, 3807–3813. [CrossRef]
45. Gröhl, J.; Kirchner, T.; Adler, T.; Maier-Hein, L. Estimation of blood oxygenation with learned spectral decoloring for quantitative photoacoustic imaging (LSD-qPAI). *arXiv* **2019**, arXiv:1902.05839.
46. Brochu, F.M.; Joseph, J.; Tomaszewski, M.; Bohndiek, S.E. Light fluence correction for quantitative determination of tissue absorption coefficient using multi-spectral optoacoustic tomography. In Proceedings of the European Conference on Biomedical Optics 2015, Munich, Germany, 21–25 June 2015; p. 95390Z.

Chapter 4

Design and fabrication of an anthropomorphic heterogeneous mouse phantom for the standardization of volumetric photoacoustic imaging*

Abstract:

In this chapter, we have established a standardized protocol for the design and fabrication of anthropomorphic heterogeneous tissue-mimicking phantoms compatible with photoacoustic imaging. Realistic phantoms enable to experimentally test newly developed methods, thus leading to higher chances of success in the in-vivo experiments. Here, we developed and fabricated a phantom that mimics the detailed morphology of a mouse, including the skeleton and the main abdominal organs, using a combination of image modeling, copolymer-in-oil-based materials, and 3D-printing techniques. Besides, optical and acoustic properties, as well as the spectral and temporal stability of the phantom have been investigated in detail. Thus, this durable anthropomorphic mouse phantom would minimize animal experiments in compliance with the 3R principle as well as open many possibilities for advanced applications.

*Part of this chapter has been published as: **Grasso, V.,** Raymond, J., Willumeit-Römer, R., Joseph, J., & Jose, J. (2023, March). *"Development and characterization of a durable tissue-mimicking phantom for calibration and standardization of photoacoustic imaging."* In Photons Plus Ultrasound: Imaging and Sensing 2023 (p. PC123793D). SPIE.

*Part of this chapter is currently under review as: **Grasso, V.,** Raymond, J., Willumeit-Römer, R., Joseph, J. & Jose, J., (2023). *"Development of a morphologically realistic mouse phantom for pre-clinical photoacoustic imaging."* Medical Physics.

Design and fabrication of an anthropomorphic heterogeneous mouse phantom for the standardization of volumetric photoacoustic imaging

Valeria Grasso[a,b], Jason L. Raymond[c], Regine Willumeit-Römer[b,d], James Joseph[e,f], Jithin Jose[a,*]

[a]*FUJIFILM VisualSonics, Amsterdam, the Netherlands*

[b]*Faculty of Engineering, Institute for Materials Science, Christian-Albrecht University of Kiel, Kiel, Germany*

[c]*Department of Engineering Science, University of Oxford, Oxford, United Kingdom*

[d]*Division Metallic Biomaterials, Institute of Materials Research, Helmholtz-Zentrum Hereon GmbH, Geesthacht, Germany*

[e]*School of Science and Engineering, University of Dundee, Dundee, United Kingdom*

[f]*Centre for Medical Engineering and Technology, University of Dundee, Dundee, United Kingdom*

[*]Corresponding author. Email: jithin.jose@fujifilm.com

Abstract

Characterizations based on tissue-mimicking phantoms are highly effective to perform the technical validation of photoacoustic imaging (PAI) systems. Commonly, hydrogel-based phantoms are widely used in PAI, as these can be prepared following a straightforward fabrication protocol. However, these are susceptible to mechanical damage, dehydration, and bacterial growth in storage and therefore do not offer a suitable combination of durability and long-term stability. Although a variety of phantom models are reported for PAI applications, an unmet need still exists to establish anthropomorphic heterogeneous phantoms that can accelerate preclinical applications of the technology. Therefore, here we designed, developed, and fabricated a stable phantom that mimics the detailed morphology of a mouse, including the skeleton and the main abdominal organs, using a combination of image modeling, copolymer-in-oil-based materials, and 3D-printing techniques. This durable anthropomorphic heterogeneous mouse phantom would minimize the animal experiments in compliance with the

3R principle. Besides, the acoustic and optical properties of the tissue-mimicking material have been broadly characterized. Furthermore, our studies also showed that the phantom is durable and stable over time under storage and repeated use, and the fabrication protocol is easy to reproduce. As a result, the proposed anthropomorphic heterogeneous mouse phantom offers a tradeoff between manufacturing abilities, durability, material compatibility, and unprecedented realistic resemblance to the actual rodents' anatomy in PAI. To our knowledge, this is the first time a heterogeneous anthropomorphic durable mouse phantom has been proposed for PAI in preclinical animal imaging.

Keywords: 3D-printing, Tissue-mimicking Phantom, Anthropomorphic, Photoacoustic, Ultrasound.

_____

1. Introduction

Over the past decades, tissue-mimicking phantoms have exhibited their utility in a broad range of applications for biomedical imaging technologies [1]. Phantom-based studies are an essential element for the development and implementation of biomedical imaging systems. Generally, the validation studies are often performed using a stable physical phantom as it enables an objective and quantitative assessment of the device's performance [2]. Further, the use of tissue-mimicking phantoms can reduce the number of animals needed for the initial validations of the imaging technologies, which complies with the 3R principles of Replacement, Reduction, and Refinement. Established imaging techniques such as MRI, CT, PET, and Ultrasound (US) rely on commercially available, well-characterized tissue-mimicking phantoms. Often, these phantoms are standardized and can be used to perform the calibration of imaging systems. However, there is currently a lack of appropriate standardization or commercial availability of tissue-mimicking phantoms for emerging technologies such as photoacoustic imaging.

Photoacoustic imaging (PAI) is a rapidly growing imaging technology capable of simultaneously providing anatomical, functional, and molecular assessment of tissue properties. In PAI, endogenous and exogenous chromophores in the tissue absorb incident pulsed laser light creating ultrasound (US) waves that can be used to reconstruct the spatial distribution of the optical absorbers [3], [4]. Therefore, advancements in PAI systems often require the development of tissue-mimicking phantoms with specific acoustic and optical properties to perform system calibration and quality assurance, as well as for the development of standardized imaging protocols.

Considering the phantom properties, an ideal tissue-mimicking phantom for PAI should have tunable acoustic and optical properties as well as maintain stability and durability over time with repeated use and storage conditions [5], [6]. A wide range of tissue-mimicking materials (TMMs) has been proposed as PAI phantom candidates, including materials based on hydrogels (i.e. agarose, gelatin), gel wax, and mineral oil. In particular, water-based materials such as agar [7], [8], gelatin [9], and polyvinyl alcohol (PVA) [10], [11] are widely used as TMMs due to their straightforward fabrication capabilities. However, techniques using these TMMs favor the fabrication of simple homogeneous phantoms with limited tunability of acoustic and optical properties. These water-based phantoms can quickly degrade, thus limiting their mechanical durability and temporal stability. A variety of other TMMs has also been used to fabricate PAI phantoms, such as paraffin gel wax [12], [13], emulsions such as Intralipid [14], glycerol-in-polydimethylsiloxane (PDMS) [8], and polyvinyl chloride plastisol (PVCP) [15]. However, all these TMMs do not offer a suitable combination of durability, long-term stability, as well as realistic tuning of the acoustic and optical properties.

Recent works that aim to overcome these limitations include silk protein-based hydrogels [16] and a copolymer-in-oil-based TMM that is formulated by the International Photoacoustic Standardization Consortium (IPASC) [17]–[21]. This copolymer-in-oil base material offers tunable acoustic and optical properties similar to soft tissue and has good durability characteristics. Furthermore, the material has shown sufficient photo-, thermomechanical- and

longitudinal- stability for short- and long-term precision studies [19]. This demonstrates that there is a move towards the standardization of PAI phantoms [19]–[21].

In addition to the generic TMM properties, phantoms with anthropomorphic geometry are idealistic models that can often provide a realistic preclinical imaging scenario. 3-dimensional (3D) printing is an advanced innovative technique that has the potential to replicate complex geometries and anatomically similar structures of living animals. While, the use of 3D-printing has been broadly applied for the development of MRI, CT/PET, and Ultrasound phantoms [22], there are currently no standard protocols for 3D-printed PAI phantoms. Recently, Dantuma et al. have designed and fabricated a multi-layered semi-anthropomorphic phantom for PAI, which mimics the human breast morphology [23], [24]. This 3D-printed phantom aims to simulate skin (made from a silicone layer), in addition to underlying fat, fibroglandular tissue, and blood vessels (made from custom polyvinyl chloride plastisol (PVCP)). Although several types of organ-specific PAI phantoms are reported, further efforts are still required to establish a preclinical imaging phantom that mimics the realistic mouse model with the possibility of tuning the optical and acoustic properties. As there are different configurations of PAI for preclinical imaging, a stable anthropomorphic phantom is required to establish standards with a community consensus, to accelerate the device design optimization. Therefore, a methodology for fabricating a realistic, durable, and stable anthropomorphic phantom for PAI is still in great need [25].

In this paper, we describe the design, fabrication, characterization, and imaging of a high-resolution anthropomorphic mouse phantom for preclinical PAI. Exhaustive characterization such as broadband acoustic measurements of sound speed and attenuation, as well as optical scattering and optical absorption measures have been performed to assess the phantom properties and PA image quality. In particular, the speed of sound and acoustic attenuation values were determined over a frequency range of 3 to 12 MHz, and optical absorption and scattering properties were evaluated over a wavelength range of 600 to 1000 nm. A customized TMM based on copolymer-in-oil with 3D-printing enabled the fabrication of the anthropomorphic mouse phantom with high accuracy, durability, stability, and tunable optical

properties. Further, we performed multispectral photoacoustic and ultrasound imaging of the mouse phantom. To our knowledge, this is the first time using 3D-printing technology to establish an anatomically accurate, durable, and heterogeneous small animal phantom for PAI. The proposed methodology can be adapted by researchers and clinicians to construct realistic tissue-mimicking phantoms for the continuous development of PAI. The reported mouse phantom can be used as a tool for many applications involving systemic whole-body investigations, inter-device comparisons, and to test newly developed image and data processing algorithms for PAI.

2. Materials and methods

2.1. Anthropomorphic mouse phantom fabrication

A realistic anthropomorphic mouse phantom was fabricated by combining 3D-printing technology with copolymer-in-oil used as a tissue-mimicking material. The fabrication process included feature extraction from a mouse atlas, object modeling and optimization, 3D-printing, and assembly. To extract the realistic features, the 3D whole-body mouse atlas obtained from co-registered CT and cryostat data was used [26]. From the mouse atlas, the skeleton and the main abdominal organs were segmented and converted into the Standard Tessellation Language (STL) format consisting of triangulated surface mesh structures. The computer-aided design (CAD) software Rhino (Rhinoceros v.6, McNeel& Associates) was used for the modeling of these anatomical parts. After the modeling, the object files were optimized and smoothed in Meshmixer (Autodesk, Inc., Toronto, Canada) to have single solid objects with a properly closed mesh. Finally, the object models were prepared in Preform (Formlabs Inc., Somerville, MA, USA) by optimizing the proper object orientation and removable supports to obtain the files suitable for 3D-printing.

For the skeleton model, two artificial cylinders were created using Meshmixer (Autodesk, Inc., Toronto, Canada) to connect the forelimbs and shoulders to the spine, thus enabling the printing of the skeleton as a single contiguous object (see Fig. 1 (A)). After this modification, the 3D model of the skeleton was smoothed and refined in Meshmixer, making it ready for 3D-

printing. In addition to the skeleton, a custom-designed mouse holder with a refillable cavity was also designed (see Fig. 1 (B)). The mouse holder and the cavity mimic the shape of the mouse and the bladder respectively. In addition to the mouse holder, the main abdominal organs such as kidneys, liver, and spleen were also segmented from the atlas and included in the mouse phantom design. After the segmentation, the respective STL files of the abdominal organs were modeled and optimized in Meshmixer. Negative molds of the organs were fabricated (see Fig. 1 (C-E)), which can be filled with the TMM with different acoustic and optical properties.

Fig. 1 depicts the STL-designed objects of the mouse phantom including the skeleton, mouse holder, and the abdominal organs' molds. The stereolithographic (SLA) 3D-printer and white standard resin (Formlabs Form 3, Formlabs Inc., Somerville, MA, USA) were used for all object printing. The 3D-printing resolution was specified as 100µm during the design process to achieve a rapid prototype with limited errors. After the printing of the objects, a double washing in an isopropyl alcohol bath for 20 minutes was performed to remove excess resin. The support materials were then removed carefully and the objects were post-cured in a UV oven for 15 minutes at 60 ^{0}C (Formlabs Form Cure, Formlabs Inc., Somerville, MA, USA).

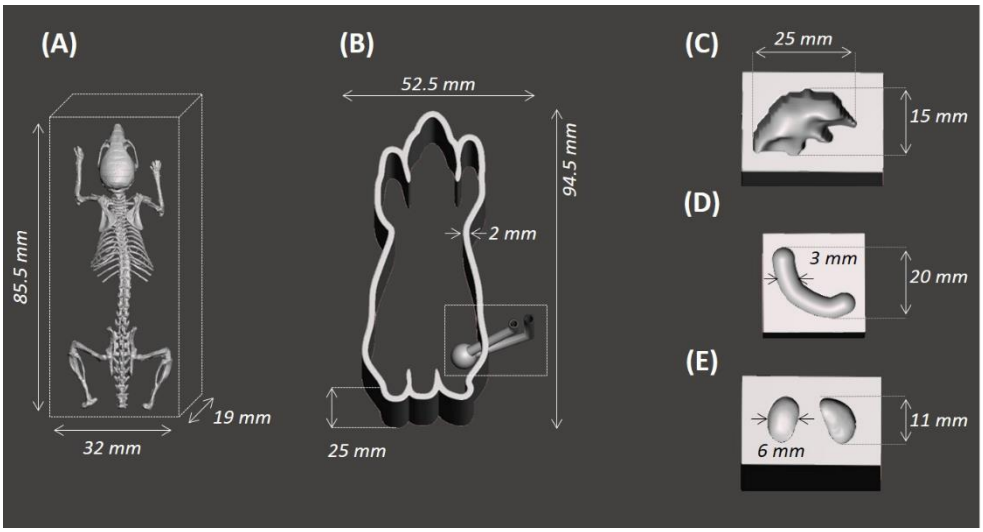

Figure 1. STL-designed models of the mouse phantom parts as the skeleton (A), mouse holder with a refillable cavity mimicking the bladder within the dashed insertion (B), and organ molds of the liver (C), spleen (D), and kidneys (E).

2.1.1. Copolymer-in-oil TMM

For synthesizing the tissue-mimicking material (TMM) the recently proposed copolymer-in-oil recipe was adapted and optimized [27]. This durable and tested soft TMM was used to prepare the organs and the bulk of the fabricated mouse phantom. The copolymer-in-oil-based material was prepared using $78\%\ w/w$ of mineral oil (Sigma Aldrich-330779-1L) mixed with three polymeric powders. Specifically, $12\%\ w/w$ of polystyrene-block-poly(ethylene-ran-butylene)-block-polystyrene (Sigma Aldrich 200557-250G), $8\%\ w/w$ of low-density Polyethylene (Alfa Aesar 43949.30), and $2\%\ w/w$ of butylated Hydroxytoluene (Sigma Aldrich W218405-1KG-K) were used. The mixture was prepared in a silicone oil bath (Sigma Aldrich 85409-1L), which was warmed up to 170°C with a stirrer set to $50\ rpm$ for uniform temperature distribution. The polymers were then sequentially added to the mineral oil under stirring conditions of $150\ rpm$, until all components were completely dissolved and the mixture turned clear. Finally, the material was carefully poured into a mold and was allowed to set at room temperature until completely polymerized. Further details of the copolymer-in-oil preparation are reported elsewhere [19].

Optically absorbing dyes were added to tune the optical properties of the soft base material. Specifically, the base TMM was doped with $0.02\%\ w/v$ of graphene powder (Sigma Aldrich 900561), and $0.05\%\ v/v$ of blue, green, and pink inks (Oil colors, Winsor & Newton, London, UK) respectively. Organs were fabricated by pouring the doped soft material into the 3D-printed organ molds. Blue and green oil color inks were used for the spleen and the liver respectively, while graphene powder additive was used for simulating the kidneys. In addition, the soft base material mixed with low-absorbing pink ink was used to mimic the background tissue. Once prepared, the copolymer-in-oil base material doped with the additives could be re-heated in a silicone oil bath and reused for pouring into the organ molds and refilling the mouse phantom holder as described above.

After the fabrication and preparation of TMM and organs, the mouse phantom was assembled by positioning all organs in realistic reciprocal positions. Firstly, a thin layer of pink background TMM was slowly poured into the mouse holder, which was temporarily fixed on a

metal plate. Before the material started solidifying, the skeleton, liver, spleen, and kidneys were positioned within the holder with the help of tweezers. Finally, the rest of the holder was slowly filled with the pink base material to complete the fabrication of the mouse phantom.

2.2. Acoustic characterization

For the acoustic characterization, copolymer-in-oil-based TMM slabs were fabricated by pouring the material into rectangular molds with different thicknesses (1.3 and $1.5\ cm$) to enable multiple evaluations. Fig. 2 depicts the diagram of the experimental setup used for performing speed of sound and acoustic attenuation measurements. Measurements were conducted in an 8 L acrylic tank ($45\ cm\ x\ 12\ cm\ x\ 15\ cm$) filled with distilled and degassed water. A pair of broadband transducers (Panametrics V313, $6.35\ mm$ diameter, $19\ mm$ focal length, $15\ MHz$ center frequency; Olympus NDT, Waltham, MA, USA) was used to acquire the through-transmission spectrum using a broadband substitution technique [28]. An ultrasound pulser-receiver (DPR300, JSR Ultrasonics, Pittsford, NY) was used to generate the excitation pulse and amplify the received signal (0-70 dB gain). Received waveforms were averaged (typically 64 traces per acquisition), digitized (LT264, LeCroy, Chestnut Ridge, NY, USA), and transferred to a computer for analysis using MATLAB (Mathworks, Natick, MA, USA). The frequency-dependent spectrum (insertion loss in dB or estimated attenuation coefficient in dB/cm) is computed from the measured voltage-time waveforms:

$$\alpha_{meas}(f) = 10\log_{10}\left(\frac{|V_{ref}(f)|^2}{|V_{sample}(f)|^2}\right)/d \quad (1)$$

where α_{meas} is the frequency-dependent attenuation coefficient of the material (in dB/cm); V_{ref} and V_{sample} are the received voltage amplitude spectra in the absence (through-water) and presence (through-sample) of the sample, respectively, and d is the thickness of the sample. For determining the thickness d, the samples were sandwiched between two glass microscope slides (thickness $1.0\ mm$) and measured with vernier calipers ($\pm\ 0.2\ mm$). The thickness of the sample was determined by subtracting $2.0\ mm$ from the overall measurement.

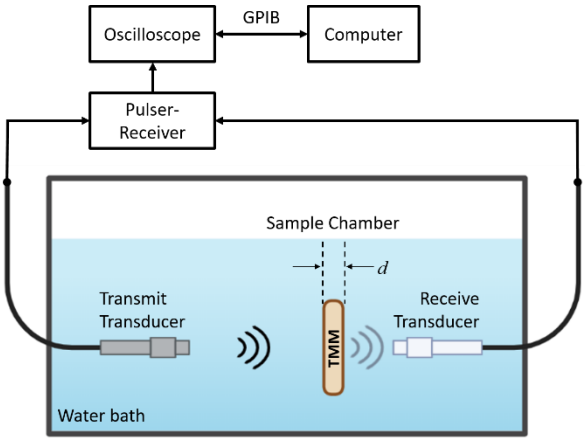

Figure 2. A schematic of the experimental setup for the insertion technique used to measure the speed of sound and acoustic attenuation. Broadband transducers are driven with a pulser-receiver in through transmission mode. The received waveforms are digitized and analyzed using MATLAB.

The attenuation was measured over the frequency range corresponding approximately to the −20 dB bandwidth of the system. From previous findings, the attenuation measurements accounting for the interfacial losses were assessed. These measures have shown that the impact of the interfacial losses is negligible [19]. Therefore, the acoustic attenuation measurements have not been corrected for reflective losses at the water/sample interface. The frequency-dependent attenuation was fit to a power-law of the form:

$$\alpha_{meas}(f) = \alpha_0 f^{PL} \tag{2}$$

where f is the frequency (in MHz) and α_0 and PL are fitting parameters [29]. The phase speed method is implemented using a spectroscopic technique and the frequency-dependent speed of sound (in m/s) has been evaluated as described elsewhere [30]–[32].

2.3. Optical characterization

The absorption and reduced scattering coefficients of TMM samples doped with different additives have been measured within the spectral range of $600 - 1000\ nm$. Copolymer-in-oil material slabs including the different additives were fabricated for measurements of optical properties. The doped TMMs were poured within a $2\ mm$ thickness spacer positioned between two glass microscope slides.

Measurements of the total transmittance and reflectance of the tissue samples were made between $600 - 1000\ nm$ using a dual-beam spectrometer (Lambda $750s$; PerkinElmer, Beaconsfield, UK) equipped with a $100\ mm$ integrating sphere (LabSphere Inc., North Sutton, NH, USA) and small spot kit to reduce the beam-illuminated area of the samples to approximately $2\ mm$ diameter for both configurations. Details of the setup have been described previously [33]. Measurements were recorded at $5\ nm$ intervals in optical wavelength, using a slit width of $5\ nm$ below $860\ nm$ and servo-controlled slit width ($2 - 20\ nm$) in the near-infrared (NIR) regime above $860\ nm$. The measurements of total transmittance and reflectance, and the sample thickness, were used to calculate the absorption coefficient $\mu_a(cm^{-1})$ and the reduced scattering coefficient $\mu'_s\ (cm^{-1})$ using the inverse adding-doubling (IAD) algorithm [34]. The spectrometer system measures the ratio of the reference and sample beam energy, therefore eliminating the need for sphere efficiency corrections. The tissue index of refraction was assumed to be 1.4, and the anisotropy factor was assumed to be 0.97 for the IAD calculations.

2.4. Photoacoustic imaging acquisition

Photoacoustic imaging of the mouse phantom was performed using a commercial high-frequency ultrasound (US) and photoacoustic (PA) platform Vevo LAZR-X (FUJIFILM VisualSonics, Inc., Toronto, ON, Canada), described in detail elsewhere [35]. The imaging setup included a high-frequency US system (Vevo 3100), an optical parametric oscillator (OPO) integrated Nd:YAG nanosecond pulsed laser, and the animal imaging platform. The US system is equipped with a linear US transducer array (MX201) that consists of 256 elements at a nominal center frequency of $15\ MHz$ and bandwidth across $10 - 22\ MHz$. This transducer results in axial and lateral resolution of $100\mu m$ and $220\mu m$ respectively. Light from the laser is delivered to the sample through optical fibers, mounted on either side of the transducer. To obtain the homogenous light illumination, the sample to be imaged was placed within the converging area of the two light beams. The repetition rate of the laser was $20\ Hz$, and the multi-spectral photoacoustic images could be acquired by tuning the laser wavelengths within the range of $680 - 970\ nm$. The system allowed the selection of any wavelength within this NIR range. In particular, for the experiments, we used a step size of $20\ nm$ between the

wavelengths to acquire the 3D multi-spectral PA images. During the image acquisition, the mouse phantom was fixed on a container filled with degassed water, which has been used as a coupling medium.

2.4.1. Statistics and image analysis

The photoacoustic signal and image analysis were conducted using VevoLAB Desktop Software (FUJIFILM VisualSonics, Inc., Toronto, ON, Canada). Linear unmixing was performed on the multi-spectral photoacoustic data to spatially differentiate the different absorbers embedded within the mouse phantom [36]. Linear unmixing of the volumetric multi-spectral photoacoustic data was also performed in VevoLAB, via the built-in unmixing tool. The source spectra were obtained by spectral photoacoustic preliminary measures on the pure absorbers, thus the respective spectra could be stored in the spectral library and further used for the unmixing as described elsewhere [37].

2.5. Photospectral photoacoustic stability

Since pulsed lasers are used in PAI, it is important to test whether a material is subjected to photobleaching under multiple laser exposures. Copolymer-in-oil doped samples were used to perform the photostability measurements. To assess the photoacoustic spectral stability, a fixed position within the doped TMM samples was irradiated with 16000 laser pulses over a period of 30 minutes using $700\,nm$, $800\,nm$, and $900\,nm$ light wavelengths. The photoacoustic spectral intensities along multiple laser pulses were measured from the different doped soft TMMs. To study the relationship between the photoacoustic signal amplitude and the light source pulse, a circular region of interest (ROI) was defined for each doped material, and the mean pixel intensity values across each ROI were calculated. The energy of the laser cart was also recorded for every pulse to normalize the photoacoustic intensity values with any laser energy fluctuations. Therefore, the stability characteristics of the material are independent of the system.

2.6. Temporal stability

The long-term stability of the soft TMMs used for the mouse phantom was also assessed. Mouse phantoms were stored in a dry steel container at room temperature and pressure. Photoacoustic images of the mouse phantoms were acquired over nine months. Over this time frame of nine months, the mean photoacoustic intensity values were evaluated from a selected ROI per each TMM doped with the different optical additives. This was used to estimate the stability of the photoacoustic properties of the material over the investigated time frame.

3. Results

3.1. Mouse phantom fabrication

Fig. 3 (A-C) show the 3D-printed objects after removing the support material and refining them with washing/curing procedures. As pointed out by the red arrows in Fig. 3 (A-B), permanent markers were added in specific positions as strategic markers for future image registration purposes. In particular, black ink (Edding 3000 Permanent Marker - $1.5 - 3\ mm$ - Black) was used to mark the shoulders, and green ink (Edding 3000 Permanent Marker - $1.5 - 3\ mm$ - Green) was adopted to mark the top part of the bladder of the mouse phantom holder. Fig. 3 (C) shows the liver, spleen, and kidney molds used to make the respective mimicking shape organs utilizing doped copolymer-in-oil material, as depicted in Fig. 3 (D).

Fig. 4 shows some of the steps in the phantom fabrication and parts assembly. Fig. 4 (A) shows an initial phase where the mouse holder was fixed on a metallic plate, where a thin layer of pink copolymer-in-oil material was poured. Besides, the skeleton and the organs were also placed and fixed by matching their relative positions in accordance with the real anatomy. Finally, the rest of the phantom was filled with pink copolymer-in-oil material poured to fill the whole thickness of the mouse holder. Fig. 4 (B-C) depicts the final mouse phantom in its supine and prone position respectively.

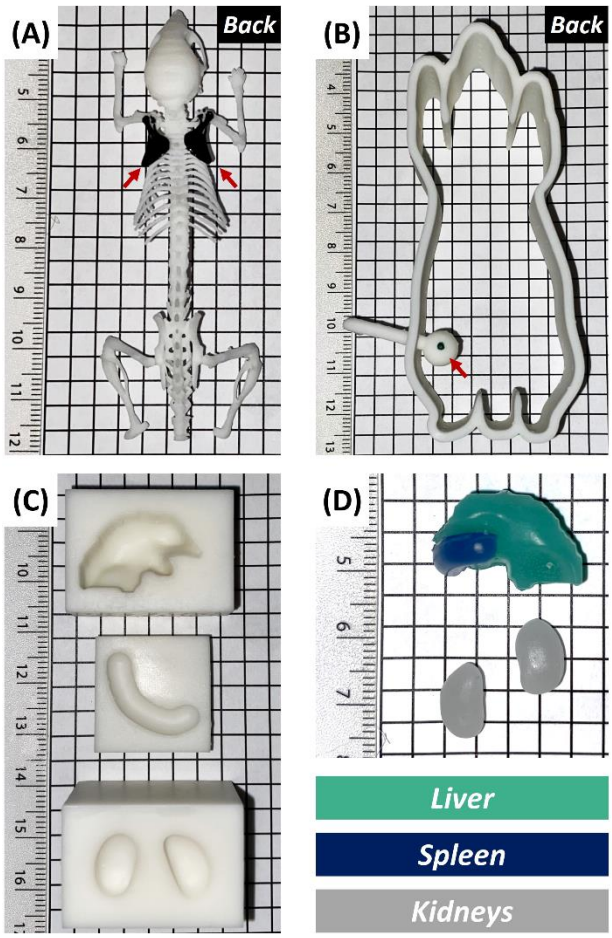

Figure 3. 3D-printed objects mimicking the skeleton (A), mouse holder with a refillable cavity (B), and organ molds (C) of liver-spleen-kidneys from top to bottom. Main abdominal mimicking organs (liver-spleen-kidneys) made of copolymer-in-oil base material doped with green ink, blue ink, and graphene powder respectively (D) obtained utilizing the organ molds.

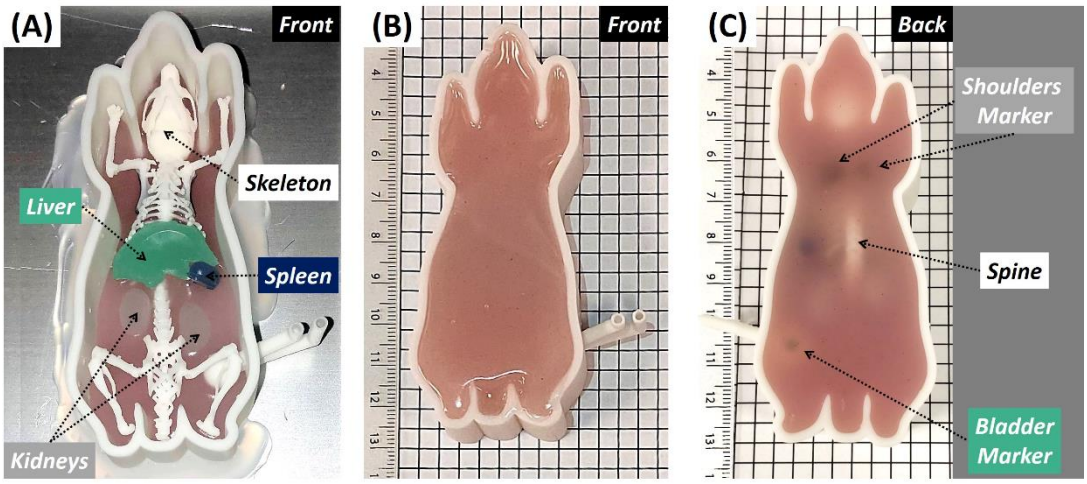

Figure 4. Assembled skeleton and copolymer-in-oil-based organs within the mouse holder with a refillable cavity (A) from the front/supine view side. This allows the internal structure to be seen for demonstration. Finalized mouse

phantom filled with copolymer-in-oil material doped with pink oil color ink from the front/supine view side (B) and back/prone view side (C).

3.2. Acoustic properties

The acoustic attenuation coefficient and the speed of sound for the samples of copolymer-in-oil TMM without and with additives were evaluated. Fig. 5 (A-B) show the frequency-dependent acoustic attenuation coefficient obtained for the samples made from copolymer-in-oil material without additives and for the samples doped with oil color inks and graphene powder respectively.

Table 1 gives the measured speed of sound (SOS). Besides, the attenuation variables α_0 and PL used to evaluate Eq. (2), which represent the best-fit parameters for the power law fit for each material are reported. These parameters were calculated over the $3-12\ MHz$ frequency range.

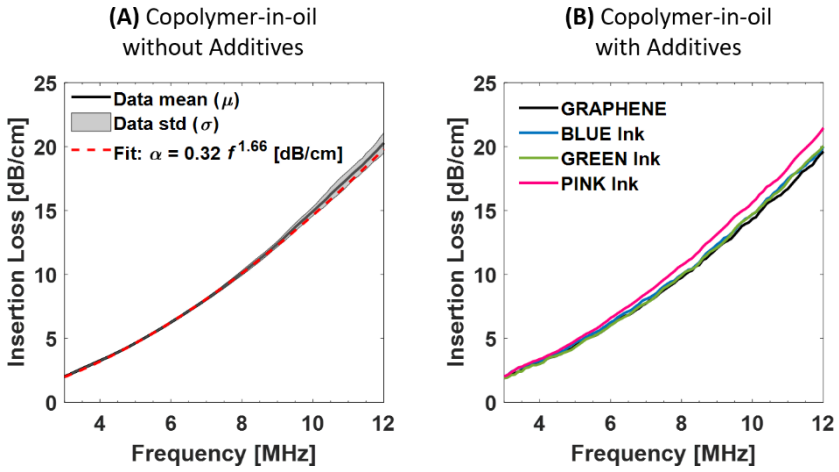

Figure 5. Acoustic attenuation of copolymer-in-oil samples without additives (A), and mixed with additives such as graphene powder, blue, green, and pink oil color inks (B).

The results obtained show that the speed of sound of the TMM ranges between $1486-1514\ m/s$. These results suggest that the material would be suitable for mimicking the speed of sound of tissues such as breast fat ($1450-1490\ m/s$), as well as for tissues such as skin, muscle, kidney, or prostate ($\approx 1520\ m/s$) [38].

Table 1. Measured physical properties of the phantom materials used in this study.

Copolymer-in-oil material	SOS [m/s]	α_0 $[dBcm^{-1}MHz^{-PL}]$	PL [a.u.]
NO Additives	1514 ± 2.53	0.32 ± 0.018	1.66 ± 0.024
GRAPHENE	1486 ± 0.91	0.31 ± 0.045	1.68 ± 0.055
BLUE Ink	1486 ± 0.71	0.32 ± 0.045	1.67 ± 0.048
GREEN Ink	1487 ± 0.78	0.29 ± 0.022	1.71 ± 0.021
PINK Ink	1511 ± 44	0.32 ± 0.022	1.69 ± 0.020

3.3. Optical properties

The optical properties of the fabricated copolymer-in-oil soft TMM used for the organs and as bulk material within the mouse phantom were evaluated.

The optical absorption and scattering properties of the base TMM without additives showed negligible absorption and did not exceed a reduced scattering value of $1\ cm^{-1}$, which is still below the threshold of most soft tissues [39]. As a result, it was possible to tune the optical properties of the material through further additives. This flexibility suggests that the optical characteristics of the proposed material can be independently tuned and adapted to any soft tissue type of interest. The optical absorption and scattering coefficients were measured within the range of $600-1000\ nm$, which includes the near-infrared range I (NIR-I) widely used for in vivo applications of PAI.

Fig. 6 (A) shows the reduced scattering coefficient (μ'_s), and Fig. 6 (B) optical absorption coefficient (μ_a) of copolymer-in-oil material samples doped with graphene powder as well as blue, green, and pink oil color inks. The plots include the mean of measures obtained from multiple samples.

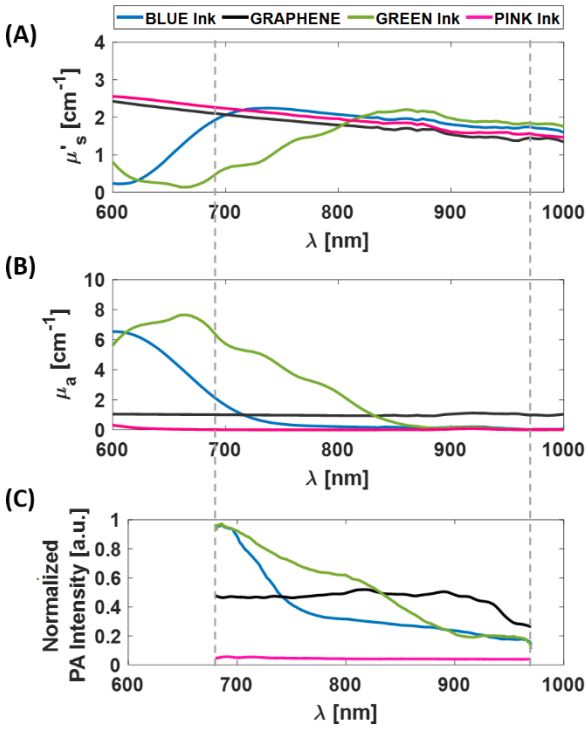

Figure 6. Reduced scattering coefficient (A), absorption coefficient (B), and photoacoustic absorption spectra (C) of the copolymer-in-oil samples mixed with additives such as graphene powder, blue, green, and pink oil color inks. The highlighted region between $680 - 970\ nm$ represents the corresponding NIR-I range used in photoacoustic imaging.

From the measured optical properties, we observed that the material intrinsically shows scattering properties, without the addition of exogenous scattering agents such as titanium dioxide. In particular, the reduced scattering coefficient showed a uniform and slightly decreasing trend for the copolymer-in-oil samples doped with graphene and pink oil color ink. While blue and green oil color inks showed an initial lower reduced scattering coefficient that becomes higher and continuous after $700\ nm$ and $800\ nm$ respectively. The measured reduced optical scattering coefficient values could be used to simulate different types of soft tissues [38], [40].

Besides, the samples with different additives showed distinct absorption spectra over the wavelength range of 600 to $1000\ nm$ (Fig. 6 (B)). These absorption characteristic spectra differed in shapes in this range. Specifically, the blue oil color ink showed an absorption peak at $600\ nm$, the green oil color ink showed a broad absorption peak centered at around $680\ nm$, while graphene and pink oil color ink showed a broad flat absorption spectrum. In addition, the optical absorption spectra of the copolymer-in-oil material doped with additives

showed different spectra from those of endogenous tissue chromophores. However, their characteristic spectral trend enables to test and evaluate spectral unmixing algorithms [41], [42].

Fig. 6 (C) shows the photoacoustic absorption spectra plotted as normalized intensity within the range of $680 - 970\ nm$ (NIR-I) obtained from the same doped samples. While the blue oil color ink absorption spectrum showed the highest absorption at $680\ nm$ and has a quasi-exponential decrease afterward, the green oil color ink showed wider absorption until around $800 - 830\ nm$ before decreasing at higher wavelengths. Besides, pink oil color ink showed a low-intensity absorption spectrum within the NIR-I range. Finally, graphene showed a broad absorption spectrum within the $680 - 900\ nm$ region and a gradual absorption decrease toward $900\ nm$. These photoacoustic spectra are then used for PAI linear unmixing, to spatially differentiate the different absorbers within the mouse phantom.

3.4. Photoacoustic spectral stability

Fig. 7 shows the normalized PA intensity over the laser pulses of the copolymer-in-oil samples doped with highly absorbing additives. No significant changes were detected in the normalized PA amplitude for the doped material. This indicates that the copolymer-in-oil material doped with different additives such as blue/green oil color inks and graphene is photostable for the entire exposure period.

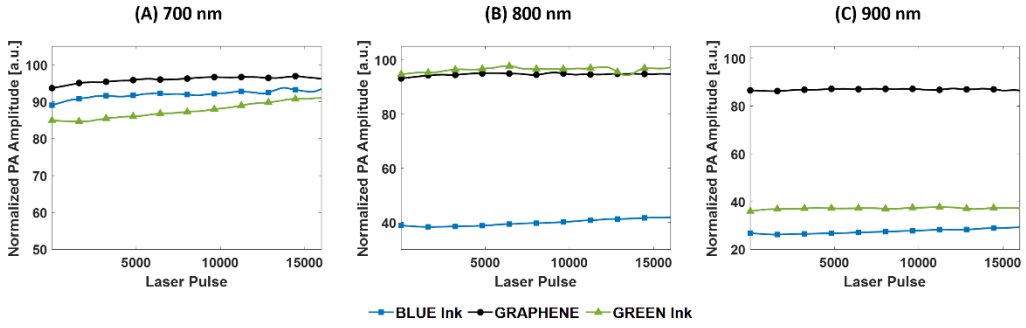

Figure 7. Normalized photoacoustic intensity of the copolymer-in-oil samples doped with graphene powder, blue and green oil color inks over 16000 laser pulses exposure to test the photostability of the phantom material during laser illumination at $700\ nm$ (A), $800\ nm$ (B), and $900\ nm$ (C).

The samples were exposed to laser pulses at different wavelengths such as $700\ nm$ (Fig. 7 (A)), $800\ nm$ (Fig. 7 (B)), and $900\ nm$ (Fig. 7 (C)). The PA intensity can vary through wavelengths due to the different absorption characteristics of the additives.

3.5. Temporal stability

The mouse phantoms were stored in air at room storage conditions. Under these conditions, the long-term stability properties of the mouse phantom TMMs were evaluated. Fig. 8 shows the mean photoacoustic intensity values undertaken over nine months for copolymer-in-oil samples doped with graphene powder, and blue/green oil color inks. Since mean PA intensity values remained constant over time, indicating the stability of the material properties over time, thereby establishes the potential of the material for the fabrication of durable PAI phantoms. Linear fits of the longitudinal stability measurements gave slopes of 0.0005 ± 0.000035, 0.0001 ± 0.00002, and 0.0002 ± 0.00005 for blue and green oil color inks and graphene respectively.

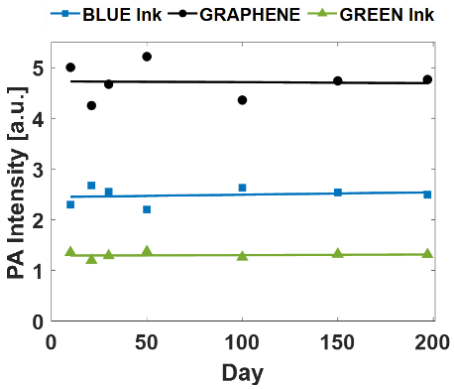

Figure 8. Photoacoustic intensity of the copolymer-in-oil samples doped with graphene powder, blue, and green oil color inks over time at $700\ nm$.

3.6. Ultrasound and photoacoustic volumetric imaging

Fig. 9 shows the US-PA imaging of the mouse phantom, where the anatomy appearance closely resembled that of the real animal. The US image (see Fig. 9 (A)) showed similarities with real preclinical whole-body US images. In addition, the PA image at a single wavelength of $700\ nm$ (see Fig. 9 (B)) showed the absorption obtained mainly from the organs-like structures (liver, spleen, and kidneys) as well as from the markers placed on the shoulders- and top of the

bladder-like structures. Finally, Fig. 9 (C) shows the result of the volumetric linear unmixing where the different absorbers are spatially and spectrally differentiated. Specifically, the liver, spleen, and kidneys are depicted in green, blue, and red, and the shoulders and bladder markers are shown in red and green respectively. Besides, the white resin used for fabricating the skeleton, mouse holder, and refillable cavity offered negligible optical absorption in PAI.

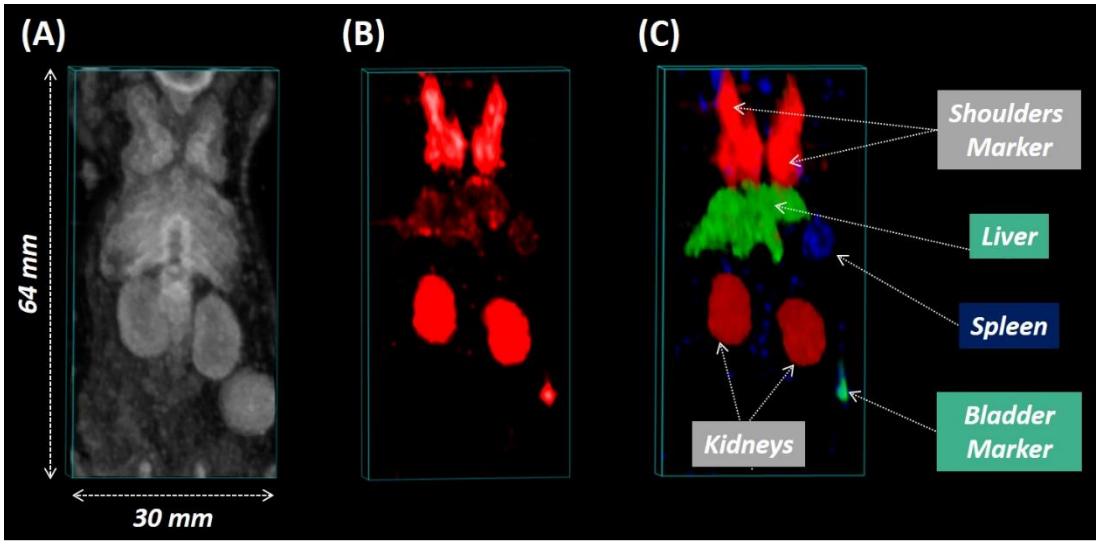

Figure 9. Ultrasound image in grayscale (A), photoacoustic image acquired at a single wavelength ($700\ nm$) in red scale (B), and linear unmixed map in the multi-color scale (C) of the mouse phantom.

4. Discussion

Here, we designed and fabricated a stable anthropomorphic mouse phantom that mimics the detailed morphology of a mouse, including the skeleton and the main abdominal organs. We used a combination of image modeling, copolymer-in-oil-based materials, and 3D-printing techniques for phantom fabrication. The overall procedure of fabrication and characterization of the mouse phantom is reported. The proposed anthropomorphic heterogeneous mouse phantom showed an accurate correspondence in US and PA imaging appearance as compared with real preclinical models imaging. The results show that the proposed phantom offers a tradeoff between simple manufacturing abilities, long durability, and high compatibility of the material in PAI. Our studies also showed that the phantom is durable and stable over time under normal room storage and repeated use conditions, and the fabrication protocol is easy to reproduce. The fabrication methodology proposed in this work can be adapted to fabricate

any anatomical target of interest and thus open opportunities in diverse applications of photoacoustic imaging. Besides, the copolymer-in-oil base material offers highly tunable optical and acoustic properties adequately to mimic different tissue types and compositions.

The mouse phantom offers a suitable combination of durability, long-term stability, and realistic acoustic/optical properties as compared to hydrogel-based phantoms that are commonly used in PAI. Therefore the proposed durable anthropomorphic heterogeneous mouse phantom aims to advance photoacoustic imaging and standardize imaging protocols by minimizing the animal experiments in compliance with the 3R principle. In the case of preclinical US-PA imaging, having realistic phantoms to test and validate newly developed imaging approaches leads to higher chances of success in the in-vivo experiments.

However, for translational applications, the usage of mouse phantom is challenged with some unaddressed limitations. For instance, flow phantoms are of great importance since they represent blood flow and perfusion. As recently proposed by Dantuma et al. [23], a breast phantom that includes a flow circuit with tunable blood oxygen saturation levels can also mimic the functional information. By leveraging such successful approaches, the field can more rapidly achieve effective tools for the clinical translation of photoacoustic systems.

In future works, we would introduce complex and interconnected vessel-like networks within the phantom in order to replicate more realistic PA scenarios. Adding the vasculature with highly absorbing constituents would help to test also additional aspects. Furthermore, the use of transparent resin might be useful to fabricate specific parts of the phantom, such as the refillable cavity which is mimicking the bladder. Thus, this might enable the use of multimodal contrast agents that can be visible in multimodality and facilitate the development of multimodal registration techniques.

Moreover, recently Nguyen et al. [16] reported that silk-based phantom materials have the advantage of not needing additional scattering materials like titanium dioxide. Just by changing silk concentration and other fabrication methods, the acoustic and optical properties of the phantoms can also be modulated. Here we have doped the copolymer-in-oil material just with optical absorbers. We will further explore the acoustic and optical properties by

tuning the characteristics of the proposed TMM in detail. The addition of extrinsic scattering components and their effect on the material properties will be also considered.

Phantoms were stable over the duration of the testing (approximately one year). A more comprehensive longitudinal study would be performed in the future to assess the stability of the phantoms over experimentally relevant storage conditions. Here the phantoms were stored at room temperature and wrapped in plastic foil to prevent dust. This changed the reflection properties of the material, by not maintaining the surface smoothness of the copolymer-in-oil material. Further improvements in the storage conditions such as using glass plates will extend the temporal stability of the phantom. Besides, additional characterization measures will be performed to evaluate the tissue-mimicking characteristics of the PA-compatible phantom.

Recently, the emergence of multimodal imaging increases the need for phantoms that can be scanned using different imaging modalities. Although the mouse phantom was optimized for US-PA imaging, the phantom also effectively showed imaging compatibility in computer tomography (CT) and magnetic resonance imaging (MRI), presenting distinguishable features in all four modalities. Thus, the 3D-printed mouse phantom has the potential to produce realistic images representing various tissues and organs for multimodal imaging applications. In the future, we aim to optimize the mouse phantom as a multi-modal compatible phantom. Therefore, the established imaging modalities will be used to validate the newly developed tools for photoacoustic imaging. Even though some materials mimic accurately the tissue properties, they only do so for a specific imaging modality. Thus, it is difficult to identify materials suitable for all imaging modalities. However, this is a rapidly growing field that has great potential to achieve more versatile phantoms.

5. Conclusions

In summary, we established a standardized protocol for the design and fabrication of anthropomorphic heterogeneous tissue-mimicking phantoms compatible with photoacoustic imaging. Realistic phantoms enable to experimentally test newly developed methods, thus leading to higher chances of success in the in-vivo experiments. Here, we developed and

fabricated a phantom that mimics the detailed morphology of a mouse, including the skeleton and the main abdominal organs, using a combination of image modeling, copolymer-in-oil-based materials, and 3D-printing techniques. Besides, optical and acoustic properties, as well as the spectral and temporal stability of the phantom have been investigated in detail. Thus, this durable anthropomorphic mouse phantom would minimize animal experiments in compliance with the 3R principle as well as open many possibilities for advanced applications.

Acknowledgments

This publication is part of a project that has received funding from the European Union's Horizon 2020 research and innovation program under the Marie Sklodowska-Curie grant agreement No 811226. Further, we acknowledge the funding received through the EPSRC-ThUNDDAR network grant EP/N026942/1. We also acknowledge the funding obtained through Academy of Medical Sciences Springboard (REF: SBF007\100007) award.

References

[1] B. W. Pogue and M. S. Patterson, Review of tissue simulating phantoms for optical spectroscopy, imaging and dosimetry, *J. Biomed. Opt.*, vol. 11, no. 4, 2006. doi: 10.1117/1.2335429.

[2] L. C. Cabrelli, P. I. B. G. B. Pelissari, A. M. Deana, A. A. O. Carneiro, and T. Z. Pavan, Stable phantom materials for ultrasound and optical imaging, *Phys. Med. Biol.*, vol. 62, no. 2, 2017. doi: 10.1088/1361-6560/62/2/432.

[3] C. Li and L. V. Wang, Photoacoustic tomography and sensing in biomedicine, *Physics in Medicine and Biology*, vol. 54, no. 19. 2009. doi: 10.1088/0031-9155/54/19/R01.

[4] C. Kim, C. Favazza, and L. V. Wang, In vivo photoacoustic tomography of chemicals: High-resolution functional and molecular optical imaging at new depths, *Chem. Rev.*, vol. 110, no. 5, 2010. doi: 10.1021/cr900266s.

[5] W. C. Vogt, C. Jia, K. A. Wear, B. S. Garra, and T. Joshua Pfefer, Biologically relevant photoacoustic imaging phantoms with tunable optical and acoustic properties, *J.*

Biomed. Opt., vol. 21, no. 10, 2016. doi: 10.1117/1.jbo.21.10.101405.

[6] S. E. Bohndiek, S. Bodapati, D. Van De Sompel, S. R. Kothapalli, and S. S. Gambhir, Development and Application of Stable Phantoms for the Evaluation of Photoacoustic Imaging Instruments, *PLoS One*, vol. 8, no. 9, 2013. doi: 10.1371/journal.pone.0075533.

[7] D. I. Nikitichev, A. Barburas, K. McPherson, J. M. Mari, S. J. West, and A. E. Desjardins, Construction of 3-dimensional printed ultrasound phantoms with wall-less vessels, *J. Ultrasound Med.*, vol. 35, no. 6, 2016. doi: 10.7863/ultra.15.06012.

[8] F. Ratto *et al.*, Hybrid organosilicon/polyol phantom for photoacoustic imaging, *Biomed. Opt. Express*, vol. 10, no. 8, 2019. doi: 10.1364/boe.10.003719.

[9] J. R. Cook, R. R. Bouchard, and S. Y. Emelianov, Tissue-mimicking phantoms for photoacoustic and ultrasonic imaging, *Biomed. Opt. Express*, vol. 2, no. 11, 2011. doi: 10.1364/boe.2.003193.

[10] W. Xia, D. Piras, M. Heijblom, W. Steenbergen, T. G. van Leeuwen, and S. Manohar, Poly(vinyl alcohol) gels as photoacoustic breast phantoms revisited, *J. Biomed. Opt.*, vol. 16, no. 7, 2011. doi: 10.1117/1.3597616.

[11] A. Kharine *et al.*, Poly(vinyl alcohol) gels for use as tissue phantoms in photoacoustic mammography, *Phys. Med. Biol.*, vol. 48, no. 3, 2003. doi: 10.1088/0031-9155/48/3/306.

[12] S. L. Vieira, T. Z. Pavan, J. E. Junior, and A. A. O. Carneiro, Paraffin-Gel Tissue-Mimicking Material for Ultrasound-Guided Needle Biopsy Phantom, *Ultrasound Med. Biol.*, vol. 39, no. 12, 2013. doi: 10.1016/j.ultrasmedbio.2013.06.008.

[13] E. Maneas *et al.*, Gel wax-based tissue-mimicking phantoms for multispectral photoacoustic imaging, *Biomed. Opt. Express*, vol. 9, no. 3, 2018. doi: 10.1364/boe.9.001151.

[14] E. Zhang, J. Laufer, and P. Beard, Backward-mode multiwavelength photoacoustic

scanner using a planar Fabry-Perot polymer film ultrasound sensor for high-resolution three-dimensional imaging of biological tissues, *Appl. Opt.*, vol. 47, no. 4, 2008. doi: 10.1364/AO.47.000561.

[15] G. M. Spirou, A. A. Oraevsky, I. Alex Vitkin, and W. M. Whelan, Optical and acoustic properties at 1064 nm of polyvinyl chloride-plastisol for use as a tissue phantom in biomedical optoacoustics, *Phys. Med. Biol.*, vol. 50, no. 14, 2005. doi: 10.1088/0031-9155/50/14/N01.

[16] C. D. Nguyen *et al.*, Investigation of silk as a phantom material for ultrasound and photoacoustic imaging, *Photoacoustics*, vol. 28, p. 100416, Dec. 2022. doi: 10.1016/j.pacs.2022.100416.

[17] L. C. Cabrelli, F. W. Grillo, D. R. T. Sampaio, A. A. O. Carneiro, and T. Z. Pavan, Acoustic and Elastic Properties of Glycerol in Oil-Based Gel Phantoms, *Ultrasound Med. Biol.*, vol. 43, no. 9, 2017. doi: 10.1016/j.ultrasmedbio.2017.05.010.

[18] L. C. Cabrelli, J. H. Uliana, L. B. Da Cruz Junior, L. Bachmann, A. A. O. Carneiro, and T. Z. Pavan, Glycerol-in-SEBS gel as a material to manufacture stable wall-less vascular phantom for ultrasound and photoacoustic imaging, *Biomed. Phys. Eng. Express*, vol. 7, no. 6, 2021. doi: 10.1088/2057-1976/ac24d6.

[19] L. Hacker *et al.*, A copolymer-in-oil tissue-mimicking material with tuneable acoustic and optical characteristics for photoacoustic imaging phantoms, *IEEE Trans. Med. Imaging*, 2021. doi: 10.1109/tmi.2021.3090857.

[20] S. Bohndiek, Addressing photoacoustics standards, *Nature Photonics*, vol. 13, no. 5. 2019. doi: 10.1038/s41566-019-0417-3.

[21] J. Palma-Chavez, T. J. Pfefer, A. Agrawal, J. V. Jokerst, and W. C. Vogt, Review of consensus test methods in medical imaging and current practices in photoacoustic image quality assessment, *J. Biomed. Opt.*, vol. 26, no. 09, 2021. doi: 10.1117/1.jbo.26.9.090901.

[22] F. Zhang *et al.*, Design and fabrication of a personalized anthropomorphic phantom using 3D printing and tissue equivalent materials, *Quant. Imaging Med. Surg.*, vol. 9, no. 1, 2019. doi: 10.21037/qims.2018.08.01.

[23] M. Dantuma, S. Kruitwagen, J. Ortega-Julia, R. P. Pompe van Meerdervoort, and S. Manohar, Tunable blood oxygenation in the vascular anatomy of a semi-anthropomorphic photoacoustic breast phantom, *J. Biomed. Opt.*, vol. 26, no. 03, 2021. doi: 10.1117/1.jbo.26.3.036003.

[24] M. Dantuma, R. van Dommelen, and S. Manohar, Semi-anthropomorphic photoacoustic breast phantom, *Biomed. Opt. Express*, vol. 10, no. 11, p. 5921, 2019. doi: 10.1364/boe.10.005921.

[25] G. Quarto, A. Pifferi, I. Bargigia, A. Farina, R. Cubeddu, and P. Taroni, Recipes to make organic phantoms for diffusive optical spectroscopy, *Appl. Opt.*, vol. 52, no. 11, 2013. doi: 10.1364/AO.52.002494.

[26] B. Dogdas, D. Stout, A. F. Chatziioannou, and R. M. Leahy, Digimouse: A 3D whole body mouse atlas from CT and cryosection data, *Phys. Med. Biol.*, vol. 52, no. 3, 2007. doi: 10.1088/0031-9155/52/3/003.

[27] S. E. Bohndiek *et al.*, IPASC: A community-driven consensus-based initiative towards standardisation in photoacoustic imaging, in *IEEE International Ultrasonics Symposium, IUS*, 2020, vol. 2020-September. doi: 10.1109/IUS46767.2020.9251362.

[28] AIUM Technical Standards Committee. “Methods for specifying acoustic properties of tissue mimicking phantoms and objects.” Laurel, MD, USA: American Institute of Ultrasound in Medicine (1995)..

[29] Y. Liu and S. Maruvada, Development and characterization of polyurethane-based tissue and blood mimicking materials for high intensity therapeutic ultrasound, *J. Acoust. Soc. Am.*, vol. 151, no. 5, pp. 3043–3051, May 2022. doi: 10.1121/10.0010385.

[30] W. Sachse and Y. H. Pao, On the determination of phase and group velocities of

595 dispersive waves in solids, *J. Appl. Phys.*, vol. 49, no. 8, 1978. doi: 10.1063/1.325484.

596 [31] J. Mobley, J. N. Marsh, C. S. Hall, M. S. Hughes, G. H. Brandenburger, and J. G. Miller,
597 Broadband measurements of phase velocity in Albunex® suspensions, *J. Acoust. Soc.*
598 *Am.*, vol. 103, no. 4, 1998. doi: 10.1121/1.421360.

599 [32] S. Rajagopal, N. Sadhoo, and B. Zeqiri, Reference Characterisation of Sound Speed and
600 Attenuation of the IEC Agar-Based Tissue-Mimicking Material Up to a Frequency of
601 60MHz, *Ultrasound Med. Biol.*, vol. 41, no. 1, 2015. doi:
602 10.1016/j.ultrasmedbio.2014.04.018.

603 [33] J. L. Raymond, R. O. Cleveland, and R. A. Roy, HIFU-induced changes in optical scattering
604 and absorption of tissue over nine orders of thermal dose, *Phys. Med. Biol.*, vol. 63, no.
605 24, 2018. doi: 10.1088/1361-6560/aaed69.

606 [34] S. A. Prahl, M. J. C. van Gemert, and A. J. Welch, Determining the optical properties of
607 turbid media by using the adding–doubling method, *Appl. Opt.*, vol. 32, no. 4, 1993.
608 doi: 10.1364/ao.32.000559.

609 [35] A. Needles *et al.*, Development and initial application of a fully integrated
610 photoacoustic micro-ultrasound system, *IEEE Trans. Ultrason. Ferroelectr. Freq.*
611 *Control*, 2013. doi: 10.1109/TUFFC.2013.2646.

612 [36] E. Betzig, Proposed method for molecular optical imaging, *Opt. Lett.*, vol. 20, no. 3,
613 1995. doi: 10.1364/ol.20.000237.

614 [37] G. P. Luke, S. Y. Nam, and S. Y. Emelianov, Optical wavelength selection for improved
615 spectroscopic photoacoustic imaging, *Photoacoustics*, vol. 1, no. 2, pp. 36–42, 2013.
616 doi: 10.1016/j.pacs.2013.08.001. http://dx.doi.org/10.1016/j.pacs.2013.08.001

617 [38] F. A. Duck, *Physical Properties of Tissue. A Comprehensive Reference Book*, vol. 18, no.
618 4. 1990.

619 [39] J. L. Sandell and T. C. Zhu, A review of in-vivo optical properties of human tissues and

its impact on PDT, *J. Biophotonics*, vol. 4, no. 11–12, 2011. doi: 10.1002/jbio.201100062.

[40] S. L. Jacques, Optical properties of biological tissues: A review, *Physics in Medicine and Biology*, vol. 58, no. 11. 2013. doi: 10.1088/0031-9155/58/11/R37.

[41] B. Cox, J. G. Laufer, S. R. Arridge, and P. C. Beard, Quantitative spectroscopic photoacoustic imaging: a review, *J. Biomed. Opt.*, 2012. doi: 10.1117/1.jbo.17.6.061202.

[42] S. Tzoumas, N. Deliolanis, S. Morscher, and V. Ntziachristos, Unmixing molecular agents from absorbing tissue in multispectral optoacoustic tomography, *IEEE Trans. Med. Imaging*, vol. 33, no. 1, 2014. doi: 10.1109/TMI.2013.2279994.

Chapter 5

Superpixel spectral unmixing framework for the volumetric assessment of tissue chromophores: A photoacoustic data-driven approach*

Abstract:

In this chapter, we have developed a superpixel spectral photoacoustic unmixing (SPAX) approach that can detect the most and less prominent absorber spectra and their volumetric distribution without any user interactions. Within the SPAX framework, we have also implemented an advanced spectral coloring compensation approach by utilizing US image segmentation and Monte Carlo light fluence simulations, based on a predefined library of tissue optical properties. The framework has been tested on tissue-mimicking phantoms and also on healthy animals.

*This chapter has been published as: **Grasso, V.**, Willumeit-Römer, R., & Jose, J. (2022). *"Superpixel spectral unmixing framework for the volumetric assessment of tissue chromophores: A photoacoustic data-driven approach."* Photoacoustics, 26, 100367.

Photoacoustics 26 (2022) 100367

Contents lists available at ScienceDirect

Photoacoustics

journal homepage: www.elsevier.com/locate/pacs

Superpixel spectral unmixing framework for the volumetric assessment of tissue chromophores: A photoacoustic data-driven approach

Valeria Grasso [a,b], Regine Willumeit-Römer [b,c], Jithin Jose [a,*]

[a] FUJIFILM VisualSonics, Amsterdam, the Netherlands
[b] Faculty of Engineering, Institute for Materials Science, Christian-Albrecht University of Kiel, Kiel, Germany
[c] Division Metallic Biomaterials, Institute of Materials Research, Helmholtz-Zentrum Hereon GmbH, Geesthacht, Germany

ARTICLE INFO

Keywords:
Blind source separation
Photoacoustic
Spectral coloring
Spectral imaging
Ultrasound
Unsupervised machine learning

ABSTRACT

The assessment of tissue chromophores at a volumetric scale is vital for an improved diagnosis and treatment of a large number of diseases. Spectral photoacoustic imaging (sPAI) co-registered with high-resolution ultrasound (US) is an innovative technology that has a great potential for clinical translation as it can assess the volumetric distribution of the tissue components. Conventionally, to detect and separate the chromophores from sPAI, an input of the expected tissue absorption spectra is required. However, in pathological conditions, the prediction of the absorption spectra is difficult as it can change with respect to the physiological state. Besides, this conventional approach can also be hampered due to spectral coloring, which is a prominent distortion effect that induces spectral changes at depth. Here, we are proposing a novel data-driven framework that can overcome all these limitations and provide an improved assessment of the tissue chromophores. We have developed a superpixel spectral unmixing (SPAX) approach that can detect the most and less prominent absorber spectra and their volumetric distribution without any user interactions. Within the SPAX framework, we have also implemented an advanced spectral coloring compensation approach by utilizing US image segmentation and Monte Carlo simulations, based on a predefined library of optical properties. The framework has been tested on tissue-mimicking phantoms and also on healthy animals. The obtained results show enhanced specificity and sensitivity for the detection of tissue chromophores. To our knowledge, this is a unique framework that accounts for the spectral coloring and provides automated detection of tissue spectral signatures at a volumetric scale, which can open many possibilities for translational research.

1. Introduction

The non-invasive assessment of molecular tissue components plays an essential role to facilitate improved medical diagnosis and treatment monitoring. In the past decade, there has been a clear emphasis to monitor physiological and pathological changes in a volumetric vision instead of specific 2-dimensional (2D) planar views of the respective organs [1]. Thus, most of the recent developments in pre-clinical imaging are evolving in the direction of whole-body visualization. This enables the systemic follow-up of disease progression and also the visualization of multiple organs, by promoting the reduction and refinement of laboratory animals [2]. Many established tomographic imaging modalities facilitate whole-body imaging in pre-clinical studies. Although these imaging techniques are widely used, they also have some drawbacks. For example, preclinical MRI suffers from long acquisition time and expensive hardware to attain a homogeneous magnetic field to guarantee high spatial resolution [3,4]. Other alternatives, such as X-ray, CT [5,6], and PET [7] use ionizing radiation that can lead to undesired side effects in longitudinal studies [8].

Optical imaging modalities, such as fluorescence [9] and bioluminescence [10], represent a radiation-free option that enables whole-body imaging [11]. Further optical imaging modalities, such as optical coherence tomography [12,13], diffuse optical tomography [14,15], and hyperspectral imaging [16,17] have been investigated in pre-clinical research and also translated towards clinical applications [18–20]. Although optical imaging technologies are promising in monitoring molecular information due to their high sensitivity, most of these approaches suffer from lower spatial resolution and imaging depth [21].

The hybrid imaging techniques that combine complementary

* Corresponding author.
E-mail addresses: valeria.grasso@fujifilm.com (V. Grasso), regine.willumeit@hereon.de (R. Willumeit-Römer), jithin.jose@fujifilm.com (J. Jose).

https://doi.org/10.1016/j.pacs.2022.100367
Received 6 March 2022; Received in revised form 4 May 2022; Accepted 6 May 2022
Available online 11 May 2022

modalities, represent the ideal solution to mitigate these limitations of imaging depth and spatial resolution. Recently, different combinations such as optical-CT, PET-CT, PET-MRI, and Ultrasound-Photoacoustic (US-PA), have been integrated to facilitate multimodal information of the tissues [22]. The combination of US-PA is a hybrid technique as it can simultaneously provide the anatomical, functional, and molecular information of the tissue of interest.

Photoacoustic (PA) is a non-ionizing technology that is based on laser-induced ultrasound waves [23–25]. In PA, near-infrared (NIR) pulsed laser light is used for tissue excitation. The optical energy absorption induces tissue thermoelastic expansion that leads to the generation of acoustic signals, which can be detected just as conventional ultrasound. Since ultrasound scattering in biological tissues is almost three orders lower than optical scattering, US-PA guarantees higher spatial resolution and imaging depth (up to several *cm*) as compared to pure optical techniques [26].

In photoacoustic the signal generation is proportional to the optical absorption contrast. Thus, illuminating the tissues at different wavelengths enables the detection of molecular tissue constituents. Particularly, since tissue chromophores have distinct spectral absorption signatures, spectroscopic PA imaging is intrinsically sensitive to detect biomarkers, endogenous, and exogenous contrast agents [27]. Recently, spectral photoacoustic imaging (sPAI) has shown potential for a wide range of applications such as tumor theranostics, oxygen saturation imaging, atherosclerotic plaque detection, and the imaging of sentinel lymph nodes [28–33].

Linear spectral unmixing is a commonly used method to differentiate specific tissue components from sPAI [34]. This is a fitting-based method to unmix the spectra, therefore it requires the user interaction to input the expected tissue chromophores. In the case of disease conditions, these types of supervised spectral unmixing can be challenging, as the actual absorption spectra of the chromophores could differ from the theoretical curves [35].

A highly sensitive spectral unmixing method that can accurately distinguish all the molecular tissue components, without any user interactions, is auspicious. Unsupervised Machine Learning (ML) approaches such as Principal Component Analysis (PCA), Independent Component Analysis (ICA), Vertex Component Analysis, and Non-negative Matrix Factorization (NNMF) are label-free methods that extract characteristic components in a data-driven way [36,37]. On the other hand, various neural network architectures have been also proposed to automatically unmix oxy- and deoxy- hemoglobin spectra, by utilizing large training datasets of sPAI [38]. Generally, these algorithms follow an iterative optimization procedure that minimizes the cost function. Besides, the strong PA signal from the oxy/deoxy hemoglobin can obscure the presence of less prominent components, such as lipids and collagen, leading to incomplete identification of tissue constituents. Thus, if the majority of the observed pixels contain high absorbing tissue components, there is a significant probability that the less prominent absorbers are discarded in the iterative optimization, as the spectra of these can be overlapped. Hence, these approaches mainly detect the most prominent absorbers, such as melanin and oxy/deoxy hemoglobin [39].

Spectral coloring effect is a known artifact, that plays a crucial role in the sensitivity and specificity of tissue biomarkers detection and thus limits the current translational research applications. This is a corruption effect that alters the spectrum of the incident light along the tissue heterogeneity at depth and consequently leads to misinterpretations of the absorption spectrum shape of the tissue components [40]. Specifically, due to light fluence attenuation along the depth, it is difficult to retrieve the actual absorption fingerprint of the tissue components from sPAI. For example, the same absorber at different depths might show a diverse absorption spectrum as the absorbed light is different. To compensate for the light fluence variations along the depth, pre-defined simulations can be used, but this approach is also complex as it requires detailed information about the tissue to be imaged [41]. Recently, Tzoumas et al. [42] have proposed an eigenspectra-based fluence correction approach and automatically estimated the blood oxygen saturation (SO_2) in deep tissue. Their proposed approach is based on fluence modeling through the eigenspectra analysis which is mainly used to compensate for SO_2. Hence, it is still challenging to automatically and accurately extract multiple molecular components, such as prominent and weaker tissue absorbers, from sPAI.

In this work, we developed a novel data-driven superpixel PA unmixing (SPAX) framework to enable the differentiation of molecular tissue components, without any user interactions. The framework is also extended to compensate for the spectral coloring artifact. To compensate for the spectral coloring we are proposing an automated US image segmentation and spectral Monte Carlo (MC) light fluence simulations based on a predefined library of tissue optical properties. The approach is also optimized for the volumetric assessments of tissue composition. Besides, it includes an optimized visualization of the molecular components' distribution with unprecedented details. This is a unique data processing procedure, that differentiates the SPAX framework from the other spectral unmixing algorithms. We benchmarked the sensitivity and accuracy of the proposed approach on tissue-mimicking phantoms, volumetric tissue composition, and also on whole-body animal imaging.

2. Material and methods

2.1. Theoretical background

In photoacoustic (PA), nanosecond pulsed laser light is used as an excitation source, causing thermoelastic expansion of the tissues. The corresponding initial pressure distribution leads to the generation of acoustic waves that propagate toward the ultrasound (US) detectors. Therefore, the reconstructed PA image is a spatial representation of the initial pressure distribution $p_0(\vec{r},\lambda)$ defined as follows:

$$p_0(\vec{r},\lambda) = \Gamma(\vec{r})\mu_a(\vec{r},\lambda)\Phi(\vec{r},\lambda;\mu_a,\mu_s,g) \tag{1}$$

where $\vec{r}$ represents the spatial coordinates of the voxel, λ is the wavelength, μ_a is the optical absorption coefficient, μ_s is the scattering coefficient, g is the optical anisotropy factor, Γ is the Grüneisen parameter, and Φ is the light fluence. As established by Eq. (1) the initial pressure distribution $p_0(\vec{r},\lambda)$ depends on the wavelength of excitation λ and the fluence Φ. During spectroscopic photoacoustic imaging (sPAI), the intensity of each pixel at different wavelengths is proportional to the absorption spectrum of a combination of tissue components $p_0(\vec{r},\lambda_i) \approx \mu_a(\vec{r},\lambda_i)$, where $\lambda_i \in \{\lambda_i,\ldots,\lambda_N\}$ and N is the total number of wavelengths of the excitation light. This is a low-rank approximation of the sPAI. Hence, the pixels intensity of the sPAI and consequently the underlying initial pressure distribution can be represented as:

$$\begin{bmatrix} p_0(\vec{r},\lambda_1) \\ \vdots \\ p_0(\vec{r},\lambda_N) \end{bmatrix} \approx \begin{bmatrix} \mu_a(\vec{r},\lambda_1) \\ \vdots \\ \mu_a(\vec{r},\lambda_N) \end{bmatrix} \xrightarrow[\lambda_i \in \{\lambda_1,\ldots,\lambda_N\}]{} \begin{bmatrix} \varepsilon_{c_1}^{\lambda_1} & \cdots & \varepsilon_{c_q}^{\lambda_1} \\ \vdots & \ddots & \vdots \\ \varepsilon_{c_1}^{\lambda_N} & \cdots & \varepsilon_{c_q}^{\lambda_N} \end{bmatrix} \begin{bmatrix} [C_1] \\ \vdots \\ [C_q] \end{bmatrix} \tag{2}$$

where q is the number of distinct dominant absorbers, $[C_1],\ldots,[C_q]$ represent the concentrations of the different components, and $\varepsilon_{C_1}^{\lambda_i},\ldots,\varepsilon_{C_q}^{\lambda_i}$ are the molar extinction coefficients of the components, $\forall\lambda_i$, where $i \in \{1,\ldots,N\}$.

In a Linear Mixture Model (LMM), the sPAI can be formalized as:

$$X \approx WH \tag{3}$$

where $X \in \mathbb{R}^{p\times N}$ is the mixture matrix of p observations and N variables. X contains per each column the vectored PA image at a specific wavelength. The matrices $W \in \mathbb{R}^{p\times q}$ and $H \in \mathbb{R}^{q\times N}$contain the abundance maps and the absorption spectra of q source components, respectively.

As described by Li et al. [43] the conventional approach to solve Eq.

(3) is to input the source spectra H as *a priori* information. Besides, blind source separation algorithms [44] can also be used to iteratively solve Eq. (3), where both H and W are unknown variables.

2.2. Superpixel Photoacoustic Unmixing (SPAX) framework

Fig. 1 shows the flowchart of the SPAX framework. Each procedure within the framework has been implemented and refined in order to minimize the user interaction. A detailed description of the SPAX framework procedures is provided below.

2.2.1. Input data

The high-resolution ultrasound (US) and multi-spectral photoacoustic images (sPAI), within the wavelength range of $680 - 970nm$,

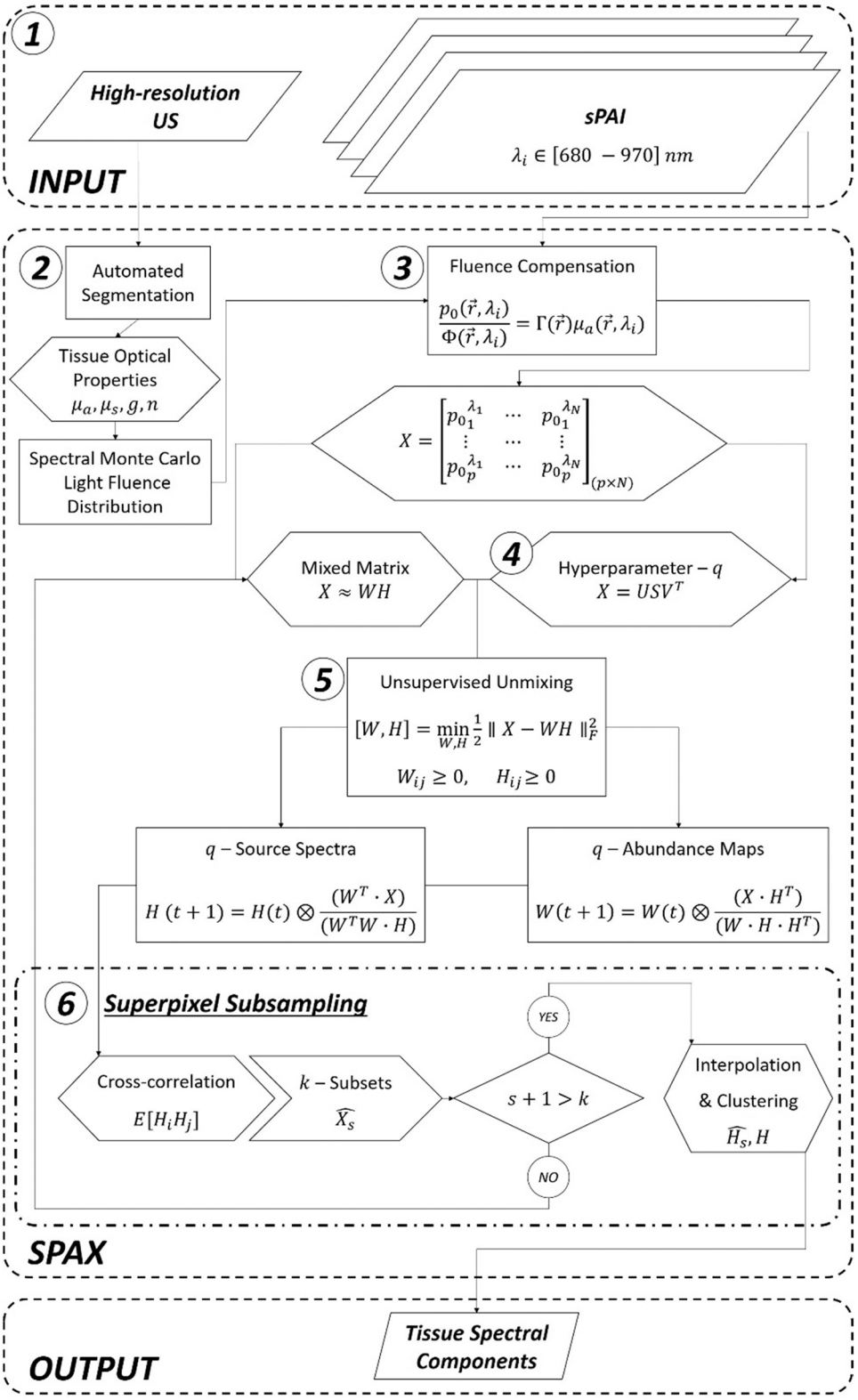

Fig. 1. Flowchart of the Superpixel Photoacoustic Unmixing (SPAX) Framework. The numbers $(1 - 6)$represent the sequence of procedures implemented within the SPAX framework. Symbols legend: λ_i: light wavelength; μ_a: absorption coefficient; μ_s: scattering coefficient; g: anisotropy coefficient; n: refractive index; p_0: initial pressure; $\vec{r}$: spatial coordinates; Φ: light fluence; Γ: Grüneisen parameter; X: mixture matrix; p: number of observations; N: number of variables; W : abundance maps; H: source spectra; U: left-eigenvectors; S: eigenvalues; V: right-eigenvectors; q: number of endmembers; $E[H_i H_j]$: cross-correlation; $\widehat{X_s}$: mixed subset; k: number of mixed subsets; $\widehat{H_s}$: source spectra of $\widehat{X_s}$.

represent the input of the proposed SPAX framework.

2.2.2. Automated segmentation

An automated segmentation approach that differentiates various tissue structures has been implemented to guide the light fluence compensation. Within this approach by utilizing the high-resolution US images, the skin line, tissue structures, and coupling medium can be detected. Specifically, the skin-line boundary was automatically obtained by determining a threshold from the ditch of the gradient histogram of the US image. After thresholding the US image, the Sobel filter is applied as edge detection method for finding the tissue boundaries. Thus, the detected skin line is then used as a watershed to distinguish the tissue structures and the background. Besides, in the case of phantom imaging, circular inclusions can be recognized by using the Hough Transform, which results in fully-automated segmentation.

Once segmented, the images are labeled and tagged with optical properties gathered from literature in terms of absorption and scattering [45–48]. Thus, each cluster is linked with the spectral optical properties collected in a predefined library. This predefined collection of spectral optical properties of the tissue components is provided in detail in the Supplementary Materials (see Supplementary Materials; SupMatTable). The tissue optical properties values have been retrieved from literature at each wavelength of the sPAI acquisition. For exogenous agents, the absorption characteristics have been measured *via* spectrophotometer and the scattering properties were evaluated according to the concentration of the pigments by following the Mie scattering theory [49]:

$$\mu_s = \frac{2 \bullet 0.016}{\lambda^{2.4}} C;\ \mu_s' = \mu_s(1-g);\ g(\lambda) = 1.1 - 0.58\lambda \tag{4}$$

where μ_s denotes the scattering coefficient in mm^{-1}, λ is the wavelength of the light in μm, C is the concentration in mL/L, μ_s' is the reduced scattering coefficient, and g is the anisotropy factor approximated by Eq. (4).

2.2.3. Fluence compensation

After the segmentation, the light fluence correction step has been incorporated into the SPAX framework. The light fluence distribution was simulated with MCXLAB [50] at each wavelength of light used during the sPAI acquisition. Fluence simulations were run with 10^9 photons, all launched isotropically at each wavelength, and voxel linear length of $0.3mm$. Although in the experiments we are using a double-side illumination as a light source, the two beams are converging, and thus guarantee a uniform illumination at the surface. Since during the US-PA image acquisition, we are normally positioning the surface of the sample/animal close to this converging point, we could approximate the light source as a truncated Gaussian beam in the simulations. Thus, the excitation light source was set as a truncated Gaussian beam with a waist radius of 200 voxels, with its center on the top of the skin line. The fluence map is obtained by integrating the flux output from MCXLAB over time, using time steps of $0.01ns$ for a total range of $50ns$. The light fluence distribution has been simulated in 2D per each slice of the volumetric domain. Finally, since the same energy has been used at each wavelength to attain the fluence in each voxel, this is normalized to the total energy from the light source. Thus, the obtained fluence maps were normalized and the results have been interpolated to render and match the volumetric imaging domain.

2.2.4. Automatic estimation of the hyperparameter

Singular Value Decomposition (SVD) is implemented to estimate the number of significant components, named hyperparameter (q), by inspecting the mixed sPAI data along orthogonal directions. The automatic tune of the rank hyperparameter is crucial to have an unbiased characterization of the tissue composition. In particular, the SVD method enables to determine and sort the directions along which the variables exhibit higher variation, which represents the low-rank approximation of the original data [51]. To estimate the number of significant components, the so-called elbow method has been applied [52]. Thus, the mixed sPAI matrix X, which is also described as a linear mixture in Eq. (3), is expressed as $X = USV^T$, where U and V are matrices of the left- and right-eigenvectors respectively. S is the diagonal matrix of eigenvalues in decreasing order. The gradient operation has been applied to the eigenvalues to determine the "elbow". By interpolating the eigenvalues after the elbow with linear fitting, the noise level is defined. We selected the SNR $2:1$ as a watershed to automatically distinguish the relevant information above the defined noise level. Consequently, all the eigenvalues that have SNR higher than $2:1$ are selected and thus it defines the actual number of endmembers q.

2.2.5. Unsupervised unmixing of prominent absorbers

The unsupervised unmixing of the prominent absorbers is based on a modified and optimized version of Non-negative Matrix Factorization (NNMF). This approach recognizes an initial set of underlying highly absorbing molecular components, such as oxy/deoxy hemoglobin. Thus, q source spectra (H) and the respective abundance maps (W) are obtained. The details of the optimized NNMF algorithm are described in our previous work [53].

2.2.6. Superpixel subsampling

After the unmixing of the prominent absorbers, to differentiate the less prominent molecular components, a novel spectral superpixel subsampling (SS) approach has been implemented and integrated within the SPAX framework. In this procedure, we further analyze the spectra H and the respective distribution pixels W, where there is an overlapping of the prominent absorbers. A detailed workflow of the superpixel subsampling procedure is provided and described below.

SS-Step1: Cross-correlation of the source components H. To select the overlapping wavelengths and pixels a cross-correlation is performed between all the prominent detected spectra H, obtained from 2.2.5. The cross-correlation matrix $E[H_iH_j]$, where $i, j \in \{1, \ldots, q\}$, is symmetric. The correlation coefficients can range from -1 to 1, with 0 representing no correlation, -1 and 1 representing a direct negative or positive correlation respectively.

SS-Step 2: Subsampling. Each matching pair of spectra (H_iH_j) with a positive correlation ($E[H_iH_j] > 0$) is analyzed in detail and the wavelengths in which the components have similar intensity are selected for further analysis.

In addition to the spectral analysis, the abundance maps (W_iW_j) obtained from 2.2.5 of the positively correlated components were also further analyzed. A pixel-to-pixel intensity comparison is performed between the respective abundance maps. A kernel of dimension three around each pixel is used to determine the pixels' average used as a threshold. The pixels with similar intensities, which are above the threshold have been selected. In this way, subgroups of meaningful wavelengths and pixels are obtained for further analysis.

In particular, by using the subgroup of wavelengths and pixels, a reduced subset ($\widehat{X_s}$) is created from the original raw dataset (X). Where $s \in \{1, \ldots, k\}$ and k represents the number of positively correlated components.

SS-Step 3: Subsets Unmixing. To detect less prominent absorbers, per each subset $\widehat{X_s}$, the unmixing procedures 2.2.4 and 2.2.5 are reiterated till the process converges. Thus, per each subset $\widehat{X_s}$, after SVD and NNMF a subgroup of spectral components $\widehat{H_s}$ is obtained. This procedure is repeated till all the k subsets have been analyzed and thus the condition $s+1 > k$ is verified.

SS-Step 4: Interpolation & Clustering. The spectral components $\widehat{H_s}$, obtained from each reduced subset $\widehat{X_s}$, are linearly interpolated to have the original number N of variables/wavelengths. Finally, *k-means* clustering approach was used to classify all the detected source components H and resized $\widehat{H_s}$, obtained from the original mixture X and all

the subsets $\widehat{X_s}$ respectively.

Further details of the superpixel subsampling data processing, with an example, are provided in Section 3.2.

2.2.7. Output data

Finally, the tissue spectral components are extracted in an unsupervised way from sPAI. A comparison with the reference absorption spectra known from the literature [47] has been performed. Thus, some of the endogenous tissue chromophores, such as oxy/deoxy hemoglobin, and fat can be recognized. Especially in the case of disease models, there is also a good chance to detect additional spectra that are unknown and that cannot be compared with spectra from the literature used as a reference. The increased number of automatically extracted spectra demonstrates the higher sensitivity of the proposed approach to reveal any spectral feature.

Besides the spectral components, the respective distribution maps have been also obtained and refined to enhance the vessel structures by using the Frangi filter [54].

2.3. Data acquisition

High-resolution Ultrasound (US) and spectral Photoacoustic imaging (sPAI) have been acquired by using the platform Vevo LAZR-X (FUJIFILM VisualSonics, Inc., Toronto, ON, Canada). The imaging setup includes a high-frequency US system (Vevo 3100), an optical parametric oscillator (OPO) integrated Nd:YAG nanosecond pulsed laser, and the animal imaging platform. The US system is equipped with a linear US transducer array (MX201) that consists of 256 elements at a nominal center frequency of $15MHz$ and bandwidth of $10-22MHz$. This transducer guarantees an axial and lateral resolution of $100\mu m$ and $220\mu m$ respectively. Light from the laser is delivered to the tissue through optical fibers, mounted on either side of the transducer. To obtain the homogenous light illumination, the sample to be imaged is placed on the converging area of the two light beams. The repetition rate of the laser is $20Hz$, and the spectral photoacoustic images can be acquired by tuning the laser wavelengths within the range of $680-970nm$. The system allows the selection of any wavelength within this NIR range. In particular, for the experiments, we have used a step size of $5nm$ between the wavelengths to acquire the spectral PA images.

During volumetric US-PA acquisitions, a stepper motor is used for the linear translation of the US transducer and optical fibers along the sample. The linear stepper motor moves in steps of a minimum of $0.1mm$ while capturing 2-D parallel images, for a maximum 3D range distance of $6.4cm$. The voxel size used for the reconstructed US and PA imaging was $(0.062\times 0.051\times 0.3)mm$. A modified animal setup (see Supplementary Materials; SupMatFig) has been used for the whole-body sPAI acquisition. A small water container with an optically and acoustically transparent thin polyurethane membrane was used to guarantee the optimal acoustic coupling during the acquisitions. The water temperature was kept at 34°C. During the whole-body acquisitions, the stepper motor translated along the animal body from cranial to caudal in steps of $0.3mm$. The configuration in epi-illumination, the ECG monitoring, and the respiratory gating have been maintained during all the *in vivo* whole-body experiments.

2.4. Experimental validation

The SPAX framework has been tested and validated by using tissue-mimicking phantoms and *in vivo* experiments.

2.4.1. Agarose phantom

The spectral coloring compensation approach included within the SPAX framework has been tested on a phantom made from agarose. The schematic illustration of the phantom is depicted in Fig. 2 (A). This includes two absorbers secured into a 3D printed chamber, fixed at $18mm$ and $28mm$ from the transducer. The inclusions have been fabricated by mixing native gel wax (FF1 003, Mindsets Online, Waltham Cross, UK) with $0.05\%w/v$ of black oil color (Winsor & Newton, London, UK) as described elsewhere [55]. The bulk material of the phantom is made of $1.5\%w/v$ Agar (Alfa Aesar, Heysham, Lancaster), mixed with Intralipid (IL) (20%, Sigma-Aldrich, Canada) and Verdye (Diagnostic Green GmbH, Aschheim, Germany). A $1:2$ dilution of Verdye $0.03\%w/v$ and IL $2\%w/v$ have been used to achieve the absorption as $\mu_a = 0.15cm^{-1}$ and the scattering as $\mu_s' = 5cm^{-1}$ of the bulk material (Agar-IL-Verdye).

The absorption spectra of Verdye and Black ink were optically characterized with the spectrophotometer and the results were shown in Fig. 2 (B). The black ink used for the inclusions shows a broad absorption spectrum while the Verdye included in the bulk material has a characteristic spectrum with an absorption peak at $880nm$. The spectral optical properties of the phantom absorber materials are reported in Supplementary Materials (see Supplementary Materials; SupMatTable) and these were used to set the Monte Carlo fluence simulations. In addition, water has been used as a coupling material to fill $15mm$ depth between the solid phantom and the US transducer.

2.4.2. Tissue phantom

A tissue phantom is used to evaluate the detection of multi-spectral components by SPAX framework. The phantom combines endogenous muscle-fat tissue layers and exogenous inclusions with different absorption characteristics. The advantage of this approach is that this tissue phantom offers good approximations of realistic samples. A schematic illustration of the phantom is depicted in Fig. 3 (A). The phantom was prepared by using a muscle layer from veal meat of $15mm$

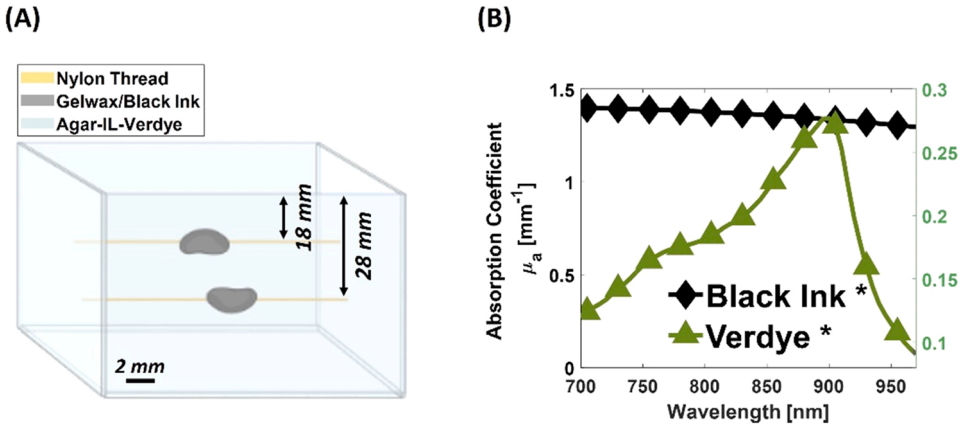

Fig. 2. Schematic of the agarose phantom (A); Absorption spectra of Verdye and Black Ink measured by spectrophotometer (B).

81

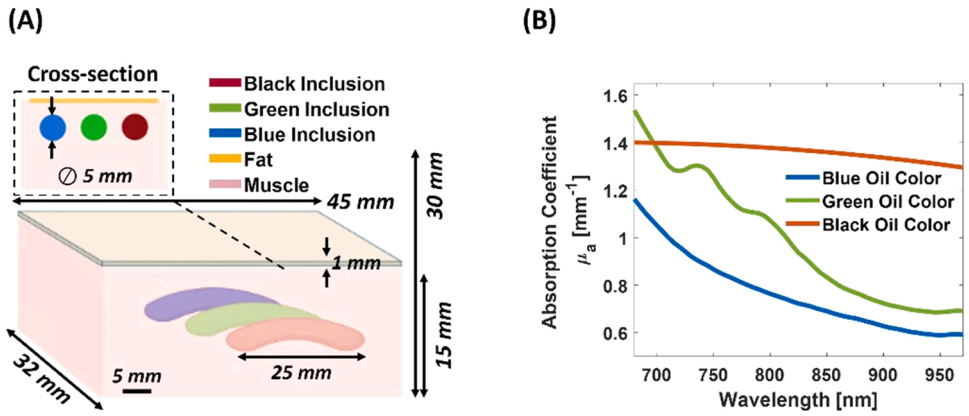

Fig. 3. Schematic of the muscle-fat tissue phantom (A); Absorption spectra of Blue, Green, and Black oil colors measured by spectrophotometer (B).

thickness. The tissue was selected to contain pure and untreated muscle tissue and not blood. Three cylindrical absorbers have been embedded within the muscle tissue. The cylindrical inclusions have been prepared by mixing gel wax (FF1 003, Mindsets Online, Waltham Cross, UK) with three different oil colors (Winsor & Newton, London, UK). Specifically, 0.05%w/v of black, green, and blue oil colors have been mixed with melted gel wax respectively. Finally, these have been poured into 3D printed cylindrical curved molds, used to shape the three inclusions (see Fig. 3 (A)). The absorption spectra of the oil colors have been measured *via* spectrophotometer and reported in Fig. 3 (B). Besides, a 1*mm* thick fat layer, from porcine lard, has been embedded on top of the muscle layer. Thus, the tissue phantom is composed of multiple components: the cylindrical inclusions that are prominent absorbers and the fat layer that has less prominent absorption characteristics. Water has been used as a coupling medium during the US-PA imaging acquisition to fill 15*mm* depth between the phantom and the US transducer.

2.4.3. *In vivo experiments*

The *in vivo* experiments were conducted at FUJIFILM Sonosite/VisualSonics facility in Amsterdam, The Netherlands. All the experiments involving animals were in full compliance with the protocol (*AVD2450020173644*) evaluated and approved by the Animal Use and Ethics Committee (CEUA) of The Netherlands. These were in accordance with FELASA guidelines and the National Law for Laboratory Animal Experimentation (*Law No.18.611*). For the hindlimb and whole-body imaging, a female CD-1 mouse model (Envigo, Horst, the Netherlands) and athymic nude-Foxn1nu mice (Envigo, Horst, the Netherlands) were used respectively. Mice were anesthetized with isoflurane (2%–3% by volume with 0.8l/min gas flow). The US and sPAI acquisition of the hindlimb region was performed with the animal in its supine position, while the whole-body imaging have been acquired from supine and prone positions with the transducer aligned perpendicularly to image the region of interest.

3. Results

This section presents the results of the SPAX framework on the tissue-mimicking phantoms and also on the volumetric animal imaging.

3.1. *Spectral coloring compensation*

The agarose phantom has been used to validate the spectral coloring compensation procedure included within the SPAX framework. Besides, the unmixing results obtained with and without the spectral fluence compensation have been evaluated. Fig. 4 (A) shows the US-PA image of the agarose phantom in cross-section at 800*nm*, where the inclusions at two depths are visible. The sPAI of the agarose phantom has been acquired within the range of 700 – 970*nm*. This wavelength range has been selected in accordance with the known spectral characteristics of the absorbers included within the agarose phantom, thus reducing the acquisition time.

The two inclusions with black ink absorber (named $Inclusion_1$ and $Inclusion_2$) show higher PA signal intensity than the surrounding. Since some fragments of black oil color may remain suspended in the gel wax, the US-PA signal within the inclusions could appear not homogenous. Fig. 4 (B) shows the PA intensity profiles from the absorbers in the wavelength range of 700 – 970*nm*. By following the conventional approach used to evaluate the spectral PA intensity, the shape of the inclusions and the respective spectra were obtained by manually drawing the ROI around the inclusions. The spectral measurements have

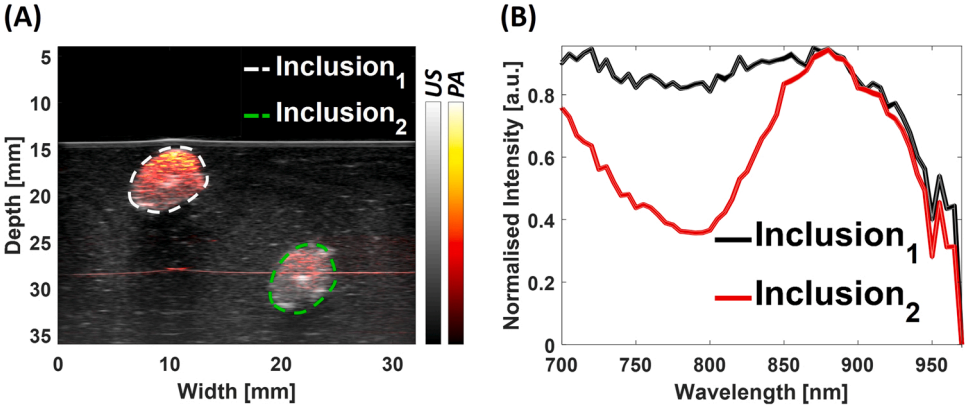

Fig. 4. US-PA image of the agarose phantom cross-section at 800*nm*, including the manually drawn ROIs around the inclusions at two depths ($Inclusion_1$ and $Inclusion_2$) (A); Averaged PA intensity of the pixels within the ROIs of $Inclusion_1$ and $Inclusion_2$ (B).

been performed over multiple slices of the phantom. To highlight the differences in the spectral shapes of the two inclusions, due to spectral coloring along depth, the spectra were normalized to visually enhance this effect. Specifically, the spectral data are shown in the graph as the normalized average of the pixels' intensity within the ROIs and the standard deviation (shown as the lighter color band along the plotline).

Although the inclusions are made of the same material, the obtained spectra show a different spectral trend. In particular, the PA spectrum from the superficial inclusion ($Inclusion_1$) showed a broad trend that is more in accordance with the measured absorption spectrum of the black ink (Fig. 2 (B)). The spectrum from the deeper inclusion ($Inclusion_2$) has shown a lower intensity within the range of $[700 - 860]nm$, while it follows the expected trend above $860nm$. These differences in spectra at depth are a clear indication of spectral coloring artifact, as the incident light attenuates along the depth and thus changes the spectral shape.

Fig. 5 (A) shows the automated segmentation obtained from the US image by using the SPAX framework. From the segmented image, it is clear that the phantom, two inclusions, and the coupling medium are accurately outlined. Based on the segmentation mask and the defined optical properties (see Supplementary Materials; SupMatTable), spectral Monte Carlo simulations have been implemented ranging from $700nm$ to $970nm$. Fig. 5 (B) represents the fluence map at a single wavelength ($800nm$), that qualitatively models the spatial distribution of light energy along the geometry.

Fig. 6 shows two different scenarios where the automatically unmixed components were obtained with and without applying the light fluence compensation.

Scenario 1: The spectra obtained without applying the fluence correction are shown in Fig. 6 (A-C), where four components have been automatically detected. Fig. 6 (A) shows two spectra that are similar to the manually obtained spectra from the inclusions (Fig. 4 (B)). In addition to the spectra of the inclusions, the SPAX framework has also detected two less prominent spectra that could represent the Verdye and the background (Fig. 6 (B-C)).

Scenario 2: Fig. 6 (D-F) show the components detected by the SPAX framework, including the segmentation and fluence compensation approach. Unlike the previous scenario, here only three spectral components have been automatically identified. Most importantly, by applying the fluence correction, both inclusions have been identified as one component with a broad absorption spectrum as shown in Fig. 6 (D). The detected spectrum from both the inclusions is in accordance with the measured spectrum of the black ink obtained by using the spectrophotometer (depicted as a dashed line). This is clear evidence of overcoming the spectral coloring artifact by using the SPAX framework. In addition, improved spectra of Verdye and background have been detected and shown in Fig. 6 (E-F).

Fig. 6 emphasizes the effect of the spectral coloring and the compensation of the SPAX framework. Besides, the correlation values between the spectra measured by the spectrophotometer and unmixed components obtained by the SPAX framework have been evaluated and reported in Table 1. Without the fluence compensation, two spectra were detected for $Inclusion_1$, $Inclusion_2$ and these have a correlation value of 0.87, 0.22 respectively, with the black ink spectrum. On contrary, when including the fluence correction, the algorithm has detected only one spectral component from both the inclusions, which has a correlation value of 0.91. This is in accordance with the expectation from the fabricated phantom, where both inclusions are made of the same component.

Furthermore, the correlation with the measured Verdye absorption spectrum has also been evaluated before and after the correction, and an improved value from 0.92 to 0.97 has been obtained. The Verdye (in Fig. 6 (E)) shows a slight shift of the absorption peak as compared with the Verdye spectrum measured *via* spectrophotometer (depicted as a dashed line). Since the Verdye absorption spectrum depends on the concentration of the dye, even small changes in the concentration may cause a change in the spectral shape.

Besides, the automatically obtained background spectrum could be related to the Intalipid, since the corresponding abundance map is mainly distributed in the surroundings of the inclusions.

3.2. Superpixel multi-component unmixing

The spectral PA images of the tissue phantom have been used to validate the superpixel spectral unmixing procedures of the SPAX framework. Fig. 7 (A) depicts the cross-sectional view of the muscle-fat tissue phantom at $700nm$, where the PA (red scale) is overlaid on the US image (grayscale). Fig. 7 (B) shows all the observed spectra from sPAI, after US segmentation and fluence compensation, which are defined as the original mixture matrix (X).

The SVD analysis is performed on these data. This analysis is crucial to automatically determine the hyperparameter (q) which represents the number of eigenvalues (S) that are significantly above the noise floor. Fig. 7 (C) shows the eigenvalues obtained from the tissue phantom sPAI dataset, where 6 shown in red are automatically selected as the hyperparameter.

After the identification of the hyperparameter, the unsupervised spectral unmixing procedure is performed on the matrix X, and the result is shown in Fig. 7 (D), where the 6 source spectra are depicted. These obtained components may not be fully unmixed or exclude some weaker absorbers. Therefore, after the detection of these 6 components, an advanced superpixel subsampling procedure is implemented to refine the unmixed spectra. Thus, the superpixel subsampling (SS) approach is applied by following the steps as described in Section 2.2.6.

SS-step1: Within the superpixel subsampling procedure the cross-

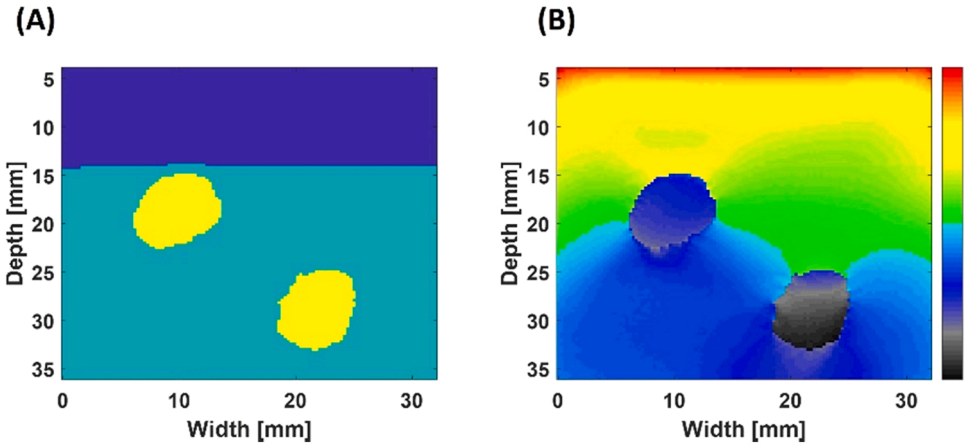

Fig. 5. Segmented mask obtained from the high-resolution US image (A); Light fluence distribution map obtained from the MCXLAB simulation at $800nm$ (B).

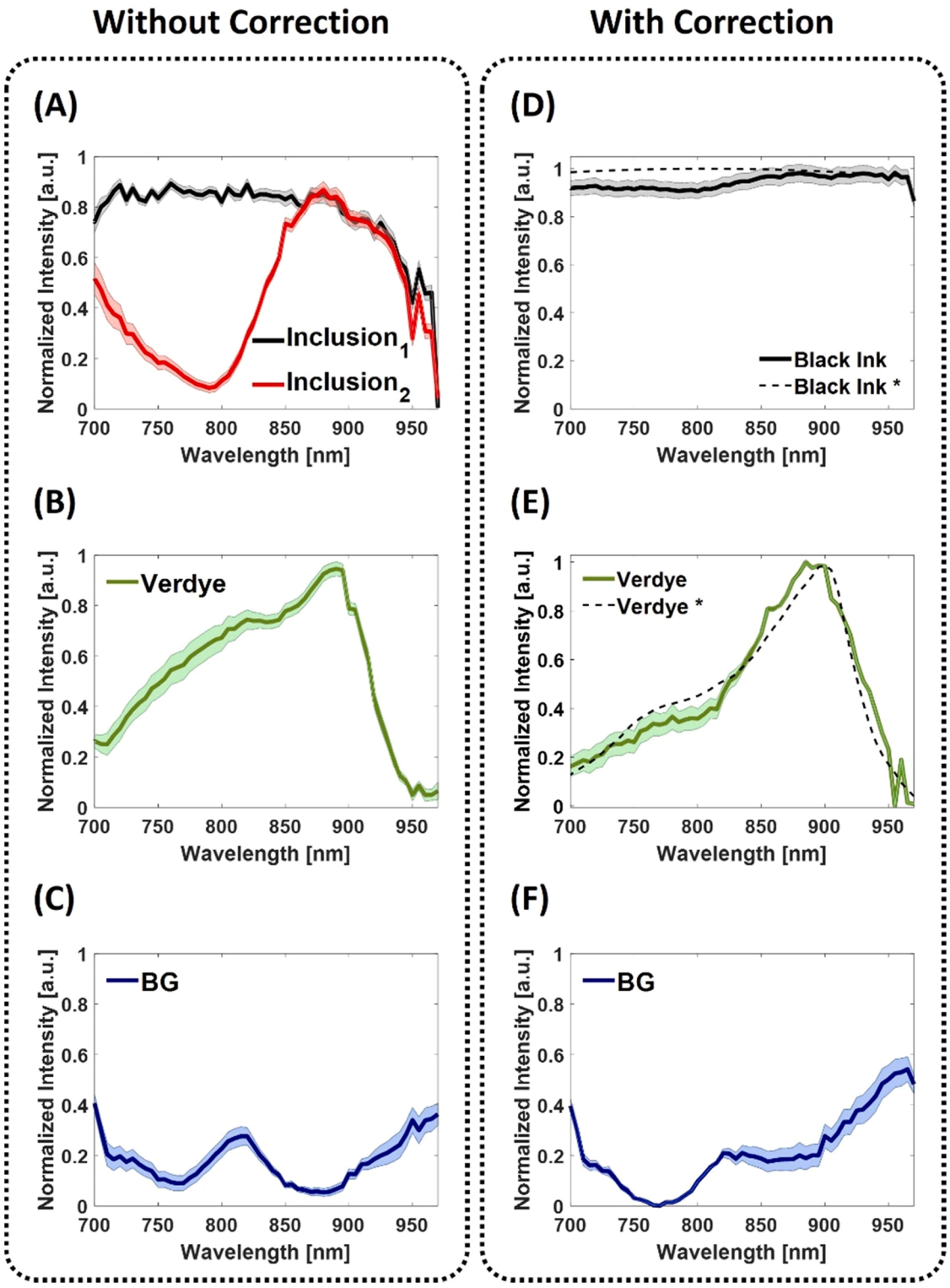

Fig. 6. Automatically unmixed spectra without the spectral fluence compensation (A-C); Automatically unmixed spectra including the spectral fluence compensation (D-F); The reference spectra of Black Ink* and Verdye* are included as dashed lines (D-E).

Table 1
Correlation Values of the Agarose Phantom Components.

Component	Without Correction	With Correction
Black Ink	0.87 (*Inclusion*$_1$); 0.22 (*Inclusion*$_2$)	0.91
Verdye	0.92	0.97

correlation values between each pair of these 6 components are evaluated. Fig. 8 (A) shows the cross-correlation matrix with the respective values obtained per each comparison. Hence, the pairs of spectra which have a similar trend will have a positive correlation, while the spectra which are easily distinguishable will have negative correlation values. To improve the specificity and also to detect the less prominent absorbers, the pairs of spectra with positive correlation values are selected

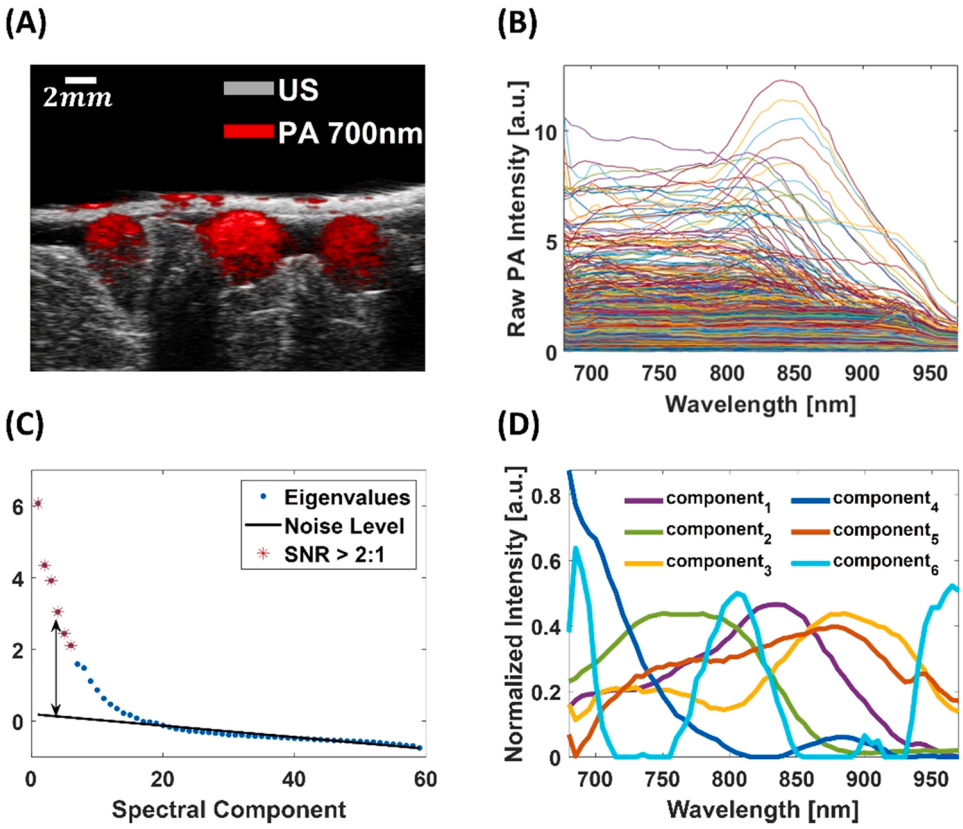

Fig. 7. US and PA image at *700 nm* of the tissue phantom in cross-section (A); PA spectra of the original mixture matrix X (B); Eigenvalues analysis for the automatic estimation of the hyperparameter q, where *6* components resulted above the noise floor (C); Source spectra obtained from the unsupervised unmixing of prominent absorbers (D).

for further analysis.

SS-step2: Specifically, per each pair of positively correlated spectra, a subset of mixed data $\widehat{X_s}$ would be created by selecting specific wavelengths and pixels. As an example, from the cross-correlation matrix, $component_1$ and $component_2$ show a positive correlation value of 0.45. For the wavelengths selection, the corresponding spectral intensities of $component_1$ and $component_2$ at each wavelength are shown in the scatter plot in Fig. 8 (B). Thus, the (x, y) coordinates of each point of the graph represent the intensities of the pair of spectra at a specific wavelength. Overall, the graph shows the positively correlated spectra at all the wavelengths, and the red lines depict the mean intensity values of each component of the considered pair. From this process, a subgroup of meaningful wavelengths, those that have comparable intensities can be selected. Generally, these would be located in the quadrants *II* and *IV*. In the example, in quadrant *II* both $component_1$ and $component_2$ result above their mean intensity values (red lines). In quadrant *IV* both components have intensity below their mean values. On contrary, the wavelengths that appear in quadrants *I* and *III* are excluded as their intensities are distinct, and thus directly distinguishable. Specifically, in quadrants *I* and *III*, one component results below and the other is above their mean values and vice-versa.

After the selection of wavelengths, a similar analysis is performed to obtain the subgroup of pixels that still need to be distinguished. To this end, the abundance maps that display the spatial distribution of the 6 components are further evaluated. The maps of the positively correlated components are used for the pixel-to-pixel intensity analysis, where the pixels with comparable intensities are selected. For the example, Fig. 8 (C) shows a composite image where the abundance maps of $component_1$ and $component_2$ are overlaid. White pixels in the composite image show where the two maps have the same intensities. Magenta and green regions show where the intensities are different. Thus, this graphically shows that the white pixels are selected for further reiterations, since the two positively correlated components are spatially overlapped in there.

Overall this process of selecting the subgroups of wavelengths and pixels is called superpixel subsampling. The same analysis is repeated for all the positively correlated pairs of components and as a result, multiple subsets $\widehat{X_s}$ with a reduced number of wavelengths and pixels are obtained.

An example, that represents a subset obtained from the original sPAI raw data X is shown in Fig. 8 (D). This represents one of the reduced subsets of observed spectra $\widehat{X_s}$. In the graph, it is evident that in comparison to the original mixture matrix X shown in Fig. 7 (B), this subset $\widehat{X_s}$ includes a smaller number of variables and observations. Specifically, the wavelengths around 850*nm* that are characteristics of the strong black absorber have been excluded. This example shows that the framework adapts the wavelengths and pixels selection to highlight the spectra that are generally obscured by the highly absorbing components.

SS-step3: Per each subset $\widehat{X_s}$ the same procedures (2.2.4 and 2.2.5) are repeated, as for the raw matrix X. The SVD and unsupervised unmixing are performed till it converges to detect the meaningful components for each subset.

SS-step4: All the spectral components $\widehat{H_s}$, obtained from each subset $\widehat{X_s}$, are resized to the same original number of wavelengths N. Finally, k-means approach is used to classify the spectral signatures obtained from all the subset $\widehat{X_s}$ and the initial mixture X. Hence, the superpixel subsampling process increases the detection of less prominent tissue chromophores, those are generally obscured from the most absorbing chromophores.

Fig. 9 (A) shows the spectral components obtained as output of the SPAX framework from the tissue phantom. In this case, in total 6 spectral components are obtained. Specifically, after superpixel subsampling 4

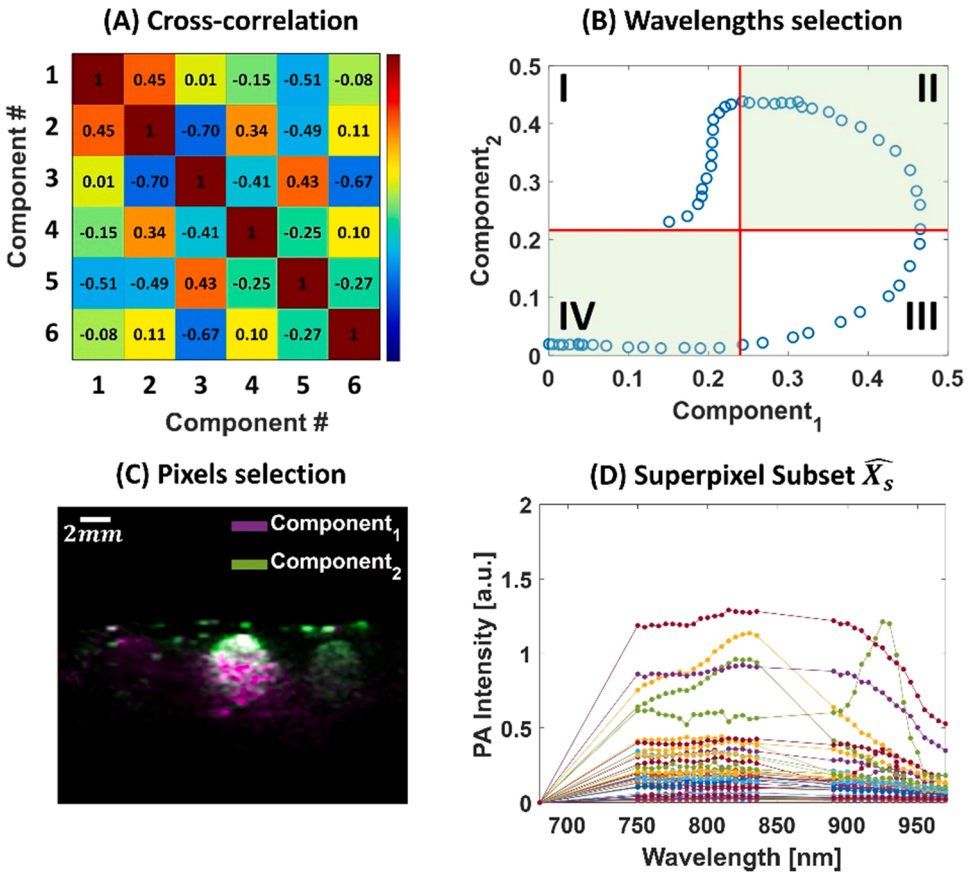

Fig. 8. Cross-correlation matrix of the detected spectral components (A); $Component_1$ and $Component_2$ are an example of positively correlated spectra, which are further analyzed to select a subgroup of wavelengths (B). Overlapped cross-sectional abundance maps of $Component_1$ and $Component_2$ used to select a subgroup of pixels (C); The scale bar size is 2*mm*; The subset of spectra obtained from the superpixel subsampling of $Component_1$ and $Component_2$ (D).

chromophores have been distinguished as black, green, blue oil colors, and fat. The additional 2 components could be related to water and background tissue. Fig. 9 (B) shows the distribution maps of the 4 unmixed components in the 2D cross-sectional view. The fat is the component depicted in yellow that is present as a top layer. Under the fat layer, the cylindrical inclusions made of highly absorbing dyes are depicted in blue, green, and red. Fig. 9 (C) shows the distribution of the 4 unmixed components in 3D where the three curved cylindrical inclusions and the layer of fat are distinguished.

3.3. *In vivo* Validation

For the *in vivo* validations, US-PA images of the mouse hindlimb have been used as input. Fig. 10 shows one of the cross-sectional views of the mouse hindlimb.

Specifically, Fig. 10 (A) shows the US image before the image segmentation. From the US image, different anatomical structures are visible such as the muscle tissue, part of the inguinal region, and the popliteal lymph node fat pad (highlighted by the dotted yellow line). Fig. 10 (B) shows the PA image at 800*nm*, before the fluence compensation, where the hemoglobin is the prominent absorber.

Fig. 11 (A) represents the segmentation mask where the skin line in yellow, the standard tissue in light blue, and the background in dark blue were identified with the automated approach. Fig. 11 (C) depicts the US image after the segmentation with the removed background. The MCXLAB simulations have been performed on the segmented masks between $[680 - 970]nm$, by utilizing the tissue optical properties summarized in the Supplementary Materials (see Supplementary Materials; SupMatTable). As an example, the result of the light fluence distribution at 800*nm* is shown in Fig. 11 (B). At each wavelength, the simulated light fluence map has been used to correct the corresponding PA image. The segmentation and the spectral fluence simulation have been performed per each 2D cross-sectional slice and finally extended to match the entire volume. Fig. 11 (D) shows the respective PA image at 800*nm* after the segmentation and fluence compensation. As a comparison, Fig. 11 (E) represents the PA intensity at 800*nm*, along the white dotted line depicted in Fig. 10 (B) and Fig. 11 (D). After the light fluence compensation, the PA intensity increases at depth within the tissue, leading to a higher contrast image. A smaller increase of the signal at the surface is also induced by the compensation, since the light fluence reaching the surface is already slightly diffused. While in deeper regions, the signal has a higher increase due to the spectral coloring compensation.

After the spectral coloring compensation, the SVD analysis is performed on these corrected sPAI data. This automatically leads to determine the hyperparameter (q), which represents the number of components significantly above the noise floor. Specifically, for the *in vivo* validation, 7 is the number that has been automatically selected as the hyperparameter. Once the hyperparameter has been identified, the unsupervised spectral unmixing procedure is performed, and the initial 7 spectral components are obtained.

Finally, the advanced superpixel subsampling procedure is implemented to refine the unmixed components. Fig. 12 (A) shows the spectral components obtained as output of the SPAX framework from the hindlimb. In this case, 7 tissue chromophores have been detected. The correlation with theoretical spectra of endogenous tissue chromophores (see Supplementary Materials; SupMatTable) is performed and Fig. 12 (B) shows the 4 spectra that have a positive correlation. Specifically, the obtained spectral signatures are matching with the theoretical spectra of oxy-hemoglobin, deoxy-hemoglobin, and fat with correlation values of 0.98, 0.96, and 0.90 respectively. In addition, the spectral $component_6$

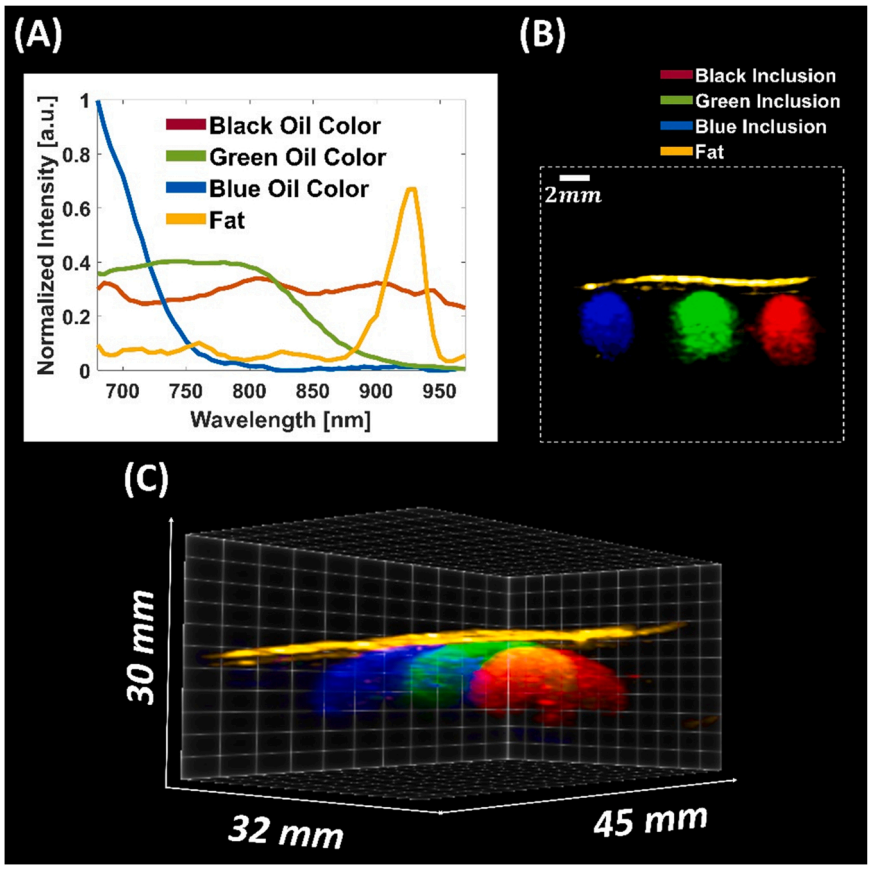

Fig. 9. Source spectra automatically obtained as output of the SPAX framework (A); Distribution maps of black, green, blue inclusions, and the layer of fat in the 2D cross-section (B), and in 3D view (C).

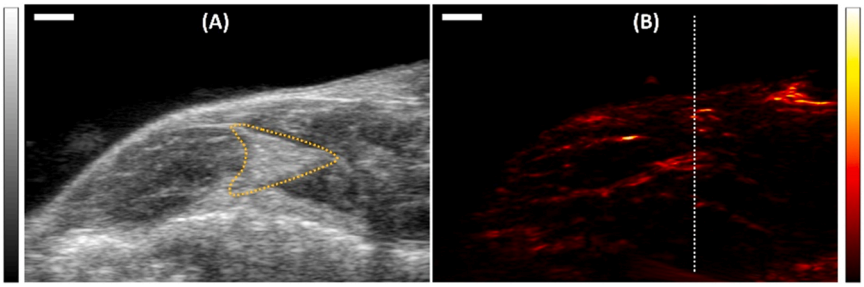

Fig. 10. The US cross-sectional image of the mouse hindlimb before segmentation (A) where the yellow dotted region indicates the popliteal fat pad which is within the intramuscular tissue; The PA image of the mouse hindlimb obtained at 800*nm* before segmentation and fluence correction (B); The scale bar size is 2*mm*.

has shown a correlation value of 0.68 with the theoretical absorption spectrum of melanin. Although the correlation value is lower, within the abundance map of $component_6$ this resulted mainly distributed along the skin line (see Fig. 14 (F)). Thus, this component could be related to skin pigmentation, and to have a real comparison with melanin a further investigation would be required. For a qualitative comparison of the spectra shapes, the theoretical absorption spectra of fat and melanin have been also overlaid in Fig. 12 (B) (depicted as dashed lines).

Besides the tissue spectral curves, the SPAX framework also provides the distribution maps of the automatically extracted components. As a comparison, Fig. 13 (A-B) shows the unmixed maps of oxy/deoxy hemoglobin obtained from the linear unmixing approach of the hindlimb. These maps have been obtained by providing the theoretical spectral curves of oxy/deoxy hemoglobin as *a priori* information.

On contrary, Fig. 14 represents the abundance maps obtained as output of the SPAX framework. The maps of oxy-deoxy hemoglobin have been reported before (Fig. 14 (A-B)) and after (Fig. 14 (C-D)) image optimization by means of the Frangi filter (FF). The vessel-like structures have been enhanced after applying the Frangi filter, thus leading to improved visualization of the oxy/deoxy hemoglobin distribution. In addition, to oxy/deoxy hemoglobin, the abundance maps of fat and skin (Fig. 14 (E-F)) have been detected. Specifically, the distribution map of fat obtained as output of the SPAX analysis, as expected, is distributed subcutaneously, within the inguinal region, and in the triangular fat pad.

The maps automatically obtained by the SPAX framework show higher accuracy than the linear unmixing. This could be explained by the iterative approach that leads to converge to a more accurate solution than a fitting-based approach.

3.4. Whole-body validation

Furthermore, the data-driven SPAX framework has been extended to

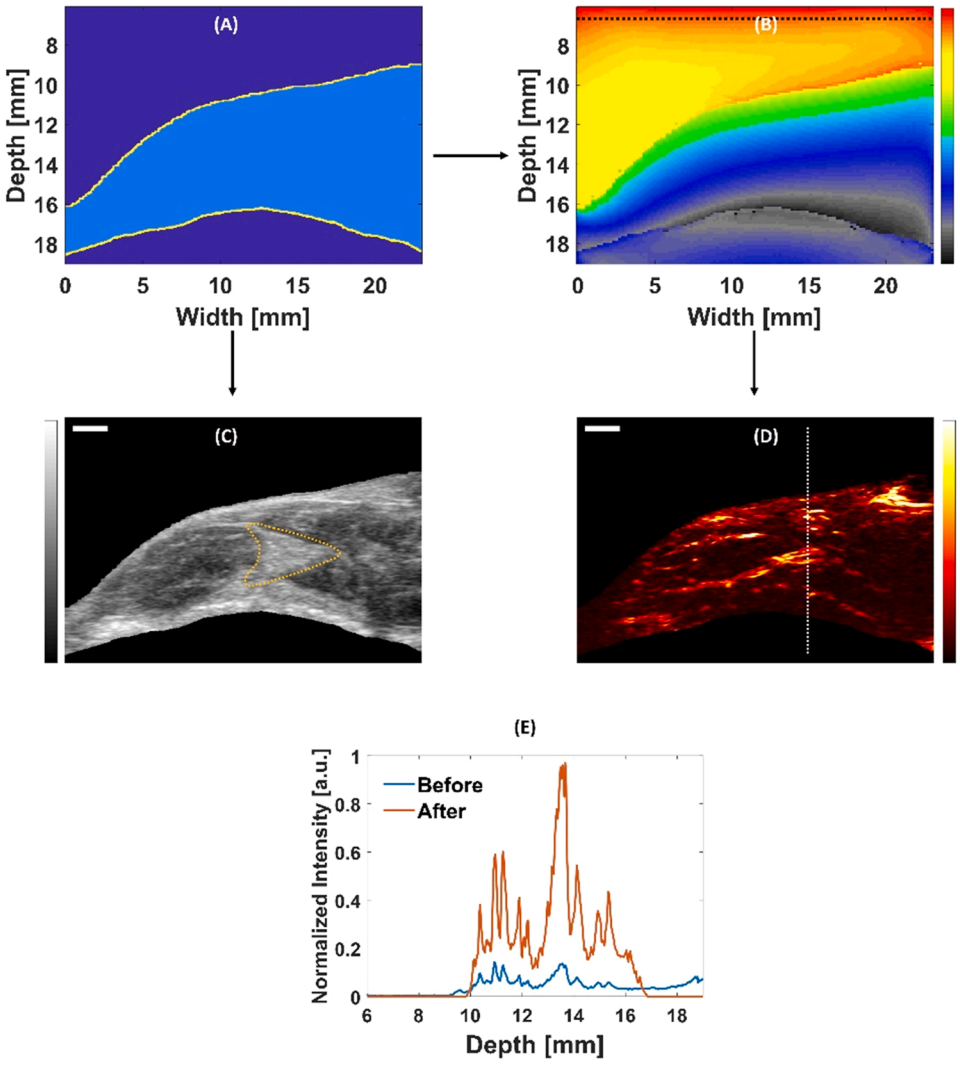

Fig. 11. Segmentation mask obtained from the US image (A); The light fluence distribution map at 800*nm*, where the dashed line indicates the light source position (B); The US cross-sectional image of the mouse hindlimb after segmentation (C) where the yellow dotted region indicates the popliteal fat pad which is within the intramuscular tissue; The PA image of the mouse hindlimb obtained at 800*nm* after segmentation and fluence correction (D); The scale bar size is 2*mm*; The PA intensity at 800*nm* before and after segmentation and fluence correction (E) of the pixels along the white dotted line in (D).

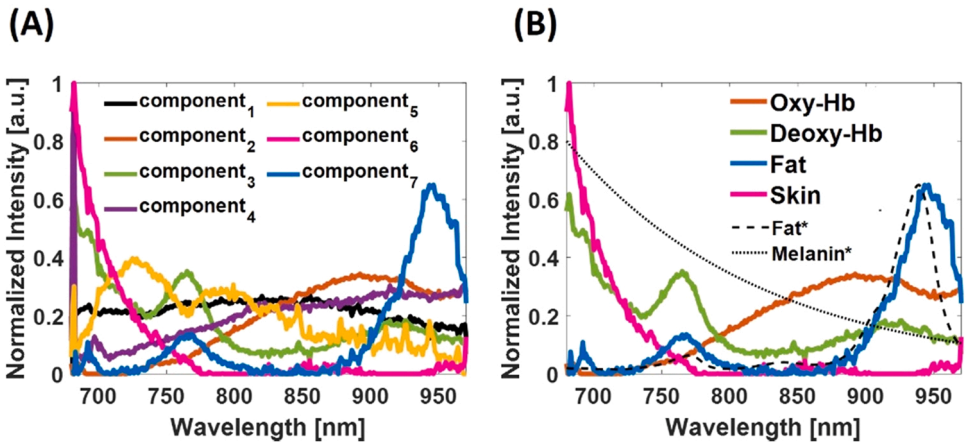

Fig. 12. Source spectra automatically identified by the SPAX framework (A); Source components identified as oxy-deoxy hemoglobin, skin, and fat (B) after the comparison with the theoretical absorption spectra.

whole-body animal imaging. US and multi-wavelength PA volumetric images have been used as input for the SPAX framework. Specifically, two whole-body scans ($30mm \times 27mm \times 64mm$) have been performed with the animal in its prone and supine position. Fig. 15 (A-C) depict the coronal US images of the animal in prone and supine position respectively. The US image guides through the anatomical structures, such as kidneys and spine are visible in Fig. 15 (A). As an output of the SPAX framework, multiple spectra have been automatically detected and the correlation with known tissue chromophores has been performed. In addition to the oxy/deoxy hemoglobin, the spectrum of fat

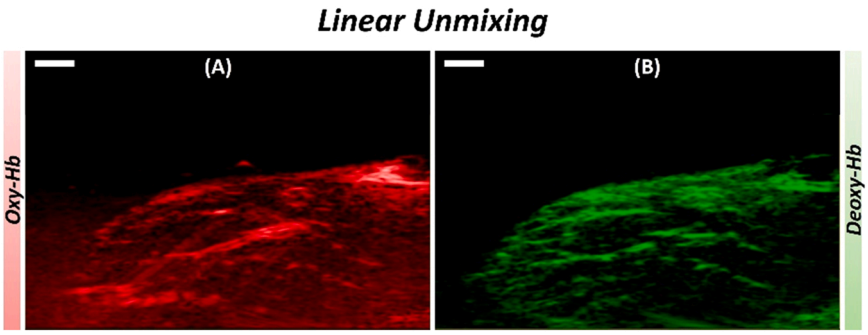

Fig. 13. Distribution maps of oxy-hemoglobin (A) and deoxy-hemoglobin (B) obtained from linear unmixing; The scale bar size is 2*mm*.

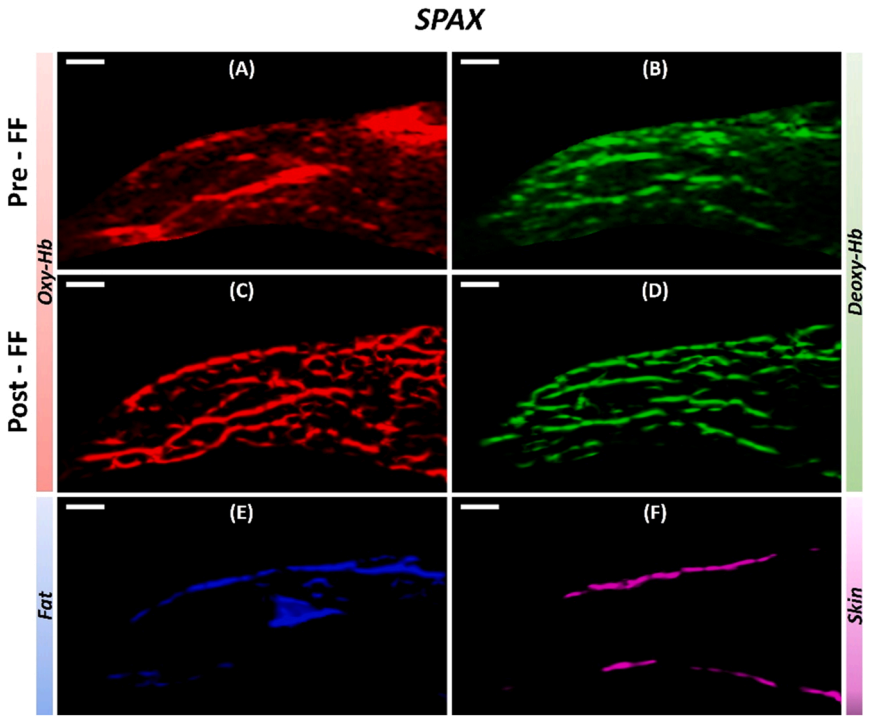

Fig. 14. Abundance maps automatically unmixed by the SPAX framework of oxy-hemoglobin, deoxy-hemoglobin before (A-B) and after (C-D) Frangi filter. The distribution maps of fat (E), and skin (F) automatically obtained as output of the SPAX framework; The scale bar size is 2*mm*.

has also been detected. Fig. 15 (B-D) show the volumetric distribution of the respective chromophores along the whole-body of the animal.

Specifically, the whole-body abundance maps of the oxy/deoxy hemoglobin are shown in red and green color respectively. The yellow color depicts the spatial overlapping of red and green, which are representative of oxy/deoxy hemoglobin. Since the hemoglobin content is mainly distributed within the blood vessels, from prone/supine view the dorsal vascular network and the mammary arteries are primarily observed in the 3-D rendering. The fat content has also been discriminated, and its spatial distribution along the whole-body is shown in the prone and supine view. The fat content is delineated in blue color along the whole-body and mostly distributed in the neck region and in the abdominal area of the mammary glands, as qualitatively observed in the 3-D rendering. Further investigations would be required to validate the components' distributions.

4. Discussion

The main objective of this study was to automatically recover the unique spectral fingerprint of the tissue chromophores and their volumetric distribution. To this end, we implemented a novel superpixel PA unmixing (SPAX) framework that can automatically detect the distribution of tissue chromophores with improved sensitivity and specificity. The highlight of this framework is the data-driven spectral unmixing approach without any *a priori* information and user interaction to detect the tissue chromophores. The SPAX framework also includes the modeling of light fluence distribution to compensate for the spectral coloring, and thus prevent the unmixing misinterpretations. The compensation approach utilizes US image segmentation and spectral Monte Carlo simulations, which are based on a predefined library of optical properties.

Spectral coloring is one of the major limitations in sPAI, which causes spectral changes at depth due to light fluence attenuation. The conventional approach to overcome the spectral coloring artifact is either an assumption of homogeneous fluence distribution along the depth or using simulations of pre-defined geometries. This is a complex approach as it requires a lot of *a priori* information such as the tissue geometry and optical properties of tissue components. Thus, this has the limitation to be generalized to other tissue types. Therefore, within the SPAX framework, we have implemented the automated segmentation of the US image that is simultaneously obtained with the multi-spectral PA images. This enables the precise modeling and simulation of the light

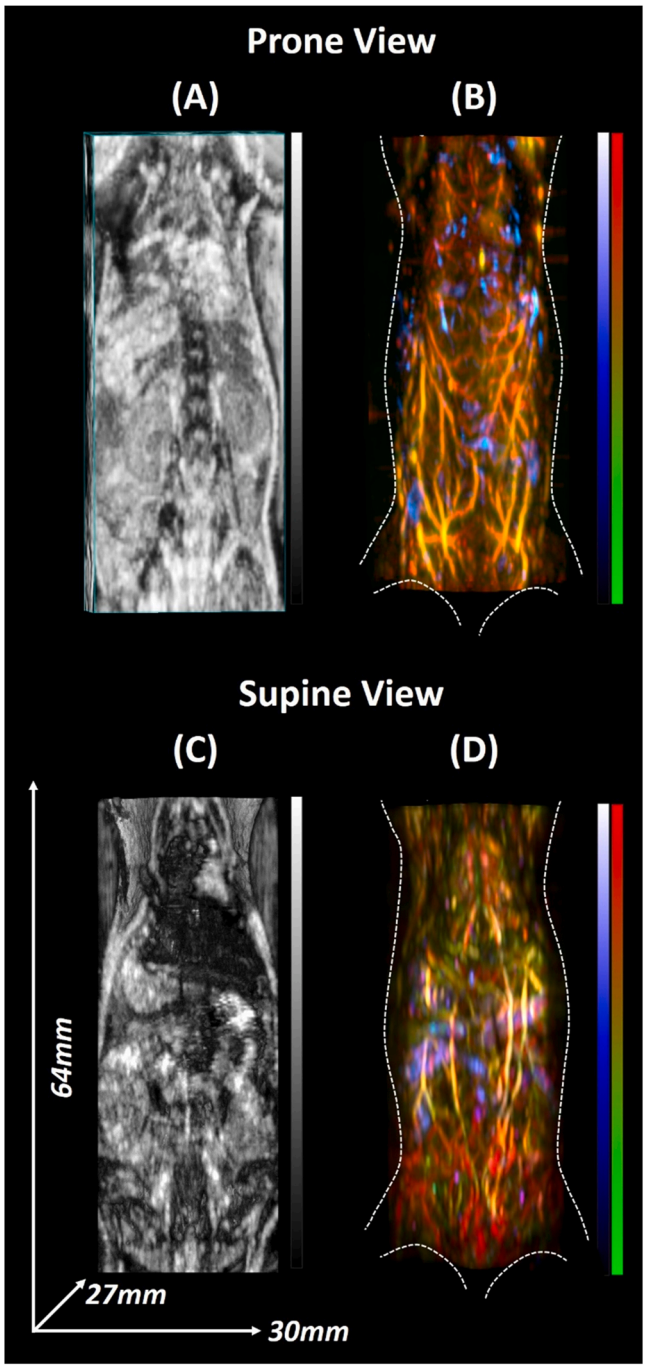

Fig. 15. Whole-body US image of the mouse in prone and supine position (A-C); Oxy/deoxy hemoglobin distribution depicted in red and green respectively and fat distribution map in blue, in prone and supine view (B-D).

fluence distribution at each wavelength of light used during the sPAI acquisition. Overall the SPAX framework facilitates overcoming the spectral coloring artifact and improving the automated extraction of the spectral features.

For the highly sensitive unmixing, an initial SVD analysis and the NNMF are applied to blindly reveal the prominent tissue components from sPAI. Besides, the framework includes a novel spectral superpixel subsampling approach to also identify less prominent tissue chromophores. Hence, less prominent tissue chromophores, such as fat, that generally remain obscured by the most prominent absorbers (like hemoglobin), can be identified. The conventional approach to detect the fat is to use the wavelengths within the Far Infrared (FIR) range, where the absorption from the hemoglobin is negligible. Since the PA excitation sources in the FIR range are having lower energy compared to NIR, the use of this range is constrained to superficial structures and microscopic applications. As the SPAX framework is optimized in the NIR range of $[680 - 970]nm$, where we have more availability of nanosecond pulsed laser sources, this can be used to detect the distribution of fat along the whole-body of the small animals.

The SPAX framework has been validated on tissue-mimicking phantoms and animal imaging. Specifically, in the agarose phantom, we showed the correction of the spectral coloring distortions at depth. This spectral compensation also promotes the accurate unsupervised unmixing of the molecular components. Besides, the muscle-fat tissue phantom has been used to benchmark the sensitivity of the SPAX framework to detect less and most prominent components. Hence, the proposed SPAX framework corrects the spectral coloring and enables the accurate identification of multiple tissue chromophores. The SPAX framework has also been used for whole-body animal imaging. In this case, the fat component has been detected, despite the oxy- and deoxy-hemoglobin show absorption intensities of two orders greater than fat.

Since the source components are extracted in an unsupervised way from sPAI, we could obtain more spectral characteristics in an unknown order. To facilitate the identification of known tissue chromophores, a correlation matrix could be evaluated between the automatically detected source spectra and a library of theoretical spectra. The correlation values are of significant importance to recognize known components from noise or unknown constituents. In healthy conditions, these values could enable to identify some of the automatically detected spectra as known components. While the identification in disease models requires further investigations, cause the tissue components tend to alter their spectral signatures in pathological conditions, due to changes at a molecular level. For example, the presence of methemoglobin is more pronounced during inflammation, and by using the SPAX framework we may be able to detect these early changes, as the correlation value with the respect to the oxy-hemoglobin might change. Thus, the SPAX framework may have the potential to monitor the spectral changes in disease conditions. However, some of the components could still remain unidentified and require further investigations to be interpreted.

Currently, the framework design includes a fully-automated segmentation step to cluster the skin line, the tissue structures, and the background. For complex tissue structures, the user can guide the US segmentation by selecting some regions of interest for active contours. This refined segmentation will result in a semi-automated approach that could lead to an improved fluence compensation. Although we are using a predefined library of optical tissue properties for the light fluence simulations, it is challenging to retrieve the optical properties from literature or characterize these *a priori*. Besides, this represents a limitation for disease models where the prediction of the tissue properties is less accurate. Thus, Brochu et al. [41] have shown a possible optimization to retrieve the tissue optical properties iteratively and speed up the computational time using finite element-based simulations, implemented on GPU cards. Very recently Gröhl et al. [56] have proposed an open-source simulation toolkit that could be feasible for these iterative approaches, by enabling realistic high-speed PA simulations. In addition to the tissue properties, to obtain the absolute quantification in PA imaging, improved measurement of the system response, and Grüneisen parameter are required. In the future, we aim to address the absolute quantification, by implementing deep learning approaches based on non-explicit light fluence estimation [57].

Finally, further efforts would be required to adjust the tradeoff between acquisition time and spectral resolution. As already demonstrated by Luke et al. [58], the selection of significant wavelengths facilitates the unsupervised unmixing and minimizes the acquisition time. In addition, the current volumetric acquisition setup is based on the translation of the linear array transducer along the animal body. For preclinical studies with high-frequency transducers, this approach

guarantees volumetric imaging with a better elevation focus and resolution. However, for clinical translation, the use of 2D matrix array transducers would be ideal as recently shown by Ron et al. [59].

Although the PA technology is already an established preclinical imaging modality, it has still some challenges for clinical translation. Therefore within the SPAX framework, we have included a combination of procedures to overcome the current limitations such as supervised unmixing techniques and misinterpretations caused by spectral coloring. Besides, a superpixel subsampling approach has been implemented to automatically extract multiple tissue components at a volumetric scale without any *a priori* information. The framework also compensates for the changes of the spectral shape along depth due to light fluence variations. Thus, the SPAX framework would be beneficial and open many possibilities to monitor molecular changes at a volumetric scale in clinical applications.

5. Conclusions

In summary, we developed the SPAX framework as a strategy to detect molecular tissue components and their volumetric distribution from spectral photoacoustic imaging. The fully-automated unmixing approach has been validated in phantoms and healthy animals. Our initial results have shown that the proposed data-driven algorithm overcomes the spectral coloring limitations and prevents unmixing misinterpretations. To our knowledge, this is a unique algorithm that accounts for the spectral coloring and provides automated detection of tissue spectral signatures in the whole-body of the animal. The initial results show that the SPAX approach is sensitive to spectral unmixing and it has the potential to discern any spectral change, that might occur in pathological conditions. Hence, the SPAX framework could be used as a predictive and monitoring tool to identify early pathological conditions and facilitate the therapeutic follow-up. To this end, in our future work, we also plan to test the SPAX framework in disease models. Finally, the SPAX framework has the potential to expedite the clinical translation of photoacoustic, as it can provide enhanced volumetric tissue characterizations.

Declaration of Competing Interest

The authors declare the following financial interests/personal relationships which may be considered as potential competing interests: Jithin Jose reports a relationship with FUJIFILM VisualSonics that includes: employment. Jithin Jose has patent pending to FUJIFILM VisualSonics.

Acknowledgments

This publication is part of a project that has received funding from the European Union's Horizon 2020 research and innovation program under the Marie Sklodowska-Curie grant agreement No 811226.

Appendix A. Supporting information

Supplementary data associated with this article can be found in the online version at doi:10.1016/j.pacs.2022.100367.

References

[1] L.H. Williams, T. Drew, What do we know about volumetric medical image interpretation?: a review of the basic science and medical image perception literatures, Cogn. Res.: Princ. Implic. 4 (1) (2019) 1–24, https://doi.org/10.1186/s41235-019-0171-6.
[2] M. Baker, The whole picture, Nature 463 (7283) (2010) 977–979, https://doi.org/10.1038/463977a.
[3] K.-H. Herrmann, S. Schmidt, A. Kretz, R. Haenold, I. Krumbein, M. Metzler, C. Gaser, O.W. Witte, J.R. Reichenbach, Possibilities and limitations for high resolution small animal mri on a clinical whole-body 3t scanner, Magn. Reson. Mater. Phys., Biol. Med. 25 (3) (2012) 233–244, https://doi.org/10.1007/s10334-011-0284-5.
[4] J. Zhang, L. Feng, R. Otazo, S.G. Kim, Rapid dynamic contrast-enhanced mri for small animals at 7t using 3d ultra-short echo time and golden-angle radial sparse parallel mri, Magn. Reson. Med. 81 (1) (2019) 140–152, https://doi.org/10.1002/mrm.27357.
[5] C.-N. Liu, J. Morin, M. Dokmanovich, C.T. Bluette, R. Goldstein, B. Manickam, C. M. Bagi, Nanoparticle contrast-enhanced micro-ct: a preclinical tool for the 3d imaging of liver and spleen in longitudinal mouse studies, J. Pharmacol. Toxicol. Methods 96 (2019) 67–77, https://doi.org/10.1016/j.vascn.2019.02.003.
[6] D. Clark, C. Badea, Advances in micro-ct imaging of small animals, Phys. Med. 88 (2021) 175–192, https://doi.org/10.1016/j.ejmp.2021.07.005.
[7] C.S. Levin, H. Zaidi, Current trends in preclinical pet system design, PET Clin. 2 (2) (2007) 125–160, https://doi.org/10.1016/j.cpet.2007.12.001.
[8] D.J. Brenner, E.J. Hall, Computed tomography-an increasing source of radiation exposure, N. Engl. J. Med. 357 (22) (2007) 2277–2284, https://doi.org/10.1056/NEJMra072149.
[9] J. Leslie, S.M. Robinson, F. Oakley, S. Luli, Non-invasive synchronous monitoring of neutrophil migration using whole body near-infrared fluorescence-based imaging, Sci. Rep. 11 (1) (2021) 1–11, https://doi.org/10.1038/s41598-021-81097-8.
[10] C. Darne, Y. Lu, E.M. Sevick-Muraca, Small animal fluorescence and bioluminescence tomography: a review of approaches, algorithms and technology update, Phys. Med. Biol. 59 (1) (2013) R1, https://doi.org/10.1088/0031-9155/59/1/R1.
[11] A.P. Dhawan, B. D'Alessandro, X. Fu, Optical imaging modalities for biomedical applications, IEEE Rev. Biomed. Eng. 3 (2010) 69–92, https://doi.org/10.1109/RBME.2010.2081975.
[12] W. Jung, D.T. McCormick, Y.-C. Ahn, A. Sepehr, M. Brenner, B. Wong, N.C. Tien, Z. Chen, In vivo three-dimensional spectral domain endoscopic optical coherence tomography using a microelectromechanical system mirror, Opt. Lett. 32 (22) (2007) 3239–3241, https://doi.org/10.1364/OL.32.003239.
[13] R.F. Spaide, J.G. Fujimoto, N.K. Waheed, S.R. Sadda, G. Staurenghi, Optical coherence tomography angiography, Prog. Retin. eye Res. 64 (2018) 1–55, https://doi.org/10.1016/j.preteyeres.2017.11.003.
[14] M. Applegate, R. Istfan, S. Spink, A. Tank, D. Roblyer, Recent advances in high speed diffuse optical imaging in biomedicine, APL Photonics 5 (4) (2020), 040802, https://doi.org/10.1063/1.5139647.
[15] J. Yoo, S. Sabir, D. Heo, K.H. Kim, A. Wahab, Y. Choi, S.-I. Lee, E.Y. Chae, H. H. Kim, Y.M. Bae, et al., Deep learning diffuse optical tomography, IEEE Trans. Med. Imaging 39 (4) (2019) 877–887, https://doi.org/10.1109/TMI.2019.2936522.
[16] P.N. Hedde, R. Cinco, L. Malacrida, A. Kamaid, E. Gratton, Phasorbased hyperspectral snapshot microscopy allows fast imaging of live, three-dimensional tissues for biomedical applications, Commun. Biol. 4 (1) (2021) 1–11, https://doi.org/10.1038/s42003-021-02266-z.
[17] M. Halicek, H. Fabelo, S. Ortega, G.M. Callico, B. Fei, In-vivo and exvivo tissue analysis through hyperspectral imaging techniques: revealing the invisible features of cancer, Cancers 11 (6) (2019) 756, https://doi.org/10.3390/cancers11060756.
[18] C. Wu, J. Gleysteen, N.T. Teraphongphom, Y. Li, E. Rosenthal, In-vivo optical imaging in head and neck oncology: basic principles, clinical applications and future directions, Int. J. Oral. Sci. 10 (2) (2018) 1–13, https://doi.org/10.1038/s41368-018-0011-4.
[19] E.R. Tkaczyk, Innovations and developments in dermatologic noninvasive optical imaging and potential clinical applications, Acta Derm. (2017) 5, https://doi.org/10.2340/00015555-2717.
[20] X. Kan, G. Zhou, F. Zhang, H. Ji, H. Zheng, J.F.B. Chick, K. Valji, C. Zheng, X. Yang, Interventional optical imaging permits instant visualization of pathological zones of ablated tumor periphery and residual tumor detection, Cancer Res. 81 (17) (2021) 4594–4602, https://doi.org/10.1158/0008-5472.CAN-21-1040.
[21] C.M. Deroose, A. De, A.M. Loening, P.L. Chow, P. Ray, A.F. Chatziioannou, S. S. Gambhir, Multimodality imaging of tumor xenografts and metastases in mice with combined small-animal pet, small-animal ct, and bioluminescence imaging, J. Nucl. Med. 48 (2) (2007) 295–303.
[22] A. Walter, P. Paul-Gilloteaux, B. Plochberger, L. Sefc, P. Verkade, J.G. Mannheim, P. Slezak, A. Unterhuber, M. Marchetti-Deschmann, M. Ogris, et al., Correlated multimodal imaging in life sciences: expanding the biomedical horizon, Front. Phys. 8 (2020) 47. . doi:10.3389/fphy. 2020.00047.
[23] J. Xia, L.V. Wang, Small-animal whole-body photoacoustic tomography: a review, IEEE Trans. Biomed. Eng. 61 (5) (2013) 1380–1389, https://doi.org/10.1109/TBME.2013.2283507.
[24] L. Li, L.V. Wang, Recent advances in photoacoustic tomography, BME Front. (2021), https://doi.org/10.34133/2021/9823268.
[25] S. Manohar, D. Razansky, Photoacoustics: a historical review, Adv. Opt. Photonics 8 (4) (2016) 586–617, https://doi.org/10.1364/AOP.8.000586.
[26] J. Yao, L.V. Wang, Recent progress in photoacoustic molecular imaging, Curr. Opin. Chem. Biol. 45 (2018) 104–112, doi:10.1016/j.cbpa.2018.03.016.
[27] B.T. Cox, J.G. Laufer, P.C. Beard, S.R. Arridge, Quantitative spectroscopic photoacoustic imaging: a review, J. Biomed. Opt. 17 (6) (2012), 061202, https://doi.org/10.1117/1.JBO.17.6.061202.
[28] L. Lin, P. Hu, J. Shi, C.M. Appleton, K. Maslov, L. Li, R. Zhang, L.V. Wang, Single-breath-hold photoacoustic computed tomography of the breast, Nat. Commun. 9 (1) (2018) 1–9, doi:10.1038/ s41467-018-04576-z.
[29] D.J. Lawrence, M.E. Escott, L. Myers, S. Intapad, S.H. Lindsey, C.L. Bayer, Spectral photoacoustic imaging to estimate in vivo placental oxygenation during

preeclampsia, Sci. Rep. 9 (1) (2019) 1–8, https://doi.org/10.1038/s41598-018-37310-2.
[30] J. Gröhl, T. Kirchner, T.J. Adler, L. Hacker, N. Holzwarth, A. Hernàndez-Aguilera, M.A. Herrera, E. Santos, S.E. Bohndiek, L. Maier-Hein, Learned spectral decoloring enables photoacoustic oximetry, Sci. Rep. 11 (1) (2021) 1–12, doi:10.1038/s41598-021-83405-8.
[31] Z. Xie, Y. Yang, Y. He, C. Shu, D. Chen, J. Zhang, J. Chen, C. Liu, Z. Sheng, H. Liu, et al., In vivo assessment of inflammation in carotid atherosclerosis by noninvasive photoacoustic imaging, Theranostics 10 (10) (2020) 4694, https://doi.org/10.7150/thno.41211.
[32] J. Jose, D. Grootendorst, T. Vijn, M. Wouters, M. Wouters, et al., Initial results of imaging melanoma metastasis in resected human lymph nodes using photoacoustic computed tomography, doi:10.1117/1.3631705.
[33] Y. Dai, X. Yu, J. Wei, F. Zeng, Y. Li, X. Yang, Q. Luo, Z. Zhang, Metastatic status of sentinel lymph nodes in breast cancer determined with photoacoustic microscopy via dual-targeting nanoparticles, Light.: Sci. Appl. 9 (1) (2020) 1–16, https://doi.org/10.1038/s41377-020-00399-0.
[34] E. Betzig, Proposed method for molecular optical imaging, Opt. Lett. 20 (3) (1995) 237–239, https://doi.org/10.1364/OL.20.000237.
[35] M.N. Fadhel, S. Appak Baskoy, Y. Wang, E. Hysi, M.C. Kolios, Use of photoacoustic imaging for monitoring vascular disrupting cancer treatments, J. Biophotonics (2020), e202000209 doi:10.1002/jbio.202000209.
[36] M. Arabul, M. Rutten, P. Bruneval, M. van Sambeek, F. van de Vosse, R. Lopata, Unmixing multi-spectral photoacoustic sources in human carotid plaques using non-negative independent component analysis, Photoacoustics 15 (2019), 100140, https://doi.org/10.1016/j.pacs.2019.100140.
[37] J. Prakash, S. Mandal, D. Razansky, V. Ntziachristos, Maximum entropy based non-negative optoacoustic tomographic image reconstruction, IEEE Trans. Biomed. Eng. 66 (9) (2019) 2604–2616, https://doi.org/10.1109/TBME.2019.2892842.
[38] J. Gröhl, M. Schellenberg, K. Dreher, L. Maier-Hein, Deep learning for biomedical photoacoustic imaging: a review, Photoacoustics 22 (2021), 100241, https://doi.org/10.1016/j.pacs.2021.100241.
[39] J. Glatz, N.C. Deliolanis, A. Buehler, D. Razansky, V. Ntziachristos, Blind source unmixing in multi-spectral optoacoustic tomography, Opt. Express 19 (4) (2011) 3175–3184, https://doi.org/10.1364/OE.19.003175.
[40] R. Hochuli, L. An, P.C. Beard, B.T. Cox, Estimating blood oxygenation from photoacoustic images: can a simple linear spectroscopic inversion ever work? J. Biomed. Opt. 24 (12) (2019), 121914 https://doi.org/10.1117/1.JBO.24.12.121914.
[41] F.M. Brochu, J. Brunker, J. Joseph, M.R. Tomaszewski, S. Morscher, S.E. Bohndiek, Towards quantitative evaluation of tissue absorption coefficients using light fluence correction in optoacoustic tomography, IEEE Trans. Med. Imaging 36 (1) (2016) 322–331, 10.1109/TMI. 2016.2607199.
[42] S. Tzoumas, A. Nunes, I. Olefir, S. Stangl, P. Symvoulidis, S. Glasl, C. Bayer, G. Multhoff, V. Ntziachristos, Eigenspectra optoacoustic tomography achieves quantitative blood oxygenation imaging deep in tissues, Nat. Commun. 7 (1) (2016) 1–10, https://doi.org/10.1038/ncomms12121.
[43] M. Li, Y. Tang, J. Yao, Photoacoustic tomography of blood oxygenation: a mini review, Photoacoustics 10 (2018) 65–73, doi:10.1016/j.pacs.2018. 05.001.
[44] P. Comon, C. Jutten, Handbook of Blind Source Separation: Independent Component Analysis and Applications, Academic press, 2010.
[45] S.L. Jacques, Optical properties of biological tissues: a review, Phys. Med. Biol. 58 (11) (2013) R37, https://doi.org/10.1088/0031-9155/58/11/ R37.
[46] H.J. Van Staveren, C.J. Moes, J. van Marie, S.A. Prahl, M.J. Van Gemert, Light scattering in lntralipid-10% in the wavelength range of 400–1100 nm, Appl. Opt. 30 (31) (1991) 4507–4514, https://doi.org/10.1364/AO.30.004507.
[47] R. Khan, B. Gul, S. Khan, H. Nisar, I. Ahmad, Refractive index of biological tissues: review, measurement techniques, and applications, Photo Photodyn. Ther. 33 (2021), 102192 doi:10.1016/j. pdpdt.2021.102192.
[48] S.L. Jacques, W.P. Roach, Optical interactions with tissue and cells xvii, Optical Interactions with Tissue and Cells XVII 6084. doi:10.1117/12. 662811.
[49] A. Kharine, S. Manohar, R. Seeton, R.G. Kolkman, R.A. Bolt, W. Steenbergen, F. F. de Mul, Poly (vinyl alcohol) gels for use as tissue phantoms in photoacoustic mammography, Phys. Med. Biol. 48 (3) (2003) 725 357, https://doi.org/10.1088/0031-9155/48/3/306.
[50] S. Yan, Q. Fang, Hybrid mesh and voxel based monte carlo algorithm for accurate and efficient photon transport modeling in complex bio-tissues, Biomed. Opt. Express 11 (11) (2020) 6262–6270, doi:10.1364/BOE. 409468.
[51] D.Xia Zhang, Tensor svd: Statistical and computational limits, IEEE Trans. Inf. Theory 64 (11) (2018) 7311–7338, doi:10. 1109/TIT.2018.2841377.
[52] F. Liu, Y. Deng, Determine the number of unknown targets in open world based on elbow method, IEEE Trans. Fuzzy Syst. 29 (5) (2020) 986–995, https://doi.org/10.1109/TFUZZ.2020.2966182.
[53] V. Grasso, J. Holthof, J. Jose, An automatic unmixing approach to detect tissue chromophores from multispectral photoacoustic imaging, Sensors 20 (11) (2020) 3235, https://doi.org/10.3390/s20113235.
[54] P. Bankhead, C.N. Scholfield, J.G. McGeown, T.M. Curtis, Fast retinal vessel detection and measurement using wavelets and edge location refinement, PloS One 7 (3) (2012), e32435 doi:10.1371/journal.pone. 0032435.
[55] E. Maneas, W. Xia, O. Ogunlade, M. Fonseca, D.I. Nikitichev, A.L. David, S.J. West, S. Ourselin, J.C. Hebden, T. Vercauteren, et al., Gel wax-based tissue-mimicking phantoms for multispectral photoacoustic imaging, Biomed. Opt. Express 9 (3) (2018) 1151–1163, doi:10.1364/BOE.9. 001151.
[56] J. Gröhl, K.K. Dreher, M. Schellenberg, A. Seitel, L. Maier-Hein, Simpa: an open source toolkit for simulation and processing of photoacoustic images, Photons Ultrasound.: Imaging Sens. Vol. 11642 (2021) 116423C, https://doi.org/10.1117/1.JBO.27.8.083010. International Society for Optics and Photonics, 2021.
[57] J. Li, C. Wang, T. Chen, T. Lu, S. Li, B. Sun, F. Gao, V. Ntziachristos, Deep learning-based quantitative optoacoustic tomography of deep tissues in the absence of labeled experimental data, Optica 9 (1) (2022) 32–41, https://doi.org/10.1364/OPTICA.438502.
[58] G.P. Luke, S.Y. Nam, S.Y. Emelianov, Optical wavelength selection for improved spectroscopic photoacoustic imaging, Photoacoustics 1 (2) (2013) 36–42, https://doi.org/10.1016/j.pacs.2013.08.001.
[59] A. Ron, S.K. Kalva, V. Periyasamy, X.L. Dean-Ben, D. Razansky, Flash scanning volumetric optoacoustic tomography for high resolution whole-body tracking of nanoagent kinetics and biodistribution, Laser Photonics Rev. 15 (3) (2021) 2000484, https://doi.org/10.1002/lpor.202000484.

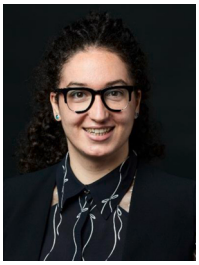

Valeria Grasso: Valeria Grasso received her Master's degree in Biomedical Engineering from the University of Pisa, Italy, in 2018. She is currently a Ph.D. candidate within the Marie Curie network called MgSAFE and she is based at FUJIFILM VisualSonics, Amsterdam, The Netherlands. Her main research interest centers on optimizing the high-resolution Ultrasound and Photoacoustic (US-PA) imaging technology to non-invasively monitor the molecular changes in the soft tissues surrounding biodegradable bone implants made of Magnesium. Her current work focuses on the development of advanced US-PA image processing algorithms and optimal hardware solutions to adapt the US-PA technology for human patients treated with biodegradable Mg-based implants in case of bone injuries.

Regine Willumeit-Römer: Prof. Dr. Regine Willumeit-Römer obtained a Ph.D. in physics for the structural characterization of ribosomes (University of Hamburg). She used spin-dependent neutron scattering, an approach which gave her the chance also to work at CERN, Geneva, Switzerland. Her habilitation and venia legendi in biochemistry about the structure-function relationship in ribosomes was also obtained from the University of Hamburg. While working at the Helmholtz-Zentrum Hereon (former "HZG") and teaching structural biology in Hamburg, Regine Willumeit-Römer became Head of the Department 'Macromolecular Structure Research' at HZG. Her field of research shifted from structural biology towards implant materials, especially biodegradable Magnesium materials. Since 2014 she is full Professor at the University of Kiel, Faculty of Engineering for the field "Biological interfaces of Implants". In 2015 she became Director of the Institute for "Metallic Biomaterials" at Hereon. She has published 297 peer-reviewed papers (H-Index 49, WoS February 2022).

Jithin Jose: Dr. Jithin Jose performed research towards his Ph. D. thesis at the Biomedical Photonic Imaging (BMPI) group, University of Twente, The Netherlands. He is specialized in biomedical imaging. During his research, he developed a Computed tomography (CT) photoacoustic imager to enable molecular imaging of tumors in small animals. He also has extensive knowledge of the exogenous contrast agents such as gold nanorods used for photoacoustic imaging. He is currently working at FUJIFILM VisualSonics, as a Global Market Leader where he is responsible for the development of Photoacoustic imaging technology and its translational aspects. He is the co-author of more than 30 refereed journal publications and maintains an active research interest in the applications of photoacoustic imaging both in pre-clinical and clinical research.

Chapter 6

Unsupervised multi-spectral photoacoustic unmixing framework for the detection and quantification of endogenous and exogenous tissue chromophores*

Abstract:

In this chapter, we tested and validated the newly developed superpixel photoacoustic unmixing (SPAX) approach to blindly distinguish endogenous and exogenous chromophores in living tissues. We aim to show the advanced applications where the proposed SPAX unmixing algorithm can be used and its beneficial aspects as compared to standard unmixing approaches.

*Part of this chapter has been published as: **Grasso, V.,** Willumeit-Römer, R., & Jose, J. (2021, September). *"Unsupervised multi-spectral photoacoustic framework for the detection and quantification of tissue chromophores."* In 2021 IEEE International Ultrasonics Symposium (IUS) (pp. 1-4). IEEE.

*Part of this chapter has been published as: **Grasso, V.**, Hassan, H. W., Mirtaheri, P., Willumeit-Römer, R., & Jose, J. (2022). *"Recent advances in photoacoustic blind source spectral unmixing approaches and the enhanced detection of endogenous tissue chromophores."* Frontiers in Signal Processing, p.67.

6.1. Introduction

Photoacoustic imaging (PAI) is a non-ionizing technology that illuminates the tissues with nanosecond laser pulses and induces the generation of acoustic waves that can be detected just as conventional ultrasound [1]–[6]. This hybrid imaging modality combines the advantages of acoustic tissue penetration depth and spatial resolution with specific optical contrast. Moreover, this combination provides anatomical, functional, and molecular information up to several centimeters deep in tissues with a resolution of up to tens of micrometers [7], [8]. PAI is mainly based on the intrinsic optical absorption of endogenous tissue chromophores such as water, oxyhemoglobin (HbO_2), deoxyhemoglobin (Hb), melanin, and lipids. Apart from the label-free nature of the PAI technology, exogenous agents that are mostly small molecule dyes such as Indocyanine green (ICG), Methylene Blue Dye (MBD), nanoparticles, or even reporter gene agents can be used to enhance the contrast in PAI. Thus, PAI can image small absorbers that provide the clinician with potentially valuable molecular data [9]–[11]. Therefore the strengths of PAI are its potential for high resolution and imaging depth as well as the ability to image both endogenous and exogenous chromophores without using ionizing radiation [12]–[14].

Several applications, such as tumor progression, therapy monitoring, imaging of tissue remodeling, and the bio-distribution of contrast agents have demonstrated the high potential of PAI in preclinical imaging [15]–[20]. Furthermore, the laser used for PAI is tunable within the near-infrared (NIR) range, therefore multi-spectral photoacoustic imaging (sPAI) can be performed by exciting the tissue at multiple wavelengths. sPAI plays a crucial role to differentiate endogenous and exogenous molecular components [21]–[24]. As each of the chromophores exhibits its own characteristic absorption spectra, sPAI at multiple wavelengths allows their relative quantification and helps to detect molecular changes related to pathological conditions. Thus sPAI is intrinsically sensitive to molecular component distribution in tissues. Linear unmixing is commonly used to differentiate the underlying components from sPAI. Specifically, sPAI fused with linear unmixing method [25], provides distribution maps of the tissue chromophores by utilizing *a priori* information. Although this fitting-based approach yields acceptable results, it requires user interaction to provide the source spectral curves as an input. For translational research with patients, this type of supervised spectral unmixing can be challenging, as the spectral signature of the tissues differs with respect to the disease condition. Imaging exogenous contrast agents and accessing their biodistribution can also be problematic, as some of the contrast agents are susceptible to change in spectral properties after the interaction with living tissues. Besides, light fluence attenuation along the imaging depth might induce spectral coloring that compromises the accurate unmixing and quantification of the chromophores. Thus, the linear unmixing algorithm can compromise the sensitivity and specificity of the imaging. An unsupervised spectral unmixing approach would be the ideal solution to overcome these limitations, and recently some studies have been reported, showing promising results [26]–[29].

In this study, we investigate the performance of our proposed unsupervised superpixel photoacoustic unmixing (SPAX) framework [30] that enables fully automatic spectral unmixing

and accurate quantification of molecular components. We tested and validated the performance of the data-driven SPAX approach on *in vitro* and also *in vivo* studies. The SPAX algorithm has shown improved sensitivity and specificity during *in vitro* experiments as well as on various *in vivo* applications. In particular, here we have investigated and reported the use of SPAX for the tissue composition analysis without user interaction for various anatomical targets considering both endogenous and exogenous contrast.

From the validation studies, we observed that the SPAX approach has the following advantages with respect to the commonly used linear unmixing approach:

- The SPAX unmixing is fully blind and automatic, thus it does not require any user interaction or *a priori* input of the expected chromophore absorption spectra.
- The SPAX framework includes a spectral decoloring approach to compensate for the misinterpretations at depth caused by ununiformed light fluence distribution.
- The SPAX framework implements an innovative superpixel subsampling approach to automatically distinguish both strong and less prominent absorbers from the original spectral photoacoustic data.
- The SPAX framework is also extended to blindly unmix 3-Dimensional (3D) multi-wavelength photoacoustic data.

6.2. Materials and methods

In the following sections, we describe the *in vitro* and *in vivo* experiments that have been conducted to test the unmixing performance of the SPAX framework for endogenous and exogenous chromophores. The advantageous aspects of the SPAX framework are validated through different experiments both using 2D spectral and 3D multi-wavelength PAI.

6.2.1. Multi-spectral photoacoustic imaging

High-resolution Ultrasound (US) and spectral photoacoustic imaging (sPAI) have been acquired using the Vevo LAZR-X technology (FUJIFILM VisualSonics, Inc., Toronto, ON, Canada). The imaging technology includes a high-frequency US system combined with an Nd:YAG nanosecond pulsed laser. The linear US transducer array (MX250) consists of 256 piezoelectric elements at a nominal center frequency of 21 MHz and bandwidth of 15 – 30 MHz. Light from the laser is delivered to the tissue through optical fibers, mounted on either side of the transducer. Multispectral PA imaging has been acquired by tuning the excitation light wavelength within the range of 680-970 nm, with a 10 nm step size. During the volumetric multi-spectral PA acquisitions, a stepper motor is used for the linear translation of the US transducer and optical fibers along the sample. The linear stepper motor moves in steps of a minimum of $0.1mm$ while capturing 2D parallel images, for a maximum 3D range distance of $64mm$. The Vevo whole-body imaging setup (FUJIFILM VisualSonics, Inc., Toronto, ON, Canada) has been used during *in vivo* experiments with the animal in its prone position. Fig. 4 (A) shows the schematic of the ultrasound-photoacoustic imaging acquisition setup. The configuration in epi-illumination, the

ECG monitoring, and the respiratory gating were kept minimally unchanged during *in vivo* experiments. The delay multiply and sum beamforming algorithm has been used for photoacoustic image reconstruction [31]. The scanning time for the acquisition of sPAI in 2D and 3D ranges between 1–10 min. The exact acquisition time depends on the number of wavelengths as well as motor step size and the consequent number of slices for volumetric data. The processing of the spectral 2D and 3D data is performed offline, after the acquisition. As an advanced data analysis, SPAX algorithm is performed offline and the computational time ranges between 1–12 min, depending on the size of the input sPAI data and the computer specifications.

6.2.2. SPAX unmixing

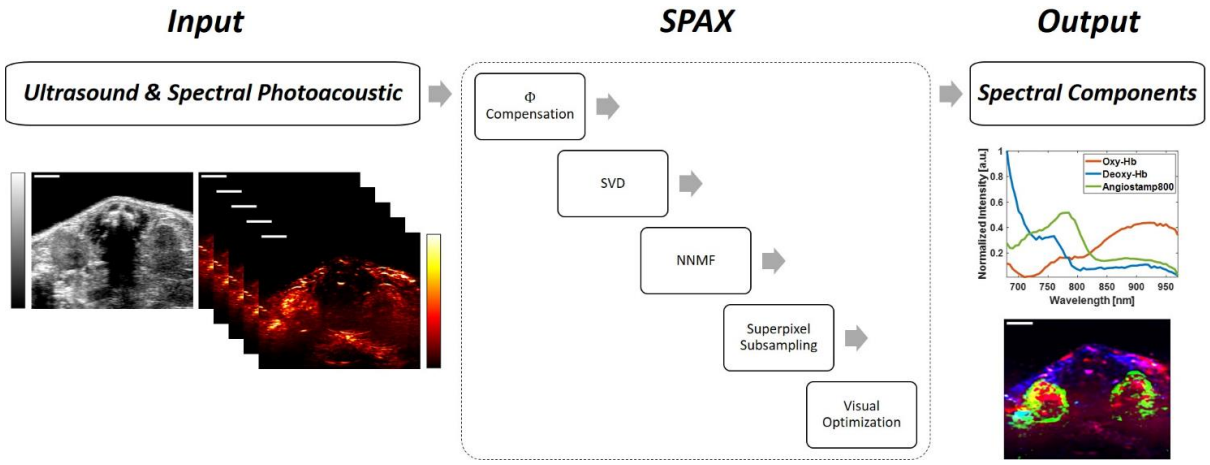

Fig. 1. Schematic flowchart of the SPAX framework including the main procedures from input to output. The data used as an example, show the kidney area of a mouse after injection of a contrast agent (Angiostamp800); the scale bar size is 2mm.

Fig. 1 schematically summarizes the main procedures implemented within the Superpixel Photoacoustic Unmixing (SPAX) framework. Specifically, the SPAX framework uses multi-spectral photoacoustic images co-registered with high-resolution ultrasound images (US-sPAI) as input to automatically identify the tissue spectral components obtained as output. First, the SPAX framework models the light fluence distribution along depth to compensate for the spectral coloring. The compensation approach utilizes Ultrasound image segmentation and spectral Monte Carlo simulations based on a predefined library of optical properties. This spectral decoloring method is a crucial step that prevents unmixing misinterpretation at depth as well as enhances the image quality. The rank hyper-parameter can be automatically tuned by performing the singular value decomposition (SVD) pre-analysis of the mixture. The core of the SPAX framework is based on non-negative superpixel unmixing, which enables the automated detection of tissue chromophores with improved sensitivity and specificity. To solve the ill-conditioned problem, positivity constraints and multiplicative update rule have been used to improve the convergence of the blind iterative method. Besides, a novel superpixel subsampling approach has been implemented to differentiate the less prominent molecular components, from the prominent absorbers. Finally, imaging optimization methods are applied to improve the

visualization of the distribution maps of the detected spectral components. Therefore, the SPAX offers several advantages over the simple blind unmixing approaches. Details of the algorithm and the validation studies are described elsewhere [30].

6.2.3. *In vitro* experiments

In vitro experiments have been designed and conducted to test the possibility of unmixing endogenous tissue chromophores and exogenous contrast agents by using the SPAX framework. A tissue-mimicking phantom composed of an *ex vivo* bovine meat sample (longissimus dorsi muscle) and capillary tubes filled with Indocyanine green (ICG), was prepared to test the performance of the unsupervised SPAX algorithm. The structure of the bovine meat sample was complex, it included muscle tissue and intramuscular fat. To mimic the presence of exogenous absorbers, we inserted the polyethylene tubes (inner diameter ≈380 µm and outer diameter ≈840 µm) filled with 800 µM ICG (PULSION Verwaltungs, GmbH) at two different depths as shown in the schematic of Fig. 2 (A). The absorption spectrum of ICG was measured via spectrophotometer (Varian, Cary 2300) and it is shown in Fig. 2 (B).

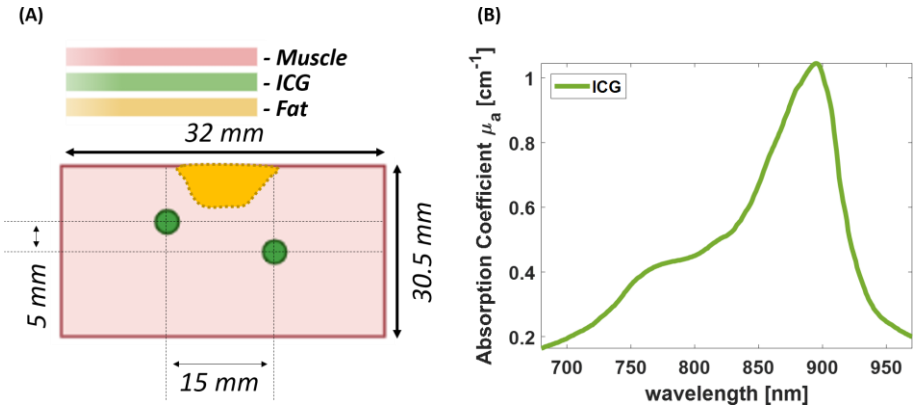

Fig. 2. Schematic of the cross-section of the tissue-mimicking phantom (A); Spectral absorption coefficient of ICG within 680-970 nm range (B).

6.2.4. *In vivo* experiments

Further, *in vivo* animal experiments were performed to evaluate the performance of the data-driven SPAX framework for sPAI obtained from living tissues. The animal experiments were performed at the FUJIFILM VisualSonics facility in Amsterdam, The Netherlands. The animal protocols used in this work were evaluated and approved by the Animal Use and Ethics Committee (CEUA) of The Netherlands (Protocol AVD2450020173644). They are in accordance with FELASA guidelines and the National Law for Laboratory Animal Experimentation (Law No. 18.611). All the animals included in this study were healthy. During image acquisition, the animal was anesthetized with isoflurane and placed on the animal imaging platform of the Vevo LAZR-X system, where temperature, heart rate, and respiration rate were monitored in real-time. During the experiments, anesthesia was maintained using a vaporized isoflurane (1 L/min of oxygen and 0.75% isoflurane) gas system.

6.2.4.1. Exogenous contrast agent detection

A CD-1 female mice model (Envigo, Horst, The Netherlands) was used for the *in vivo* experiments to investigate the detection of exogenous tissue components as well as to evaluate the advantages of the SPAX approach as compared to standard linear unmixing (LU) [32]. A recently developed photoacoustic contrast agent, called Angiostamp800, has been prepared and used as described elsewhere [33]. Specifically, Angiostamp800 (Fluoptics, France) was diluted in PBS to concentrations of 200 and 50 µM. The contrast agent was injected intravenously via the tail vein (200 µL). Before the injection, the contrast agent has been characterized into a tube phantom (FUJIFILM VisualSonics, Inc., Toronto, ON, Canada) and the spectral photoacoustic characteristic has been obtained as shown in Fig. 3. Three hours post-injection the spectral photoacoustic images from the kidney region of the mouse from its prone position have been acquired with the transducer in epi-illumination configuration (light from one side only). As a comparison, the data have been unmixed by using the newly developed SPAX framework with and without fluence correction. The signal-to-noise ratio (SNR) along depth was calculated on the normalized unmixed map of Angiostamp800 distribution obtained with the SPAX approach with and without applying the fluence compensation function. This aims to show the enhancement in the sensitivity and specificity of the unmixing, especially when including the effect of the spectral decoloring approach.

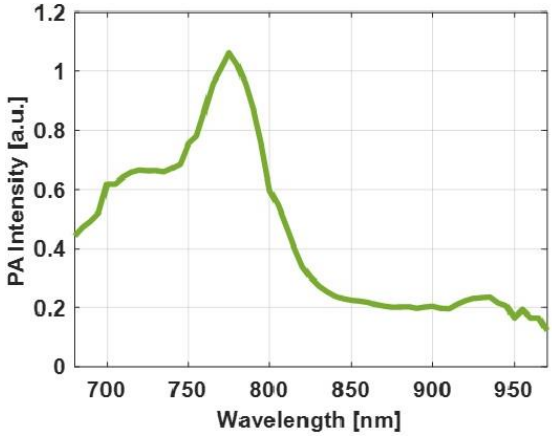

Fig. 3. Photoacoustic absorption spectrum of Angiostamp800, characterized in a tube phantom.

6.2.4.2. Endogenous tissue chromophores detection

A CD-1 female mice model (Envigo, Horst, The Netherlands) was used for the experiments to investigate the automated unmixing of endogenous tissue components via SPAX. Besides, this experiment also aims to evaluate the advantage of the SPAX approach in distinguishing strong and weak absorbers. The data set was obtained by performing the spectral PAI acquisition with the animal in its prone position and the transducer was aligned perpendicularly to image the lower abdominal area at the level of the kidneys.

Besides, 3D multi-wavelength PAI acquisition has also been performed. Specifically, three female CD-1 mice models (Envigo, Horst, the Netherlands) 9 weeks old, were used to image the cervical-thoracic region. During imaging acquisition, the mice were anesthetized with isoflurane (2-3% by volume with 0.8l/min gas flow). The US and sPAI acquisition was performed with the animal in its prone position within the Whole-Body imaging setup, with the transducer aligned perpendicularly to image the region of interest. After *in vivo* acquisition, the adipose tissue from the cervical-thoracic area was dissected post-mortem and used for spectral measurements conducted via a portable NIR spectrophotometer (see Section 6.2.4.2.1.). We focused on this anatomical area where the interscapular adipose tissue is present, which represents a weak endogenous absorber.

6.2.4.2.1. Near-infrared spectroscopy measurements

Fig. 4 (B) depicts the schematic of a portable near-infrared spectroscopic (NIRS) probe that has been used to validate the spectral absorption curves of the chromophores involved in the *in vivo* study.

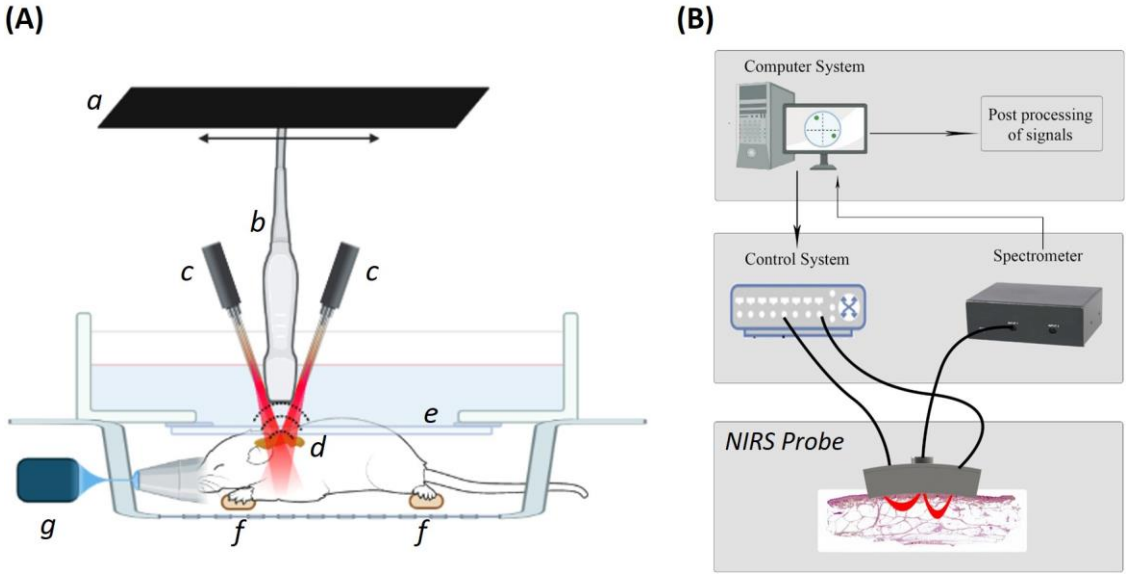

Fig. 4. Schematic of the ultrasound-photoacoustic (US-PA) whole-body acquisition setup (A) that includes: a linear stepper motor (a), the ultrasound transducer (b) with optical fibers on the sides (c) to illuminate the tissue chromophores (d), optical and acoustic compatible membrane (e) in a water bath to maintain the sound coupling, ECG electrodes to monitor the physiological parameters *in vivo* (f), and the anesthesia system (g). Schematic of the near-infrared spectroscopy (NIRS) optical probe setup (B) that also includes: a control system for the optical source, a spectrometer for the detection, and a computer for the signals post-processing.

Specifically, to compare the spectral fingerprint of the adipose tissue deposited within the cervical-thoracic region of the mice. To this end, a customized NIRS probe was designed at the Optical lab in OsloMet (Oslo Metropolitan University, Norway) [34], [35]. Unlike commercially available solutions, this NIRS probe is designed to target two regions of interest at two different

depths. Specifically, the OsloMet's probe uses a broadband LED light source (650 to 1050 nm) and works with two depth ranges (2-2.25 mm and 3-3.5 mm respectively). In addition, the optical probe's light sources ensure the safety of the operations, in compliance with the NIR safety guidelines [36]. This NIRS probe uses a source-detector pair that generates a banana-shaped optical path that narrows at the source and detector's locations and broadens as it penetrates deeper into the tissue [37]. The depth of a photon before detection is proportional to the square root of the source-detector separation [38]. Hence, optical depth is generally 1/2 to 1/3 of the source-detector distance [39]. The spectra from the optical probe are then collected by a spectrometer (Avaspec 2048x14, Avantes BV, The Netherlands). An integration time of 4 seconds, was selected to make sure that enough photons are collected by the detector. In this experiment, a distance of 6mm between the source and detector was used to get a focal depth of 2-2.5 mm and the wavelength range has been fixed to 680-970 nm as the one used for sPAI. Finally, the obtained spectra from NIRS have been used as a reference to be compared with the automatically unmixed signatures from sPAI via SPAX.

6.3. Results

6.3.1. *In vitro* experiments

Fig. 5 (A) shows the source spectral components automatically obtained by using the proposed SPAX approach. From the automatically extracted spectra, the spectrum represented in green follows a similar trend as the measured absorption spectral characteristic of ICG shown in Fig. 2 (B).

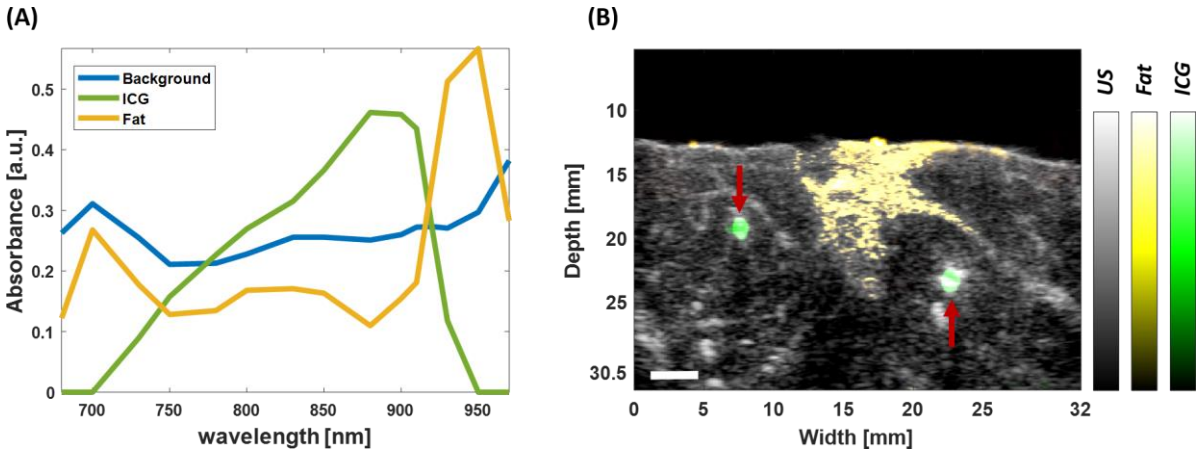

Fig. 5. Automatically extracted source spectra of ICG (in green), fat flecks (in yellow), and muscle background tissue (in blue) by unsupervised SPAX framework (A); Extracted abundance maps of ICG (green map) present within the capillary tubes (the tubes cross sections are referred by the red arrows) and intramuscular fat flecks content (yellow map) overlapped on the US image in grayscale (B); the scale bar size is 5mm.

Although the obtained spectral shape of ICG is similar to the expected spectrum, there is a discrepancy in the spectral shape in the range of 700-820 nm. This could be due to the spectral coloring effect as reported elsewhere [40]. In addition to the ICG, the unsupervised SPAX

framework also detected two other components represented in blue and yellow. According to the spectral trend, presumably, the blue spectrum could be related to the background muscle tissue and the yellow represents the intramuscular fat [41]. Fig. 5 (B) shows the multicomponent maps of ICG and fat (in green and yellow respectively) overlaid on the US image that is represented in grayscale. The image shows the cross-sectional view where the capillary tubes filled with ICG are shown in green color and the intramuscular fat deposition in the central region of the muscle is depicted in yellow.

Here, the beneficial effect of spectral fluence compensation is less evident, due to the small size of the ICG tubes placed at 2 depths within the muscle tissue. Besides, the muscle tissue has a negligible absorption, which prevents prominent fluence inhomogeneity along depth.

6.3.2. *In vivo* exogenous contrast agent

Fig. 6 (A-B) show the US and PA images obtained from the kidney area of the mouse after intravenous injection of Angiostamp800. The US image (see Fig. 6 (A)) depicts the short axis view and the anatomical structures, such as kidneys and spine (pointed by green and white arrows respectively), are distinguished.

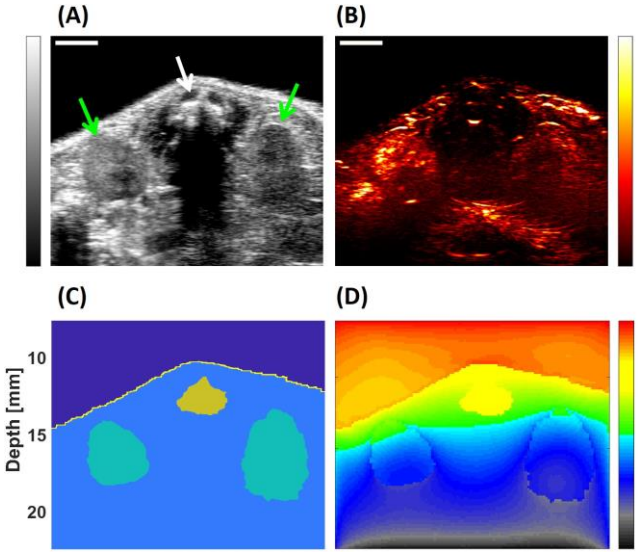

Fig. 6. Ultrasound (US) image, in grayscale, of the short axis view of the kidneys (green arrows), and the location of the spine is referred to by the white arrow (A); The respective photoacoustic (PA) image at 800nm shown in red scale (B); the scale bar size is 2mm. Segmentation mask obtained from US image (C) and light fluence distribution map at 800nm obtained by Monte Carlo simulations (D) that are used for the spectral decoloring approach included within the SPAX framework.

Fig. 6 (C) shows the segmented mask obtained from the US image used to guide the light fluence compensation approach included within the SPAX framework. Fig. 6 (D) shows the light fluence map obtained at 800 nm via Monte Carlo simulations that is based on the segmentation mask and the library of tissue optical properties. The light fluence map is obtained at all the

wavelengths used during the acquisition of sPAI, thus the acquired data are compensated for the light fluence inhomogeneity along depth and wavelengths.

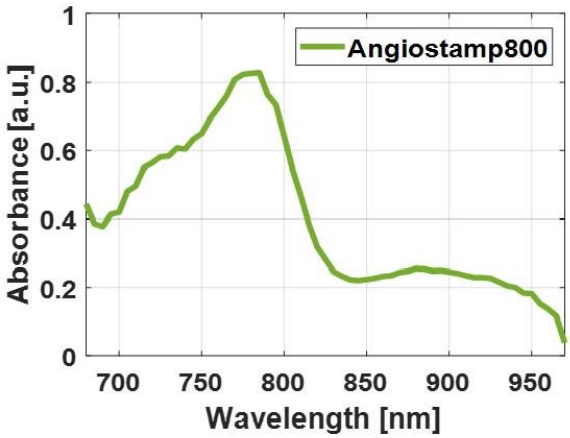

Fig. 7. Source spectra of oxy/deoxy hemoglobin and Angiostamp800 automatically extracted by the unsupervised SPAX framework (A). Abundance maps of oxy/deoxy hemoglobin and Angiostamp800 obtained before fluence compensation (B) and after fluence compensation (C) are depicted in red/blue and green color respectively; the scale bar size is 2mm.

After the fluence compensation, Fig. 7 shows one of the spectra automatically identified via the SPAX. Specifically, the Angiostamp800 spectral characteristics obtained without *a priori* information. As expected from the kinetics of the contrast agent, the Angiostamp800 is mainly distributed in the renal cortex as shown in Fig. 8 (A-B). From Fig. 8 (A-B) of the unmixed map of Angiostamp800 before and after fluence compensation, it is possible to observe changes in the uniformity of the intensity map along the depth. In particular, without applying the fluence compensation approach the map shows that the Angiostamp800 is distributed only on the top part of the renal cortex (see Fig. 8 (A)). This is a misinterpretation due to the light fluence degradation along depth. Fig. 8 (B) shows the distribution map of Angiostamp800 after the fluence compensation. From the image it is evident that the Angiostamp800 is uniformly distributed along the whole renal cortex.

The effect of fluence compensation along depth is also quantitatively shown in Fig. 8 (C), which depicts the SNR values obtained from the Angiostamp800 maps from the top (yellow arrow) and bottom (red arrow) parts of the kidney before and after fluence compensation. Without applying the fluence compensation (Φ Uncorrected) the SNR decreases from the top to the bottom part of the kidney. While, when the fluence compensation approach is applied (Φ Corrected), the SNR is higher and uniform from the top to the bottom part of the kidney.

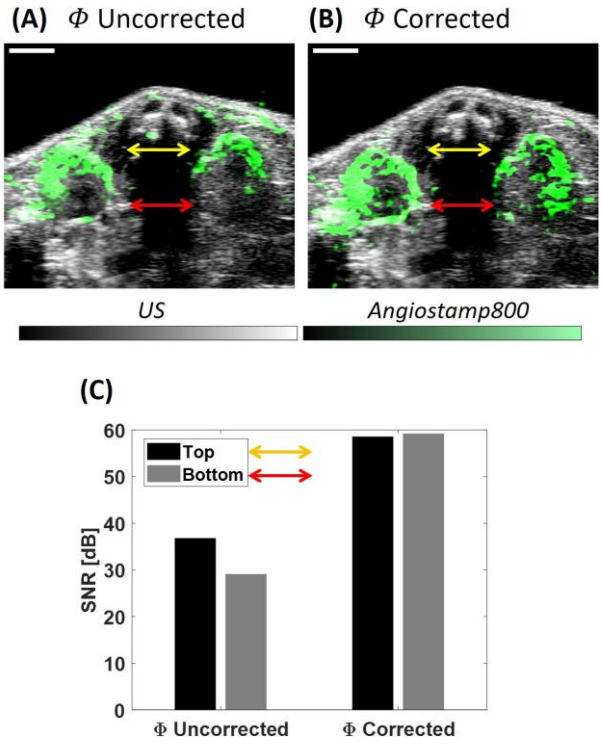

Fig. 8. Angiostamp800 unmixed maps in green color overlaid on US image used as anatomical guidance in grayscale before and after fluence compensation (A-B); the scale bar size is 2mm. The SNR values obtained along depth from the Angiostamp800 unmixed maps with and without fluence compensation (C).

6.3.3. *In vivo* endogenous chromophores

Fig. 9 (A) shows the US-PAI of the lower abdominal region of the mouse. In particular, the kidneys in the short axis view have been imaged, as indicated by the green arrows. Fig. 9 (B) shows the source spectral components obtained automatically by using the proposed approach. The red and blue spectral curves represent the oxy and deoxy hemoglobin respectively.

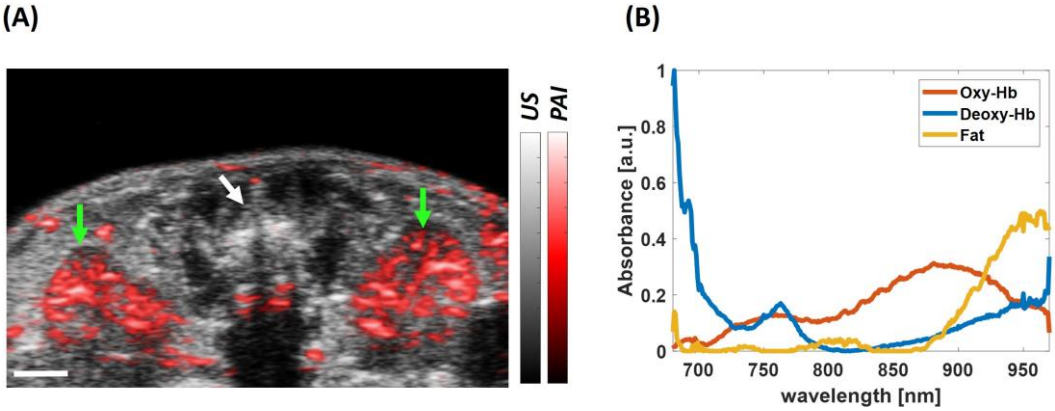

Fig. 9. Ultrasound (US) and Photoacoustic (PAI) images, in gray and red scale respectively, of the short axis view of the kidneys (green arrows), the location of the spine is referred by the white arrow (A); the scale bar size is 2mm. Source spectra of fat and oxy/deoxy hemoglobin automatically extracted by the unsupervised framework (B).

In addition, the fully automated algorithm showed a great potential to detect the adipose tissue component, depicted in yellow, which is typically difficult to differentiate without any *a priori* information or exogenous contrast. Fig. 10 (A-C) shows the distribution maps of oxy/deoxy hemoglobin and subcutaneous adipose tissue.

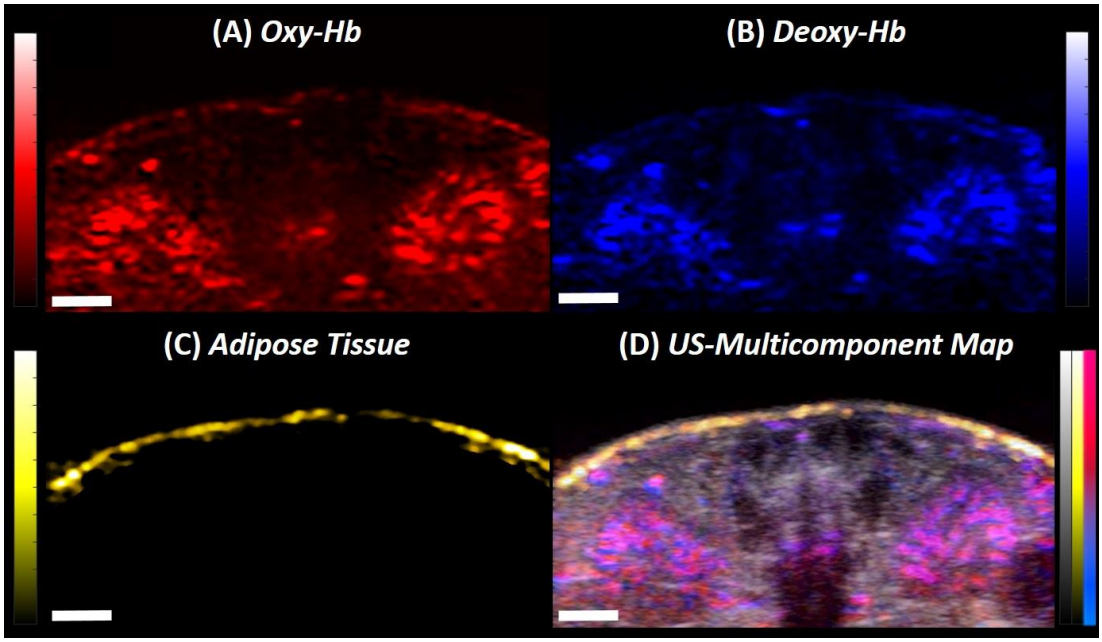

Fig. 10. Distribution maps automatically extracted by the unsupervised framework of oxygenated hemoglobin (A), deoxygenated hemoglobin (B), and subcutaneous lipid (C); Abundance maps of subcutaneous lipid (yellow map) and oxy/deoxy hemoglobin (red/blue map) overlaid on US image (gray map) (D); the scale bar size is 2mm.

Fig. 10 (D) shows the multi-parametric map of oxy/deoxy hemoglobin and lipid on the high-resolution US image. The red/blue scale represents the oxy/deoxy hemoglobin distribution which is mainly present in the kidneys' vessel network. While the yellow map, which refers to the adipose tissue content, is mainly distributed subcutaneously as expected in a healthy animal.

The results obtained *in vivo* have shown the feasibility of the automatic SPAX approach to extract less and most prominent absorbers without *a priori* information.

Fig. 11 (A) shows the source components unmixed via SPAX algorithm on the interscapular region of the mouse *in vivo*. Although the sPAX automatically extracted seven components, here we reported five identified components of interest: oxygenated hemoglobin, deoxygenated hemoglobin, skin line, white adipose tissue (WAT), and water. These have a high correlation with the theoretical absorption spectra, reported in the literature, of oxygenated hemoglobin, deoxygenated hemoglobin, melanin, fat, and water respectively [13].

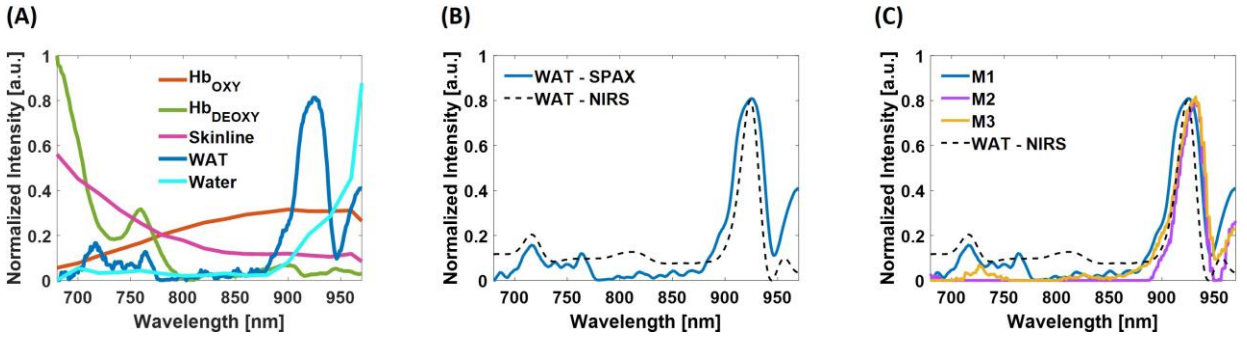

Fig. 11. Tissue component spectra unmixed by the SPAX from the cervical-thoracic area of the mouse *in vivo*. Oxygenated hemoglobin, deoxygenated hemoglobin, skinline, WAT, and water are the identified components from the seven source components (A). Comparison between the spectrum of WAT extracted by SPAX and the WAT absorption spectrum measured via NIRS (B). Comparison between the WAT spectrum extracted by SPAX from three different animals *in vivo* and the WAT absorption spectrum measured via NIRS (C).

For a qualitative validation of the spectra, spectral measures of endogenous chromophore via NIRS have been conducted. The interscapular fat pad has been dissected from the cervical-thoracic area of the mouse post-mortem and the sample has been prepared to contain pure fat. Thus, to avoid confounding factors and ensure the measure of the absorption spectrum from the fat only. NIRS measurements have been performed and used as a reference to validate the unmixed spectra via SPAX. Finally, the obtained NIR spectrum has been compared with the WAT spectrum automatically unmixed *in vivo* from sPAI. Fig. 11 (B) shows the overlay of the measured spectrum of WAT via NIR spectrophotometer and the spectrum automatically unmixed via SPAX from the sPAI data. Spectrally, the WAT absorbs primarily in the 900–950 nm region, as shown by the measured signature of the dissected interscapular fat pad acquired by the NIR spectrophotometer. The obtained WAT spectrum, unmixed via SPAX, shows a characteristic peak at around 930 nm and a local maximum at around 750 nm, which are representative of absorption by lipids. Besides, the correlation values, between the unmixed spectrum of WAT and the NIRS reference, show that the SPAX approach could reveal the WAT presence even with skin intact during *in vivo* experiments with ~96% correlation. Fig. 11 (C) depicts the WAT components automatically extracted via SPAX from multiple animals, for a total number of three (M1, M2, and M3). The WAT spectrum obtained from NIRS is also plotted as a reference. Thus, in the inter-animals comparison, the WAT components obtained via SPAX have also shown a similar trend, maintaining the characteristic peak at around 930nm. The SPAX framework guarantees to distinguish the WAT, which is typically a weak absorber and difficult to unmix in the presence of highly absorbing components such as hemoglobin [42], [43], with a low residual spectral fit independently of tissue depth.

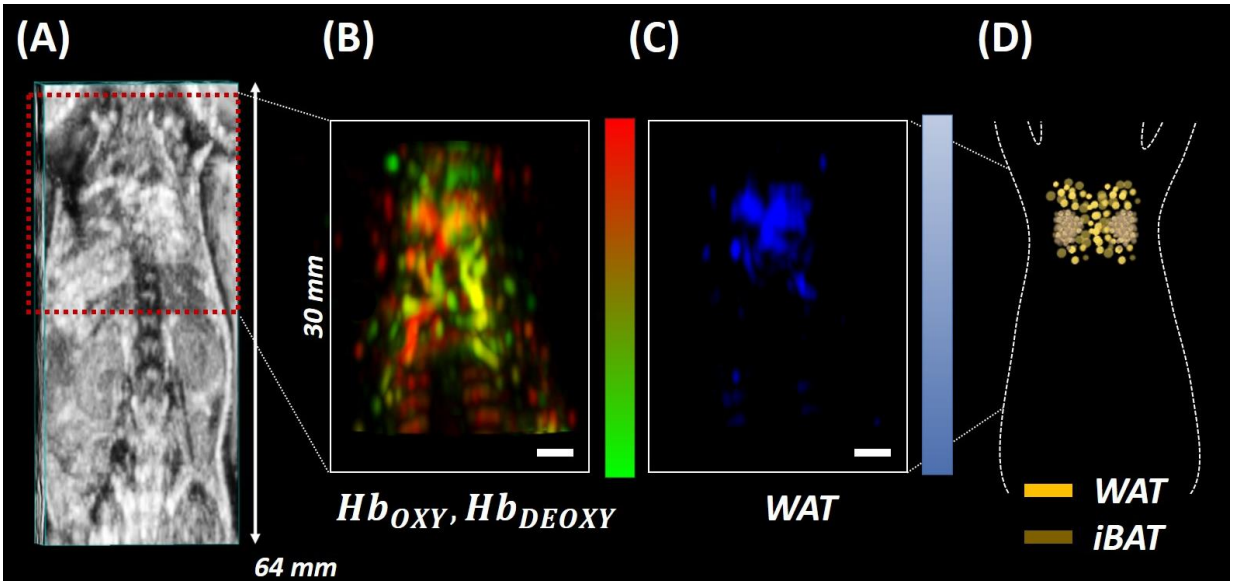

Fig. 12. Whole-body US image of the mouse in a prone position with the cervical-thoracic area highlighted by the red ROI (A); Oxy/deoxy hemoglobin (B) and WAT (C) abundance maps obtained via SPAX depicted in red/green and blue respectively. Schematic of a mouse interscapular adipose tissue including WAT and iBAT (D). The scale bar size is 2mm.

In addition to the unmixed spectra, Fig. 12 shows the abundance maps of the components of interest obtained from SPAX during *in vivo* acquisitions. The whole-body US image is obtained simultaneously during the sPAI acquisition, thus enabling the recognition of anatomical structures such as the cervical-thoracic area with high accuracy (see Fig. 12 (A)). Fig. 12 (B), depicts the oxy/deoxy hemoglobin distribution map in red/green respectively. Fig. 12 (C), shows the distribution map of WAT in the blue colormap that matches the WAT distribution within the interscapular region as confirmed by the schematic reported in Fig. 12 (D). High fidelity and quality of the tissue component unmixing maps were estimated with in situ visualization performed after dissection. In particular, as observed in Fig. 12 (D) from the schematic of the interscapular adipose tissue of a mouse, the WAT has an arrangement between the shoulders adjacent to the interscapular brown adipose tissue (iBAT) which has a bilateral symmetrical shape. The SPAX framework has distinguished WAT *in vivo*, non-invasively, and label-free. Therefore, it has been assessed that the adipose tissue can be separated from other tissue chromophores *in vivo*, within the NIR range of 680–970 nm. This has also been confirmed from *ex vivo* evaluations where it is possible to verify that the WAT is localized within the cervical-thoracic region and shows the same arrangement between the shoulders as automatically obtained *in vivo* via SPAX [43], [44]. The interscapular fat pad represents the largest brown adipose tissue (BAT) depot, located on the dorsal side of the animal, immediately inferior to the shoulders as shown from the rodents' atlas of adipose tissue by Zhang et al. [42]. The interscapular BAT (iBAT) is covered with white adipose tissue (WAT), which is highly efficient energy storage. Conventionally, the WAT is a weaker absorber that shows an absorption intensity of around two orders lower than BAT, thus it is difficult to be automatically differentiated [44].

In this study, the fat spectrum identified by SPAX (see Fig. 11), from healthy animals, shows the characteristic WAT peak at 930 nm, also confirmed by NIRS measurements. According to the adipose tissue atlas [42], the distribution map of fat obtained via SPAX is also matching the WAT distribution depicted in the schematic (see Fig. 12 (C-D)). On contrary, the iBAT significantly contributes to the nonshivering thermogenic response and regulates the body temperature homeostasis. Thus iBAT can be activated via cold exposure. Once activated, the iBAT becomes highly vascularized which may contribute to greater absorption than WAT. Beyond WAT, as demonstrated elsewhere [44], the activation of BAT can be also indirectly monitored by tracking hemodynamic changes as a marker of BAT's metabolic state. Thus the activation of BAT can be also monitored via sPAI. However, in this study, we focused on the label-free detection of less prominent tissue components such as WAT, via SPAX framework.

6.4. Discussion

Here, a recently developed unmixing framework named superpixel photoacoustic unmixing (SPAX) has been tested and validated experimentally [30]. Specifically, the SPAX framework includes multiple procedures to accurately identify the tissue composition by minimizing user interaction and *a priori* knowledge about the tissue components. Specifically, within the SPAX an initial fluence compensation step based on US image segmentation and spectral Monte Carlo simulation enables to mitigate unmixing misinterpretations caused by the spectral coloring artifact at depth. The singular value decomposition (SVD) analysis, included within the SPAX, allows the automated choice of the hyperparameter. Therefore, the SPAX framework has shown higher sensitivity than the classic blind source separation (BSS) methods for sPAI. Specifically, the SPAX approach is more robust against nonlinearities caused by inaccurate fluence estimation, converging to source components strengthened by a meaningful positivity constraint. Besides, when the mixing matrix is more ill-conditioned, as in the case of low SNR, SPAX provides significantly more accurate results as it is based on a parts-based decomposition. Besides, by including the innovative superpixel subsampling approach, the SPAX framework enables to automatically identify both strong and weak absorbers.

We have validated the SPAX on *in vitro* and preclinical *in vivo* studies focusing on the automated detection of less and most prominent endogenous and exogenous chromophores. Specifically, during *in vivo* experiments, the SPAX has shown the ability to detect endogenous and exogenous chromophores with higher sensitivity and specificity at depth. In addition, the SPAX enables to resolve not only hemoglobin, considered the main source of endogenous contrast in sPAI, but also less prominent and weaker tissue absorbers such as white adipose tissue (WAT) which is an important biomarker in several diseases [45]. Finally, the results obtained from the cervical-thoracic area in 3D via SPAX have been compared to the NIR spectroscopic measures. A Pearson's correlation value of 96% has been obtained for the WAT, thus showing the high sensitivity of SPAX to unmix WAT from highly absorbing components. Therefore, it has been assessed that by using SPAX the WAT can be separated from other tissue chromophores *in vivo*, non-invasively, and label-free within the NIR range of 680–970 nm.

Although the SPAX framework has demonstrated exemplary performance as a data-driven unmixing approach for sPAI, additional aspects can still compromise the performance of the spectral unmixing. For instance, the accuracy of the spectral photoacoustic imaging reconstruction could also impact the unmixing. Specifically, the recorded photoacoustic spectral signals can be corrupted by many noise sources. To overcome this limitation, advanced image reconstruction techniques, which lead to a reduced alteration caused by artifacts and noise [46], have been developed to guarantee higher quality sPAI and, consequently, more robust unmixing results. Moreover, spectral unmixing still has absolute quantification limits caused by additional uncertainties within the spectral coloring compensation. Specifically, improved measurements of the tissue properties, system response, and Gruneisen parameter are still required. To this end, Brochu et al. [47] have demonstrated to retrieve the tissue optical properties iteratively using finite element-based simulations, thus no predefined library of properties is needed. Besides, deep learning approaches based on non-explicit light fluence estimation have been proposed [48] for application-specific tasks. Thus, in the future, developing deep learning approaches that can be data-driven based would be beneficial.

Furthermore, blind approaches like SPAX produce a number of components that need to be visually inspected by an expert to select the most relevant one based on experience and prior knowledge or determined using e.g. a spectrophotometer. This may introduce uncertainties, especially, in pathological conditions where there is no theoretical comparison with the spectral components automatically unmixed. Thus, future implementations of prediction models based on simulations could help to recognize meaningful features and their relation with specific disease conditions. Finally, to promote the clinical translation of the sPAI technology real-time unmixing processing would be beneficial. Typically, spectral unmixing techniques are not feasible for real-time applications due to the long acquisition time associated with transmitting multiple laser wavelengths in sPAI. Thus, further efforts would be required to adjust the tradeoff between acquisition time and spectral resolution. Currently, the SPAX is optimized for spectral PAI including a spectral decoloring approach based on high-resolution US images and multi-wavelength Monte-Carlo light fluence simulations. This approach is ideal for accurate and highly sensitive offline unmixing analysis. However, opportunely choosing a minimum number of excitation wavelengths during PAI acquisition, which maintains the accuracy and sensitivity of the spectral unmixing approach, would reduce the acquisition and processing times. As already demonstrated by Luke et al. [32], the implementation of advanced algorithms for the selection of significant wavelengths could facilitate unsupervised unmixing using an optimum number of wavelengths, thus minimizing the acquisition time and speeding up the analysis.

In addition to the number of wavelengths, the linear motor step size and consequently the number of slices of 3D multi-wavelength data also limits the real-time acquisition. Thus, the motor step size can be selected to minimize imaging artifacts by maintaining a good compromise between speed of acquisition, resolution, and continuity of volumetric imaging. Besides, the optimization of spectral Monte Carlo simulations for fluence compensation by using GPU-based implementations would also speed up the computational processing time, encouraging the use

of SPAX in further applications. By optimizing these parameters, acquisition and processing time can be improved, thus facilitating the translation of the approach into clinical practice.

References

[1] M. Xu and L. V. Wang, "Photoacoustic imaging in biomedicine," *Rev. Sci. Instrum.*, vol. 77, no. 4, 2006.

[2] B. Cox, J. G. Laufer, S. R. Arridge, and P. C. Beard, "Quantitative spectroscopic photoacoustic imaging: a review," *J. Biomed. Opt.*, vol. 17, no. 6, p. 061202, 2012.

[3] E. Y. Park, S. Park, H. Lee, M. Kang, C. Kim, and J. Kim, "Simultaneous dual-modal multispectral photoacoustic and ultrasound macroscopy for three-dimensional whole-body imaging of small animals," *Photonics*, 2021.

[4] C. Li and L. V. Wang, "Photoacoustic tomography and sensing in biomedicine," *Physics in Medicine and Biology*, vol. 54, no. 19. 2009.

[5] S. Manohar and D. Razansky, "Photoacoustics: a historical review," *Adv. Opt. Photonics*, vol. 8, no. 4, 2016.

[6] M. Suheshkumar Singh, S. Paul, and A. Thomas, "Fundamentals of Photoacoustic Imaging: A Theoretical Tutorial," 2020.

[7] D. Biqin, C. Sun, and H. F. Zhang, "Optical Detection of Ultrasound in Photoacoustic Imaging," *IEEE Transactions on Biomedical Engineering*, vol. 64, no. 1. 2017.

[8] F. Gao, X. Feng, and Y. Zheng, "Coherent photoacoustic-ultrasound correlation and imaging," *IEEE Trans. Biomed. Eng.*, vol. 61, no. 9, 2014.

[9] V. Ntziachristos and D. Razansky, "Molecular imaging by means of multispectral optoacoustic tomography (MSOT)," *Chem. Rev.*, vol. 110, no. 5, 2010.

[10] J. Weber, P. C. Beard, and S. E. Bohndiek, "Contrast agents for molecular photoacoustic imaging," *Nature Methods*, vol. 13, no. 8. 2016.

[11] J. Brunker, J. Yao, J. Laufer, and S. E. Bohndiek, "Photoacoustic imaging using genetically encoded reporters: a review," *J. Biomed. Opt.*, vol. 22, no. 7, 2017.

[12] L. V. Wang, "Multiscale photoacoustic microscopy and computed tomography," *Nat. Photonics*, vol. 3, no. 9, 2009.

[13] S. L. Jacques, "Optical properties of biological tissues: A review," *Physics in Medicine and Biology*, vol. 58, no. 11. 2013.

[14] D. Wu, L. Huang, M. S. Jiang, and H. Jiang, "Contrast agents for photoacoustic and thermoacoustic imaging: A review," *International Journal of Molecular Sciences*. 2014.

[15] J. Jose, S. Manohar, R. G. M. Kolkman, W. Steenbergen, and T. G. Van Leeuwen, "Imaging of tumor vasculature using Twente photoacoustic systems," vol. 717, no. 12, pp. 701–717, 2009.

[16] J. G. Laufer *et al.*, "In vivo preclinical photoacoustic imaging of tumor vasculature development and therapy," *J. Biomed. Opt.*, vol. 17, no. 5, 2012.

[17] S. Mallidi, G. P. Luke, and S. Emelianov, "Photoacoustic imaging in cancer detection, diagnosis, and treatment guidance," *Trends in Biotechnology*, vol. 29, no. 5. 2011.

[18] C. M. Deroose *et al.*, "Multimodality imaging of tumor xenografts and metastases in mice with combined small-animal PET, small-animal CT, and bioluminescence imaging," *J. Nucl. Med.*, vol. 48, no. 2, 2007.

[19] R. T. Zaman *et al.*, "A Dual-Modality Hybrid Imaging System Harnesses Radioluminescence and Sound to Reveal Molecular Pathology of Atherosclerotic Plaques," *Sci. Rep.*, vol. 8, no. 1, 2018.

[20] M. Capozza *et al.*, "Photoacoustic imaging of integrin-overexpressing tumors using a novel ICG-based contrast agent in mice," *Photoacoustics*, vol. 11, 2018.

[21] M. Halicek, H. Fabelo, S. Ortega, G. M. Callico, and B. Fei, "In-vivo and ex-vivo tissue analysis through hyperspectral imaging techniques: Revealing the invisible features of cancer," *Cancers*, vol. 11, no. 6. 2019.

[22] G. P. Luke, D. Yeager, and S. Y. Emelianov, "Biomedical applications of photoacoustic imaging with exogenous contrast agents," *Ann. Biomed. Eng.*, vol. 40, no. 2, 2012.

[23] Y. Cao *et al.*, "Spectral analysis assisted photoacoustic imaging for lipid composition differentiation," *Photoacoustics*, 2017.

[24] D. J. Lawrence, M. E. Escott, L. Myers, S. Intapad, S. H. Lindsey, and C. L. Bayer, "Spectral photoacoustic imaging to estimate in vivo placental oxygenation during preeclampsia," *Sci. Rep.*, vol. 9, no. 1, 2019.

[25] C. Bench and B. Cox, "Quantitative photoacoustic estimates of intervascular blood oxygenation differences using linear unmixing," *J. Phys. Conf. Ser.*, 2021.

[26] S. Tzoumas *et al.*, "Eigenspectra optoacoustic tomography achieves quantitative blood oxygenation imaging deep in tissues," *Nat. Commun.*, 2016.

[27] D. A. Durairaj, S. Agrawal, K. Johnstonbaugh, H. Chen, S. P. K. Karri, and S.-R. Kothapalli, "Unsupervised deep learning approach for photoacoustic spectral unmixing," 2020.

[28] M. U. Arabul, M. C. M. Rutten, P. Bruneval, M. R. H. M. van Sambeek, F. N. van de Vosse, and R. G. P. Lopata, "Unmixing multi-spectral photoacoustic sources in human carotid plaques using non-negative independent component analysis," *Photoacoustics*, vol. 15, no. June, p. 100140, 2019.

[29] V. Grasso, J. Holthof, and J. Jose, "An automatic unmixing approach to detect tissue chromophores from multispectral photoacoustic imaging," *Sensors (Switzerland)*. 2020.

[30] V. Grasso, R. Willumeit-Römer, and J. Jose, "Superpixel spectral unmixing framework for the volumetric assessment of tissue chromophores: A photoacoustic data-driven approach," *Photoacoustics*, vol. 26, p. 100367, 2022.

[31] G. Matrone, A. S. Savoia, G. Caliano, and G. Magenes, "The delay multiply and sum beamforming algorithm in ultrasound B-mode medical imaging," *IEEE Trans. Med. Imaging*, 2015.

[32] G. P. Luke, S. Y. Nam, and S. Y. Emelianov, "Optical wavelength selection for improved spectroscopic photoacoustic imaging," *Photoacoustics*, vol. 1, no. 2, pp. 36–42, 2013.

[33] J. Lavaud *et al.*, "Noninvasive monitoring of liver metastasis development via combined multispectral photoacoustic imaging and fluorescence diffuse optical tomography," *Int. J. Biol. Sci.*, vol. 16, no. 9, 2020.

[34] H. W. Hassan, A. Mathew, H. Khan, O. Korostynska, and P. Mirtaheri, "Feasibility Study of Multi-Wavelength Optical Probe to Analyze Magnesium Implant Degradation Effects," in *Proceedings of IEEE Sensors*, 2021, vol. 2021-October.

[35] H. W. Hassan, V. Grasso, O. Korostynska, H. Khan, J. Jose, and P. Mirtaheri, "An overview of assessment tools for determination of biological Magnesium implant degradation," *Medical Engineering and Physics*, vol. 93. 2021.

[36] IEC, "IEC 80601-2-71 : 2015 Medical electrical equipment – Part 2-71: Particular requirements for the basic safety and essential performance of functional near-infrared spectroscopy (NIRS) equipment," *Int. Stand.*, vol. EN80601, no. Part 2-71, 2015.

[37] S. Feng, F.-A. Zeng, and B. Chance, “Photon migration in the presence of a single defect: a perturbation analysis,” *Appl. Opt.*, vol. 34, no. 19, 1995.

[38] G. H. Weiss, R. Nossal, and R. F. Bonner, “Statistics of penetration depth of photons re-emitted from irradiated tissue,” *J. Mod. Opt.*, vol. 36, no. 3, 1989.

[39] E. S. Papazoglou, M. S. Weingarten, L. Zubkov, L. Zhu, S. Tyagi, and K. Pourrezaei, “Optical properties of wounds: Diabetic versus healthy tissue,” *IEEE Trans. Biomed. Eng.*, vol. 53, no. 6, 2006.

[40] F. M. Brochu, J. Joseph, M. Tomaszewski, and S. E. Bohndiek, “Light fluence correction for quantitative determination of tissue absorption coefficient using multi-spectral optoacoustic tomography,” vol. 9539, pp. 1–8, 2015.

[41] R. L. P. van Veen, H. J. C. M. Sterenborg, A. Pifferi, A. Torricelli, and R. Cubeddu, “Determination of VIS- NIR absorption coefficients of mammalian fat, with time- and spatially resolved diffuse reflectance and transmission spectroscopy,” in *Optics InfoBase Conference Papers*, 2004.

[42] F. Zhang *et al.*, “An Adipose Tissue Atlas: An Image-Guided Identification of Human-like BAT and Beige Depots in Rodents,” *Cell Metab.*, vol. 27, no. 1, 2018.

[43] D. P. Bagchi and O. A. Macdougald, “Identification and dissection of diverse mouse adipose depots,” *J. Vis. Exp.*, vol. 2019, no. 149, 2019.

[44] J. Reber *et al.*, “Non-invasive Measurement of Brown Fat Metabolism Based on Optoacoustic Imaging of Hemoglobin Gradients,” *Cell Metab.*, vol. 27, no. 3, 2018.

[45] B. Erhayiem, R. Dhingsa, C. J. Hawkey, and V. Subramanian, “Ratio of Visceral to Subcutaneous Fat Area Is a Biomarker of Complicated Crohn’s Disease,” *Clin. Gastroenterol. Hepatol.*, vol. 9, no. 8, 2011.

[46] Y. Han, S. Tzoumas, A. Nunes, V. Ntziachristos, and A. Rosenthal, “Sparsity-based acoustic inversion in cross-sectional multiscale optoacoustic imaging,” *Med. Phys.*, vol. 42, no. 9, 2015.

[47] F. M. Brochu, J. Brunker, J. Joseph, M. R. Tomaszewski, S. Morscher, and S. E. Bohndiek, “Towards quantitative evaluation of tissue absorption coefficients using light fluence correction in optoacoustic tomography,” *IEEE Trans. Med. Imaging*, 2017.

[48] J. Li *et al.*, “Deep learning-based quantitative optoacoustic tomography of deep tissues in the absence of labeled experimental data,” *Optica*, vol. 9, no. 1, 2022.

Chapter 7

Photoacoustic imaging to monitor the remodeling of soft tissues surrounding a biodegradable bone implant made of Magnesium*

Abstract:

In this chapter, we investigated the potential of ultrasound and photoacoustic (US-PA) imaging to non-invasively monitor soft tissue remodeling in the presence of biodegradable bone implants. In particular, the newly developed Superpixel Photoacoustic Unmixing (SPAX) framework has been applied to *in vivo* monitor tissue remodeling in presence of Magnesium-based (Mg) implants without any user interaction. Mg-based implants are an innovative alternative to bio-inert implants used to treat bone fractures. SPAX data-driven approach has shown great potential to automatically distinguish the implant from the surrounding soft tissues. Besides, correlation analysis has been performed to estimate hemoglobin spectral changes as well as measurements of oxygen saturation (SO_2) longitudinally. These measures represent promising biomarkers to study inflammatory response and tissue oxygenation function in bone regeneration.

*Part of this chapter has been published as: Hassan, H.W., **Grasso, V.**, Korostynska, O., Khan, H., Jose, J., & Mirtaheri, P. (2021). *"An overview of assessment tools for determination of biological Magnesium implant degradation."* Medical Engineering & Physics, 93, 49-58.

*Part of this chapter has been published as: Hassan, H.W., Mota-Silva, E., **Grasso, V.**, Riehakainen, L., Jose, J., Menichetti, L., & Mirtaheri, P. (2023). *"Near-infrared spectroscopy for the in vivo monitoring of biodegradable implants in rats."* Sensors, 23(4), 2297.

7.1. Introduction

Photoacoustic imaging (PAI) combines the advantages of ultrasound and optical methods [1]. Currently, most optical imaging technologies use lasers or light-emitting diodes (LED) as a probing source with the added advantage of being non-ionizing and the possibility of performing spectroscopic imaging. Optical imaging techniques such as confocal microscopy (CM) and optical coherence tomography (OCT) enable resolution at the micron level at a limited imaging depth. Diffuse Optical tomography (DOT) is another commonly used imaging technique for the detection of molecular composition in tissue, and this approach enables deeper imaging (< 100mm) but with a resolution in millimeters. Conversely, as a hybrid modality combining optical and acoustic advantages, PAI offers a good compromise of visualizing tissue structures with micrometer resolution at deeper imaging depth (up to several centimeters). Since ultrasound scattering is two to three orders of magnitude weaker than optical scattering in biological tissues [1], PAI can provide a better resolution than pure optical imaging by detecting acoustic phonons instead of ballistic photons. PAI has been used in a wide range of applications such as imaging tissue vasculature and angiogenesis, detection of tumor metastases, tissue oxygen saturation changes, and therapy monitoring [2]–[4]. In addition to the endogenous absorbers, PAI is also used to detect exogenous contrast agents. Indocyanine Green (ICG) is an exogenous molecular imaging agent widely used for various near-infrared fluorescence imaging technologies and ideally applied to PAI. Naturally, the use of contrast agents enhances the optical contrast increasing the PAI intensity. ICG is a clinically approved dye detected using photoacoustic in several medical applications such as cardiology, liver function, perfusion studies, ophthalmic angiography, and cancer imaging [5]–[9]. Besides, the potential to image lymphatic drainage has been shown by performing ICG lymphography in patients with severe lymphedema [10]. Recently, PAI has also been used to monitor metallic implants and improve surgical procedures. Considering the high absorption coefficient in the near-infrared (NIR) range of the metal or composite materials, PAI is well-suited to image coronary artery stents, needles, dental prostheses, and brachytherapy seeds. Su et al. demonstrate the ability to visualize the vascular stent during the surgery positioning procedure and post-surgery evaluations by using PAI [11]. Further, Lee et al. have conducted *ex vivo* PAI of a dental implant embedded in a porcine jawbone. In the study, they showed that PAI could provide information regarding the implant fixture, the bone anatomical features, and the thickness of the soft tissue above the bone [12].

Considering the current developments, PAI is a promising technology to follow the evolution of tissue remodeling in the presence of advanced biodegradable Magnesium-based (Mg) implants [13]–[15]. The PAI technology can image functional/molecular information by using the optical absorption of oxygenated and deoxygenated hemoglobin in the vicinity of the Mg-based implant. Indeed, continuous assessments of the oxygenation levels are essential to early identify issues due to the implantation procedure, as well as to follow up on the bio integration between the living tissues and the metallic implant. As an example, inadequate and prolonged tissue oxygenation indicates irreversible tissue damage. However, if an inflammatory response occurs, there will be oxygenation variations and spectral molecular alterations. The excitation laser used

for PAI is tunable in the NIR wavelength range; hence it is possible to illuminate the tissues sequentially at different wavelengths. Multi-wavelength photoacoustic imaging modality (also referred to as spectral PAI) can be used to also monitor other endogenous biomarkers such as melanin and lipids and the detection of exogenous contrast agents [16], [17]. Since the tissue chromophores have distinct spectral signatures, multi-wavelength PAI can also be used to monitor the tissue's spectral changes, which could be related to the disease conditions. For example, if the metallic implant alters the tissue's physiological state, hemoglobin spectral variations or additional absorbers could be detected using a multi-spectral PAI approach. Multispectral PAI acquisitions, commonly use linear regression algorithms to separate the different chromophores. These techniques have the limitation of being dependent on *a priori* knowledge of spectral signatures. Especially during inflammatory responses, this approach can be challenging due to the high variability and unpredictability of the absorption of the spectral components. Indeed research efforts have been focused on developing automatic unmixing methods based on blind source separation algorithms that can be used to detect the prominent and less prominent absorbers in the tissue without any user interactions [18], [19].

Here we investigated the use of a newly developed superpixel photoacoustic unmixing SPAX framework [20] to reveal the tissue components in presence of Mg-based implants in a data-driven way. This automated processing will open many possibilities for unbiased investigations in tissue composition and remodeling in presence of biodegradable implants.

7.1.1. Background of Mg-based implants and tissue response

The main advantage of Magnesium (Mg) based metal implants over standard permanent materials is their biodegradability. Thus, the removal operation can be avoided after the bone healing is completed and the implant has accomplished its fixation function during bone injury treatment. Besides, Magnesium and its alloys corrode within living tissues without generating any toxic products. This characteristic makes them suitable candidate materials for biodegradable temporary implants. However, pure Mg has a very high corrosion rate that limits its use as a bone implant since this can lead to mechanical instability even before bone healing is completed. On the other hand, low degradation can lead to inappropriate tissue response causing complications. To this end, alloying has been used as a possible strategy to improve the corrosion rate, mechanical properties, and production cost of Magnesium [21]. The basic elements commonly used for Mg alloying are Al, Ca, Cu, Fe, Li, Mn, Ni, Sr, Y, Zn, Zr, and rare earth elements [22], [23].

The basic corrosion reactions are influenced, as well as affect, the environment around the implant. In particular, Mg alloy after insertion into the organism, corrode by mainly releasing Magnesium hydroxide ($Mg(OH)_2$) and hydrogen gas. $Mg(OH)_2$ is not soluble and forms a protective layer on the alloy surface. The amount of tissue water and blood flow can affect the removal of degradation products and prevent the formation of this protective layer on the material surface [21]. Thus, the tissue response to the Mg and Mg alloy degradation can determine the implant's success or failure [22], [24].

Some of the main *in vivo* tissue interactions/responses in presence of biodegradable implants are the following:

- The bone healing process is mainly related to highly complex osteoclast and osteoblast activity [25].
- Blood vessel formation, or angiogenesis, and tissue regeneration that are crucial parts of tissue healing [26]. Adequate vascularization of the peri-implant zone is crucial for bone healing [27].
- The inflammatory response in presence of degrading implants plays also a vital role in well-coordinated tissue damage and subsequent repairing processes [28], [29].

Most of the current works on the Mg implant follow-up focus on structural bone remodeling, however functional and molecular assessment plays a crucial role in providing information about physiological changes in tissues, which can be used as an early indicator of healing. To this end, it is crucial to monitor the soft tissue remodeling at early time points [30] to detect the tissue changes and predict acute and chronic inflammatory responses [31] that can affect implantation success at later stages. Thus, PAI can be an ideal imaging technology with a high potential for monitoring the surrounding tissues' revascularization and inflammation in presence of Mg-based implants. In particular, PAI has a unique ability to image many endogenous molecules involved in the angiogenetic and inflammatory process, such as hemoglobin and collagen, as well as label other inflammatory cells or molecules using exogenous contrast agents as described elsewhere [32]–[35].

Tang et al. showed that PAI can monitor spectral changes in hemoglobin that may be related to methemoglobin. Methemoglobin is an abnormal type of hemoglobin that contains oxidized iron atoms in the ferric state and is incapable of transporting oxygen that can potentially have a role in inflammation [36]–[38]. Besides, oxygen saturation (SO_2) changes represent a crucial biomarker to estimate angiogenesis at early time points and predict implant osseo-integration at later stages [39].

The purpose of this study is to investigate the potential of the Superpixel Spectral unmixing approach (SPAX) for the *in vivo* monitoring of spectral hemoglobin changes and oxygen saturation (SO_2). The spectral molecular changes can be used as a possible biomarker to indicate tissue remodeling during implant degradation. In particular, the combination of ultrasound-photoacoustic (US-PA) imaging and highly sensitive data-drive unmixing approaches, such as the recently developed SPAX [20] can help to detect specific tissue components for monitoring Mg implant degradation level, tissue regeneration, and inflammatory condition with enhanced specificity. The hybrid US-PA technology can provide anatomical, functional, and molecular information simultaneously. US-PA has the potential to non-invasively characterize the tissue composition in living tissues without the use of ionizing radiations.

7.2. Materials and methods

7.2.1. Tissue-mimicking phantom

To evaluate the spectral characteristics of Mg implants, multi-spectral PAI of a tissue-mimicking phantom has been performed. Fig. 1 depicts the tissue-mimicking phantom setup, which includes an Mg pin and a capillary tube filled with Indocyanine Green (ICG). Both samples were inserted into a chicken breast at a depth of 10mm from the surface and carefully positioned with a spacing of 5 mm. The diameter of the Mg pin (XHP − ZX00 MgZnCa, BRI.TECH GmbH) was 1.6 mm, and the length was 8 mm. A capillary polyethylene tube (inner diameter ≈380 µm, outer diameter ≈840 µm, and 16.5 mm length) was filled with Indocyanine Green (ICG, PULSION Verwaltungs, GmbH), which was obtained at a concentration of 800 µM by resuspending 25 mg vial of ICG in sterile water. Multispectral PAI was performed with Vevo LAZR-X (FUJIFILM VisualSonics, Inc., Toronto, ON, Canada) with a linear array transducer of central frequency 21MHz (MX250). The details of the PAI setup can be found elsewhere [19], [20].

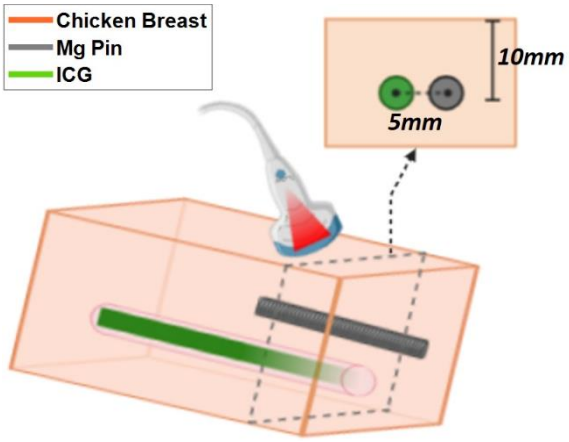

Fig. 1. Schematic of the tissue-mimicking phantom including Mg pin and ICG capillary tube embedded in chicken breast.

7.2.2. *In vivo* study

The *in vivo* experiments involved female Wistar rats of twelve-week-old. Animals were anesthetized with an intraperitoneal injection of 5 mg/kg Xylazine (Rompum Elanco, Italy) and 10 mg/kg Zoletil (Virbac, Switzerland). Before surgery, the hind limbs were shaved using a depilatory cream. During the surgery, an incision was made on the leg's lateral, and the Biceps Femoris muscles were carefully teased away to expose the diaphyseal region of the femur. A transcortical hole on the femur has been created with a 1.55 mm diameter drill. A low drilling rotational speed was selected, and physiological saline (Fresenius Kabi, Italy) was dripped to minimize frictional heat and thermal damage to the tissue. Both hind limbs of a group of 5 animals were implanted with Mg alloy pin implants (WE43, Syntellix AG, Hannover, Germany) with a length of 8 mm and 1.6 mm in diameter. Another group of 5 animals got both hind limbs implanted with equivalent

geometry of Titanium (Ti) pin implants. The cylindrical implant is inserted by gentle tapping, resulting in a uniform press fit. After pin placement, the wound site is cleaned with sterile cotton tips for remaining bone debris and the wound is closed with resorbable sutures (Johnson & Johnson Medical, Italy). Fig. 2 shows the μCT image of the implanted hind limb of the rat with Mg pins, 45 days after the surgery. The Sham group was composed of 3 animals. Both hind limbs of each animal of the Sham group received the same surgical procedure, but no implant has been inserted in the femur hole.

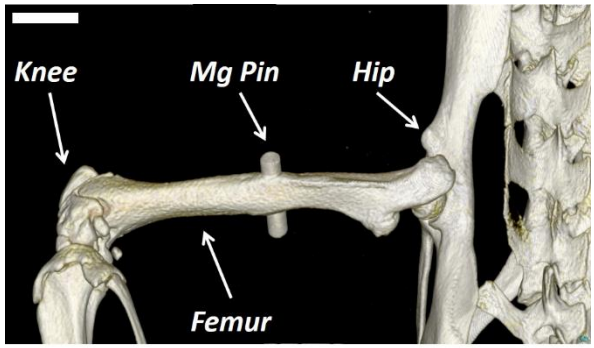

Fig. 2. μCT image of the implanted hind limb of the rat with Mg pin 45 days after the surgery; the scale bar size is 2 mm.

All *in vivo* experiments were carried out in accordance with the National Ethical Guidelines (Italian Ministry of Health; D.L.vo 26/2014) and the guidelines from Directive 2010/63/EU of the European Parliament. The protocol was approved by the Instituto Superiore di Sanità on behalf of the Italian Ministry of Health and Ethical Panel (Prot. n° 299/2020-PR) and the local ethics committee. Additionally, the protocol conformed to the ARRIVE guidelines.

Table 1 summarizes the total number of animals per group along time points where the right and left hind limbs of the same animal are considered separate samples.

Table 1. The number of limbs/samples (n) involved in the *in vivo* analysis per group along the time points.

Group	D3	D7	D14	D28	D45
Sham	**6**	**6**	**6**	**6**	**6**
Ti	**10**	**10**	**10**	**10**	**6**
Mg	**10**	**10**	**10**	**10**	**10**

7.2.3. *In vivo* US-PA imaging protocol

In vivo US-PA imaging studies with transcortical femur implantation rat models have been performed longitudinally. High-resolution Ultrasound (US) and Photoacoustic (PA) imaging (US-PA) have been acquired by using the platform Vevo LAZR-X (FUJIFILM VisualSonics, Inc., Toronto, ON, Canada). A linear US transducer array (MX550S) consisting of 256 elements at a nominal

center frequency of 40 MHz and bandwidth of 25-55 MHz, is coupled with narrow optical fibers, mounted on either side of the transducer. This high-frequency transducer guarantees high spatial resolution (axial resolution of ≈40 μm and lateral resolution of ≈80 μm), and the narrow optical fibers enable focused illumination. Homogenous light illumination is guaranteed by placing the sample to be imaged on the converging area of the two light beams. Spectral photoacoustic imaging (sPAI) has been performed, within the wavelength range of 680-970 nm with a 1nm step [40]. The imaging acquisition has been conducted on the implanted rats' hind limbs positioned on their lateral recumbency on days 3, 7, 14, 28, and 45 after surgery. Rats were anesthetized with isoflurane (2%-3% by volume with 0.8l/min gas flow) and the transducer was aligned perpendicularly to image the region of interest.

7.2.4. Superpixel photoacoustic unmixing (SPAX) and analysis

For the *in vivo* study instead of using the conventional linear unmixing approach which requires the absorption spectra of the expected tissue components as *a priori* information [41], we have used a newly developed superpixel data-driven unmixing (SPAX) framework described in detail elsewhere [20]. In addition to the automated detection of the HbO_2 and Hb content, the characteristic broad absorption spectrum of the metallic implant and its spatial distribution has also been obtained by the unsupervised SPAX approach. The framework implements an SVD-based analysis to automatically distinguish the relevant spectral information above the noise level. SPAX is also extended to compensate for the spectral coloring artifact combining US image segmentation and spectral Monte Carlo (MC) light fluence simulations based on a predefined library of tissue optical properties. Besides, the advanced superpixel subsampling integrated within SPAX enables to detect less and most prominent components, without *a priori* information.

After the spectral unmixing, the identified endogenous tissue chromophore spectra were correlated with the theoretical absorption spectra [42]. In addition to the unmixed chromophore spectra and correlation, the oxygen saturation (SO_2) of the surrounding soft tissue was also evaluated. Specifically, the SO_2 has been calculated from the normalized unmixed maps of HbO_2 and Hb, obtained as the output of the SPAX analysis. When the implant is present (for Ti and Mg groups), its normalized unmixed map has been used to exclude the pixels of the implanted area, if any, from the HbO_2 and Hb maps. This ensures a more accurate SO_2 evaluation, since eventual artifact pixels coming from the implant area in the HbO_2 and Hb maps are excluded.

Thus, the oxygen saturation has been evaluated from the unmixed maps of oxy/deoxy hemoglobin, obtained *in vivo* via the SPAX, as follows:

$$SO_2 = \frac{mean\ (HbO_2)}{[mean\ (HbO_2) + mean(Hb)]} \quad (1)$$

where the mean value of the non-zero pixels of the HbO_2 and Hb maps has been used. The SO_2 values might be related to angiogenesis phenomena occurring during the healing process. In

particular, the new vessel formation can be indirectly monitored as a function of the SO_2. Therefore, the correlation analysis and the SO_2 measures are used as possible biomarkers that indicate the soft tissue remodeling in presence of the bone implant.

7.3. Results

7.3.1. Phantom imaging

Fig. 3 (A), shows the spectral curves of ICG and Mg pin in the wavelength range of 680 – 970nm. The spectral absorption graphs within the NIR range clearly show that Mg has a broad absorption spectrum, and the ICG has an absorption peak at around 880nm. Fig. 3 (B) shows the spectrally unmixed 3D PA image, where green and red voxels represent the spatial distribution of ICG and Mg, respectively. Since the chicken breast has limited absorption it is not detected but visible in the ultrasound image and represented in grayscale. When imaging in PA-Mode, the standard US transducer is combined with optical fibers fixed on the sides of the experimental setup. This guarantees that the high-resolution US images are naturally registered to the laser-induced PA ultrasonic signals during spectral PAI acquisition. Therefore it is evident that the co-registration of US-PA imaging demonstrates the feasibility of detecting anatomical, functional, and molecular information.

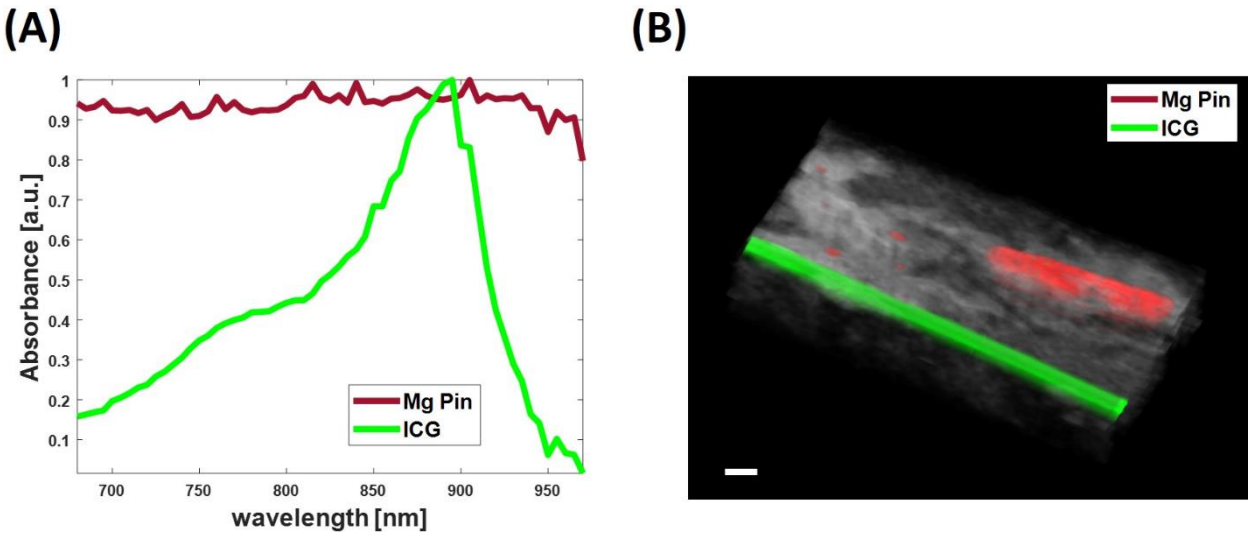

Fig. 3. Normalized intensity of PA absorbance spectral graphs of ICG and Mg pin (A). Spectrally unmixed 3D PA image (B); The scale bar size is 2 mm.

7.3.2. *In vivo* tissue monitoring

Here the longitudinal *in vivo* spectral data have been unmixed via SPAX and spectral variations as well as SO_2 changes have been evaluated. Fig. 4 shows the US image (grayscale) and PA image at 800nm (red scale) extracted from the multispectral data set of the implanted rats with an Mg pin. The US images in grayscale show the anatomy in detail. In particular, the image shows the cross-sectional view of the diaphyseal region of the femur, three days after implantation. Often, on day 3 after implantation, the hydrogen gas bubble generated by the degradation of the Mg

pin interacting with living tissues is visible. As shown in Fig. 4 (A), the presence of the gas bubble will cause an artifact that hides the tip of the pin, which is not visible. On contrary, Fig. 4 (B), shows the case where the gas bubble is resorbed and the tip of the pin is distinguishable as well as the surgical wound. Besides, the strong absorption from the tip of the pin might cause a reverberation artifact which is visible at the bottom of the PA image. Usually, at later time points, the bubble is resorbed and the US-PA view would be similar to the scenario shown in Fig. 4 (B).

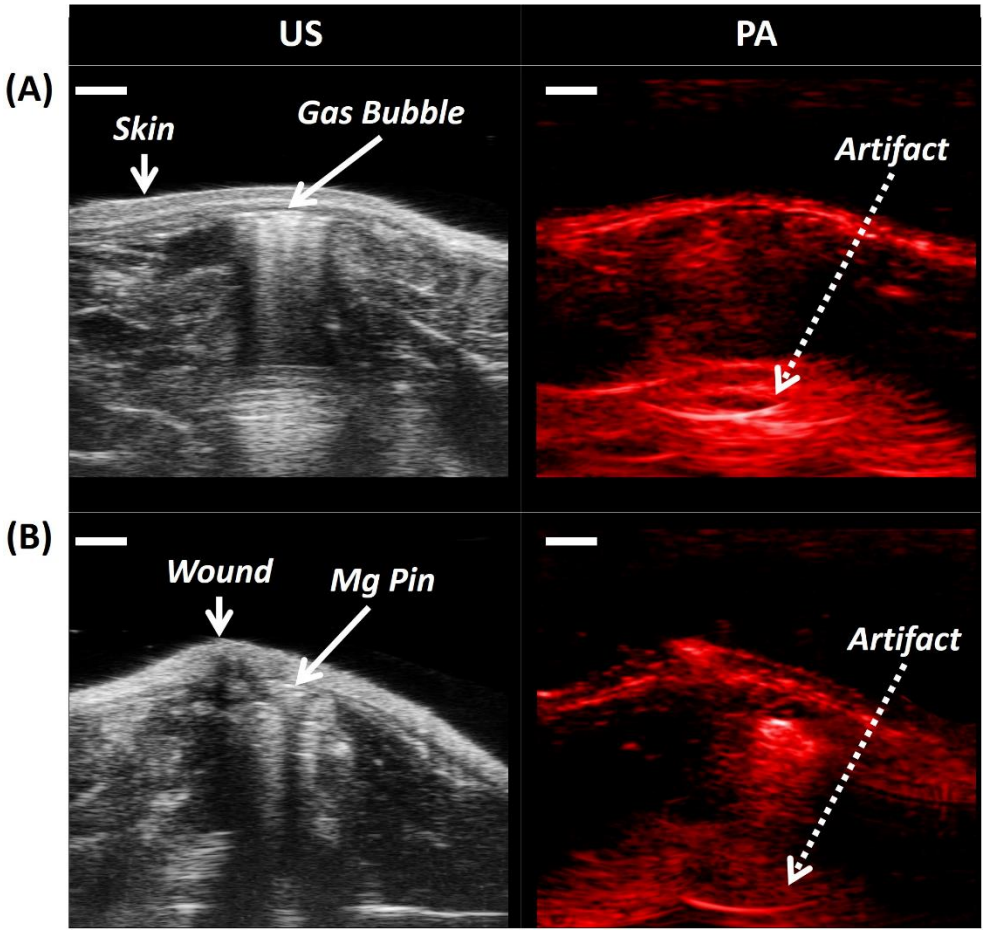

Fig. 4. Ultrasound (grayscale) and Photoacoustic (redscale) image of Mg implanted rat's femur on day 3 after surgery in presence of hydrogen gas bubble (A), and in the case where the gas bubble is resorbed (B); The scale bar size is 2mm.

The data-driven SPAX analysis has been applied longitudinally to the spectral data of Sham, Ti, and Mg groups. From the automated unmixing the spectra of HbO_2, Hb, and implant when present have been identified. Fig. 5 longitudinally depicts the mean μ (solid lines) and standard deviation σ (shaded area) of the identified source spectra for Sham, Ti, and Mg groups.

Fig. 6 (A-C) show only the mean of the source spectra obtained from Sham, Ti, and Mg groups, respectively. The mean spectra of HbO_2 and Hb of all the groups have been used for the correlation analysis. In particular, the correlation between each mean spectrum and the respective theoretical absorption spectra of HbO_2 and Hb has been evaluated. Thus, Fig. 7 (A-C)

show the correlation values obtained for HbO_2 (top row) and Hb (bottom row) for the Sham (n=6), Ti (n=10), and Mg (n=10) groups respectively. While the HbO_2 spectra for Sham and Ti remain similar to the theoretical spectra (correlation high and steady see Fig. 7 (A, B) top row), for the Mg group there is a drop in correlation at Day 3 and Day 28, however, the respective standard deviation is high. Besides, the correlation values of Hb (Fig. 7 (A-C) bottom row) for the Sham, Ti, and Mg groups show steady high values except low values at day 45 for Sham, day 3 and 14 for Ti, and day 3 for Mg. However, these low correlation values for the Hb spectra have a correspondingly high standard deviation.

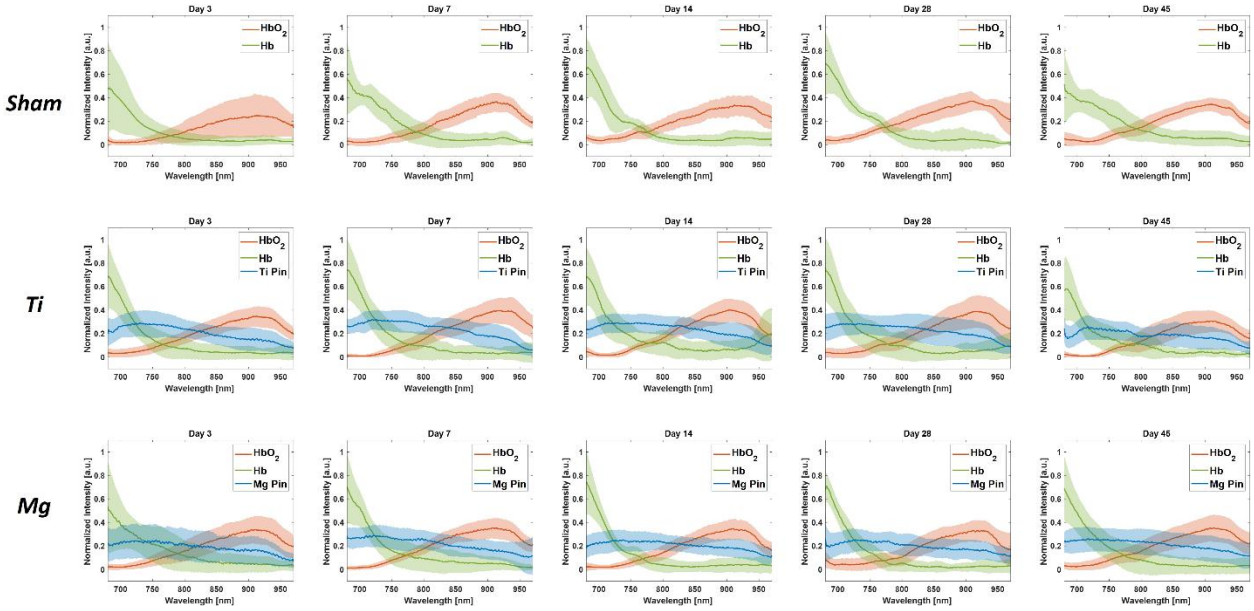

Fig. 5. Absorption spectra identified via SPAX analysis of oxy-hemoglobin (HbO_2) in red, deoxy-hemoglobin (Hb) in green, and implant (Mg and Ti pin) in blue. The mean μ (solid lines) and standard deviation σ (shaded arear) of the source spectra obtained from sPAI of the Sham, Ti, and Mg groups at days 3, 7, 14, 28, and 45 after surgery are included.

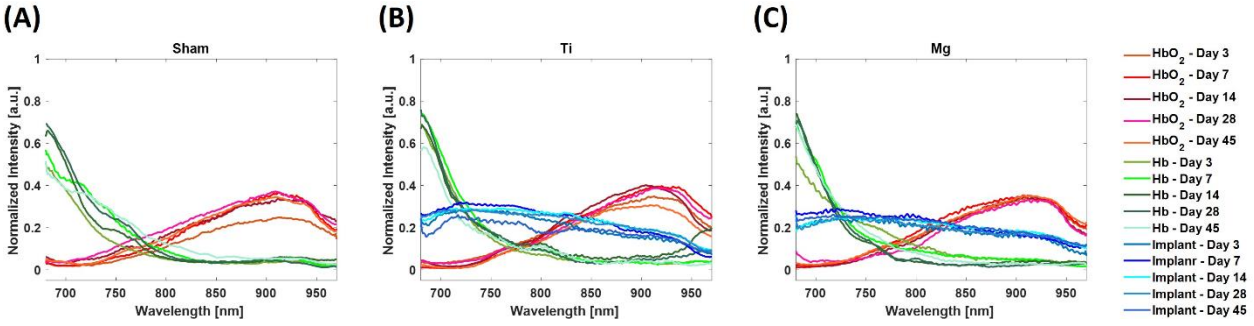

Fig. 6. Mean absorption spectra of oxy-hemoglobin (HbO_2) in red shades, deoxy-hemoglobin (Hb) in green shades, and implant (Mg and Ti pin) in blue shades detected longitudinally via SPAX for Sham (A), Ti (B), and Mg (C) groups.

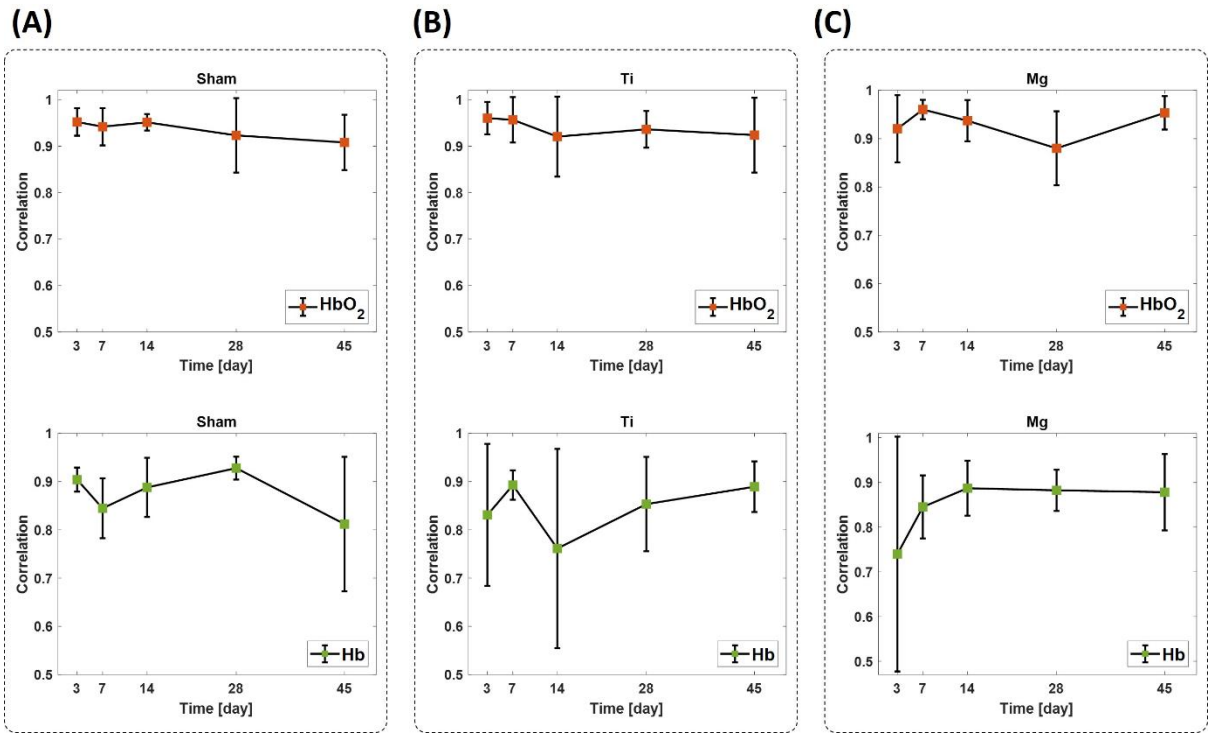

Fig. 7. Longitudinal correlation between mean absorption spectra of oxy-hemoglobin (HbO_2) and deoxy-hemoglobin (Hb) with the respective theoretical absorption spectra, for Sham (A), Ti (B), and Mg (C) groups.

Fig. 8 shows the unmixed abundance maps, obtained in a data-driven way via SPAX, where the oxygenated hemoglobin (HbO_2), deoxygenated hemoglobin (Hb), and the implant are represented in red, green, and blue respectively. The blind unmixing analysis has been performed longitudinally at days 3, 7, 14, 28, and 45 post-surgery. These maps enable enhanced visualization of the HbO_2, Hb, as well as Ti or Mg pin when present. The SPAX framework also includes a light fluence compensation function to overcome the spectral unmixing misinterpretation caused by spectral coloring artifacts, thus enabling accurate quantifications of the unmixed components.

From the unmixed maps of HbO_2 and Hb, the measures of tissue oxygen saturation (SO_2) have been evaluated as shown in Fig. 9.

In particular, to accurately evaluate the SO_2 by using the HbO_2 and Hb maps the abundance map of the implant, for Ti and Mg group, is used to exclude the pixels of the implant. Fig. 9 shows the longitudinal SO_2 values per each animal group evaluated by using Eq. (1). As shown from the box plots, the solid black line connects the mean SO_2 values through time points, to highlight the SO_2 the trend in average per each group. For all the groups (Sham, Ti, Mg) the mean SO_2 values range between $75\% - 80\%$, which is a normal oxygenation level range [43]. In particular, Fig. 9 (A-C) depicts the longitudinal SO_2 distributions of the Sham (n=6), Ti (n=10), and Mg (n=10) groups, respectively.

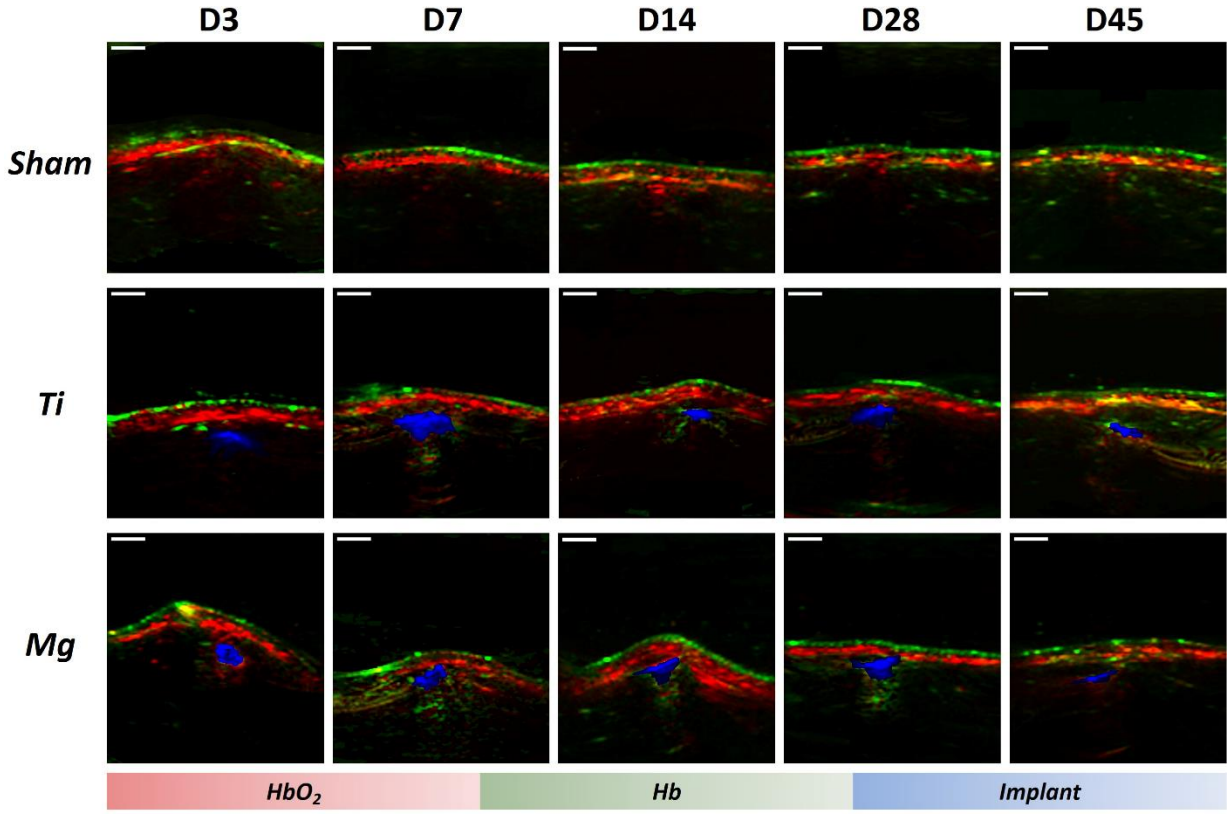

Fig. 8. Distribution unmixed maps obtained via SPAX of oxy-hemoglobin (HbO_2) in redscale, deoxy-hemoglobin (Hb) in greenscale, and implant (Mg and Ti pin) in bluescale obtained for the Sham, Ti, and Mg groups at days 3, 7, 14, 28, and 45 after surgery; The scale bar size is 2 mm.

The mean SO_2 values for the Sham and Ti groups (see Fig. 9 (A-B)) fluctuate within this normal oxygenation level range over time. On contrary, for the Mg group (see Fig. 9 (C)), early time points correspond to higher SO_2 values on average, while from day 14 the SO_2 shows a plateau. This may suggest that immediately after implantation since the Mg-based implants immediately start to react in contact with living tissues, the rise in SO_2 values may be related to inflammatory and angiogenesis processes mainly. This is also in accordance with the degradation rate trend of Mg-based implants that show a peak of degradation/interaction at early time points. While at later stages, the steady SO_2 trend is in accordance with the decrease in the degradation rate as shown from the analysis of the material elsewhere [44].

Longitudinally, the SO_2 values for Mg implanted group are in accordance with the degradation rate of the Mg-based implants. Outliers can be explained by a slight misalignment of the imaging spot or change in energy of the light source of excitation of sPAI, as well as a bruise caused by the depilatory cream irritating the skin.

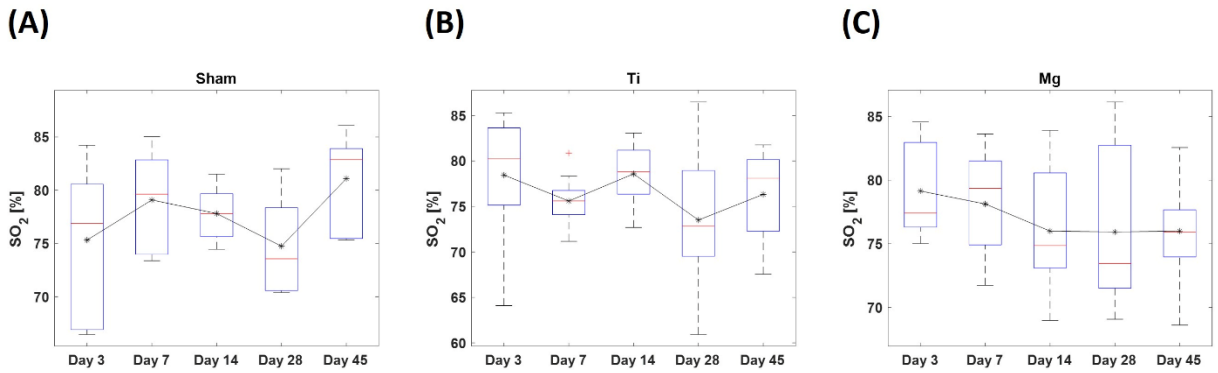

Fig. 9. Box plot of the oxygen Saturation (SO_2) values obtained from the unmixed maps of oxy-hemoglobin (HbO_2) and of deoxy-hemoglobin (HbO_2) of the Sham (A), Ti (B), and Mg (C) groups at days 3, 7, 14, 28, and 45 after implantation.

7.4. Discussion

We have investigated the use of spectral photoacoustic imaging (sPAI) and superpixel photoacoustic unmixing (SPAX) method to non-invasively monitor possible biomarkers that can indicate the soft tissue remodeling in the presence of biodegradable bone implants made of Magnesium. Therefore, we herein studied whether photoacoustic may be used to image functional and molecular parameters related to soft tissue remodeling in presence of biodegradable implants through a tissue-mimicking study and *in vivo* murine implanted model. Specifically, the *in vivo* longitudinal study included Ti- and Mg-based implants and Sham groups imaged at days 3, 7, 14, 28, and 45 after surgery. sPAI and SPAX data-driven analysis has enabled to automatically identify oxy/deoxy hemoglobin components and implants when present. Thus, the correlation between the oxy/deoxy unmixed spectra and the respective theoretical spectra has been evaluated longitudinally. This correlation might be used as an indication to detect significant spectral changes related to hemoglobin variations during the inflammatory response. Besides, the longitudinal SO_2 evaluation has been performed, as this might give information regarding angiogenesis during tissue healing and remodeling.

In summary, spectral photoacoustic imaging and SPAX have shown promising initial results to study angiogenesis and inflammation during tissue healing and remodeling in the presence of biodegradable bone implants made of Magnesium. The proposed superpixel data-driven unmixing framework outperformed the standard unmixing methods to automatically detect and quantify the molecular components and the implant. The measures obtained from the framework have the potential to monitor the soft tissue remodeling and evaluate the implant osseointegration. This innovative data-driven approach opens many opportunities for further applications to non-invasively monitor tissue remodeling in presence of bone implants.

However, since the *in vivo* study was based on a limited number of animals (see Table 1) there are still challenges to make significant evaluations from the performed analysis.

Current limitations of the study

- The SPAX analysis has identified components such as HbO_2, Hb, and Ti/Mg implants when present as well as additional unidentified components that require further investigations.
- Focused optical fibers have been used for sPAI acquisition. Although the focused illumination has effectively illuminated up to the tip of the implant, this has limited the penetration of light to deeper regions. Therefore, even though light fluence compensation has been applied, at deeper regions the correction enhances the signal and also the noise which is more prominent at depth in this configuration. Thus, deeper regions have not been considered. In future studies, changing the illumination setup might guarantee the acquisition of images with a more uniform light fluence distribution.
- High-frequency transducers enhance the image resolution limiting the imaging depth as well. Thus, the possibility of using lower frequency transducers can enable to perform photoacoustic imaging at depth.
- Although the sPAI unmixing provides highly sensitive results about the molecular tissue components spectra and their distribution maps, the SO_2 evaluation is not an absolute measure. Thus, to obtain the absolute quantification in PA imaging, improved measurement of the system response, tissue optical properties, and Grüneisen parameters are required. In the future, we aim to address the absolute quantification, by implementing deep learning approaches based on non-explicit light fluence estimation, leading to high fidelity SO_2 estimations.
- Only endogenous tissue components might be not enough for a complete tissue component analysis. For example using exogenous contrast agents such as Angiostamp800 that targets for $\alpha v\beta 3 - integrin$, which is a regulatory factor within the inflammatory response.
- Further validations via soft tissue histology as multimodal imaging (using CT/PET) would lead to a more robust analysis.

References

[1] M. Xu and L. V. Wang, "Photoacoustic imaging in biomedicine," *Rev. Sci. Instrum.*, vol. 77, no. 4, 2006.

[2] S. Mallidi, K. Watanabe, D. Timerman, D. Schoenfeld, and T. Hasan, "Prediction of tumor recurrence and therapy monitoring using ultrasound-guided photoacoustic imaging," *Theranostics*, 2015.

[3] J. Jose, S. Manohar, R. G. M. Kolkman, W. Steenbergen, and T. G. Van Leeuwen, "Imaging of tumor vasculature using Twente photoacoustic systems," vol. 717, no. 12, pp. 701–717, 2009.

[4] Y. Zhu *et al.*, "Towards clinical translation of LED-based photoacoustic imaging: A review," *Sensors (Switzerland)*. 2020.

[5] M. Filippi *et al.*, "Indocyanine green labeling for optical and photoacoustic imaging of mesenchymal stem cells after in vivo transplantation," *J. Biophotonics*, 2019.

[6] N. N. Nyström, L. C. M. Yip, J. J. L. Carson, T. J. Scholl, and J. A. Ronald, "Development of a human photoacoustic imaging reporter gene using the clinical dye indocyanine green," *Radiol. Imaging Cancer*, vol.

1, no. 2, 2019.

[7] H. F. Zhang, K. Maslov, G. Stoica, and L. V. Wang, “Functional photoacoustic microscopy for high-resolution and noninvasive in vivo imaging,” *Nat. Biotechnol.*, vol. 24, no. 7, 2006.

[8] I. J. FOX, L. G. BROOKER, D. W. HESELTINE, H. E. ESSEX, and E. H. WOOD, “A tricarbocyanine dye for continuous recording of dilution curves in whole blood independent of variations in blood oxygen saturation,” *Proc. Staff Meet. Mayo Clin.*, vol. 32, no. 18, 1957.

[9] J. CAESAR, S. SHALDON, L. CHIANDUSSI, L. GUEVARA, and S. SHERLOCK, “The use of indocyanine green in the measurement of hepatic blood flow and as a test of hepatic function.,” *Clin. Sci.*, vol. 21, 1961.

[10] G. Giacalone, T. Yamamoto, F. Belva, and A. Hayashi, “Bedside 3D Visualization of Lymphatic Vessels with a Handheld Multispectral Optoacoustic Tomography Device,” *J. Clin. Med.*, 2020.

[11] J. L.-S. Su, B. Wang, and S. Y. Emelianov, “Photoacoustic imaging of coronary artery stents,” *Opt. Express*, 2009.

[12] D. Lee, S. Park, W.-C. Noh, J.-S. Im, and C. Kim, “Photoacoustic imaging of dental implants in a porcine jawbone ex vivo,” *Opt. Lett.*, 2017.

[13] F. Witte, “The history of biodegradable magnesium implants: A review,” *Acta Biomaterialia*, vol. 6, no. 5. 2010.

[14] R. Willumeit-Römer *et al.*, “The Comparability of In Vitro and In Vivo Experiments for Degradable Mg Implants,” in *Minerals, Metals and Materials Series*, 2022.

[15] H. Helmholz *et al.*, “Tissue responses after implantation of biodegradable Mg alloys evaluated by multimodality 3D micro-bioimaging in vivo,” *J. Biomed. Mater. Res. - Part A*, vol. 109, no. 8, 2021.

[16] Y. Cao *et al.*, “Spectral analysis assisted photoacoustic imaging for lipid composition differentiation,” *Photoacoustics*, 2017.

[17] E. Park, Y.-J. Lee, C. Lee, and T. J. Eom, “Effective photoacoustic absorption spectrum for collagen-based tissue imaging,” *J. Biomed. Opt.*, 2020.

[18] S. Tzoumas *et al.*, “Eigenspectra optoacoustic tomography achieves quantitative blood oxygenation imaging deep in tissues,” *Nat. Commun.*, 2016.

[19] V. Grasso, J. Holthof, and J. Jose, “An automatic unmixing approach to detect tissue chromophores from multispectral photoacoustic imaging,” *Sensors (Switzerland)*. 2020.

[20] V. Grasso, R. Willumeit-Römer, and J. Jose, “Superpixel spectral unmixing framework for the volumetric assessment of tissue chromophores: A photoacoustic data-driven approach,” *Photoacoustics*, vol. 26, p. 100367, 2022.

[21] F. Witte *et al.*, “Degradable biomaterials based on magnesium corrosion,” *Curr. Opin. Solid State Mater. Sci.*, vol. 12, no. 5–6, 2008.

[22] F. Witte *et al.*, “In vivo corrosion of four magnesium alloys and the associated bone response,” *Biomaterials*, vol. 26, no. 17, 2005.

[23] F. Witte *et al.*, “In vitro and in vivo corrosion measurements of magnesium alloys,” *Biomaterials*, vol. 27, no. 7, 2006.

[24] W. A. Badawy, N. H. Hilal, M. El-Rabiee, and H. Nady, “Electrochemical behavior of Mg and some Mg alloys in aqueous solutions of different pH,” *Electrochim. Acta*, vol. 55, no. 6, 2010.

[25] F. Loi, L. A. Córdova, J. Pajarinen, T. hua Lin, Z. Yao, and S. B. Goodman, “Inflammation, fracture and bone

repair," *Bone*, vol. 86. 2016.

[26] W. yong Zhu *et al.*, "Biodegradable magnesium implant enhances angiogenesis and alleviates medication-related osteonecrosis of the jaw in rats," *J. Orthop. Transl.*, vol. 33, 2022.

[27] M. Pogorielov, E. Husak, A. Solodivnik, and S. Zhdanov, "Magnesium-based biodegradable alloys: Degradation, application, and alloying elements," *Interventional Medicine and Applied Science*, vol. 9, no. 1. 2017.

[28] S. A. Eming, T. A. Wynn, and P. Martin, "Inflammation and metabolism in tissue repair and regeneration," *Science*, vol. 356, no. 6342. 2017.

[29] L. Chen *et al.*, "Inflammatory responses and inflammation-associated diseases in organs," *Oncotarget*, vol. 9, no. 6. 2018.

[30] G. Zhang, J. Huang, K. Yang, B. Zhang, and H. Ai, "Experimental study of in vivo implantation of a magnesium alloy at early stage," *Jinshu Xuebao/Acta Metall. Sin.*, vol. 43, no. 11, 2007.

[31] F. Witte, H. Ulrich, M. Rudert, and E. Willbold, "Biodegradable magnesium scaffolds: Part I: Appropriate inflammatory response," *J. Biomed. Mater. Res. - Part A*, vol. 81, no. 3, 2007.

[32] S. Manohar and D. Razansky, "Photoacoustics: a historical review," *Adv. Opt. Photonics*, vol. 8, no. 4, 2016.

[33] S. Tzoumas, N. Deliolanis, S. Morscher, and V. Ntziachristos, "Unmixing molecular agents from absorbing tissue in multispectral optoacoustic tomography," *IEEE Trans. Med. Imaging*, vol. 33, no. 1, 2014.

[34] B. Cox, J. G. Laufer, S. R. Arridge, and P. C. Beard, "Quantitative spectroscopic photoacoustic imaging: a review," *J. Biomed. Opt.*, vol. 17, no. 6, p. 061202, 2012.

[35] A. Sarantopoulos, N. Beziere, and V. Ntziachristos, "Optical and opto-acoustic interventional imaging," *Ann. Biomed. Eng.*, vol. 40, no. 2, 2012.

[36] J. Umbreit, "Methemoglobin - It's not just blue: A concise review," *American Journal of Hematology*, vol. 82, no. 2. 2007.

[37] M. Tang, L. V Wang, M. Tang, Y. Zhou, R. Zhang, and L. V Wang, "Noninvasive photoacoustic microscopy of methemoglobin in vivo Noninvasive photoacoustic microscopy of methemoglobin in vivo," *J. Biomed. Opt.*, vol. 20, no. 3, 2019.

[38] K. Aizawa, S. Sato, D. Saitoh, H. Ashida, and M. Obara, "In vivo photoacoustic spectroscopic imaging of hemoglobin derivatives in thermally damaged tissue," *Jpn. J. Appl. Phys.*, vol. 48, no. 6, 2009.

[39] M. M. Menger *et al.*, "Photoacoustic imaging for the study of oxygen saturation and total hemoglobin in bone healing and non-union formation," *Photoacoustics*, 2022.

[40] A. Needles *et al.*, "Development and initial application of a fully integrated photoacoustic micro-ultrasound system," *IEEE Trans. Ultrason. Ferroelectr. Freq. Control*, vol. 60, no. 5, pp. 888–897, 2013.

[41] R. Hochuli, L. An, P. C. Beard, and B. T. Cox, "Estimating blood oxygenation from photoacoustic images: can a simple linear spectroscopic inversion ever work?," *J. Biomed. Opt.*, vol. 24, no. 12, 2019.

[42] S. L. Jacques, "Optical properties of biological tissues: A review," *Physics in Medicine and Biology*, vol. 58, no. 11. 2013.

[43] G. A. Harrop, "The oxygen, and carbon dioxide content of arterial and of venous blood in normal individuals and in patients with anemia and heart disease," *J. Exp. Med.*, vol. 30, no. 3, 1919.

[44] D. Zhao, F. Witte, F. Lu, J. Wang, J. Li, and L. Qin, "Current status on clinical applications of magnesium-based orthopaedic implants: A review from clinical translational perspective," *Biomaterials*, vol. 112. 2017.

Chapter 8

Multi-frequency photoacoustic imaging for tissue monitoring in presence of biodegradable bone implants:

"En route to the clinics"*

Abstract:

In this chapter, we investigated the potential of multi-frequency bandwidth ultrasound transducers for photoacoustic imaging to fuse multi-scale features with unprecedented details. This approach has the potential to image biomarkers and tissue structures with varying sizes, resolutions, and depths. Here, we characterized an innovative open architecture system that enables the co-localization of low and high-frequency photoacoustic signals within the frequency range of 1-71 MHz. The technology showed to be adaptable for imaging small to large structures through simulations and customized tissue-mimicking phantoms experiments. This could facilitate the translation of photoacoustic technology for advanced applications such as tissue monitoring in presence of biodegradable bone implants.

*Part of this chapter has been published as: **Grasso, V.,** Willumeit-Römer, R., & Jose, J. (2023, March). *"Development of an AI-assisted multi-spectral photoacoustic imaging for volumetric molecular tissue composition: a multi-frequency translational approach".* In Photons Plus Ultrasound: Imaging and Sensing 2023 (Vol. 12379, p. 1237902). SPIE.

*Part of this chapter has been submitted for publication as: **Grasso, V.,** Willumeit-Römer, R., & Jose, J. (2023) *"Multi-frequency photoacoustic imaging for tissue monitoring in presence of biodegradable bone implants: "En route to the clinics"."* Sensors.

sensors

MDPI

Article

Multi-frequency photoacoustic imaging for tissue monitoring in presence of biodegradable bone implants: "En route to the clinics"

Valeria Grasso [1,2], Regine Willumeit-Römer [2,3] and Jithin Jose [1,*]

[1] FUJIFILM VisualSonics, Amsterdam, the Netherlands
[2] Christian-Albrecht University of Kiel, Kiel, Germany
[3] Helmholtz-Zentrum Hereon GmbH, Geesthacht, Germany

* Correspondence: jithin.jose@fujifilm.com

Abstract: Multi-scale assessment of tissue biomarkers via photoacoustic imaging (PAI) is crucial, especially in clinical settings. Generally, photoacoustic signals have broadband frequency content by nature, which can span from Kilohertz to several tens of Megahertz. However, the ultrasound (US) transducers used in PAI are not ideal point detectors with infinite bandwidth. In PAI, the limited frequency bandwidth has a significant impact on the resolution and depth of the reconstructed image. Specifically, the use of lower frequency transducers (below 10 MHz), enables imaging at depth and provides spatial resolutions in the range of 150 − 200 microns. On the other hand, high-frequency transducers within the range of 15 − 50 MHz can enable spatial resolutions of around 40 microns. However, this results in increased acoustic attenuation, which limits the imaging depth. Therefore, PAI may require the use of a low or high-frequency transducer depending on the application. In general scenarios, it would be ideal to use the combination of photoacoustic imaging at high-frequency to monitor superficial highly detailed features and low frequency for targets at depth. To this end, here the use of multiple US transducers with different frequency bands for PAI has been investigated through simulations and tissue-mimicking phantom studies. Besides the impact of the frequency response of the US transducer on the PAI depth and resolution has been evaluated in detail, laying the fundamentals for the translation of PAI in clinics.

Citation: To be added by editorial staff during production.

Academic Editor: Firstname Lastname

Received: date
Accepted: date
Published: date

1. Introduction

In photoacoustic imaging (PAI), the hybrid combination of acoustic and optical principles offers structural, functional, and molecular information based on either endogenous chromophores (like oxygenated/deoxygenated hemoglobin, lipid, melanin, collagen, and water) or a variety of exogenous contrast agents or both. In particular, as PAI uses the same data acquisition process as ultrasound imaging, it can reveal various features with strong optical contrast at acoustic resolution in deep tissue, non-invasively, and without the use of ionizing radiations. These characteristics have contributed to PAI's success in preclinical research and its use in advanced applications. Recently we have explored the use of PAI as a method of monitoring tissue regeneration in presence of biodegradable bone implants [1]–[4]. However further developments are still required to facilitate the translation of the technology into the clinical practice for this advanced application.

Over the last decades, various PAI system configurations have been optimized for the rapidly expanding clinical potential of photoacoustic imaging [5] including dermatology, vascular, musculoskeletal, gastrointestinal, breast, and adipose tissue imaging [6]. Hence, many clinical studies have been reported such as the use of PAI to differentiate malignant and benign thyroid nodules by Kim et al. [7], [8]. Manohar et al. [9]–[11] have reported the current and future trends of photoacoustic for breast imaging. Besides, Malmsjo et al. [12], [13] have performed PAI for cutaneous microvasculature, melanoma, and temporal artery applications. Kajita et al. [14], [15] have studied the use of PA for the lymphatic system and peripheral vascular imaging in extremities. Petri et al. have been monitoring tissue remodeling in wound imaging [16] and adipose tissue imaging of carotid vessels [17]. Recently, Ali et al. [18] have proposed the emerging application of a photoacoustic endoscope for human gastrointestinal tract imaging. Furthermore, PAI has also been used to monitor metallic implants, localize needles, and improve image-guided surgical procedures in clinical applications [19]–[22].

However, further efforts are needed to expand PAI to cover a broader range of clinical applications at multiple scales. In particular, photoacoustic signals have broadband frequency content that includes information about structures of different sizes [23]. On the other hand, the transducers used for measuring the PA signals are not ideal point detectors with infinite bandwidth. Conventionally, the PAI systems typically work either in the lower frequency or in the higher frequency due to the limited frequency bandwidth of the transducers and data acquisition (DAQ) systems. In PAI, the limited frequency bandwidth has a significant impact on the resolution and depth of the reconstructed image. Therefore, depending on the transducer frequency bandwidth, PAI can be scaled over a wide range of imaging resolutions and depths [24]. Specifically, the use of lower frequency transducers (below 10 MHz), enables imaging at depth and provides spatial resolutions in the range of 150 − 200 microns. On the other hand, high-frequency transducers within the range of 20 − 50 MHz can enable spatial resolutions below 80 microns. However, this results in increased acoustic attenuation, which limits the imaging depth.

Therefore, PAI may require the use of a low or high-frequency transducer depending on the application. For instance, for skin cancer imaging, a high-frequency transducer may be beneficial to retrieve high details of the angiogenesis processes at a superficial level. While for breast cancer imaging, a low-frequency transducer might be preferred to access bigger structures with lower resolution at a deeper level. Furthermore, advanced applications such as the use of biodegradable bone implants are becoming increasingly popular for treating bone fractures in humans. In this case, it would be more effective the combination of photoacoustic imaging at high-frequency to monitor superficial revascularization and low-frequency for implant osseointegration at depth. Thus, a multi-frequency bandwidth imaging acquisition protocol that can be adapted to various applications in biomedical imaging would be beneficial. Ideally, a flexible PAI system in terms of frequency bandwidth and optical illumination would open many possibilities for translational photoacoustic imaging.

This study aims to characterize the performance of a newly developed open architecture imaging system, the Vevo-F2 LAZR-X (FUJIFILM VisualSonics), that enables the detection of photoacoustic signals in the frequency range of 1 − 71 MHz. This is a unique platform that provides complete flexibility to researchers to expand the range of applications in preclinical imaging and translational research, by customizing the use of multiple transducers and specific optical fiber bundles. Due to the broadband nature of the PA acquisition, the approach can create multiscale and multi-contrast images of structures ranging from small to large and facilitate respective spatial resolutions.

Thus, we have evaluated the advantages of the multi-frequency bandwidth photoacoustic approach via numerical simulations first. Then, experimentally we characterized the Vevo-F2 LAZR-X system at multiple frequency bands, by sequentially using different compatible transducers, through customized tissue-mimicking phantoms. Thus, the effect on image resolution, sensitivity, and penetration depth has been investigated in detail.

Finally, we have fabricated a human hand-shaped phantom to mimic a realistic clinical scenario to prove the advantages of a multi-frequency bandwidth approach to reveal features of different sizes and depths in photoacoustic imaging. This configuration was demonstrated to be highly useful in understanding conditions related to human tissue features, especially in presence of bone implants. Besides, a multi-frequency bandwidth photoacoustic imaging protocol is also provided. Furthermore, the design and fabrication of the ad hoc tissue-mimicking phantoms are described in detail.

2. Materials and methods

In the following sections, we describe the ultrasound-photoacoustic system specification, by using multiple transducers with various frequency bandwidths. The characterization of the multi-frequency bandwidth approach for photoacoustic imaging aims to show its suitability to reach multi-scale information at multiple imaging depths and resolutions. The evaluation of multi-frequency bandwidth imaging demonstrates the relevance to translate photoacoustic technology into clinical practice. The effect of multi-frequency bandwidth acoustic sensors on the photoacoustic image resolution and depth has been evaluated through numerical simulation and experimentally via customized designed tissue-mimicking phantoms.

Thus at first, the k-wave [25] toolbox was used for the simulations of photoacoustics signals as well as the reconstruction of the images to demonstrate the potential and limitations of using sensors covering multi-frequency bandwidths. Finally, we experimentally accessed the photoacoustic system's performance through customized tissue-mimicking phantoms including a realistic mimicking clinical scenario. This characterization opens many translational possibilities for using the technology for future clinical applications, especially with implanted patients where the combination of multi-frequency bandwidth photoacoustic imaging can cover multi-scale imaging enhancing complementary features at various resolutions from different depths.

2.1. Simulation of multi-frequency bandwidth photoacoustic image

Numerical simulations have been implemented to estimate the effect of varying the frequency bandwidth of the acoustic detector to the degree of spatial resolution and depth of the photoacoustic images. The k-wave MATLAB toolbox [25] was used to simulate various domain configurations. This set of open-source MATLAB tools allows the time domain simulation of photoacoustic as well as ultrasound wave propagation and image reconstruction using the time-reversal technique. A pc with an Intel i7 processor and 16 GB RAM was used for all the simulations done in this study. Specifically, two sets of photoacoustic simulations have been designed and implemented to show imaging resolution and depth using sensors at multi-frequency bandwidths.

The first set of numerical phantoms was used to simulate the blurring and edge-enhancing effects caused by the limited frequency bandwidth of the ultrasound detectors. These effects are prominent when there is no matching between the frequency bandwidth of the sensor and the spatial frequency content of the imaged target object. Thus, in this set of simulations the target object size and transducer frequency bandwidth were varied to see the effect on the photoacoustic signals and the spatial resolution of the reconstructed photoacoustic image.

Specifically, Fig. 1 shows the numerical domains with multi-scale geometrical targets used in the simulations. Fig. 1 (A) shows a geometrical domain that includes a circular absorber of 1.5 mm in diameter that mimics the shape of a tumor. Fig. 1 (B) includes the geometry of a blood vessel network with branches of various diameter sizes such as 0.1 mm, 0.15 mm, 0.2 mm, and 0.4 mm as pointed by the cyan, orange, green, and yellow arrows respectively. Finally, Fig. 1 (C) depicts a domain that includes both structures such as the tumor and the blood vessel network. Multi-scale objects, such as a tumor and a blood vessel network, have low and high spatial frequency content respectively, while the

domain where both structures are included has a broadband spatial frequency content. These simulations with multi-scale domains aim to demonstrate the effect of the transducer frequency bandwidth on the photoacoustic imaging resolution where target objects with different sizes are included. The initial pressure rise in the tumor and in the blood vessel network was assumed to be 3 Pa and 5 Pa respectively. The schematic domains shown in Fig. 1 were simulated using a computational grid of 128 × 128 pixels (pixel size 0.1 mm). A perfectly matched boundary layer (PML) was used to satisfy the boundary condition.

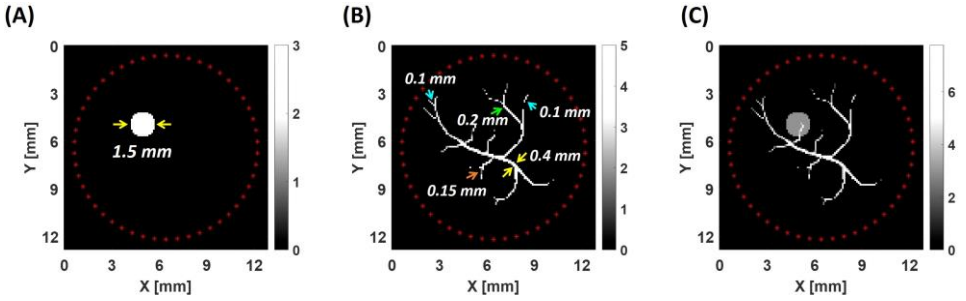

Figure 1. Simulated geometrical domains of a tumor (A), blood vessel tree (B), and their combination (C). The dots in red represents the ultrasound sensors' configuration. These geometries have been implemented to demonstrate the effect of multi-frequency bandwidth transducers on image resolution, showing the effects of blurring and edge enhancement.

Besides, Fig. 1 (A-C) depicts in red the 50 ultrasound sensors placed at a 5.8 mm distance from the center of the simulated domain. This sensor's configuration of point detectors placed in a circular shape surrounding the absorbing target is used to avoid any influence of the depth as well as avoiding any influence from the size and shape of the acoustic detectors. In order to quantitatively compare the resolution at multiple frequency bandwidths, we used full-width at half-maximum (FWHM) as an indication of the resolution of the reconstructed PA image.

The first set of simulations aims to demonstrate that using a multi-frequency bandwidth approach has a positive effect of merging multi-scale information. In this set of simulations, the effect of the transducer frequency bandwidth on the photoacoustic imaging depth has not been considered. This has been investigated in the second set of numerical simulations.

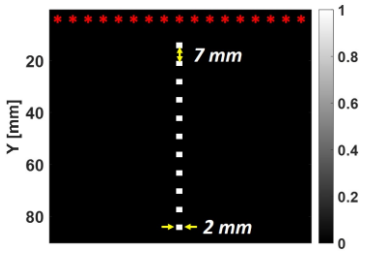

Figure 2. Simulated geometrical domain of multiple point absorbers along the depth. This geometry has been implemented to demonstrate the effect of multi-bandwidth frequency transducers on the image depth and the respective sensitivity. For this simulation, a linear ultrasound transducer placed at the surface of the domain, as depicted by the red dots, has been used.

Specifically, to demonstrate the sensitivity along the depth of sensors at multiple-frequency bandwidth, we simulated a geometrical domain where several point absorbers are positioned along a domain of 9 cm depth as shown in Fig. 2. Each absorber along depth has a diameter of 2 mm and inter-distance between the absorbers of 7 mm. The initial pressure intensity of the absorbers was assumed to be 1 Pa. The ultrasound sensors are

placed linearly on top of the domain as depicted in red in Fig. 2. The size of the simulated domain is 90 mm × 90 mm with a computational grid of 128 × 128 pixels. PML was used here as well.

Finally, acoustic sensors with different frequency bandwidths have been used per each simulated domain. Specifically, sensors with a central frequency of 8 MHz, 15 MHz, 20 MHz, and 30 MHz with a bandwidth of 80 % have been used. The time step chosen was 10 ns with a total of 728 time steps. The simulations assumed a sound speed of 1500m⁄s. For simplicity, the medium was considered acoustically homogeneous and there was no absorption or dispersion of sound. However, any other medium (acoustically and optically inhomogeneous) can also be considered and similar results may be obtained. The photoacoustic image reconstruction was done using the time-reversal method in k-wave for both sets of simulations.

2.2. Multi-frequency bandwidth system characterization

After the numerical simulations, various experimental measurements by means of customized tissue-mimicking phantoms have been performed. These aim to access the suitability of photoacoustic multi-frequency bandwidth imaging for translational applications. Here we focused on ultrasound and photoacoustic system characterization in a frequency-dependent analysis. Specifically, real evaluations of photoacoustic resolution and imaging depth have been conducted via tissue-mimicking phantom experiments. Specifically, the design and fabrication of customized tissue-mimicking phantoms have been conducted to characterize various aspects of the multi-frequency bandwidth ultrasound and photoacoustic imaging approach with the ultimate goal to translate the technology into clinical practice. In the following sections, the development of three phantoms is described in detail. The phantoms are mainly used to assess the spatial resolution and imaging depth as well as to mimic a realistic clinical scenario by imaging with the use of multiple transducers, thus covering multi-frequency bandwidths.

All the tissue-mimicking phantoms designed for the multi-frequency bandwidth system characterization were prepared by using the same base material made of agarose. Specifically, the bulk material of the phantoms is made of 1.5% w/v Agar (Alfa Aesar, Heysham, Lancaster) mixed with 2% w/v Intralipid (IL) (20%, Sigma-Aldrich, Canada).

2.3. Multi-frequency bandwidth ultrasound and photoacoustic imaging system

The photoacoustic data of the tissue-mimicking phantoms were acquired using the preclinical Vevo-F2 LAZR-X technology (FUJIFILM VisualSonics, Toronto, Canada). This system is a hybrid ultrasound and photoacoustic system that expand imaging capabilities from ultra-high to low frequency within the range of 71–1 MHz. In this study, three different linear array transducers have been used. Specifically, the L38xp, UHF22x, and UHF29x operate at a central frequency of 8 MHz, 15 MHz, and 20 MHz respectively. Table 1 includes the technical specifications declared by the manufacturer for the linear transducers used in this work.

Table 1. Ultrasound transducer frequency specifications.

Transducer	Center Frequency	Bandwidth
L38xp	8 MHz	5-10 MHz
UHF22x	15 MHz	10-22 MHz
UHF29x	20 MHz	15-29 MHz

The ultrasound and photoacoustic Vevo-F2 LAZR-X system includes a Q-switched pulsed OPO laser pumped by a double Nd:YAG with 5 ns pulse width and 45 mJ pulse

energy. The laser was tuned to the wavelength of 750 nm and delivered at an angle of 30° with the help of optical fiber bundles mounted on each side of the ultrasound transducer. Before image acquisition, the laser calibration process has been performed, by using an external energy sensor. The laser calibration is crucial to characterize the transmission efficiency of the optical fibers and to ensure that data is normalized to the same energy scale. Then the acquisition was done by placing the samples at a focal distance from the transducer, as the image would show low contrast in the vicinity of the transducer. Finally, the photoacoustic data have been acquired (RF and raw format) by sequentially switching the different transducers in order to acquire the same target with multi-frequency bandwidths.

2.4. Vessel-shaped phantom

A blood vessel network-shaped phantom has been designed to evaluate the image resolution changes at a volumetric scale along the various transducers used for multi-frequency bandwidth photoacoustic imaging. Fig. 3 shows the designed blood vessel network with branches of different diameters. The object was 3D printed (Formlabs Form 3, Formlabs Inc., Somerville, MA, USA) in white resin (Formlabs Inc., Somerville, MA, USA). Besides, the final 3D-printed object has been coated using black spray ink (Liquitex). Once the dye has completely dried the vessel network has been fixed in a chamber and filled with the bulk material till the solidification at 4°C has been completed.

To evaluate the resolution from the reconstructed photoacoustic images acquired with multiple ultrasound transducers, the intensity profiles have been extracted and the FWHM has been evaluated. Finally, these measurements have been compared with the original design dimensions to evaluate the blurring effect induced by the different transducers.

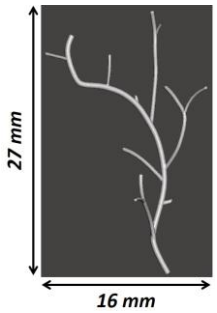

Figure 3. Geometrical design of the 3D printed blood vasculature, which has been included within the tissue-mimicking phantom to experimentally investigate the photoacoustic image resolution using multi-frequency bandwidth transducers.

2.5. X-shaped phantom

An X-shaped phantom has been designed to evaluate the changes in terms of sensitivity along the depth, signal-to-noise ratio (SNR), and resolution by using multi-frequency bandwidth transducers for photoacoustic imaging. A cubic open chamber (12cm x 12cm x 12cm) has been 3D printed (Formlabs Form 3, Formlabs Inc., Somerville, MA, USA) in white resin with corresponding holes in 2 parallel faces of the chamber in a custom X-shaped design, as shown in Fig. 4. The holes have been designed to insert light absorbing threads. Specifically, transparent nylon threads (Almega Nylon, Albatros) with 0.50 mm of diameter have been coated using spray ink (Liquitex) in a black shade. After the ink has completely dried the black nylon threads have been inserted within the respective holes to have the absorbers in 3D. Once the threads have been secured in the phantom chamber using tape and hot glue in the holes to avoid leakage, the bulk material has been poured into the chamber and left there till complete solidification at 4°C.

The image contrast is defined as a ratio of photoacoustic signal (S) and background noise (N) intensity. To measure the signal and the noise along the depth, 8 regions of

interest (ROIs) were placed where the image has a high photoacoustic intensity, such as at the level of the absorbing threads along the depth, as depicted by the dotted regions in Fig. 4. The mean values of the intensity of the pixels in these ROIs were calculated. The same procedure was utilized to measure the background/noise intensity. An ROI was positioned 2 mm away from the threads at the same depths, and the standard deviation values of the background pixels' intensity were measured.

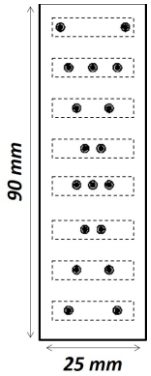

Figure 4. Schematic representation of the cross-section of the X-shaped phantom used to experimentally evaluate the photoacoustic image depth obtained with multi-frequency bandwidth transducers.

The SNR has then been calculated in decibels (dB) per each ROI along depth as follows:

$$SNR = 20\log_{10}\frac{\mu(S)}{\sigma(N)}, \quad (1)$$

The X-shaped phantom has also been used to measure the lateral resolution along depth at multi-frequency bandwidth. The lateral profile in correspondence of the threads was extracted and fitted to a Gaussian distribution. The full width half maximum (FWHM) was calculated using MATLAB software (MathWorks Inc.).

2.6. Human hand-shaped phantom

A human hand-shaped phantom has been designed and fabricated to test the multi-frequency bandwidth photoacoustic imaging approach in a realistic clinical scenario. As shown in Fig. 5 (A) a hand-shaped holder has been designed and 3D printed in 2 complementary parts, to fit into the 14.5cm × 14.5cm × 18.5cm build volume of the 3D printer (Formlabs Form 3, Formlabs Inc., Somerville, MA, USA). After printing, washing, and curing procedures, the two complementary parts of the hand-shaped holder have been fixed together with hot glue.

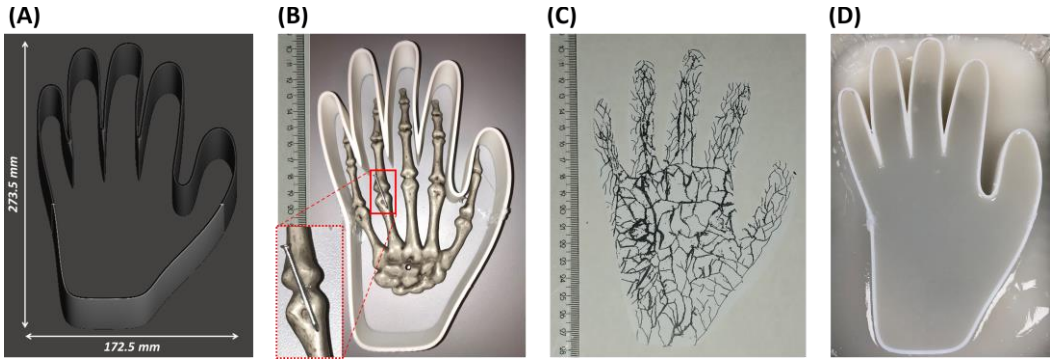

Figure 5. Hand-shaped holder modeled in two complementary parts (A); 3D printed hand-shaped holder with hand skeleton and implant (B); hand vessels representation printed on a white paper used to mimic the superficial hand vasculature (C); assembled hand-shaped phantom including vasculature, skeleton, and implant (D).

The hand-shaped phantom includes a realistic human hand skeleton made of high-quality plastic (size 15.5 cm x 10 cm) as well as a metallic screw fixed between the ring proximal phalange and the ring metacarpal bone by using hot glue as shown in Fig. 5 (B). The screw aims to mimic the presence of a bone implant. Besides, a representation of the human hand vasculature has been printed on white paper using black ink as shown in Fig. 5 (C). The blood vasculature paper has been embedded within the hand holder in turbid bulk agarose material as a more superficial layer to mimic the skin vasculature. Besides, the hand skeleton including the implant has been positioned deeper following the real human hand anatomy. Finally, Fig. 5 (D) depicts the assembled hand-shaped phantom.

2.6.1. Imaging acquisition protocol, registration, and 3D rendering of big volumes

Customized imaging acquisition protocol, registration, and 3D rendering have been implemented for the multi-frequency bandwidth acquisition of the hand-shaped phantom. The goal of the multi-frequency bandwidth photoacoustic imaging approach is to fuse multi-scale features acquired with different resolutions and depths, thus enhancing the imaging characteristics and opening future possibilities in clinics. In particular, the transducers L38xp and UHF29x combined with wide- and medium-width optical fibers respectively, have been sequentially used for the photoacoustic imaging acquisition of the hand-shaped phantom. The sequential use of these two transducers aims to guarantee the desired combination of depth and sensitivity of photoacoustic imaging. Specifically, the low-frequency transducer (L38xp) aims to acquire bigger and deeper structures, while the high-frequency transducer (UHF29x) can capture superficial small structures with higher resolution. This combination results optimal to reveal the bone surface with the implant at depth and the vasculature at the skin level with high resolution.

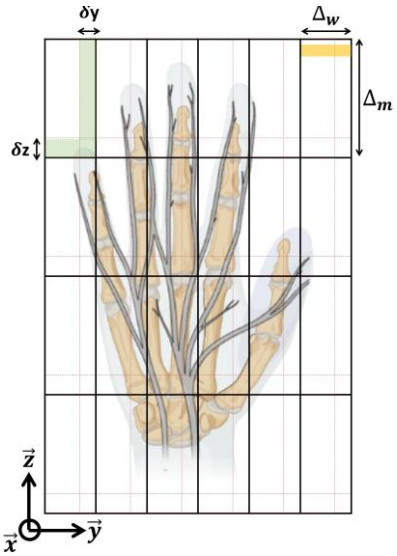

Figure 6. Schematic of the sequential photoacoustic image acquisition setup for big volumes. The green areas $(\delta z, \delta y)$ refer to the overlapping areas between consecutive acquired imaging blocks (indicated by the grid). Δ_w represents the width of the transducer and Δ_m refers to the maximum linear movement of 4.5 cm of the transducer done by the linear stepper motor along the $\vec{z}$ direction.

As shown in Fig. 6, the acquisition of a big volume of interest, as the size of a human hand ($\approx$ 20 cm x 12 cm), requires sequential acquisitions of smaller blocks. The block size, shown in Fig. 6 as Δ_m x Δ_w, is 4.5 cm x 3.6 cm at central frequency (f_c) f_c = 8 MHz or 4.5 cm x 2.6 cm at f_c = 20 MHz. Δ_m represents the max length of the linear stepper motor along $\vec{z}$ direction, while Δ_w is the image width, which is 3.6 cm for the L38xp and 2.6 cm

for the UHF29x transducer. The motor guarantee to maintain an orthogonal angle between the transducer and the object during the image acquisition. For coherent image acquisition and registration, the motor has been fixed to linearly move only on the $\vec{z}$ direction. Thus, to acquire the whole hand-shaped phantom, the phantom has been fixed into an open chamber filled with water, which maintains the acoustic coupling during the image acquisition. Then the whole chamber was fixed on a moving plate that can linearly shift along $\vec{y}$ and $\vec{z}$ directions as shown in Fig. 6. $\vec{x}$ indicates the imaging depth direction.

The grid in Fig. 6 schematizes the series of imaging volumes acquired sequentially to cover the entire big volume. Each volume is acquired by positioning the phantom systematically on the grid and then the motor linearly moves the transducer to acquire the data. Then, the phantom is manually moved to the next optimal position. Specifically, the order of volumes acquisition proceeds per column of the grid by moving the phantom of δz steps till the complete column is acquired. Then the phantom is shifted of δy to acquire the next column. This procedure continues till the whole phantom is acquired following a customized grid design that is used as a guideline. The steps $\delta z, \delta y$ guarantee an overlapping between consequent volumes, which finally facilitates the concatenation of the acquired volumes. Delay and sum algorithm has been applied to reconstruct the ultrasound and photoacoustic images per each imaging block [26].

Besides, the local structural similarity index has been calculated to find the overlapping areas between the subsequent blocks and thus coherently register the various imaging volumes to obtain the full view of the big volume. The same acquisition protocol is repeated by using multiple transducers, by maintaining the whole setup mostly unchanged, in order to guarantee consistent imaging of the same object with multi-frequency bandwidth transducers.

3. Results

We present the results obtained using multi-frequency bandwidth transducers along with simulation and tissue-mimicking phantoms studies. Besides, the system performance in terms of resolution, sensitivity, and penetration depth is evaluated.

3.1. Simulation of multi-frequency bandwidth transducers' effect on photoacoustic imaging spatial resolution

Fig. 7 shows the three simulated domains, such as the tumor shape (A), the blood vasculature network (B), and their combination (C). These are used as targets to investigate the effect of multi-frequency bandwidth transducers on the multi-scale photoacoustic features reconstruction and resolution. Fig. 7 shows the simulated domains, the 2D Fast Fourier Transform (FFT2) of the target objects, and the reconstructed photoacoustic images obtained from the simulation by using acoustic transducers with central frequency (f_c) at 8 MHz, 15 MHz, 20 MHz, and 30 MHz respectively at 80% bandwidth.

The FFT2 has been applied to the simulated domains to inspect the actual frequency content of the targets. This shows the transformation from the image spatial domain to the frequency domain. The FFT2 decomposes an image into sines and cosines of varying amplitudes and phases, which reveals repeating patterns within the image. Specifically, low frequencies represent gradual spatial variations in the image, typical of large objects. Essentially, the low frequencies contain the most information about the overall shape or pattern in the image. On the other hand, high frequencies correspond to abrupt variations in the image. These high frequencies contain more detail in the image, such as the edge of the objects or thinner structures in the spatial domain.

Therefore, when applying the FFT2 to transform a large-size target, such as the tumor shape in Fig. 7 (A), the FFT2 shows a high presence of low frequencies that are shown by a high-intensity peak in the origin (0, 0) of the x- and y-frequencies shifted to the center. In

Fig. 7 (B) the FFT2 of the blood vasculature domain shows that the amplitude of the frequency components is increasing with distance from the origin, which represents high-frequency content. Finally, when the FFT2 is applied to the combined domain where multi-sized objects are included (see Fig. 7 (C)), the components in the frequency space are both low and high.

Besides, for the different simulated domains, the reconstructed PA images show that using multi-frequency bandwidth sensors can enable the differentiation of the varying-sized optical absorbers. Thus, it is clear that where there is no matching between the spatial frequency content of the target object and the transducer frequency bandwidth, then the image results have blurring or edge enhancement effects. Specifically, if a low-frequency object, such as the tumor shape target (Fig. 7 (A)), is acquired with high-frequency transducers the smooth spatial characteristics of the target will be missing, while the edge will be enhanced. The edge enhancement effect in the reconstructed photoacoustic images was clearly evident and it gains by increasing the central frequency of the transducer.

On the other hand, when a high-frequency object, such as the blood vasculature target (Fig. 7 (B)) is acquired with a low-frequency transducer the fine structure will result as blurred and spatially smoothed, thus losing its sharpness. The blurring effect in the reconstructed photoacoustic images raises by decreasing the central frequency of the transducer.

In a more realistic scenario where targets of different sizes coexist in the same domain, such as in the domain with combined targets (Fig. 7 (C)), then a singular transducer will not be enough to acquire all the frequency components. Thus, the reconstructed images either preserve an accurate detection of low-frequency targets and maintain the fine structures as blurred or enable to reveal high details of the small structures and maintain only the edges of bigger objects.

Other features of the detectors such as the detector aperture can cause blurring in the lateral direction, which becomes more severe near the recording surface. The finite bandwidth, on the other hand, causes spatially invariant blurring.

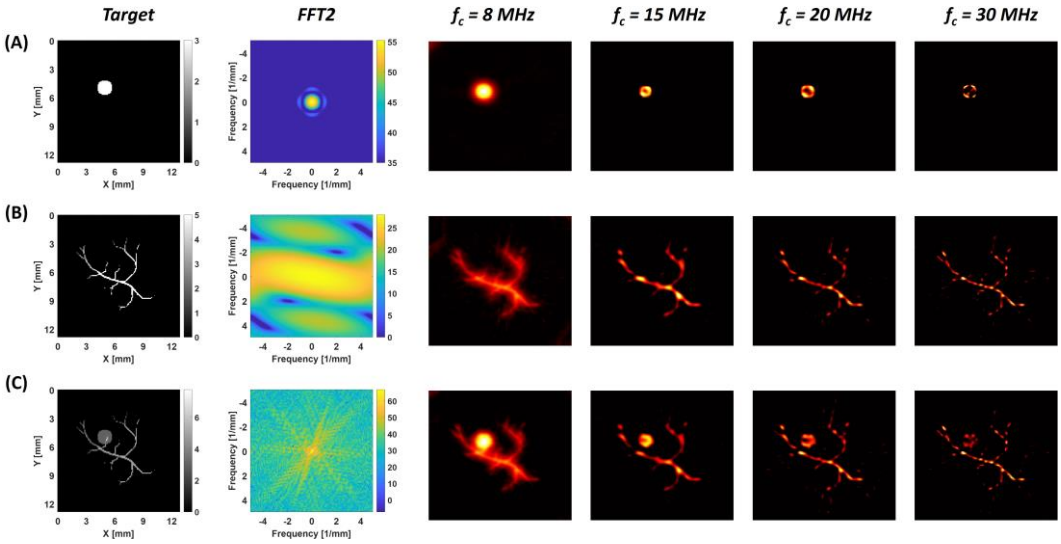

Figure 7. Simulated domains including the different geometrical targets such as the tumor (A), the blood vessel network (B), and their combination (C). Per each domain, the FFT2 has been evaluated to investigate the spatial frequency content of the target objects. Besides, the photoacoustic images of the targets have been simulated using multi-frequency bandwidth sensors. Specifically elements with central frequency (f_c) of 8 MHz, 15 MHz, 20 MHz, and 30 MHz at 80% bandwidth have been used.

Here we calculated the FWHM along different profiles, referred to by the dotted yellow lines in Fig. 8, from the simulated photoacoustic images at multi-frequency bandwidth. Fig. 8 (A) shows the intensity profiles obtained along the tumor shape target at multi-frequency bandwidths depicted as a blue line in the plots and the ground truth is shown as the black dotted line. When increasing the frequency of the sensor, from the profiles it is evident the edge-enhancing effect. On the other end, the profiles obtained from the blood vessel network target along two lines (see Fig. 8 (B-C)) show the blurring effect caused by the low-frequency transducer when imaging sharp structures.

Table 2 reports the FWHM measures obtained from the profiles through the simulated photoacoustic images at multi-frequency bandwidth. As confirmed by the profiles, the measures are more accurate and similar to the reference size when the sensor frequency is matching the frequency content of the target object. Therefore, a low-frequency sensor (f_c = 8 MHz) can exactly image the tumor target, while high-frequency sensors (f_c = 20 MHz, f_c = 30 MHz) can accurately capture the fine structures as the vessel branches of the target.

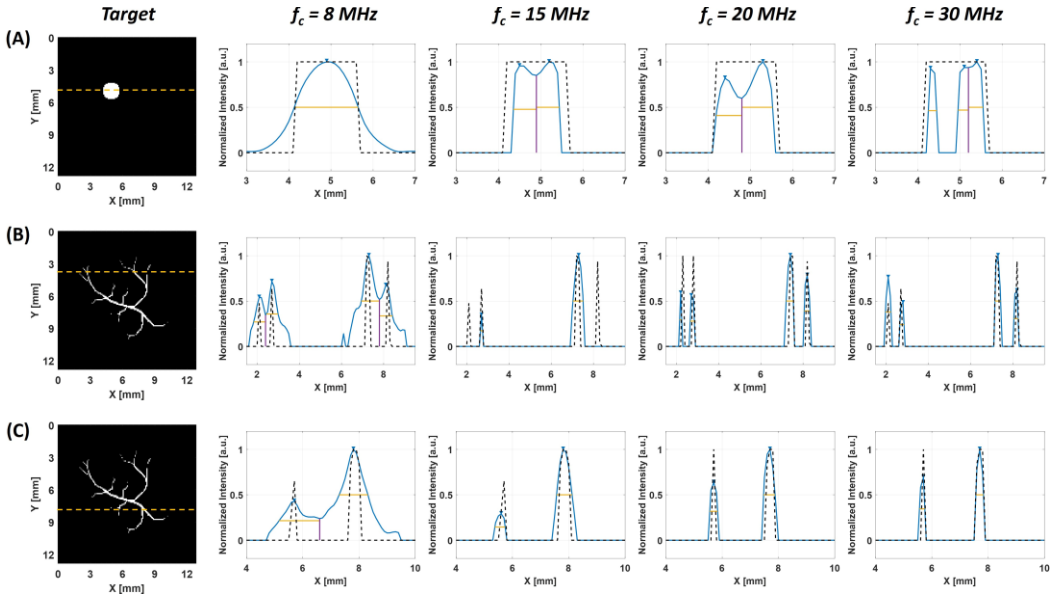

Figure 8. Intensity profiles (blue solid lines) obtained from the simulated photoacoustic images of the different targets at multi-frequency bandwidths. The profiles have been extracted along the center of the tumor (A), as well as along the blood vessel network (B-C) through the yellow dotted lines. The reference profiles from the geometry used for the simulated domains are plotted as black dotted lines.

Table 2. FWHM size estimation of the targets from the intensity profiles of the simulated photoacoustic images at multi-frequency bandwidth. All the measures are expressed in [mm].

Target	Reference	f_c = 8 MHz	f_c = 15 MHz	f_c = 20 MHz	f_c = 30 MHz
Tumor	1.5	1.5	1.1	1.3	0.8
Vessel – line 1	0.1	0.6	-	0.1	0.3
	0.1	0.6	0.1	0.2	0.2
	0.2	0.9	0.5	0.3	0.3
	0.1	0.6	-	0.3	0.2
Vessel – line 2	0.15	1.4	0.4	0.3	0.2
	0.4	1	0.5	0.4	0.3

3.2. Simulation of multi-frequency bandwidth transducers' effect on photoacoustic imaging depth

The simulated domain shown in Fig. 2 has been used to evaluate the effect of multi-frequency bandwidth transducers on the photoacoustic image depth. Fig. 9 depicts the depth profiles obtained from the simulated photoacoustic images with multi-frequency bandwidth sensors across the absorbers.

The blue line in the plots of Fig. 9 represents the photoacoustic intensity profiles along depth while the ground truth, which refers to the position of the absorbers along depths, is shown as a black dotted line. The minimum detectable photoacoustic intensity has been set to 1.5 mPa. Thus, Table 3 reports the maximum detectable depth values obtained by using multi-frequency bandwidth sensors.

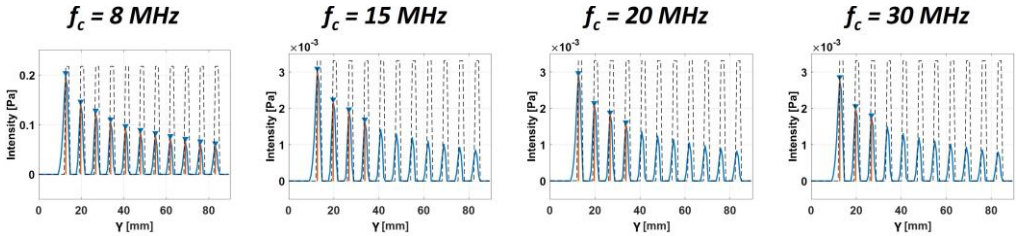

Figure 9. Intensity profiles obtained from the simulated photoacoustic images at multi-frequency bandwidth using the domain including multiple absorbers along the depth.

Thus, Table 3 reports the maximum depth detectivity values obtained by using multi-frequency bandwidth sensors. The sensitivity in deeper regions increases by using low-frequency transducers. In particular, from the simulated domain, the imaging depth ranges between 84 mm to 27 mm by using sensors with central frequency within the range of 8 – 30 MHz.

Table 3. Maximum depth detectivity from the simulated photoacoustic images obtained with multi-frequency bandwidth transducers.

	f_c = 8 MHz	f_c = 15 MHz	f_c = 20 MHz	f_c = 30 MHz
Depth	84 mm	34 mm	32 mm	27 mm

3.3. Experimental multi-frequency bandwidth imaging resolution

After the simulation, we experimentally investigated the effect of multi-frequency bandwidth transducers on photoacoustic image resolution.

Fig. 10 shows the photoacoustic images of the vessel-shaped phantom described in Section 2.4., acquired using multiple transducers. Specifically, here we used the L38xp (Fig. 10 (A)), UHF22x (Fig. 10 (B)), and UHF29x (Fig. 10 (C)) linear transducers at central frequencies of 8 MHz, 15 MHz, and 20 MHz respectively.

Fig. 11 (A) shows the 3D-printed vessel-shaped network that has been embedded in the agarose-based material, which represents the absorbing target of the tissue-mimicking phantom. The yellow dotted lines represent the two lines along with we evaluated the intensity profiles from the photoacoustic images. Fig. 11 (B) shows the intensity profiles along the top line extracted from the photoacoustic images obtained by using multiple transducers. The top line intersects three branches of the vessel network with a reference diameter of 2 mm, 1 mm, and 1.5 mm from left to right respectively. The vessel branch on the right is positioned in 3D at a deeper location than the other two branches, therefore its intensity profile reported with dotted blue lines in the graphs of Fig. 11 (B) shows a lower

intensity. Fig. 11 (C) shows the intensity profiles along the bottom line extracted from the photoacoustic images obtained by using multiple transducers. The bottom line intersects only one branch of the vessel network with a reference diameter of 2 mm.

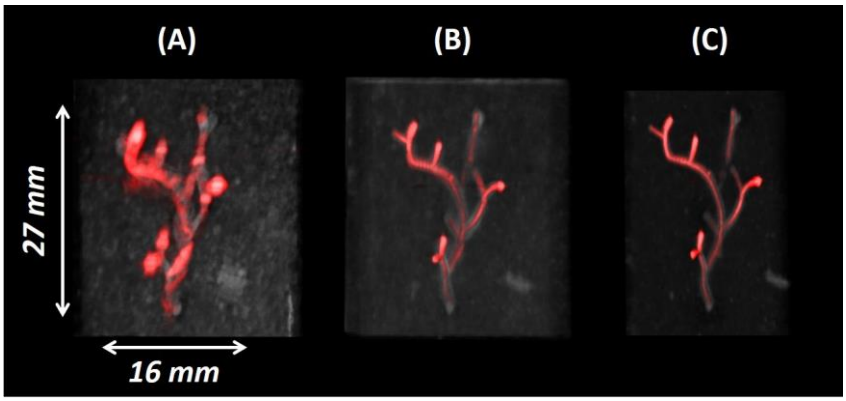

Figure 10. 3D Ultrasound (grayscale) and photoacoustic (red scale) images of the vessel-shaped phantom acquired at 750 nm using L38xp (A), UHF22x (B), and UHF29x (C) transducers.

By observing the profiles, it can be noticed that broader peaks are obtained by using a low-frequency transducer, which indicates the blurring effect. On contrary, sharper peaks are obtained when using higher-frequency transducers. This shows the higher resolution obtained by using higher-frequency transducers.

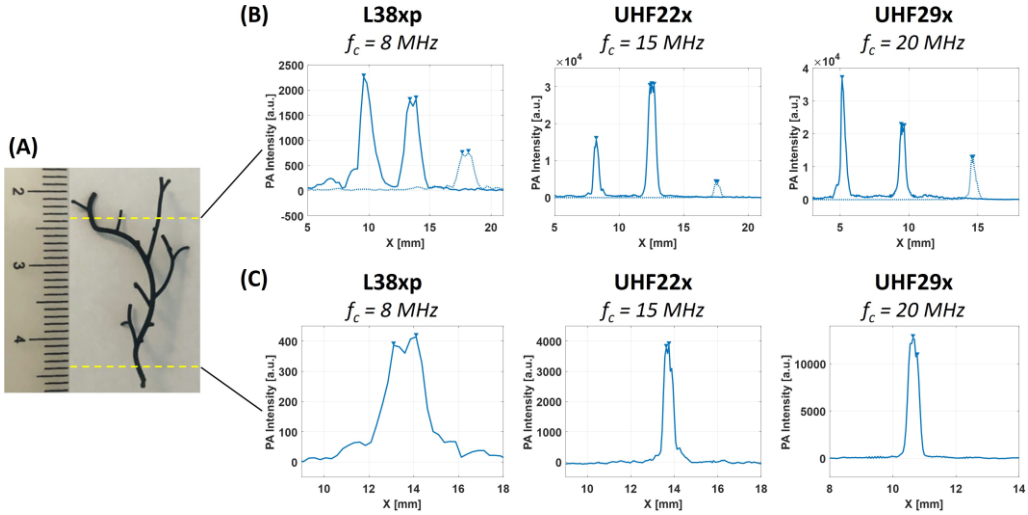

Figure 11. 3D printed blood vessel network coated with black ink, which represents the absorber structure included within the vessel-shaped tissue-mimicking phantom (A). Intensity profiles from the 3D photoacoustic images of the vessel-shaped phantom acquired using L38xp, UHF22x, and UHF29x transducers along the top (B) and bottom (C) dotted yellow line.

Table 4. Size estimation of the diameter of the vessel branches from the intensity profiles of the photoacoustic images of the vessel-shaped phantom acquired by using L38xp, UHF22x, and UHF29x transducers. All the measures are expressed in [mm].

Vessel	Reference	L38xp	UHF22x	UHF29x
Line 1	2 1 1.5	1.1 1.3 1.4	0.45 0.7 0.55	0.34 0.5 0.43
Line 2	2	1.95	0.5	0.4

The resolution is then estimated by measuring the FWHM from the peaks obtained along the profiles. Table 4 reports these measures from the profiles extracted from the photoacoustic images acquired with multiple transducers. As shown from the profiles and estimated as FWHM, thicker branches, as reported from the reference sizes, are imaged more accurately with a low-frequency transducer as the L38xp. On contrary, thinner branches are accurately imaged via the higher frequency transducers.

3.4. Experimental multi-frequency bandwidth imaging depth

Here we experimentally investigated the effect of multi-frequency bandwidth transducers on photoacoustic image depth. Fig. 12 shows the photoacoustic images of the X-shaped phantom described in Section 2.5., acquired using multiple transducers. Specifically, here we used the L38xp (Fig. 12 (A)), UHF22x (Fig. 12 (B)), and UHF29x (Fig. 12 (C)) linear transducers at the central frequencies of 8 MHz, 15 MHz, and 20 MHz respectively.

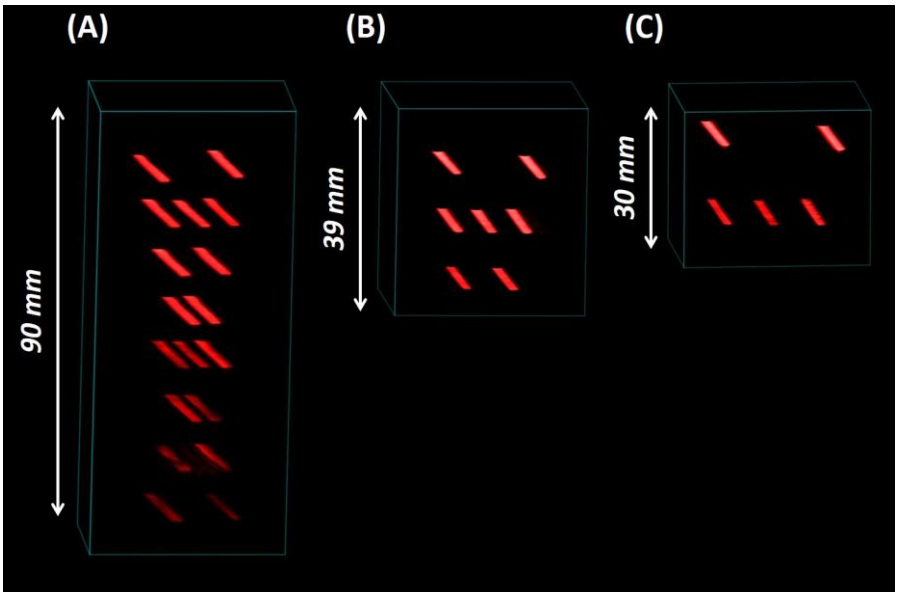

Figure 12. Photoacoustic 3D images of the X-shaped phantom acquired at 750 nm using L38xp (A), UHF22x (B), and UHF29x (C) transducers.

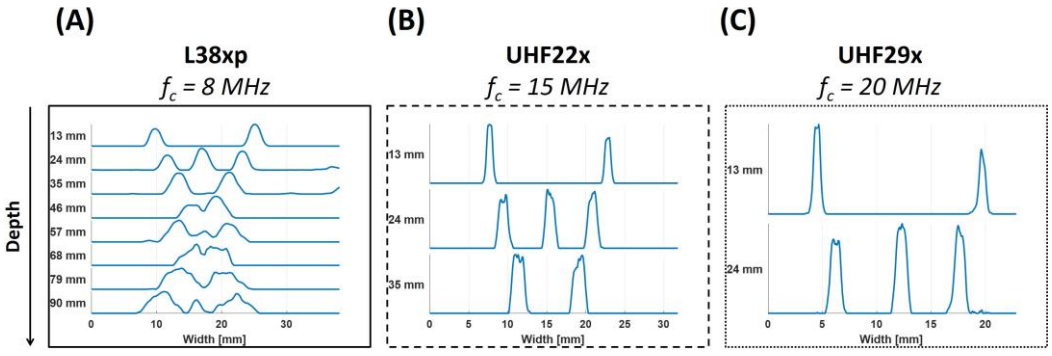

Figure 13. Intensity profiles at the level of the inserted absorbing threads within the X-shaped phantom obtained from the photoacoustic images acquired using L38xp (A), UHF22x (B), and UHF29x (C) transducers.

From the photoacoustic image of the X-shaped phantom reported in Fig. 12 (A), imaging depth up to 90 mm can be achieved by using an L38xp low-frequency transducer.

Lower imaging depths ranging from 39 mm to 30 mm can be achieved by using UHF22x and UHF29x higher frequency transducers (Fig. 12 (B-C)).

Fig. 13 shows the intensity profiles obtained across the absorbing threads of the X-shaped phantom along the depth, from the photoacoustic images obtained by using L38xp (Fig. 13 (A)), UHF22x (Fig. 13 (B)), and UHF29x (Fig. 13 (C)) transducers. From the profiles in Fig. 13, it is possible to observe that broader peaks are obtained by lower frequency transducer and sharper peaks are detected at a higher frequency. Besides, observing the profiles along the depth, these became noisy in deeper positions, especially for the L38xp transducer that can image up to 90 mm.

Fig. 14 (A) shows the SNR measures from the photoacoustic images obtained by using the different transducers along the depth. As observed from the images and intensity profiles the SNR decreases along the depth, thus the image sensitivity and specificity at depth are reduced. This is not only caused by the frequency bandwidth of the transducer but also depends on the non-uniform light fluence distribution along the depth. This effect is also known as spectral coloring artifact [27].

Fig. 14 (B) shows the estimated size of the threads included within the X-shaped phantom. The thread size has been evaluated as the FWHM value from the peaks along the lateral profiles. The size of nylon threads declared by the manufacturer (Almega Nylon, Albatros) is 0.50 mm. However, by using the lower frequency transducer (L38xp with f_c = 8 MHz), at deeper regions the estimated size error is higher as a result of the combination of blurring and spectral coloring effects. While higher frequency transducers show high accuracy in imaging small objects, as for the nylon threads.

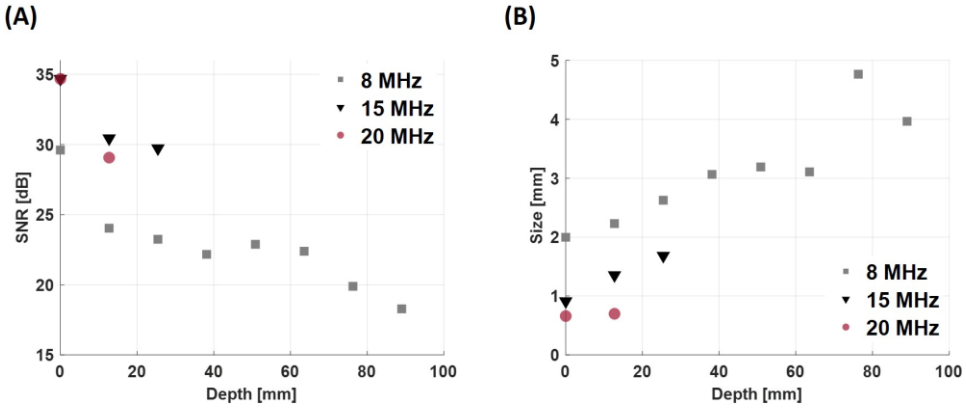

Figure 14. SNR measurements (A) and diameter estimation of the threads (B) obtained from the photoacoustic images of the X-shaped phantom acquired by using L38xp, UHF22x, and UHF29x transducers.

3.5. Multi-scale hand-shaped phantom imaging

Finally, by using the hand-shaped phantom (described in detail in Section 2.6.) we evaluated the feasibility of multi-frequency bandwidth photoacoustic imaging in a more realistic clinical scenario. The ultrasound and photoacoustic images of the hand-shaped phantom have been acquired by using the L38xp and UHF29x transducers by following the imaging protocol described in detail in Section 2.6.1.

Fig. 15 (A) shows the maximum intensity projection of the volumetric PA image obtained by using the high-frequency transducer (UHF29x), where the vessel network at a more superficial depth can be visualized with high resolution. Fig. 15 (B) shows the US-PA volumetric low-frequency image (L38xp) of the region where the pin has been placed within the hand-shaped phantom. The deeper structures such as the surface of the skeleton from the US image depicted in grayscale and the metallic pin from the PA image shown in red scale can be visualized.

The hand-shaped phantom and this initial attempt of acquiring multi-frequency bandwidth US-PA images in a phantom that mimics a realistic clinical scenario demonstrate the advantages of such an approach to reveal multi-scale features. This aims to open further developments and optimizations for the real use of the technology in clinical practice.

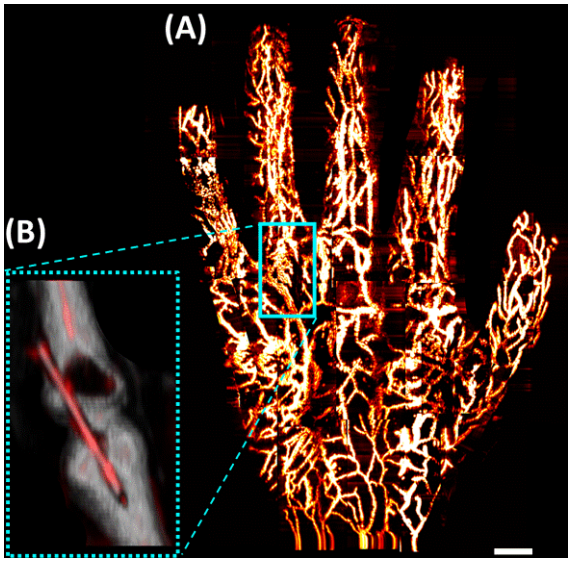

Figure 15. PA image of the hand-shaped phantom obtained by using the UHF29x transducer at 20 MHz central frequency where the superficial vasculature is captured (A). US-PA image of the hand-shaped phantom obtained by using the L38xp transducer at 8 MHz central frequency where the skeleton and implant can be identified (B); the scale bar size is 1cm.

4. Discussion

In this work, we investigated multi-frequency bandwidth photoacoustic imaging to cover multi-scale applications and facilitate the translation of the technology into the clinics. Thus, we explored the effect of multi-frequency bandwidth transducers on the reconstructed photoacoustic imaging of absorbers with various sizes and shapes. Specifically, we have investigated the effect on image resolution and depth of PA signals generated by targets with different sizes and received by ultrasound transducers with various frequency bandwidths. In general, larger structures are characterized by lower frequency content whereas smaller structures are described by higher frequency signals. The suitability of multi-frequency bandwidth photoacoustic to image objects at multi-scale has been tested through simulations and experimentally on customized tissue-mimicking phantoms. Besides, a realistic human hand-shaped phantom has been designed and fabricated to replicate a realistic clinical scenario. The hand-shaped phantom has been used to validate the multi-frequency bandwidth imaging approach and the image acquisition protocol dedicated to big volumes.

The use of multi-frequency bandwidth transducers to acquire photoacoustic images of the same object at multiple bands has shown the potential to enhance various aspects of the target of interest, thus avoiding misinterpretations. Besides, this enables compromising imaging depth and resolution, which are crucial aspects for the clinical translation of photoacoustic imaging technology. Hence, the use of multi-frequency bandwidth transducers can guarantee the ability to penetrate deep into tissue and the high resolution of superficial structures, which is important for many imaging applications in clinical practice.

The study showed that multi-frequency bandwidth PA imaging is adaptable for imaging small to large structures and provides unique opportunities for translational research. However, further optimizations are still needed to improve the acquisition protocol and the image processing to enhance the visualization and fuse multi-resolution

features at multiple depths in a real clinical scenario. This study is a proof of principle that opens many possibilities to optimize the US-PA technology, on the hardware and software side, to facilitate the multi-frequency bandwidth approach for clinical applications. Besides the resolution aspects related to the transducer frequency response, imaging depth is also a crucial aspect. Apart from other several parameters such as excitation source, excitation wavelength, and imaging target, the transducer specification has a significant effect on photoacoustic penetration depth.

The current limitations of the approach and future developments are discussed in detail in Chapter 9.

References

[1] Y. Sun, H. Helmholz, and R. Willumeit-Römer, "Preclinical in vivo research of magnesium-based implants for fracture treatment: A systematic review of animal model selection and study design," *Journal of Magnesium and Alloys*, vol. 9, no. 2. 2021.

[2] D. Zhao, F. Witte, F. Lu, J. Wang, J. Li, and L. Qin, "Current status on clinical applications of magnesium-based orthopaedic implants: A review from clinical translational perspective," *Biomaterials*, vol. 112. 2017.

[3] H. Windhagen *et al.*, "Biodegradable magnesium-based screw clinically equivalent to titanium screw in hallux valgus surgery: Short term results of the first prospective, randomized, controlled clinical pilot study," *Biomed. Eng. Online*, vol. 12, no. 1, 2013.

[4] H. Helmholz *et al.*, "Tissue responses after implantation of biodegradable Mg alloys evaluated by multimodality 3D micro-bioimaging in vivo," *J. Biomed. Mater. Res. - Part A*, vol. 109, no. 8, 2021.

[5] G. Paltauf, R. Nuster, and M. Frenz, "Progress in biomedical photoacoustic imaging instrumentation toward clinical application," *Journal of Applied Physics*, vol. 128, no. 18. 2020.

[6] A. B. E. Attia *et al.*, "A review of clinical photoacoustic imaging: Current and future trends," *Photoacoustics*, vol. 16. 2019.

[7] J. Kim *et al.*, "Multispectral photoacoustic assessment of thyroid cancer nodules in vivo," 2020.

[8] A. Dima and V. Ntziachristos, "In-vivo handheld optoacoustic tomography of the human thyroid," *Photoacoustics*, vol. 4, no. 2, 2016.

[9] S. Manohar and M. Dantuma, "Current and future trends in photoacoustic breast imaging," *Photoacoustics*, vol. 16, no. February, p. 100134, 2019.

[10] S. Manohar, A. Kharine, J. C. G. Van Hespen, W. Steenbergen, and T. G. Van Leeuwen, "The Twente Photoacoustic Mammoscope: System overview and performance," *Physics in Medicine and Biology*, vol. 50, no. 11. 2005.

[11] M. Heijblom, W. Steenbergen, and S. Manohar, "Clinical photoacoustic breast imaging: The twente experience.," *IEEE Pulse*, vol. 6, no. 3, 2015.

[12] J. Hult *et al.*, "Comparison of photoacoustic imaging and histopathological examination in determining the dimensions of 52 human melanomas and nevi ex vivo," *Biomed. Opt. Express*, vol. 12, no. 7, 2021.

[13] R. Sheikh *et al.*, "Clinical Translation of a Novel Photoacoustic Imaging System for Examining the Temporal Artery," *IEEE Trans. Ultrason. Ferroelectr. Freq. Control*, vol. 66, no. 3, pp. 472–480, 2019.

[14] H. Kajita *et al.*, "Visualization of Lymphatic Vessels Using Photoacoustic Imaging," *Keio J. Med.*, vol. 70, no. 4, 2021.

[15] H. Kajita *et al.*, "Photoacoustic lymphangiography," *J. Surg. Oncol.*, vol. 121, no. 1, 2020.

[16] M. Petri *et al.*, "Photoacoustic imaging of real-time oxygen changes in chronic leg ulcers after topical application of a haemoglobin spray: A pilot study," *J. Wound Care*, vol. 25, no. 2, 2016.

[17] A. Karlas *et al.*, "Cardiovascular optoacoustics: From mice to men – A review," *Photoacoustics*, vol. 14, no. March, pp. 19–30, 2019.

[18] Z. Ali *et al.*, "360º optoacoustic capsule endoscopy at 50 Hz for esophageal imaging," *Photoacoustics*, vol. 25, 2022.

[19] E. A. Gonzalez and M. A. L. Bell, "GPU implementation of photoacoustic short-lag spatial coherence imaging for improved image-guided interventions," *J. Biomed. Opt.*, vol. 25, no. 07, 2020.

[20] H. Wang, S. Liu, T. Wang, C. Zhang, T. Feng, and C. Tian, "Three-dimensional interventional photoacoustic imaging for biopsy needle guidance with a linear array transducer," *J. Biophotonics*, vol. 12, no. 12, 2019.

[21] J. L.-S. Su, B. Wang, and S. Y. Emelianov, "Photoacoustic imaging of coronary artery stents," *Opt. Express*, 2009.

[22] D. Lee, S. Park, W.-C. Noh, J.-S. Im, and C. Kim, "Photoacoustic imaging of dental implants in a porcine jawbone ex vivo," *Opt. Lett.*, 2017.

[23] M. Vallet, F. Varray, M. A. Kalkhoran, D. Vray, and J. Boutet, "Enhancement of photoacoustic imaging quality by using CMUT technology: Experimental study," in *IEEE International Ultrasonics Symposium, IUS*, 2014.

[24] M. Omar, D. Soliman, J. Gateau, and V. Ntziachristos, "Ultrawideband reflection-mode optoacoustic mesoscopy," *Opt. Lett.*, vol. 39, no. 13, 2014.

[25] B. E. Treeby and B. T. Cox, "k-Wave: MATLAB toolbox for the simulation and reconstruction of photoacoustic wave fields," *J. Biomed. Opt.*, vol. 15, no. 2, 2010.

[26] G. Matrone, A. S. Savoia, G. Caliano, and G. Magenes, "The delay multiply and sum beamforming algorithm in ultrasound B-mode medical imaging," *IEEE Trans. Med. Imaging*, 2015.

[27] J. Gröhl *et al.*, "Learned spectral decoloring enables photoacoustic oximetry," *Sci. Rep.*, vol. 11, no. 1, 2021.

Chapter 9

Conclusions and Outlook

Abstract:

This final chapter aims to discuss the conclusions of the research work conducted throughout the dissertation. Besides, an overview of future developments is provided.

9.1. Conclusions

In this dissertation, we derived and implemented a novel method named Superpixel Photoacoustic Unmixing (SPAX) framework. The SPAX enables the data-driven differentiation of molecular tissue components, without any user interactions. The framework is also extended to compensate for the spectral coloring artifact. Furthermore, we formulated and implemented an advanced superpixel subsampling process that increases the detection of less prominent tissue chromophores, those which are generally obscured from the most absorbing molecules. Besides, the SPAX also includes an optimized visualization of the molecular components' distribution with unprecedented details. Extensive analysis has been conducted to benchmark the performance of the formulated SPAX approach. To this end, the SPAX shows that data-driven approaches have the potential to solve many of the challenges that still limit the sensitivity and specificity of photoacoustic image unmixing.

In addition, established imaging techniques such as MRI, CT, PET, and Ultrasound (US) rely on commercially available, well-characterized tissue-mimicking phantoms for technical validation studies. In PAI there are currently no standard protocols for realistic durable phantoms. To this end, here the design and fabrication of an anthropomorphic heterogeneous mouse phantom compatible with PA have been conducted. To our knowledge, this is the first time of using 3D-printing technology to establish an anatomically accurate, durable, and heterogeneous small animal phantom for PAI. The proposed methodology can be adapted by researchers and clinicians to construct realistic tissue-mimicking phantoms for the continued development of PAI technology. The mouse phantom has enabled the testing of the newly developed image processing tools, as well as the standardization of PA imaging protocols, thus leading to higher chances of success during the in-vivo experiments.

Further, the SPAX approach has been used for different *in vivo* applications to automatically monitor endogenous and exogenous tissue chromophores. Besides, the novel spectral superpixel subsampling approach has shown great potential to identify less prominent tissue chromophores, such as fat, that generally remain obscured by the most prominent absorbers (like hemoglobin), during in-vivo studies. The conventional approach to detect the fat is to use the wavelengths within the Far Infrared (FIR) range, where the absorption from the hemoglobin is negligible. Since the PA excitation sources in the FIR range have lower energy compared to NIR, the use of this range is constrained to superficial structures and microscopic applications. As the SPAX framework is optimized in the NIR-I range of [680−970]nm, where we have more availability of nanosecond pulsed laser sources, this can be used to detect the distribution of fat along the whole-body of the small animals, without *a priori* information.

Besides, for the first time, spectral PAI and SPAX approach have been used for highly advanced applications involving biodegradable bone implants made of magnesium (Mg) in preclinical models. Mg-based implants are an innovative alternative to bio-inert implants to treat bone fractures. Here the SPAX data-driven approach has shown great potential to reveal the tissue components and oxygen saturation ($SO2$) tissue changes in presence of Mg-based implants in a

data-driven way. These measures represent promising biomarkers to study inflammatory response and tissue oxygenation function during bone regeneration. Thus, the SPAX opens many possibilities for unbiased investigations of tissue composition and remodeling in presence of biodegradable implants.

Finally, we have explored the possibilities of translating the approach in clinical settings. Generally, photoacoustic signals have broadband frequency content by nature, which can span from Kilohertz to several tens of Megahertz. However, the US transducers used in PAI are not ideal point detectors with infinite bandwidth. In PAI, the limited frequency bandwidth has a significant impact on the resolution and depth of the reconstructed image. Specifically, the use of lower frequency transducers (below 10 MHz), enables imaging at depth and provides spatial resolutions in the range of 150 − 200 microns. On the other hand, high-frequency transducers within the range of 15 − 50 MHz can enable spatial resolutions of around 40 microns. However, this results in increased acoustic attenuation, which limits the imaging depth. Therefore, PAI may require the use of a low or high-frequency transducer depending on the application. In general scenarios, it would be ideal to use the combination of photoacoustic imaging at high-frequency to monitor superficial highly detailed features and low frequency for targets at depth. To this end, the effect of using multiple US transducers with different frequency bandwidths on the resolution and depth of PA imaging has been investigated through simulation and tissue-mimicking phantom experiments. This was useful to lay the fundamentals for future developments of the superpixel PAI method.

Herewith, we make the following conclusions:

Unsupervised machine learning algorithms have the potential to accurately unmix spectral photoacoustic imaging without *a priori* information.

As described in **Chapter 2**, we have explored the feasibility of various unsupervised machine learning methods classified as blind source separation (BSS) algorithms to identify and separate the most prominent tissue components from spectral PAI. The BSS approaches enabled the unmixing without *a priori* knowledge of the expected constituent tissue components as source spectra. However, as shown in the comparative study, independent component analysis (ICA) and principle component analysis (PCA) algorithms have shown a lower capability to accurately unmix while non-negative matrix factorization (NNMF) has shown potential higher performance for sPAI blind unmixing.

Non-negative constraints in the iterative optimization process have shown superior performance for the blind unmixing of spectral photoacoustic imaging.

As described in **Chapter 3**, NNMF has shown promising unmixing performance to accurately unmix sPAI. This is thanks to the non-negativity constraints implemented within NNMF that are

in accordance with the physical meaning of sPAI. Here the NNMF approach has been tested and validated through *in vivo* experiments. However, from the obtained results, the NNMF identifies only the most prominent tissue chromophores such as oxy and deoxy hemoglobin and contrast agents. While the NNMF approach has shown lower sensitivity in the detection of weaker absorbers from sPAI. In addition, the NNMF is prone to unmixing misinterpretation at depths due to the spectral coloring effect, and the user interaction is still required to select the number of source components to unmix as *a priori* knowledge.

A standardized protocol for the fabrication of anthropomorphic phantoms compatible with photoacoustic imaging facilitates the testing and validation of innovative imaging approaches.

In **Chapter 4** we have described the need for a PA-compatible tissue-mimicking phantom to facilitate the benchmarking of newly developed approaches for PAI. Thus, we have designed and developed an anthropomorphic heterogeneous mouse phantom that uses a combination of image modeling, copolymer in oil-based materials, and 3D printing techniques. The results have shown the potential of the mouse phantom to be used for the optimization, validation, and standardization of preclinical PAI techniques.

The newly developed superpixel photoacoustic unmixing (SPAX) framework has shown improved sensitivity and specificity of the unmixed components at a volumetric scale without any user interaction, by also compensating for the spectral coloring effect.

As described in detail in **Chapter 5**, to overcome the current limitation of blind unmixing, a novel SPAX framework has been formulated and implemented. The results have shown that the proposed data-driven SPAX algorithm differentiates, without any *a priori* information and user interactions, the tissue components. The SPAX also includes an initial singular value decomposition (SVD) analysis to reveal the number of significant components to detect. The NNMF is then applied to blindly reveal the prominent tissue components from sPAI. Besides, the framework includes a novel spectral superpixel subsampling approach to also identify less prominent tissue chromophores. Furthermore, the SPAX approach overcomes the spectral coloring limitations and prevents unmixing misinterpretations at depth and it is also extended to reveal molecular components at a volumetric scale.

Multi-spectral photoacoustic imaging and SPAX unmixing have the potential to *in vivo* monitor endogenous and exogenous tissue chromophores.

As described in **Chapter 6**, the application through *in vivo* experiments of the SPAX framework for tissue composition monitoring has shown promising results. In particular, during *in vivo* experiments, the SPAX has shown the ability to detect endogenous and exogenous

chromophores with higher sensitivity and specificity at depth. Thus, the SPAX approach has the potential to discern any spectral change that might occur in pathological conditions. Hence, the SPAX framework could be used as a predictive and monitoring tool to identify early pathological conditions and facilitate therapeutic follow-up.

Multi-spectral photoacoustic imaging and SPAX unmixing have the potential to *in vivo* monitor tissue remodeling in presence of biodegradable bone implants without any user interaction.

After showing the potential of SPAX in healthy living tissues through chapters 5 and 6, spectral changes and tissue oxygen saturation changes have been monitored in presence of biodegradable bone implants made of Magnesium. This could be beneficial to predict the success or failure of bone fixation as described in **Chapter 7**. Monitoring the soft tissue remodeling, angiogenesis, and inflammation is crucial to evaluate the tissue healing in the surrounding of the biodegradable bone implant used to fix a bone fracture. Thus, this has shown great potential to use SPAX for these advanced applications.

A multi-frequency photoacoustic imaging approach has the potential to translate the technology into clinical practice.

As described in **Chapter 8**, to expand the potential of using sPAI and SPAX in clinical applications, a multi-resolution approach would be beneficial to merge information from the surface and at depth with unprecedented details. Thus, this will also open many opportunities to translate the findings into clinical practice. Here, we have provided the first in-depth characterization of using multiple US transducers with different frequency bandwidths for photoacoustic imaging to investigate tissue composition at multiple depths and resolutions.

Table 1 summarizes the novel aspects and respective scientific contributions achieved through this thesis work.

Table 1. Overview of the thesis chapters' content and related scientific contribution.

Chapter	*Novelty*	*Scientific Contribution*	
2, 3	Unsupervised machine learning unmixing methods for sPAI.	**Grasso, V.,** Hassan, H. W., Mirtaheri, P., Willumeit-Römer, R., & Jose, J. (2022). "*Recent advances in photoacoustic blind source spectral unmixing approaches and the enhanced detection of endogenous tissue chromophores."* Frontiers in Signal Processing, p.67.	Published
		Grasso, V., Holthof, J., & Jose, J. (2020). "*An automatic unmixing approach to detect tissue chromophores from multispectral photoacoustic imaging."* Sensors, 20(11), 3235.	Published
4	Anthropomorphic heterogeneous durable phantoms development.	**Grasso, V.,** Raymond, J., Willumeit-Römer, R., Joseph, J., & Jose, J. (2023, March). "*Development and characterization of a durable tissue-mimicking phantom for calibration and standardization of photoacoustic imaging."* In Photons Plus Ultrasound: Imaging and Sensing 2023 (p. PC123793D). SPIE.	Published
		Grasso, V., Raymond, J., Willumeit-Römer, R., Joseph, J. & Jose, J., (2023). "*Development of a morphologically realistic mouse phantom for pre-clinical photoacoustic imaging."* Medical Physics.	Under Review
5	Superpixel photoacoustic unmixing (SPAX) framework.	**Grasso, V.,** Willumeit-Römer, R., & Jose, J. (2022). "*Superpixel spectral unmixing framework for the volumetric assessment of tissue chromophores: A photoacoustic data-driven approach."* Photoacoustics, 26, 100367.	Published
6, 7	Advanced applications of SPAX for endogenous and exogenous tissue chromophores detection, as well as for tissue monitoring in presence of biodegradable bone implants made of Magnesium.	**Grasso, V.,** Willumeit-Römer, R., & Jose, J. (2021, September). "*Unsupervised multi-spectral photoacoustic framework for the detection and quantification of tissue chromophores."* In 2021 IEEE International Ultrasonics Symposium (IUS) (pp. 1-4). IEEE.	Published
		Hassan, H. W., **Grasso, V.,** Korostynska, O., Khan, H., Jose, J., & Mirtaheri, P. (2021). "*An overview of assessment tools for determination of biological Magnesium implant degradation."* Medical Engineering & Physics, 93, 49-58.	Published
		Hassan, H. W., Mota-Silva, E., **Grasso, V.,** Riehakainen, L., Jose, J., Menichetti, L., & Mirtaheri, P. (2023). "*Near-infrared spectroscopy for the in vivo monitoring of biodegradable implants in rats."* Sensors, 23(4), 2297.	Published
8	Multi-frequency PAI: "En route to the clinics".	**Grasso, V.,** Willumeit-Römer, R., & Jose, J. (2023, March). "*Development of an AI-assisted multi-spectral photoacoustic imaging for volumetric molecular tissue composition: a multi-frequency translational approach".* In Photons Plus Ultrasound: Imaging and Sensing 2023 (Vol. 12379, p. 1237902). SPIE.	Published
		Grasso, V., Willumeit-Römer, R., & Jose, J. (2023) "*Multi-frequency photoacoustic imaging for tissue monitoring in presence of biodegradable bone implants: "En route to the clinics".*" Sensors.	Submitted

9.2. Outlook

Overall, the development of the superpixel spectral photoacoustic imaging method is a major achievement in the field of tissue chromophores unmixing and its quantification. This would have a positive impact on disease diagnosis, treatment, and monitoring for clinical applications. However, when translating the technology, the hardware and software setup must be optimized to image large areas of interest. Therefore, further efforts are needed to translate the technology and the current developments into clinical practice. To this end, our future goal is to combine our recent developments done on the data-driven unmixing side with the optimization of the translational aspects to use the technology to monitor the tissue remodeling process in human patients. At present, there still exist certain challenges that need to be addressed to broaden the potential of the technology. Future developments aim to push the photoacoustic imaging modality toward its limits, to monitor and diagnose undesired tissue changes that can occur in presence of biodegradable bone implants, thus predicting implant-bone fixation failure. This will result in increasing the level of safety for monitoring human patients currently treated with biodegradable implants and will boost the further development of PAI on a clinical level.

Listed below are some of the key factors that will be further investigated in the future:

Acquisition and processing computational time: To promote the clinical translation of the superpixel sPAI technology real-time unmixing processing would be beneficial. Typically, spectral unmixing techniques are not feasible for real-time applications due to the long acquisition time associated with transmitting multiple laser wavelengths in sPAI. Thus, further efforts would be required to adjust the tradeoff between acquisition time and spectral resolution. As already demonstrated by Luke et al. [1], the implementation of advanced algorithms for the selection of significant wavelengths could facilitate unsupervised unmixing and thus minimize the acquisition time. Besides, the optimization of spectral Monte Carlo simulations for fluence compensation by using GPU-based implementations would also speed up the computational processing time, encouraging the use of sPAI in further applications.

Multi-frequency PAI imaging: Currently, preclinical high-frequency PAI technologies can image structures up to several centimeters deep inside the tissue. Such penetration depth significantly exceeds pure optical imaging techniques with a better spatial resolution (at comparable depths). However, reliable and clinically useful PAI at depths exceeding 2–3 cm is still a challenge. Multi-frequency photoacoustic imaging may mitigate this limitation, expanding the possibilities for clinical applications. Recently, dual-frequency excitation-detection US transducers have been demonstrated to minimize loss of information as broadband frequency content can be detected [2]. Through this dissertation, we provided the proof-of-concept of implementing the multiple-frequency imaging method by combining different US transducers to enable the acquisition of complete PAI information. However, advanced software optimization to merge imaging with multiple resolutions and depths would be required to fuse and co-localize imaging features of vital importance for clinical applications.

Hand-held PAI configuration: Besides, to facilitate the application in clinics, a hand-held PAI configuration would be preferred. In particular, for many clinical applications, it is not feasible to surround the area of interest with US detectors from all sides. To overcome this limited view in PAI, proper hardware configuration and customized reconstruction techniques are necessary to guarantee accurate image acquisition and formation. To this end, GPS-based tracking imaging has the potential to convert a standard PAI system into a tomographic imaging device. This combined with AI-based image rendering would enable 3D PAI imaging for a wide range of clinical applications. Besides, the optimized setup for volumetric PA imaging should also consider the patient comfort aspects and ergonomics of the hand-held technology. Furthermore, proper acoustic coupling between bigger tissues and the ultrasound transducer must be always maintained. This limitation can be overcome, or at least reduced, by a customized setup for human patients using advanced bubble-free gel materials. Finally, the removal of artifacts arising from the patient or operator motion during hand-held acquisition would enhance the robustness to noise as well as imaging quality.

Safety aspects and FDA approval: Although a considerable volume of preclinical studies has reported the potential of PAI in clinics, the availability of clinical PAI systems is still very limited. However, there are several attempts for translating photoacoustic technologies into the clinic. Improvements in hardware/software of the technology may facilitate the translation process, leading to more PAI FDA-approved systems.

In summary, Superpixel Spectral Photoacoustic Imaging method has shown promising achievements in a multitude of biomedical applications. However, further refinements and optimizations, as listed above, are needed to expand its applicability for unexplored areas and ensure its successful translation “En route to the clinics”. Ultimately, future goals include additional developments of the technology so that it can be adapted to more preclinical and clinical applications.

References

[1] G. P. Luke, S. Y. Nam, and S. Y. Emelianov, “Optical wavelength selection for improved spectroscopic photoacoustic imaging,” *Photoacoustics*, vol. 1, no. 2, pp. 36–42, 2013.

[2] I. G. Newsome *et al.*, “Implementation of a Novel 288-Element Dual-Frequency Array for Acoustic Angiography: In Vitro and in Vivo Characterization,” *IEEE Trans. Ultrason. Ferroelectr. Freq. Control*, vol. 68, no. 8, 2021.

Acknowledgments

I would like to take a moment to thank all the people who helped and supported me through my Ph.D. Without them, this journey would not have been as successful.

As first and foremost, I wish to express my sincere gratitude to my Ph.D. supervisor **Dr. Jithin Jose** for his constant guidance, encouragement, and support. The enthusiasm and passion he has for the field, combined with his knowledge, innovative vision, hard-working, outstanding problem-solving attitude, perseverance, and honesty have deeply motivated and inspired me in my work. I'm truly thankful for the unique opportunity of working under his supervision and mentorship as well as conducting research in the industry, which has broadened my knowledge from different perspectives. The insightful discussions with him and his invaluable advice have encouraged me to work hard and pushed me to go farther than I thought I could go. This helped in shaping me into the person and scientist I am today. "Dream Big" was his initial advice that has been a driving force during my Ph.D. journey and made me overcome any challenges. I can't be thankful enough for everything he did!

I'm deeply grateful to my co-supervisor **Prof. Dr. Regine Willumeit-Römer** for her prompt and proactive guidance and support at any moment during the Ph.D. project. Her precious scientific knowledge has been an invaluable lesson. Besides, she has been a real role model for me as a woman in science with her dedication and ability to manage a multitude of projects always with the same enthusiasm and professionality. She has been a fundamental scientific mentor to me over the years.

I wish to thank the second reviewer **Prof. Dr. Jan-Bernd Hövener** and the committee **Prof. Dr. Zeynep Altintas** and **Prof. Dr. Rainer Adelung** for their time and effort in reviewing this thesis.

In addition, I would like to thank all my colleagues from **FUJIFILM VisualSonics**. They have been my second family here in Amsterdam. A special thanks to **Dr. Lydia Eidemueller** and **Dr. Greg Nesbitt** who have approved and sustained all the project developments with trust and sincere support.

I'm extremely thankful to **Dr. Dieter Fuchs** for all the training in the lab, his expertise in designing and performing experiments, as well as his endless scientific support and encouragement during conferences. His precious help, patient teaching, and expert advice have been so constructive through the years.

A special thanks to **Dr. Magdalena Steiner** for her sincere support since the day of the phone interview. I am deeply grateful for all her help and guidance during conferences and workshops

we attended together, as well as for her prompt feedback on the “Zusammenfassung” of this thesis.

I’m deeply grateful to **Laurence Rayssiguier** for her genuine support during conferences and through all the developments of this project. Her enthusiasm and positivity have been always of great help as well as her constant support through marketing activities.

I’m infinitely grateful to **Angela Kost** and **Ildiko Fazekas** for being the best colleagues and friends, and for providing me with a warm and welcoming work environment since the day I arrived at the office. Our “VSI ladies' office” has become my second home lately, and they are like two sisters with whom I can always openly share my feelings and worries as well as have our big laughing moments. They have been really fundamental in every moment of the Ph.D. roller coaster. Thanks for being always supportive and for being there to help me in any situation, and for making Amsterdam a homely place for me.

I wish to thank **Dr. Caroline O'Riordan** for being so special, for always coming to my rescue in the lab when I was struggling, for always having a supportive word, and for making the long days in the lab really fun while ensuring that I enjoyed my life outside work as well.

A special thanks to **Elena De Francisco** for being always friendly and supportive over the years and for being there any time I needed a solace chat in my mother tongue. All the past experiences we have shared have been of huge encouragement to me.

Big thanks to **Dr. Peter Kesa, Dr. Philippe Trochet, and Dr. Shripad Bangale** for their help in the lab and the scientific support anytime I need it. They have thought me a lot from their experience in photoacoustic imaging and animal experiments.

Thanks to all the sales managers namely **Dr. Savino Lacerenza, Dr. Philippe Davault, Dr. Milan Kopecek, Dr. Wayne Evans, Dr. Adrie Gubbels,** and **Dr. Marcus Salmon** for all the support during conferences and for being an amazing example to me of professionality, knowledge, and business skills.

Thanks to the **R&D Toronto team** namely **Dr. Andrew Needles, Dr. Andrew Heinmiller**, **Dr. Chris White, Dr. Alex Forbrich**, **and Dr. Stanley Poon** for their expertise and outstanding support at any time.

An endless thank goes to all the colleagues of the Amsterdam Sonosite/VisualSonics office, for all the Friday lunches and parties we have enjoyed together, for having always supportive words for me during the experiments in the lab, and for making every day in the office a happy day! In particular, I want to thank the **logistic**, **financial**, and **technical support** departments as well as all the colleagues from the **warehouse** and the **HR** team, their help has been fundamental to me over the years.

I wish to extend my sincere appreciation to my current and previous colleagues namely **Dr. Ariana Foinquinos** for being a real friend who I can always count on since we first met. She has

been a real personal and scientific mentor throughout my Ph.D. I'm really thankful to have her always by my side in life and in the lab. We had a ton of fun exploring the Netherlands and trying out delicious food together. She's very knowledgeable, honest, and made the trip a lot of fun for me. The lab advice and lessons she taught me made me a better scientist and I can't thank her enough.

A special thanks to **Dr. Katrin Suppelt** with whom I had a very good connection since the day of the interview (at the airport!!). During conferences and workshops, she has always been a constant source of support for me. It is always fun and a pleasure to meet and spend time with her. Her exceptional management skills, her honest feedback, and her professionality have had a huge impact on my growth along the Ph.D. journey.

I'm deeply thankful to **Joost Holthof** for his endless support and help in the lab. The lab was so much fun with him. He has been always available to help at any moment and I'm deeply thankful for all the experiments we did together.

Thanks to **Dr. Sandra Meyer** for all the time spent together anytime she was visiting the Amsterdam office. I'm grateful for her precious guidance inside and outside the lab. She has been a very special help and support for me.

I would further like to thank **Dr. Alwin de Jong** and **Prof. Dr. Margreet de Vries** for their support and insightful collaboration as well as for all the "Leiden Experiments" I had the possibility to participate in.

A special thanks to **Prof. Dr. James Joseph** and **Prof. Dr. Jason Raymond** for their collaboration, expertise, knowledge, and valuable advice through the anthropomorphic heterogeneous mouse phantom characterization. Their feedback has been always so constructive.

This Ph.D. project is part of the **MgSAFE** training network that has received funding from the European Union's Horizon 2020 research and innovation program under the **Marie Sklodowska-Curie** grant agreement No 811226. I'm tremendously grateful to have been part of such a prestigious program and to all the researchers I had the possibility to work with. A special thank goes to **all the PIs and scientists** that have been always of great help and open to collaborations. In particular, I'm very thankful to **Prof. Dr. Luca Menichetti**, **Prof. Dr. Peyman Mirtaheri, Dr. Martin Meier, Dr. Bruno Koller, and Prof. Dr. Håvard Haugen** for hosting me in their labs and for their enriching collaboration. I'm extremely thankful for the scientific conversations I had during the MgSAFE workshops with **Prof. Dr. Annelie Weinberg, Dr. Nicole Sommer**, **Prof. Dr. Peter Thomsen, Prof. Dr. Wojciech Święszkowski, Prof. Dr. Tomasz Płociński, Prof. Dr. Toralf Niendorf, and Dr. Jan-Marten Seitz**, for their expert advice which has been an exceptional lesson of growth for me.

I'm deeply grateful to **Prof. Dr. Berit Zeller-Plumhoff** for her endless support during conferences and scientific activities. Her talks and knowledge have been always so inspiring.

A special thanks to **Dr. Katharina Philipp** and **Dr. Annette Havelberg** for their constant support, endless patience, kindness, and hard work in coordinating the activities of the MgSAFE network.

On a personal note, I would like to thank **Diana, Jon, Edu, Begüm, Sebastian, Christina, Romy, Leon, Kamila, Hanna, Heithem, Wajahat, Mostafa, Masha, Maryam, and Marwa** for the real friendship bond that we have created over the years, for the moral support, for the laughs, for the scientific meetings and the parties, for the travels, and for all the unforgettable memories we have shared during the Ph.D. This journey has been so special thanks to each of you guys. I have learned many different things from your uniqueness and I'm so thankful I had the pleasure to meet each of you, thanks for always being there for me!! Both personally and professionally, I will always be there for you.

I am thankful to all **my dear friends from Pisa** as well as my former lab mates and supervisors for their scientific discussions, support, collaborations, and friendship over the years. They have helped me in my research whenever they could and it has been always special to re-meet them around the world.

I would also like to express my gratitude to **my best friends from Mazzarino** for their friendship, wholehearted moral support, and encouragement throughout this time.

Most importantly, my heartfelt love, gratitude, and sincere thanks to **my family** and especially my big brother for their constant faith in my capabilities. I am extremely grateful to my parents who have always inspired me through their hard work and motivation and taught me to take everything with a positive attitude and see every challenge as an opportunity to expand my knowledge.

Love you all,

Valeria

List of publications

Journal articles (peer-reviewed)

- **Grasso, V.,** Holthof, J. & Jose, J., (2020). An automatic unmixing approach to detect tissue chromophores from multispectral photoacoustic imaging. Sensors, 20(11), p.3235.
- **Grasso, V.,** Willumeit-Römer, R., & Jose, J. (2022). Superpixel spectral unmixing framework for the volumetric assessment of tissue chromophores: A photoacoustic data-driven approach. Photoacoustics, 26, 100367.
- **Grasso, V.,** Hassan, H. W., Mirtaheri, P., Willumeit-Römer, R., & Jose, J. (2022). Recent advances in photoacoustic blind source spectral unmixing approaches and the enhanced detection of endogenous tissue chromophores. Frontiers in Signal Processing, p.67.
- Hassan, H.W., **Grasso, V.,** Korostynska, O., Khan, H., Jose, J. & Mirtaheri, P., (2021). An overview of assessment tools for determination of biological Magnesium implant degradation. Medical Engineering & Physics, 93, pp.49-58.
- Hassan, H. W., Mota-Silva, E., **Grasso, V.,** Riehakainen, L., Jose, J., Menichetti, L., & Mirtaheri, P. (2023). Near-Infrared Spectroscopy for the In Vivo Monitoring of Biodegradable Implants in Rats. Sensors, 23(4), 2297.

Articles under review

- **Grasso, V.,** Raymond, J., Willumeit-Römer, R., Joseph, J. & Jose, J., (2023). Development of a morphologically realistic mouse phantom for pre-clinical photoacoustic imaging. Medical Physics.

Conference proceeding

- **Grasso, V.,** Willumeit-Römer, R., & Jose, J. (2021, September). Unsupervised Multi-spectral Photoacoustic Framework for the Detection and Quantification of Tissue Chromophores. In 2021 IEEE International Ultrasonics Symposium (IUS) (pp. 1-4). IEEE.

- **Grasso, V.,** Willumeit-Römer, R., & Jose, J. (2023, March). Development of an AI-assisted multi-spectral photoacoustic imaging for volumetric molecular tissue composition: a multi-frequency translational approach. In Photons Plus Ultrasound: Imaging and Sensing 2023 (Vol. 12379, p. 1237902). SPIE.
- **Grasso, V.,** Raymond, J., Willumeit-Römer, R., Joseph, J., & Jose, J. (2023, March). Development and characterization of a durable tissue-mimicking phantom for calibration and standardization of photoacoustic imaging. In Photons Plus Ultrasound: Imaging and Sensing 2023 (p. PC123793D). SPIE.

Manuscript submitted

- **Grasso, V.,** Willumeit-Römer, R. & Jose, J., (2023). Multi-frequency photoacoustic imaging for tissue monitoring in presence of biodegradable bone implants: "En route to the clinics". Sensors.

Patent

- **U.S. Patent: "SYSTEM, METHOD, AND APPARATUS FOR MULTI-SPECTRAL PHOTOACOUSTIC IMAGING"**

  Inventors: Valeria Grasso (Amsterdam, The Netherlands) & Jithin Jose (Manchester, UK)

  Application No. 17/957,400

  Filing Date: September 30, 2022

  Ref.: 63/002,714 (2020)

Honors & Awards

- **Best Paper Award – March 2022**

  Awarding institution: International Conference on Recent Trends in Photonics NPS 2022, by IEEE Photonics Society Kerala.

  Title: "Broadband photoacoustic imaging for biodegradable bone implant applications."

- **Best Paper Award – Applications of 3D Printing – January 2022**

  Awarding institution: SPIE Photonics West 2022 by Henry Helvajian, Chair of SPIE Applications of 3D Printing.

  Title: "An advanced 3D-printed anthropomorphic phantom for the multimodality imaging of CT, MRI, Ultrasound, and Photoacoustic calibration."

  This award recognizes outstanding contributions in the merging of tools and techniques used in 3D printing, fabrication, and manufacturing. This paper is recognized for the development and fabrication of a phantom that mimics the detailed morphology including the skeleton and the main abdominal organs using a combination of image modeling, gel-based materials, and 3D printing. The phantom has multimodal imaging capability (CT, MRI, Ultrasound, and Photoacoustic).

- **Best Presentation Award – August 2020**

  Awarding institution: European Society for Molecular Imaging - EMIM 2020.

  Title: "An advanced machine learning algorithm for the automated detection of tissue chromophores from multi-spectral photoacoustic images."

About the author

Valeria Grasso received her Master's degree in Biomedical Engineering from the University of Pisa, Italy, in 2018. She has worked as an Early Stage Researcher (Ph.D. student) within the Marie Curie network called MgSAFE since April 2019. She conducted her research activity based at FUJIFILM VisualSonics, Amsterdam, The Netherlands, and was affiliated with the Christian-Albrecht University of Kiel, Kiel, Germany. Her main research interest centers on optimizing the high-resolution Ultrasound and Photoacoustic (US-PA) imaging technology to non-invasively monitor the molecular changes in the soft tissues surrounding biodegradable bone implants made of Magnesium (Mg). Her current work focuses on the development of advanced US-PA image processing algorithms and optimal hardware solutions to adapt the US-PA technology for human patients treated with biodegradable Mg-based implants in case of bone injuries.